Virginia Commonwealth University
VCU Scholars Compass

Theses and Dissertations | Graduate School

2011

Vapor Transport and Aerosol Dynamics in the Respiratory Airways

Geng Tian
Virginia Commonwealth University

Follow this and additional works at: https://scholarscompass.vcu.edu/etd

 Part of the Engineering Commons

© The Author

Downloaded from
https://scholarscompass.vcu.edu/etd/2442

This Dissertation is brought to you for free and open access by the Graduate School at VCU Scholars Compass. It has been accepted for inclusion in Theses and Dissertations by an authorized administrator of VCU Scholars Compass. For more information, please contact libcompass@vcu.edu.

© Geng Tian 2011
All Rights Reserved

VAPOR TRANSPORT AND AEROSOL DYNAMICS IN THE RESPIRATORY AIRWAYS

A dissertation submitted in partial fulfillment of the requirements for the degree of Doctor of Philosophy at Virginia Commonwealth University.

by

GENG TIAN

Master of Science, Saint Mary's University, Canada, 2005

Bachelor of Science, Xi'an University of Science and Technology, China, 2002

Director: Dr. P. WORTH LONGEST

Associate Professor, Department of Mechanical and Nuclear Engineering and Department of Pharmaceutics

Virginia Commonwealth University

Richmond, Virginia

May, 2011

Acknowledgement

Working as a Ph.D. student in the Department of Mechanical and Nuclear Engineering at Virginia Commonwealth University was a magnificent as well as challenging experience to me. It was hardly possible for me to thrive in my doctoral work without the precious support of these personalities. Here is a small tribute to all those people.

First of all, I would like to express my deep and sincere gratitude to my advisor, Dr. Worth Longest, for introducing me to the world of respiratory drug delivery research. His immense knowledge, cheerful enthusiasm, and his logical way of thinking have been of great value for me. His understanding, encouragement, patience, inspiration, motivation, and personal guidance have provided a good basis for the present dissertation. I would have been lost without him. For me, he is not only a scientist, but also a lifetime friend and mentor.

I wish to express my gratitude to my dissertation committee members, Dr. Ramana M. Pidaparti, Dr. Hooman V. Tafreshi, Dr. Michael Hindle, and Dr. Rebecca Segal for their great assistance with writing this dissertation, giving wise advice and suggestions, and so on.

I would like to thank the School of Engineering and Department of Mechanical Engineering for their support in the form of scholarships. I am grateful to the faculty and staff of the Department of Mechanical Engineering, for assisting me in many different ways. I especially thank Dr. Karla Mossi, who is our director of graduate studies.

I am indebted to my many student colleagues and friends for providing a stimulating and fun environment in which to learn and grow. I am especially grateful to Ross L. Walenga, Landon T. Holbrook, Joshua Clarke, Ryan Tate, Rachel Waxman, Qiang Wang, Hao Zhang, Yezuo Wang, Renishhumar Delvadia, Casey Grey, and Dr. Guoguang Su.

I would also like to thank all my friends for helping me get through the difficult times, and for all the emotional support, entertainment, and caring they provided. A special thanks to Robert Rhinehart.

Finally, I want to express my appreciation to my parents, Wenmin Tian and Hali An, my sister and her husband, Jing Tian and Elvis Essavi, for their love, understanding, patience, endless support, and never failing faith in me. To them I dedicate this dissertation.

Table of Contents

List of Tables

List of Figures

Abstract

VAPOR TRANSPORT AND AEROSOL DYNAMICS IN THE RESPIRATORY AIRWAYS

By Geng Tian

A dissertation submitted in partial fulfillment of the requirements for the degree of Doctor of Philosophy at Virginia Commonwealth University.

Virginia Commonwealth University, 2011

Director: Dr. P. Worth Longest

Associate Professor, Department of Mechanical Engineering and Department of Pharmaceutics

Predicting vapor transport and aerosol dynamics in the respiratory airways is important for analyzing both environmental exposure and respiratory drug delivery. A large number of analytical models, computational studies, and experiments on vapor and aerosol transport in the respiratory tract have been conducted previously. However, a number of critical questions remain unanswered. In this study, computational fluid dynamics (CFD) is primarily employed with frequent comparisons to existing and new experimental data sets to address previously unanswered issues related to the transport of vapors and aerosol in the respiratory tract. The three objectives of this study are further described below.

Objective 1: A CFD model was developed to predict the transient absorption of inhaled vapors in the respiratory tract. Results indicated that

transient absorption can significantly influence the transport and uptake of vapors in the walls of the conducting airways.

Objective 2: The concept of enhanced condensational growth (ECG) applied to respiratory drug delivery was tested in a representative airway model extending from the oral cavity to the end of the tracheobronchial (TB) airways. Results indicated that ECG is an effective method to provide near full lung retention of the aerosol. The CFD results also indicated that the ECG delivery approach under transient inhalation conditions increased aerosol deposition in the TB airways by only a small amount, as compared with steady state conditions.

Objective 3: The effect of transient waveforms on the transport and deposition of pharmaceutical aerosols from inhalers in the upper airways was considered. Results indicated that the CFD model predictions matched the *in vitro* experiments to a high degree. The CFD results also indicated that it was critical to consider transient inhalation effects when assessing aerosol deposition. The stochastic individual path (SIP) modeling approach was then introduced and implemented to evaluate the transport and deposition of pharmaceutical aerosols from inhalers in medium and small TB airways. Results indicated that steady state inhalation could be used to predict deposition efficiencies in the TB airways between the 4th branch (B4) and the bronchioles (B15).

Chapter 1. Specific Aims

The overall goal of this project is to investigate under-explored areas of vapor transport and aerosol dynamics in the respiratory tract. Computational fluid dynamics (CFD) is primarily employed with frequent comparisons to existing and new experimental data sets. New experimental data related to this project was developed in collaboration with the VCU Department of Pharmaceutics (Dr. Michael Hindle) as part of an active NIH R21 grant and FDA contract. Applications of this research include developing a better understanding of the dosimetry of gaseous pollutants in the respiratory tract and the development of new therapeutic techniques for treating lung diseases and systemic conditions. Specifically, this work will develop dosimetry models for inhaled gaseous species, optimize the use of the enhanced condensational growth approach to improve the delivery of therapeutic aerosols to the lungs, and predict local and regional deposition of pharmaceutically relevant polydisperse aerosols from pressurized metered dose inhalers (MDIs) and dry powder inhalers (DPIs) throughout the tracheobronchial (TB) airways. These applications are further described below in the form of objectives.

Objective 1: Transient Absorption of Inhaled Vapors.

Current models of vapor absorption in the respiratory airways assume that transport into the walls is a steady state process. However, simple non-dimensional analysis reveals that airway wall resistance makes absorption a transient process over the course of an inhalation cycle. As a result, current models of vapor absorption may significantly over- or under predict uptake and dose by an order of magnitude or more. The objective of this study is to develop a CFD model to predict the transient absorption of inhaled vapors in the respiratory tract. This objective is divided into the following three tasks.

Task 1.1. Determine if transient absorption is significant over the course of an inhalation cycle in a simple mucus-tissue-blood representation of the airway wall.

Task 1.2. Develop a CFD boundary condition for predicting transient wall absorption and uptake in a complex respiratory geometry.

Task 1.3. Apply the transient CFD boundary condition to evaluate the effects of both transient inhalation and transient absorption on regional and local uptake in a model upper airway geometry.

To determine if transient absorption is important, both numerical and analytical solutions of absorption will be considered in a multilayer approximation of the respiratory wall. The absorption of highly and moderately soluble compounds will be considered over the time cycle of one inhalation (~ 2 seconds). Provided transient effects are important, the analytical solution will be

extended to allow for implementation as a CFD boundary condition. This will require the addition of an air-phase and a variable air-mucus concentration value. The CFD boundary condition will then be applied in a mouth-throat upper airway geometry. Comparison will be made between absorption predictions based on the standard steady state model and the new transient boundary condition. The effects of steady state vs. transient flow will also be evaluated. These results will provide a new, more accurate method to predict vapor absorption in the respiratory tract. It is expected that the transient model will ultimately improve upon the steady state predictions by a factor of 10X or more.

Objective 2: The Concept of Enhanced Condensational Growth.

Our group has recently proposed the concept of enhanced condensational growth (ECG) for improved respiratory drug delivery. In this approach, a nanoaerosol containing at active agent (drug or marker) is initially generated and inhaled past the mouth-throat (MT) resulting in low deposition and loss. The nanoaerosol is delivered with sufficient water vapor to cause supersaturation and aerosol growth to micrometer size in the tracheobronchial (TB) and/or alveolar airways, which facilitates pulmonary retention. As a result, negligible MT and near 100% lung deposition is possible. Furthermore, regional TB or alveolar deposition can be engineered allowing for drug targeting by controlling the rate of size increase. Factors affecting the rate of growth include the initial aerosol size, drug hygroscopicity, and the gas phase conditions of the humidity and aerosol delivery streams (i.e., temperature, relative humidity, and flow rate).

The prediction of aerosol growth in the ECG approach requires accurate knowledge of the relative humidity (RH) field surrounding the nanoaerosol. To extend this concept, the following tasks are proposed.

Task 2.1. Determine the size increase of aerosols in a single path model from the MT region through the TB geometry (~ generation G16).

Task 2.2. Consider the effects of transient inhalation waveforms on the ECG process in the upper TB airways.

Previous studies have indicated that ECG increases aerosol size from the submicrometer range to approximately 2 - 3 μm. However, transient inhalation will affect both aerosol inertia and RH conditions. Furthermore, only delivery in the upper airways has been explored. Relative humidity and growth conditions need to be investigated throughout the TB region. Finally, the ECG approach can potentially be tailored for targeted respiratory drug delivery. Conditions for lung deposition in the upper, mid, and lower regions of the respiratory tract should be explored.

Objective 3: Local and Regional Deposition of Pharmaceutical Aerosols.

Previous whole-lung particle deposition models have been used to assess branch-averaged deposition. However, inaccurate predictions of absorption associated with using idealized aerosols and neglecting interactions at the patient-device interface remain significant shortcomings of these models. In contrast, fully resolved three-dimensional (3-D) models with pharmaceutical delivery devices can predict local and regional deposition in the TB airways. Furthermore, local and regional deposition can be extended to predict dissolution and

absorption into the airways and bloodstream. Therefore, the objective of this study is to develop a CFD model of orally inhaled drug products that can account for inhaler attributes (spray or jet momentum), physicochemical properties (aerodynamic size distribution and dissolution), and physiological parameters (breathing pattern and airway geometry) in determining local and regional deposition throughout the TB airways. Specifically, this objective is divided into the following two tasks.

Task 3.1. Develop a CFD model to evaluate aerosol deposition in a realistic MT and upper TB model and validate the developed model using new *in vitro* results in the geometries considered for specific inhaler devices.

Task 3.2. Characterize deposition within the right lower lung lobe using the stochastic individual path (SIP) model approach.

For accurate delivery predictions, MDI and DPI inhaler types have been considered based on (i) the exceedingly large drug losses in the upper airways, and (ii) the effect of reduced drug aerosol fractions and induced turbulence on deposition in the lower airways.

Chapter 2. Background

Predicting vapor transport and aerosol dynamics in the respiratory airways is important for analyzing both environmental exposure and respiratory drug delivery. A large number of analytical models, computational studies, and experiments on vapor and aerosol transport in the respiratory tract have been conducted previously. However, a number of critical questions remain unanswered. For example, the effects of transient vapor absorption into the walls of the conducting airways have not previously been considered. The delivery of inhaled medicines to the lungs is known to be highly inefficient due to large depositional losses in the delivery device and extrathoracic region. In this study, computational fluid dynamics (CFD) is primarily employed with frequent comparisons to existing and new experimental data sets to address previously unanswered issues related to the transport of vapors and aerosol in the respiratory tract. Background information further motivating the objectives of this study is provided in this chapter.

2.1 Objective 1: Transient Absorption of Inhaled Vapors.

Determining the transport and absorption of inhaled vapors in the respiratory tract is an important step in predicting the biological responses and health effects of exposures (Jarabek 1995). Sources of inhaled vapors may include potentially toxic environmental pollutants, noxious compounds released in a chemical terrorist attack, combustion byproducts resulting from fires, and medical gases. The dosimetry of these chemical species in the respiratory tract is controlled by both gas-phase motion in the airways and mass transport through

the respiratory liquid and tissue layers and into the bloodstream. A number of studies have considered the gas-phase transport and surface absorption of inhaled chemical species (Frederick et al. 1998; Kimbell and Subramaniam 2001; Shi et al. 2006; Zhang and Kleinstreuer 2006; Zhang et al. 2006b). Other studies have more directly focused on the mass transport process through the walls of the respiratory tract (Aharonson et al. 1974; Anderson et al. 2003; Chang et al. 1983; Cohen Hubal et al. 1996a; Morris and Blanchard 1992; Morris and Cavanagh 1986; Morris and Cavanagh 1987).

The mass transport of chemical species within the lining of the respiratory tract is controlled by solubility, diffusion, and wall structure. Motion of the liquid lining and blood can also create convective transport. Highly and moderately soluble compounds are largely absorbed in the upper respiratory tract (URT), which effectively protects the more sensitive alveolar airways. Some highly soluble compounds like formaldehyde are almost completely absorbed in the extrathoracic airways during nasal inhalation (Chang et al. 1983; Cohen Hubal et al. 1997; Kimbell et al. 2001b). Even relatively insoluble compounds like ozone are largely absorbed in the lower tracheobronchial airways as surface area increases, thereby significantly reducing the amount reaching the alveolar region. For species absorbed in the URT, the mucus layer serves as a barrier that reduces absorption in the tissue and blood components of the wall structure. Therefore, an accurate view of absorption into the mucus is essential to determine doses received in the lower layers. Doses of inhaled vapors that reach the respiratory tract tissue may be associated with a local response such as bronchoconstriction

and injury in the case of inhaled pollutants. Compounds that reach the blood may result in systemic uptake and related toxicological effects. Furthermore, an accurate prediction of absorption in the URT is important to determine penetration depth of inhaled vapors traveling down the respiratory tract and into the highly sensitive alveolar region.

Mass transport through the walls of the URT has been modeled using a variety of approaches. Cohen Hubal et al. (1996a) summarized previous models of URT absorption and categorized the existing models as early, lumped parameter, and distributed parameter approaches. Early models were used to gain qualitative physical insight regarding the absorption process (LaBelle et al. 1955). Lumped parameter models assume well-mixed compartments and consider only time-dependent concentration variables (Chang et al. 1983; Morris and Blanchard 1992; Morris and Cavanagh 1986; Morris and Cavanagh 1987). Distributed parameter models consider both spatial and temporal concentrations (Aharonson et al. 1974; Kimbell et al. 1993). The first distributed parameter model was reported by Aharonson et al. (1974) to examine the effects of airflow rate on the uptake of soluble vapors in the nose. In this model, a transient expression for total uptake was developed based on a local mass transfer coefficient. As with Aharonson et al. (1974) most of the lumped parameter and distributed parameter models reviewed by Cohen Hubal et al. (1996a) considered the effect of absorption time on uptake into the mucus and tissue. However, these models assumed that a steady state diffusion flux through the respiratory airway wall was reached instantaneously. This assumption neglects the effects of transient

diffusion on the absorption and uptake of vapors. To gain a better understanding of the time scale for absorption in a multilayer system consisting of air, mucus, tissue, and blood, transient flux boundary conditions were implemented in a multilayer CFD model of the transport in the upper airways.

Computational fluid dynamics (CFD) modeling provides a distributed parameter approach that has been used to simulate the transport and uptake of vapors in the respiratory tract. This approach uses CFD to simulate airflow dynamics and applies an analytically determined boundary condition to model absorption in either a mucus or a mucus-tissue representation of the wall. Some studies assume high reactivity of the inhaled vapor and apply a zero concentration boundary condition at the wall surface (Shi et al. 2006; Taylor et al. 2007; Zhang and Kleinstreuer 2003). Studies considering solubility and potential reactions in a mucus layer include Keyhani et al. (1997), Zhang et al. (2006), and Zhao et al. (2004). Other studies have considered solubility and reactivity in a mucus-tissue representation of the URT (Cohen Hubal et al. 1996b; Cohen Hubal et al. 1997; Frederick et al. 1998; Kimbell et al. 2001a). However, as with previous studies, all computational models assume that steady state diffusion through the mucus or mucus and tissue layers is reached instantaneously. That is, the concentration profiles are immediately linear and a constant flux is assumed through the mucus and tissue walls into the blood.

In previous mass transport models, the assumption of steady state diffusion through the mucus and tissue of the URT was based on the observation that these layers are thin compared with the airway lumen. However, this assumption

neglects the fact that diffusion is much slower in liquids than in air. To gain a better understanding of the time scale for absorption, the mass transfer Fourier number (Fo_m) should be considered, which is defined as

$$Fo_m = \frac{D}{H^2} t \qquad (2.1)$$

In this expression, D is the diffusivity of the chemical species in mucus or tissue, H is the height of the layer, and t is the absorption time. Values of Fo_m less than 10 typically indicate that transient effects are significant in the diffusion process. Considering the mucus layer ($H_m \sim 10$ μm and $D_m \sim 5\times10^{-6}$ cm^2/s) (ICRP 1994) for a characteristic inhalation time scale of 1 second, the Fourier number is 5. For a combined mucus and tissue layer ($H_{mt} \sim 60$ μm and $D_{mt} \sim 5\times10^{-6}$ cm^2/s) (ICRP 1994), the Fourier number is approximately 0.14. As a result, transient effects in the diffusion process may significantly influence the uptake of chemical species through a mucus or mucus-tissue barrier. For example, flux into the mucus may be faster than predicted with a steady state assumption due to higher initial concentration differences. In contrast, flux into the blood may be slower than predicted with steady state conditions based on transient resistance in the higher layers. However, a more detailed analysis is needed to determine the quantitative effects of transient diffusion on the absorption and uptake of vapors over a characteristic time in a multilayer model of the respiratory walls.

2.2 Objective 2: The Concept of Enhanced Condensational Growth.

Enhanced Condensational Growth (ECG) Concept

Enhanced condensational growth (ECG) applied to respiratory drug delivery is a recently proposed concept that seeks to combine the advantages of both submicrometer and micrometer aerosols. In this approach, a submicrometer aerosol is delivered to the respiratory airways in conjunction with an airstream that is saturated or supersaturated with water vapor and above body temperature. The initially submicrometer particles or droplets, in the approximate size range of 100 – 900 nm, have very low deposition values in the mouth-throat (MT) and upper tracheobronchial regions (Cheng 2003; Cohen et al. 1990; Xi and Longest 2008a; Xi and Longest 2008b). As a result, aerosol loss in the MT can be largely eliminated. The inhaled water vapor is used to create supersaturation conditions within the respiratory airways. Submicrometer droplets in this supersaturated environment will increase in size at a controlled rate due to condensation. Size increases to within the range of 2 – 3 μm can be used to ensure full lung retention of the aerosol. Furthermore, engineering the rate of size increase can be used to target deposition within specific regions of the lung. Factors influencing the amount and rate of size increase with the ECG approach include the degree of supersaturation, temperature, particle or droplet hygroscopicity, initial size, and aerosol number concentration. However, the effects of these variables on aerosol size growth have only been investigated on a very limited basis.

Hygroscopic Aerosol Growth in the Lungs

The relative humidity (RH) of the tracheobronchial airways beyond the first several bronchi is generally expected to be 99.5% (Ferron 1977). Furthermore, many inhaled environmental and pharmaceutical aerosols are soluble. As a result, hygroscopic effects are known to influence the deposition of these inhaled respiratory aerosols (Ferron 1977; Ferron et al. 1988; Finlay and Stapleton 1995; Li and Hopke 1993; Martonen et al. 1982; Zhang et al. 2006b). Hygroscopic particle growth has been investigated experimentally for NaCl particles (Cinkotai 1971), pharmaceutical aerosols (Peng et al. 2000), and combustion droplets (Li and Hopke 1993). A number of mathematical models have also been formulated for the hygroscopic growth of respiratory aerosols at RH values below 100% (Broday and Georgopoulous 2001; Ferron 1977; Ferron et al. 1988; Ferron et al. 1989; Finlay and Stapleton 1995; Robinson and Yu 1998; Varghese and Gangamma 2009). These studies typically indicate a maximum size increase of approximately 400% for NaCl particles. The hygroscopic growth of most other salts and most pharmaceutical aerosols result in size increases less than 100% at RH values of 99.5% and below (Ferron et al. 1988; Ferron et al. 1989). Recently, Zhang et al. (2006a) developed a CFD model of hygroscopic growth in the upper respiratory tract. It was found that saline concentrations of 10% and higher were required for hygroscopic growth to have a significant impact on deposition. Finlay and Stapleton (1995) applied a numerical model to show that mass coupling between aerosol droplets and the continuous phase was significant for

droplet concentrations above 25,000 part/cm^3. However, all of these previous studies have only considered RH conditions up to 100%.

Supersaturation in the Respiratory Airways

Very little work has been done to evaluate the effects of RH conditions above 100% (i.e., supersaturated conditions) on the condensational growth of respiratory aerosols. However, supersaturated conditions can be achieved in the respiratory tract through the inhalation of warm ($T > T_{body}$) saturated air. Ferron et al. (1984) has shown that RH above 100% is possible in the upper respiratory tract under some inhalation conditions. Significant growth of NaCl particles was observed for very localized supersaturation in the nasal cavity (Ferron et al. 1984). Longest and Xi (2008) considered the inhalation of warm humidified air during smoking. Computational fluid dynamics simulations indicated that the inhalation of warm saturated air approximately 3 ^oC above body temperature could result in supersaturation conditions (RH > 100%) through approximately the 6th respiratory bifurcation. Moreover, submicrometer aerosols exposed to RH conditions in the range of 101% experienced a large and rapid increase in size.

2.3 Objective 3: Local and Regional Deposition of Pharmaceutical Aerosols.

Inhalation of aerosol drugs is widely used in the treatment of asthma and chronic obstructive pulmonary disease (COPD). Predicting the regional and highly localized deposition of pharmaceutically aerosols from oral drug delivery devices is a critical component in determining the dose received and the resulting

local and systemic responses (Isaacs et al. 2005; Martonen et al. 2005a; Martonen et al. 2005b). Whole-lung and regional models as well as experiments in respiratory casts have been employed to investigate aerosol dynamics and deposition in the lung (Balashazy et al. 2003; Comer et al. 2000; Darquenne 2002; Darquenne and Paiva 1996; Hofmann et al. 2003; Karl et al. 2004; Kimbell and Subramaniam 2001; Liu et al. 2002; Martonen et al. 2003; Martonen et al. 2001; Schroeter et al. 2001; Zhang and Kleinstreuer 2002; Zhang et al. 2005; Zhang et al. 2004). Whole-lung deposition models can predict deposition based on the branch-averaged correlations (Asgharian et al. 2001; ICRP 1994; Martonen 1993; NCRP 1997). Additionally, CFD models have been used to determine branch-averaged deposition in whole-lung modeling (Balashazy et al. 2003; Hofmann et al. 2003; Zhang et al. 2005). These models considered the effects of multiple physiological, geometric, and particle characteristics on deposition patterns. A number of these studies have quantitatively validated the resulting aerosol deposition rates with *in vitro* data (Liu et al. 2002; Longest and Vinchurkar 2007b; Martonen et al. 2001; Oldham et al. 2000; Zhang and Kleinstreuer 2002). However, these models neglected the importance of the interface between device and patient in achieving efficient aerosol drug delivery to the lungs. For this reason, a validated CFD model is needed which can account for inhaler characteristics (spray or jet momentum), drug physiochemical properties (aerodynamic size distribution, dissolution) and physiological parameters (breathing pattern, geometry) in determining local and regional deposition in the TB airways. Specifically, pressurized metered dose inhalers (MDIs) and dry

power inhalers (DPIs) deliver drug while target inflammation control and airway dilation (Ibsen and Bratton 1999), are considered in this study. These two representative classes of inhalers are the most common devices for administering drugs for inhalation. Pharmaceutical aerosols from MDIs are delivered as a spray droplet by actuation of the canister contains a pressurized propellant drug formulation, in contrast, DPIs are breath actuated and deliver a power aerosol.

Chapter 3. Transient Absorption of Inhaled Vapors into a Multilayer Mucus-Tissue-Blood System

3.1 Introduction

Individual multilayer models are considered that represent the wall dimensions of the nasal extrathoracic, upper, and lower tracheobronchial airways. A constant concentration of vapor species is assumed at the air-mucus interface and zero concentration is assumed in the blood. The sample vapors considered are highly or moderately soluble in mucus and tissue. To determine absorption, mass transport is calculated based on an existing analytical steady state solution, a new analytical transient solution, and a numerical transient solution. Comparisons of results from multiple approaches are used to assess solution quality. Differences between steady and transient solutions are used to evaluate the importance of transient effects on the diffusion and uptake process. The effects of chemical reactions in the mucus and tissue over time are also explored for a range of first-order reaction rate constants using the numerical model. These results can be implemented to (i) expand previous estimates of steady state diffusion to more realistic transient conditions and (ii) lay the foundation for an analytic boundary condition that accounts for transient diffusion in a CFD model of respiratory tract absorption and uptake. Furthermore, the solution techniques developed in this study can be applied to analyze the transport of chemicals in other multilayer systems such as absorption through mucus in the gastrointestinal tract and dermal uptake.

The objective of this study was to evaluate the mass transport of sample chemical species through a simple multilayer system composed of mucus, tissue, and blood components on a transient basis and compare with steady state results.

3.2 Methods

In this study, vapor absorption and transport are considered through the walls of the conducting airways, which are responsible for delivering air to the alveolar region. Using the notation of Weibel (1963), the conducting airways originate at the nose or mouth and extend to approximately generation 16. The walls of the conducting airways are lined with a thin layer of protective mucus (Yeates et al. 1997). The mucus layer is typically considered to keep the surfaces of the airways moist, condition incoming air, and trap inhaled particles and microorganisms. In addition, mucus also serves as a barrier that controls the absorption of gases and drugs into the walls of the conducting airways. Clearance of soluble and insoluble compounds trapped in the mucus is accomplished by ciliary motion, which propels the mucus up the respiratory tract to be expelled or swallowed (Yeates et al. 1997). The cilia move in a watery substance that lies under the mucus and is referred to as sol, which also helps lubricate the motion of the more viscous mucus layer. Cilia are present throughout the conducting airways and are secured to an epithelial layer, which is mostly composed of ciliated, basal, and goblet cells. The epithelial layer is attached to a basement membrane, which is then followed by a sub-epithelium layer that is highly vascularized (ICRP 1994).

To approximate transport within the walls of the conducting airways in this study, a model system was considered that consists of mucus, tissue, and blood layers (Fig. 3.1). The liquid mucus and sol regions, which contain the cilia, were considered to form a single mucus layer. As described below, convection due to ciliary motion and clearance were neglected in this study. The epithelial region was approximated as a generalized tissue layer. Finally, the highly vascularized sub-epithelium region was assumed to form a blood layer. The resulting multilayer model is identical to the mucus-tissue-blood airway approximation considered by Cohen Hubal et al. (1996b; 1997) and adds tissue and blood layers to the previous approximations considered by Keyhani et al. (1997), Zhang et al. (2006), and Zhao et al. (2004).

In this study, convection due to mucus motion was neglected and transport through the multilayer system was assumed to result from pure diffusion. This assumption was based on the relative rates of convective transport due to mucus motion compared with diffusive transport through the thin mucus layer. For example, the average rate of mucus motion in the trachea, which has the fastest clearance in the tracheobronchial region, is 9.2×10^{-2} mm/s (Foster et al. 1980). For approximate tracheal conditions ($H_m \sim 1\times10^{-3}$ cm and $D_m \sim 5\times10^{-6}$ cm^2/s), the timescale for diffusive transport through the mucus (H_m^2/D_m) is 0.2 s. Based on mucus velocity, the mucus moves approximately 0.02 mm over the timescale required for diffusive transport across the boundary. Considering the length of the trachea is approximately 9 cm (ICRP 1994), it is concluded that convective mucus motion can be neglected compared with diffusive transport across the

barrier and into the tissue. Similar results are found for lower lung generations, arising from the fact that mucus velocity decreases with depth into the lungs (Foster et al. 1980).

The purpose of this study is to evaluate the time dependent transport of vapors across a multilayer airway wall system. To facilitate this evaluation, constant concentrations of vapor species were assumed at the air-mucus and tissue-blood interfaces (Fig. 3.1). During inhalation *in vivo*, concentrations of vapors in the air, mucus, tissue, and blood are all interconnected. For example, decreasing the solubility of a species in the tissue layer will increase concentrations in the air and mucus phases. However, it is not necessary to consider variable air phase concentrations in order to determine the transient behavior of transport across the airway wall. As a result, to assess transient effects on diffusional wall uptake in this study, the air phase concentration is assumed constant and known *a priori*. At the tissue-blood interface, zero concentration of the vapor species is assumed. This approximation is justified for vapors absorbed in small quantities compared with blood volumes, compounds with high solubility in blood, or materials that are metabolized in downstream tissues and organs, such as the liver.

To approximate wall dimension for the conducting airways, multiple regions were considered. The conducting airways were divided based on the ICRP (1994) dosimetry model convention into extrathoracic (ET_2), bronchial (BB), and bronchiolar (bb) regions. The ET_2 region includes the nasal passages distal to the nasal valve, pharynx, and larynx. The BB region consists of the trachea

(generation 0), main bronchi, and distal bronchi ending with approximately generation 8. Finally, the conducting airways conclude with the bb region, which extends from generation 9 to approximately generation 16. Dimensions of each region are reported in Table 3.1, based on ICRP (1994) estimates. Considering the relative thicknesses of each layer, diffusive transport in the ET_2 and BB regions is expected to be similar. In contrast, the thin layers of the bb region will likely result in much faster absorption compared with the other models.

Vapor Species and Properties

Representative environmental pollutants considered in this study are acetaldehyde and benzene, which are highly soluble and moderately soluble in mucus, respectively. Substances with relatively low solubilities were neglected because they are already considered to be dependent on transient effects during the absorption process. Benzene is a known human carcinogen that may also cause nervous system disorders, immune system suppression, and anemia (ATSDR 2007b). Benzene is considered a hazardous air pollutant by the United States Environmental Protection Agency (US EPA) (1999) and is also found in mainstream and sidestream cigarette smoke (Sakuma et al. 1984). Acetaldehyde is also classified as a hazardous air pollutant (EPA 1999) that is a potential carcinogen in humans and may cause respiratory tract irritation and lesion formation at sufficient concentrations (ATSDR 2007a). Recently, acetaldehyde in cigarette smoke was linked to the formation of MAO-inhibitors, which may play a role in reinforcing tobacco smoke dependence and addiction (Talhout et al. 2007).

Transport through the airway wall is controlled by absorption into the mucus, diffusion across the mucus barrier, partitioning into the tissue, diffusion within the tissue, and partitioning into the blood. Therefore, two diffusional coefficients and three partition coefficients are needed to describe uptake in the multilayer system. Considering diffusion, the transport of a vapor species in mucus was assumed to be equivalent to diffusion in water at the same temperature (Cohen Hubal et al. 1996a). The diffusivity of a species in tissue was assumed to be approximately one-third of the value in water (George et al. 1996; Hlastala and Robertson 1998). The resulting diffusivities in mucus (D_m) and in tissue (D_t) are reported in Table 3.2 for a body temperature of 37 ^{o}C.

The mucus-air partition coefficient is defined in nondimensional form as

$$\lambda_{ma} = \frac{C_m}{C_a} \tag{3.1}$$

where the concentration of a species on the mucus side of the mucus-air interface, C_m (g/cm^3), is in equilibrium with the concentration on the air side C_a (g/cm^3). Considering that mucus is primarily composed of water (Yeates et al. 1997), the mucus-air partition coefficients were assumed to be equal to well known water-air coefficients. Species with $\lambda_{ma} >> 1$ are considered to be highly soluble in mucus, and coefficients in the range of 1 are assumed to be moderately soluble. Specific values of mucus-air partition coefficients are reported in Table 3.2 for acetaldehyde and benzene.

For most vapor species, the blood-tissue partition coefficient, λ_{bt}, is assumed to be equal to one (Anderson et al. 2003). The tissue-mucus partition coefficient, λ_{tm}, can be approximated as (Anderson et al. 2003)

$$\lambda_{tm} = \frac{1}{\lambda_{bt}} \frac{\lambda_{ba}}{\lambda_{ma}} \tag{3.2}$$

where λ_{ba} is the frequently reported blood-air partition coefficient. Values of both λ_{ba} and λ_{tm} are reported in Table 3.2 for the compounds of interest.

Governing Equations and Boundary Conditions

The transient diffusion equations governing absorption into the mucus and tissue can be expressed as

$$\frac{\partial C_m(y,t)}{\partial t} = D_m \frac{\partial^2 C_m(y,t)}{\partial y^2}, \quad y \in [0, H_m] \tag{3.3a}$$

$$\frac{\partial C_t(y,t)}{\partial t} = D_t \frac{\partial^2 C_t(y,t)}{\partial y^2}, \quad y \in [H_m, H_m + H_t] \tag{3.3b}$$

where y is the spatial coordinate defining the depth into the mucus and tissue. Heights of the mucus and tissue layers are denoted H_m and H_t, respectively. Concentrations $C_m(y,t)$ and $C_t(y,t)$ are the bulk densities of chemical species in mucus and tissue with units of g/cm^3. These concentrations are spatially and time dependent in each material. In the equations above, the left-hand-side accounts for temporal variations in concentration at a fixed location and the right-hand-side accounts for net diffusive transport through a control volume. Initially, zero concentration is assumed in the mucus and tissue. The boundary conditions of the multilayer system are

$$C_m(y,t)|_{y=0} = \lambda_{ma} C_{air}, \tag{3.4a}$$

$$C_t(y,t)|_{y=H_m} = \lambda_{tm} C_m(y,t)|_{y=H_m}, \tag{3.4b}$$

$$-D_m \frac{\partial C_m(y,t)}{\partial y}\Big|_{y=H_m} = -D_t \frac{\partial C_t(y,t)}{\partial y}\Big|_{y=H_m}, \quad (3.4c)$$

$$C_t(y,t)\big|_{y=H_m+H_t} = 0, \quad (3.4d)$$

where C_{air} is the concentration on the air side of the mucus-air interface (assumed to be constant). Equations (3.4a and 3.4b) imply that equilibrium occurs on each side of the thin mucus-air and mucus-tissue interfaces. Equation (3.4c) implies that the vapor species mass flux (mass flow rate of a compound per unit area with units of *g/s-cm*^{2}) leaving the mucus is equal to the flux entering the tissue. As indicated above, zero concentration of the vapor species was assumed in the blood. A summary of the multilayer system considered with the appropriate governing equations and boundary conditions is shown in Fig. 3.2.

Constant air-phase boundary conditions of acetaldehyde and benzene are taken to be 100 ppm (1.83×10^{-7} *g/cm*^{3}) and 1 ppm (3.19×10^{-9} *g/cm*^{3}), respectively, which are below OSHA short term exposure limits. Breathing frequencies for sedentary, light, and heavy activity conditions are 14, 21, and 33 breaths per minute, respectively (ICRP 1994). Assuming that inhalation occurs for one-half of the breathing cycle, the associated inhalation times are 2.2, 1.4, and 0.9 s. As a result, inhalation can be characterized as occurring for a period of approximately 1 to 2 s. Based on these estimates, transient effects that are significantly less than 1 s can be considered negligible. However, transient effects on the order of 1 s may significantly affect absorption over the inhalation period. In this study, transient absorption is considered for periods of 2 s and beyond to evaluate a range of potential breathing conditions and the time required to reach steady state. Furthermore, some simulations are conducted in which a 2 s inhalation period is

followed by a 2 s exhalation period with zero air phase concentration to evaluate the potential for species buildup in the mucus over multiple breath cycles.

Solution Techniques

In this study, the governing equations were solved using three different solution approaches with the goals of (*i*) evaluating the influence of transient effects on absorption and (*ii*) developing the form of an analytic solution that can be used as a boundary condition in a CFD model. First, a common steady state analytical solution was performed for comparison with transient solutions over time. An analytical transient solution was then developed by splitting the steady and time-dependent components of the governing equations and performing a Fourier series solution. To verify the transient analytical results, a numerical solution of the equations was then conducted with the Transient Absorption of Chemical Species (TAOCS) 1.0 program. Each of these solution techniques is described in more detail below.

Analytical Steady State Solution

For steady state conditions, the time derivative is not present in Equations (3.3a and b), and the resulting coupled ordinary differential equations have the solution

$$\tilde{C}_m(y) = \lambda_{ma} C_{air} - \frac{\lambda_{ma} C_{air} - \tilde{C}_m(y)|_{y=H_m}}{H_m} y, \qquad y \in [0, H_m] \tag{3.5a}$$

$$\tilde{C}_t(y) = \frac{\lambda_{tm} \tilde{C}_m(y)|_{y=H_m}}{H_t}(H_m + H_t) - \frac{\lambda_{tm} \tilde{C}_m(y)|_{y=H_m}}{H_t} y, y \in [H_m, H_m + H_t]$$

(3.5b)

In the expressions above, $\tilde{C}_m$ and $\tilde{C}_t$ represent concentrations in the mucus and tissue at steady state. The concentration on the mucus side at the mucus-tissue interface is obtained by substituting Equations (3.5a and 3.5b) into the flux condition provided by Equation (3.4c), resulting in

$$\tilde{C}_m(y)|_{y=H_m} = \frac{H_t D_m \lambda_{ma} C_{air}}{H_m \lambda_{tm} D_t + H_t D_m} \tag{3.5c}$$

Analytical Transient Solution

An analytical solution to the coupled transient set of partial differential equations is presented in Appendix A. Briefly, the transient ($\hat{C}_m$) and steady state ($\tilde{C}_m$) components of the solution can be separated. A substitution approach can then be used to evaluate the transient components of the equations. The resulting combined Fourier series and linear solution is expressed

$$\begin{aligned} C_m(y,t) &= \hat{C}_m(y,t) + \tilde{C}_m(y) \\ &= \sum_{n=1}^{\infty} W_n \sin(\mu_n \sqrt{\frac{D_m}{D_t}} \frac{H_t}{H_m}) \sin(\frac{\mu_n y}{H_m}) e^{-\mu_n^2 \frac{D_m}{H_m^2} t} + \lambda_{ma} C_{air} - \frac{\lambda_{ma} C_{air} - \tilde{C}_m(y)|_{y=H_m}}{H_m} y, \end{aligned} \tag{3.6a}$$

and

$$\begin{aligned} C_t(y,t) &= \hat{C}_t(y,t) + \tilde{C}_t(y) \\ &= \lambda_{tm} \sum_{n=1}^{\infty} W_n \sin(\mu_n) \sin(\mu_n \sqrt{\frac{D_m}{D_t}} \frac{H_m + H_t - y}{H_m}) e^{-\mu_n^2 \frac{D_m}{H_m^2} t} + \frac{\lambda_{tm} \tilde{C}_m(y)|_{y=H_m}}{H_t} (H_m + H_t - y) \end{aligned} \tag{3.6b}$$

In these equations, the eigenvalues μ_n were determined by solving a transcendental equation using Brent's method (Brent 1973), as described in

Appendix A. The Fourier series coefficients were determined by utilizing the orthogonal relation and zero concentration initial conditions. Compared with the steady solution (Eqs. 3.5a and 3.5b), the transient solution is observed to include a series expression, that decreases exponentially as a function of the transient mass Fourier number presented as Eq. (2.1).

Numerical Transient Solution

Equations (3.3a and 3.3b) and (3.4a-d) were also solved as a coupled set using the TAOCS 1.0 program. Zero initial concentration was assumed in the mucus and tissue layers as with the analytical solution. A finite volume method was used for the spatial discretization of the well-posed set of equations. Time integration was performed with a stiff implicit multi-step solver. The relative tolerance for numerically evaluating the equations was set to 1×10^{-12}. Decreasing the relative tolerance by an order of magnitude had a minimal impact (less than 1% difference) on concentration and uptake values throughout the system.

3.3 Results

Concentration Values

Concentration values for acetaldehyde and benzene within the model systems considered are shown in Fig. 3.3 based on the analytical transient and steady state solutions. In each case, the transient results are shown to approach the steady state solution over time. In the ET_2 region (Fig. 3.3a), significant differences between the transient and steady state solutions are observed at both 1 and 2 s. Again, a typical inhalation period is expected to last for approximately 2

s or less. These differences in concentration values over time will result in a variable flux and rate of absorption into the multilayer system. Temporal differences from steady state conditions appear more significant for benzene, which is less soluble in mucus but more soluble in tissue compared with acetaldehyde. for both compounds, the transient solution is shown to agree with the steady state conditions after 10 s.

Considering the BB region (Fig. 3.3b), concentrations over time are nearly identical to those found in the ET_2 region. This similarity is expected because there is little difference in layer heights between the ET_2 and BB models (Table 3.1). As a result, transient effects are also shown to be highly significant in the BB region over a timescale of approximately 2 seconds.

In the bb region (Fig. 3.3c), concentrations evolve approximately one order of magnitude faster in time compared with the upper airway models. Significant differences in mucus and tissue concentrations are observed to remain at 0.2 s. However, the analytical steady state and transient solutions are nearly identical at 1 s.

A comparison of analytical and numerical transient solutions of concentration over time is provided in Fig. 3.4 for acetaldehyde and benzene. Concentrations are only reported in the BB region to illustrate the close match between the analytical and numerical results. In each case, a point by point comparison of concentration values indicates that the analytical and transient solutions were on average within 0.1%. Similar results were found for the ET_2 and bb regions. Agreement between the approaches considered provides

confidence that the analytical solution includes a sufficient number of terms in the series summation (cf. Eqs. 3.6a and 3.6b) and is correct. The close match also indicates that numerical errors are small and controlled in the simulations.

Concentration values of acetaldehyde and benzene at the mucus-tissue interface are displayed in Fig. 3.5 over time. These results indicate the timeframe for establishing steady state transport through the mucus. The relative values of concentrations on the mucus and tissue sides of the interface also illustrate the effects of the mucus-tissue partition coefficients. For example, benzene is more soluble in tissue than in mucus ($\lambda_{tm} > 1$). Therefore, concentrations of benzene are higher in the tissue compared with the mucus. In each case, the concentration curves become flat over time as steady state conditions are approached. Considering the BB region (Fig. 3.5a), temporal effects for acetaldehyde and benzene appear relatively small after approximately 2 and 4 s, respectively. Results are similar for the ET_2 region (not shown). In the bb region, where the individual layers are significantly thinner, temporal effects for acetaldehyde and benzene are diminished after approximately 0.2 and 0.4 s, respectively (Fig. 3.5b).

Flux and Uptake

Flux values (g/s-cm^2) into the tissue and blood phases are reported in Fig. 3.6 for acetaldehyde and benzene in the BB and bb regions. Under steady state conditions, the fluxes into the tissue and blood are equal and are constant over time. However, results in Fig. 3.6 indicate that the transient flux values are highly variable over time. Flux into the tissue spikes just after t = 0 due to zero initial concentrations and the thin mucus layer. In contrast, flux into the blood

experiences a gradual increase as concentrations cross the thick tissue region and reach the lower boundary. In the BB region, fluxes of acetaldehyde and benzene reach constant steady state conditions in approximately 6 and 8 s, respectively (Fig. 3.6a). In contrast, fluxes of acetaldehyde and benzene in the bb region reach steady state conditions approximately one order of magnitude faster (Fig. 3.6b). However, transient effects appear potentially significant compared to an inhalation period of 1 s for all cases considered.

Uptake of chemical species in each layer is calculated as the time integral of the difference between the inlet and outlet fluxes, i.e.,

$$Uptake_i = \int_0^t \left(Flux_{i,in} - Flux_{i,out} \right) dt \tag{3.7}$$

In the expression above, uptake is calculated for layer *i* in units of g/cm^2 based on the flux values presented in Fig. 3.6. No outlet flux is assumed for the blood, so the blood uptake is simply the time integral of the inlet flux. Under steady state conditions, fluxes into and out of the mucus and tissue are equal at all times. Therefore, steady state uptake in these layers is zero. The resulting uptake values in the BB and bb regions for acetaldehyde and benzene are presented in Fig. 3.7. For steady state conditions, the constant flux values in the blood result in a liner estimate of uptake. In contrast, transient flux values produce non-linear uptake profiles, as shown in Fig. 3.7. Uptake differences between transient and steady state conditions are highly significant in the BB region (Fig. 3.7a). Again, steady state predictions of tissue uptake are zero compared with the nonzero transient tissue uptake values. At 1 s, the transient blood uptake of acetaldehyde and benzene is lower than steady state conditions by a factor of approximately 30 in

the BB model. In contrast, differences between transient and steady state blood uptake values are significantly less in the bb region (Fig. 3.7b). Specifically, transient and steady state predictions of blood uptake differ by factors ranging from 1.2 to 1.3 at 1 s.

Comparisons of steady state and transient uptake in the BB and bb regions over time are presented in Fig. 3.8 as percent differences. The percent difference values are calculated as the absolute difference between steady and transient results divided by the transient value. As shown in Fig. 3.8, percent differences in tissue uptake are 100% for all times considered because the steady state tissue uptake value is zero. In the BB region, percent differences for blood uptake of acetaldehyde and benzene range from approximately 1×10^5 % to 100% through 4 s (Fig. 3.8a). At 1 s, the percent differences in BB blood uptake for acetaldehyde and benzene are 2,900% and 2,500%, respectively. In the bb region, differences in steady vs. transient blood uptake range from approximately 100% to below 10% (Fig. 3.8b). After 1 s, the bb percent differences for acetaldehyde and benzene are 23% and 27%, respectively. These percent differences between steady and transient uptake values are also presented in Tables 3.3 and 3.4.

Multiple Breath Cycles

The previous results considered zero initial vapor concentrations in the mucus and tissue and a single inhalation period. However, vapor concentrations may build up over time in the mucus and tissue regions during multiple inhalation and exhalation cycles. Transient effects may be dimensioned if the concentrations of vapor in the mucus and tissue are near steady state conditions at the start of an

inhalation cycle. To test for the buildup of vapor species, a case was considered in which the system was exposed to a constant concentration for 2 s (inhalation period). The concentration was then removed for 2 s (exhalation period). This model assumes that the vapor species is completely absorbed into the blood and removed in the deeper alveolar region, which is reasonable for highly and moderately soluble components. As a result, zero concentrations are applied during the exhalation phase.

Concentrations at the mucus-tissue interface over 2 breathing cycles in the BB region are illustrated in Fig. 3.9. Minimum differences are observed in the quantitative concentration values between cycles 1 and 2 at the end of inhalation and exhalation (< 10% difference). Subsequent breathing cycles resulted in negligible differences of concentration values (< 1%). Based on these observations, it is concluded that the effects of transient absorption are not diminished by multiple breaths, provided that full downstream blood absorption can be assumed.

Effects of Chemical Reactions

Chemical reactions of some absorbed species are known to occur in the mucus and tissue layers of the upper respiratory tract (Cohen Hubal et al. 1996a). For reactive species, these conversions may significantly alter the transient uptake characteristics. However, reactivity levels that may influence transient absorption have not been previously considered. To better evaluate the effects of chemical reactions on mucus and tissue uptake, acetaldehyde and benzene were considered over a range of first order reaction rate constants extending from $0.01 - 1\times10^{4}$

min^{-1} (1.67×10^{-4} – 167 s^{-1}). First order reaction rate constants are presented in Table 3.5 for a range of compounds considered to be non-reactive through highly reactive in mucus and tissue. As shown in the table, benzene was reported as non-reactive and a representative first-order reaction rate constant of 0.01 min^{-1} was assumed. Acetaldehyde may be reactive with a first order reaction rate constant in tissue of approximately 0.1 min^{-1}, which is approximately equal to that of $S0_2$. In comparison, formaldehyde and ozone are typically considered to be highly reactive with first order reaction rate coefficients ranging from 1 – 300,000 min^{-1}.

Evaluation of chemical reactions requires that the governing diffusional equation in mucus, Equation (4a), be written as

$$\frac{\partial C_m(y,t)}{\partial t} = D_m \frac{\partial^2 C_m(y,t)}{\partial y^2} - K_m C_m\left(y,t\right), \qquad y \in [0, H_m] \tag{3.8}$$

where K_m is the first-order reaction rate coefficient in mucus. The governing equation for diffusion in tissue contains a similar reaction term for K_t. The boundary conditions expressed as Equations (3.4a-d) remain unchanged for the reactive case. Solutions to the coupled reaction equations were obtained using the TAOCS 1.0 program in a manner identical to the non-reactive equations. The resulting transient uptake values in tissue and blood are shown in Figures. 3.10 and 3.11, respectively, for acetaldehyde and benzene across a range of K values. In the numerical simulations, K values were assumed equal in mucus and tissue to maximize the effects of reactivity.

Considering transport in the tissue (Fig. 3.10), reactivity appears to only begin influencing uptake for K values greater than 100 min^{-1} in both the BB and

bb regions. This reaction rate coefficient is three orders of magnitude greater than the reported value of 0.1 min^{-1} for acetaldehyde and four orders of magnitude greater than the value assumed for benzene. Therefore, it can be concluded that reactions do not influence the transient uptake of acetaldehyde and benzene at the concentrations considered in this study. Moreover, a K value of 100 min^{-1} is two orders of magnitude greater than the reaction rate coefficient reported for formaldehyde (Table 3.5). In contrast, K values of approximately 10,000 min^{-1} eliminate nearly all of the acetaldehyde in the BB tissue region and reduce concentrations in the bb model by an order of magnitude, resulting in greatly reduced uptake values (Fig. 3.10). While not shown in Fig. 3.10, it is clear that the K value of ozone ($K \approx 300{,}000\ min^{-1}$) will result in nearly 100% removal in both the BB and bb regions. Results are similar for uptake in the blood (Fig. 3.11), with K values of 100 min^{-1} and below having a minimal impact on transient uptake. As a result, it can be concluded that chemical reactions have a negligible impact on the transient uptake of both benzene and acetaldehyde. Moreover, of the species shown in Table 3.5 only ozone has a sufficiently large K value to influence the transient uptake values.

3.4 Discussion

This study considered the transient absorption and uptake of representative vapor species in a model multilayer system representing the walls of the conducting airways. Three models of the wall were evaluated based on dimensions for the ET_2, BB, and bb regions (ICRP 1994). No previous study of which the authors are aware has considered the effects of time-dependence on the

transport and absorption of vapors into the walls of the respiratory tract. Results indicated that concentrations within the mucus and tissue layers were highly time dependent in the ET_2 and BB regions and moderately time dependent in the bb model over the timescale of an inhalation cycle, which is approximately 1 – 2 s. Fluxes of vapors into the tissue and blood varied with time for approximately 6 – 8 seconds in the BB region and 0.6 – 0.8 s in the bb model. The associated transient blood uptake of acetaldehyde and benzene in the upper ET_2 and BB regions varied from steady state values by a factor of approximately 30 after 1 s. Under similar conditions, transient blood uptake in the bb model varied from steady state conditions by a factor of approximately 1.3 after 1 s. For all cases considered, transient uptake in the tissue was greater and transient uptake in the blood was less than predicted under steady state conditions. As a result, it was concluded that the absorption and uptake of moderately and highly soluble vapors in the conducting airways are time-dependent over a period consistent with one inhalation cycle. This time dependence is highly significant for the ET_2 and BB regions, which extend through respiratory generation 8, and less significant for the remainder of the conducting airways.

A primary implication of this study is that transient absorption effects should be considered when evaluating the uptake of moderately and highly soluble compounds in the upper respiratory tract. Based on this analysis, both mucus and lung tissue serve as effective "temporal" barriers that prevent the entry of inhaled vapors into the blood stream. Studies that ignore this temporal effect over predict blood uptake by a factor of approximately 30 in the ET_2 and BB

regions. As described, differences are significantly less in the bb region, due to the thinner mucus and tissue layers. These results can be used to improve absorption and uptake predictions made in previous studies. Furthermore, future studies of vapor absorption and uptake should consider transient absorption effects or at least correct estimates made for steady state flux conditions based on the results of this study.

Both analytical and numerical transient solutions were considered in this study. This approach provided the advantage of ensuring correctness of the analytical solution and accuracy of the numerical simulation. In addition, an analytical solution of wall conditions is needed to formulate a transient absorption boundary condition for CFD simulations of gas phase transport and uptake. To derive the appropriate CFD boundary condition, the existing analytical solution needs to be extended to account for air phase resistance and a variable air phase vapor concentration. The resulting air-mucus-tissue-blood analytical expression can then be used to develop a transient flux boundary condition at the air-mucus interface.

Chemical reactions are typically considered to influence the mucus and tissue absorption of some vapor species (Cohen Hubal et al. 1996a; ICRP 1994). Mucus contains enzymes to break down foreign substances (Yeates et al. 1997). Tissue reactions are also frequent for inhaled vapors (Cohen Hubal et al. 1997; Miller et al. 1985). Benzene is generally considered to have a low reactivity once absorbed. In contrast, acetaldehyde is typically expected to have some reactivity in the tissue under steady state conditions (Morris and Blanchard 1992).

Interestingly, results of this study showed that chemical reactions had a negligible effect on the transient absorption of both acetaldehyde and benzene. A reaction rate constant of approximately 100 min^{-1} was required for chemical reactions to influence transient absorption at 2 s, which is three orders of magnitude greater than the reported K value of acetaldehyde. Furthermore, the K value of formaldehyde did not result in significant reactions through 2 s. Based on steady state analysis, chemical reactions in the upper airways for SO_2, acetaldehyde, formaldehyde, and ozone are generally thought to be significant (Cohen Hubal et al. 1997; Franks 2005; ICRP 1994; Morris and Blanchard 1992). In comparison, the results of this study imply that transient effects may diminish the influence of chemical reactions. When transient absorption is considered, initial flux values into the mucus and tissue are higher and concentrations are lower compared with steady state. Both of these factors serve to reduce the relative contribution of chemical reactivity. As time proceeds, transient effects decrease and reactivity contributions increase to a steady state level. Increases in reactivity effects over time are observed in Fig 10a as the curve for K = 100 min^{-1} increasingly separates from the other cases. This separation eventually reaches a steady state, as shown in Fig. 3.10b for the bb region. As a result, it appears critical to consider transient absorption effects when evaluating the influence of reaction on vapor uptake. Moreover, including transient absorption may practically eliminate the effect of chemical reactions for many compounds over the timescale of one inhalation cycle. These estimates of reactivity may be a function of air phase concentration values. However, significant increases in air phase concentration will be required

to overcome the observed three order of magnitude deficit in the K value required for reactivity to become important. Future studies are needed to further explore the effects of reaction coefficients and air phase concentrations on transient absorption.

Limitations of the current study include the assumptions of a constant air phase concentration, isothermal conditions, thermodynamic equilibrium at the interfaces, and a lack of data for some material properties. A constant air phase concentration was assumed to simplify the evaluation of transient absorption in the mucus, tissue, and blood layers. In the body, air phase concentrations vary with both space and time. However, spatial and temporal variations of air phase concentrations are expected to enhance temporal variations in the wall layers. Future analyses are required to extend the analytical solution of this study to variable air phase concentrations. Nevertheless, modifying the constant air phase concentration does not alter the reported uptake differences between the transient and steady state solutions shown in Fig. 3.8. Similarly, the assumption of zero concentration during exhalation is only a first order approximation for species that are fully absorbed in the deeper lung. Considering isothermal conditions, inhalation and exhalation may result in significant changes in the mucus and tissue temperatures, as a function of environmental conditions. These temperature variations will influence the species vapor pressures on the mucus surface, the partition coefficients, and the diffusion coefficients. Thermodynamic equilibrium was assumed at each interface to allow for the implementation of standard partition coefficients. This assumption requires that the interfaces are infinitely

thin and that the mass transfer coefficients are not too high, which is typically the case in biological systems (Bird et al. 1960). Transient effects are then controlled by diffusion in the much thicker mucus, tissue, and blood layers. Finally, the transport properties in mucus, tissue, and blood are not fully known. For example, the diffusion coefficients of the chemical species in tissue were set to be one-third their values in water, as reported by George et al (George et al. 1996). Additional simulations (not shown) indicated that setting the diffusion coefficients in tissue equal to the corresponding water values decreased the time to steady state conditions by a factor of approximately two.

In conclusion, this study has demonstrated that transient absorption can significantly influence the transport and uptake of vapors in the walls of the conducting airways. The importance of transient effects was observed for multiple regional models, moderately and highly soluble compounds, and over multiple breathing cycles. The quantitative results presented in this study can be used to improve previous estimates of vapor absorption and uptake in the mucus, tissue, and blood layers. Furthermore, the analytical solution developed in this study provides the basis for a boundary condition in future CFD simulations of coupled air-phase transport and wall absorption. Future studies are needed to evaluation the effects of air-phase resistance, variable air-phase concentrations, chemical reactions at multiple concentrations, and non-zero blood concentration levels.

Table 3.1. Thickness of mucus and tissue in each region.

Region	Mucus (μm)	Tissue (μm)
Nasal-extrathoracic region (ET_2)	15	50
Bronchial region (BB) G0 – G8	11	55
Bronchiolar region (bb) G9 – G16	6	15

Table 3.2. Values of transport parameters.

Model parameter	Acetaldehyde	Benzene
Air		
D_a (cm^2/s)	8×10^{-2} [a]	8.8×10^{-2} [a]
Mucus		
D_m (cm^2/s)	8×10^{-6} [a]	9.8×10^{-6} [a]
λ_{ma}	3.2×10^{2} [b]	4.4 [b]
Tissue		
D_t (cm^2/s)	2.64×10^{-6} [c]	3.23×10^{-6} [c]
λ_{tm}	5.9×10^{-1} [d]	4.1 [d]
Blood		
D_b (cm^2/s)	2.31×10^{-6} [e]	2.84×10^{-6} [e]
λ_{bt}	1 [d]	1 [d]
λ_{ba}	1.9×10^{2} [f]	1.8×10^{1} [g]

[a] US Department of Environmental Quality (1994)

[b] NIST Chemistry WebBook (2008)

[c] Calculated as one-third value of mucus

(George et al. 1996; Hlastala and Robertson 1998)

[d] Anderson et al. (2003)

[e] Estimated using the Stokes–Einstein–Sutherland equation

[f] Karch and Peat (2007)

[g] McClellan and Henderson (1995)

Table 3.3. Blood uptake difference (%) between steady state and transient conditions for acetaldehyde.

Time	ET_2	BB	bb
t=0.5 *s*	6.1×10^{4}	1.1×10^{5}	5.8×10^{1}
t=0.75 *s*	6.6×10^{3}	1.0×10^{4}	3.3×10^{1}
t=1 *s*	2.1×10^{3}	2.9×10^{3}	2.3×10^{1}
t=2 *s*	3.1×10^{2}	3.9×10^{2}	1.0×10^{1}
t=3 *s*	1.4×10^{2}	1.7×10^{2}	6.0×10^{0}
t=4 *s*	8.4×10^{1}	1.0×10^{2}	4.9×10^{0}

Table 3.4. Blood uptake difference (%) between steady state and transient conditions for benzene.

Time	ET_2	BB	bb
t=0.5 *s*	3.3×10^{4}	5.8×10^{4}	7.0×10^{1}
t=0.75 *s*	5.1×10^{3}	7.5×10^{3}	3.9×10^{1}
t=1 *s*	1.9×10^{3}	2.5×10^{3}	2.7×10^{1}
t=2 *s*	3.4×10^{2}	4.0×10^{2}	1.2×10^{1}
t=3 *s*	1.6×10^{2}	1.8×10^{2}	7.6×10^{0}
t=4 *s*	9.8×10^{1}	1.1×10^{2}	5.6×10^{0}

Table 3.5. Reactivity constants of common chemicals in mucus and tissue.

Compound		K in mucus (min^{-1})	K in tissue (min^{-1})
Benzene	Reported values	Non-reactive[c]	Non-reactive[c]
	This study	0.01[a]	0.01
SO_2	Reported values	0.1020[c]	0.1020[c]
Acetaldehyde	Reported values	Non-reactive [d]	0.0921[d]
	This study	0.1[b]	0.1
Formaldehyde	Reported values	Non-reactive [e]	1.08 [e]
Ozone	Reported values	71,880 [f]	300,000 [f]

[a] Assumed to be a non-reactive baseline value.

[b] Reactivity was set equal in the mucus and tissue to estimate a maximum possible effect.

[c] Hlastala and Robertson (1998)

[d] Goswami and Banerji (1970)

[e] Franks (2005)

[f] Miller et al. (1985)

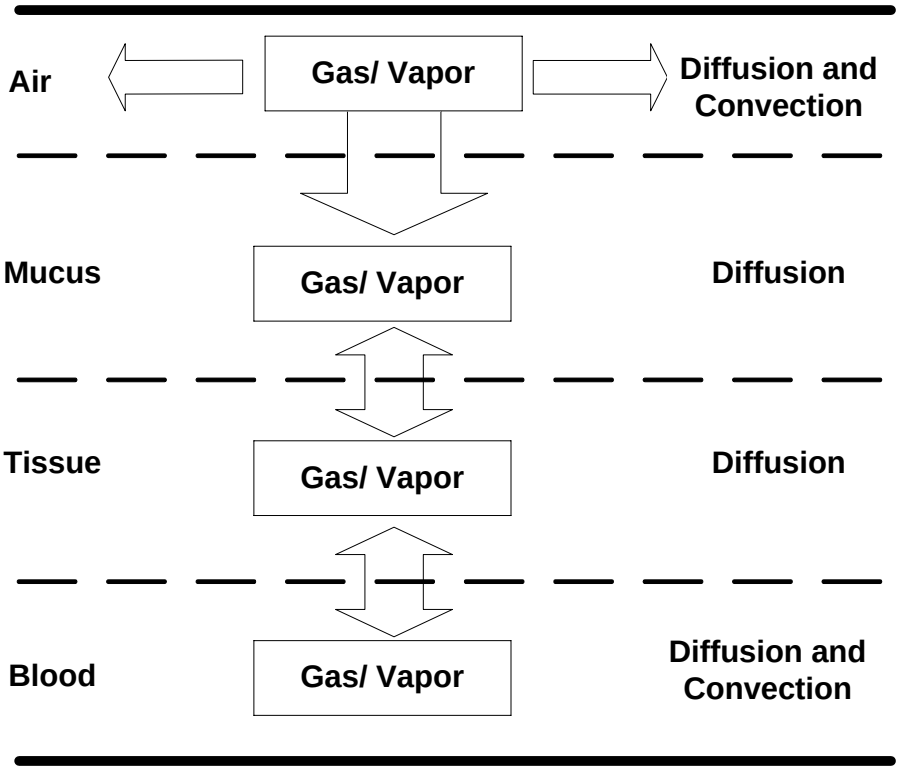

Figure 3.1. Multilayer system representing the absorption and transport of respiratory vapors into the walls of the conducting airways. Adapted from ICRP.

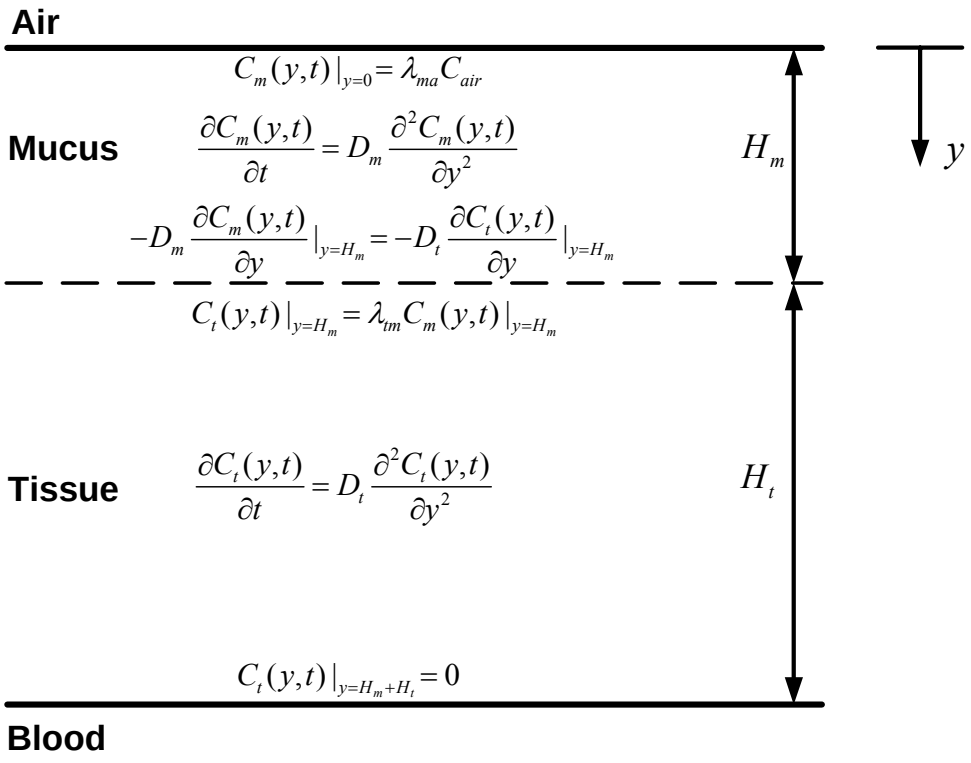

Figure 3.2. Approximate wall model consisting of mucus, tissue, and blood regions with governing equations and boundary conditions.

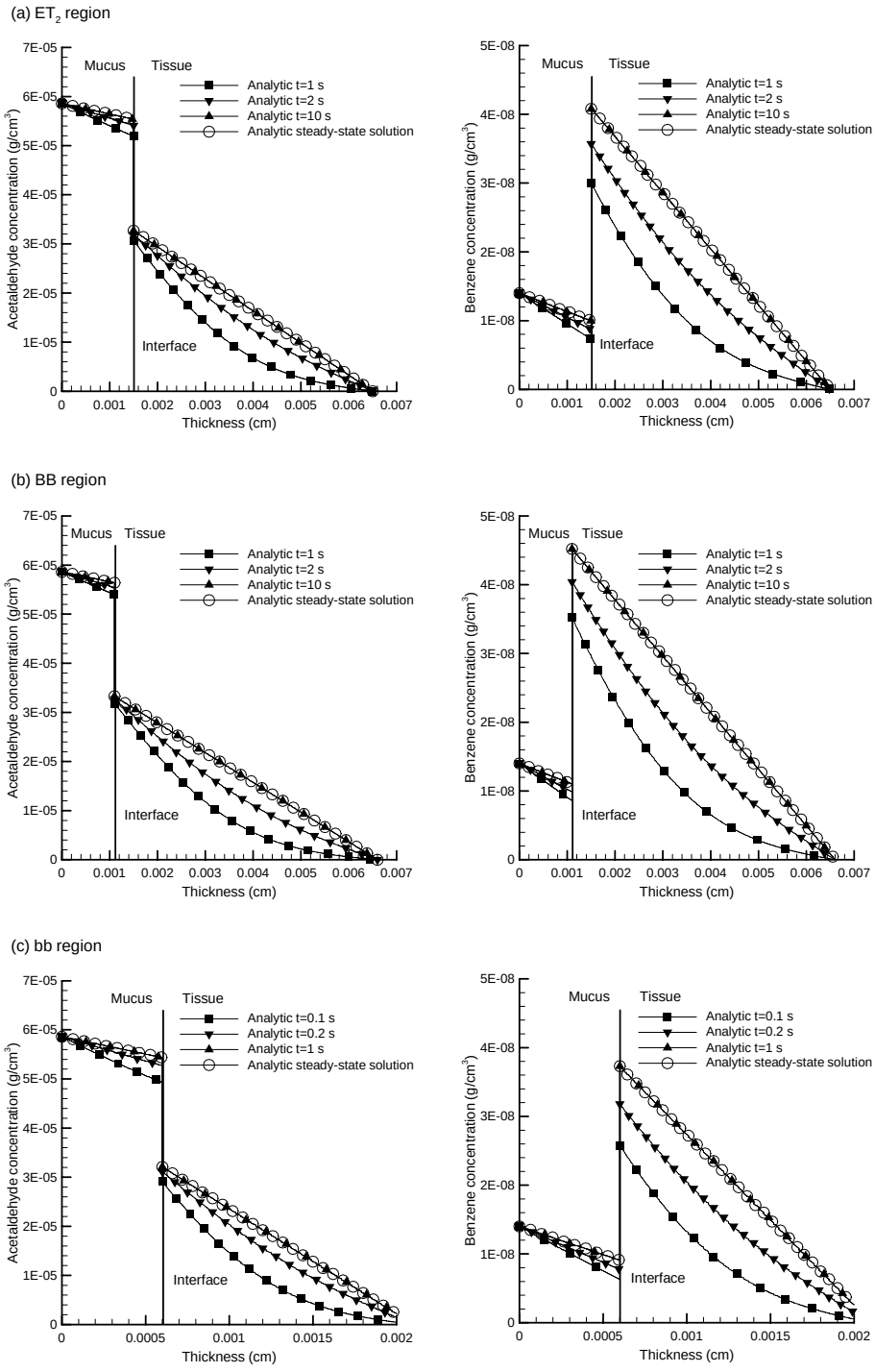

Figure 3.3. Concentrations of acetaldehyde and benzene over time compared with steady state results in the (**a**) ET_2, (**b**) BB, and (**c**) bb regions.

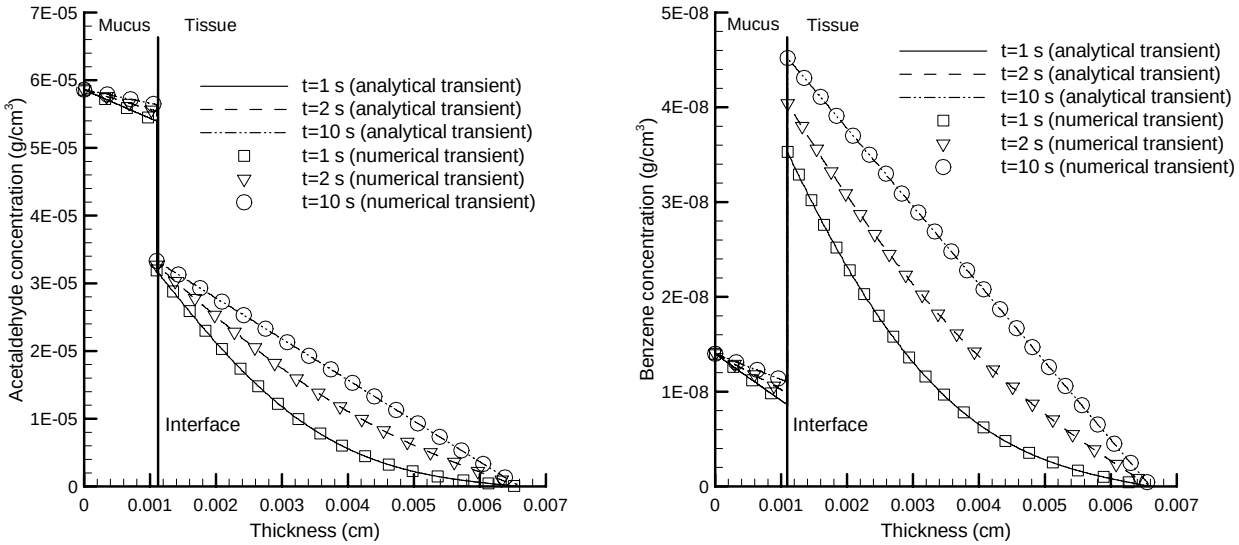

Figure 3.4. Comparison of analytical and numerical transient solutions for acetaldehyde and benzene concentrations in the BB region.

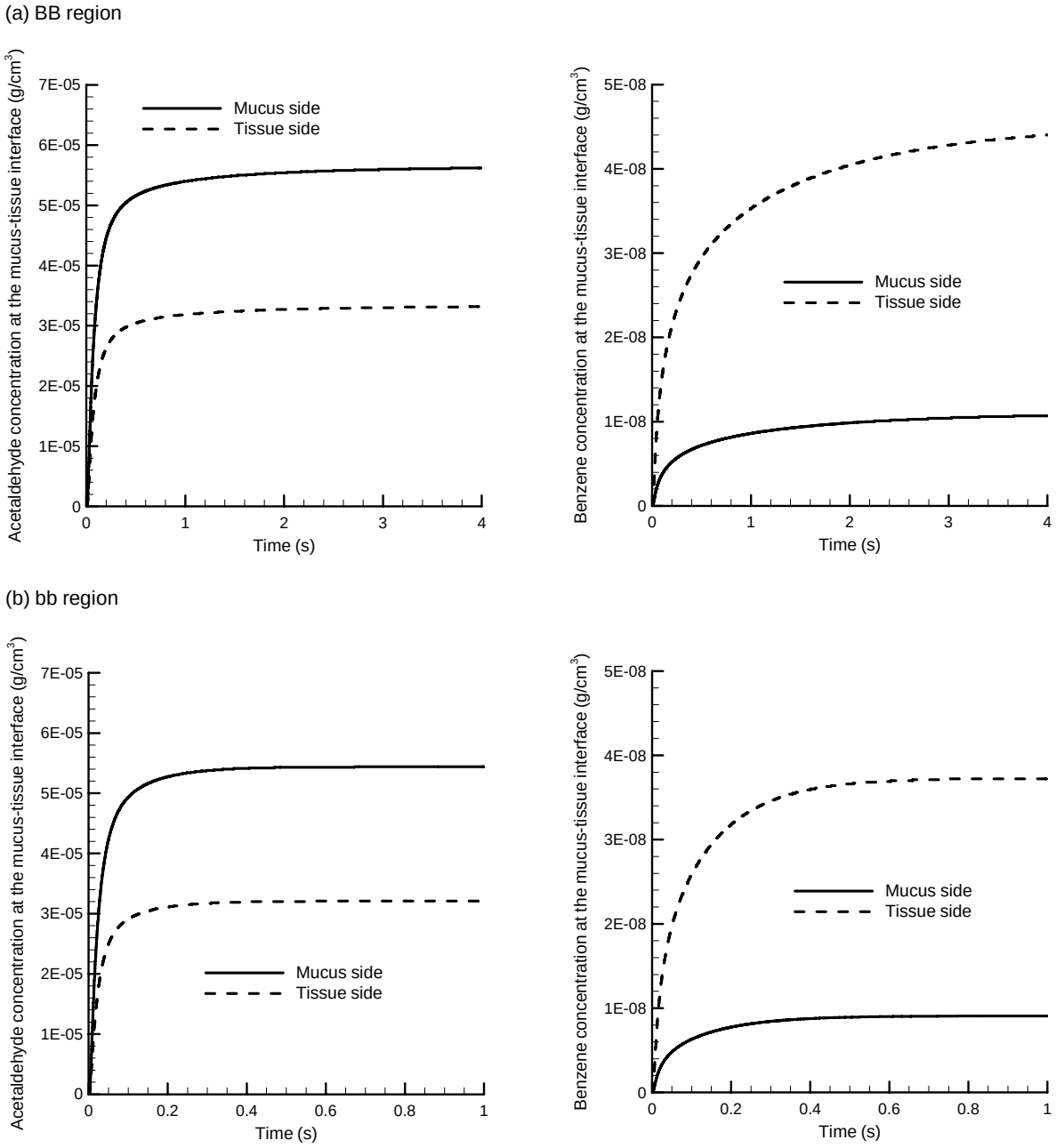

Figure 3.5. Acetaldehyde and benzene concentrations at the mucus-tissue interface in the (**a**) BB and (**b**) bb regions.

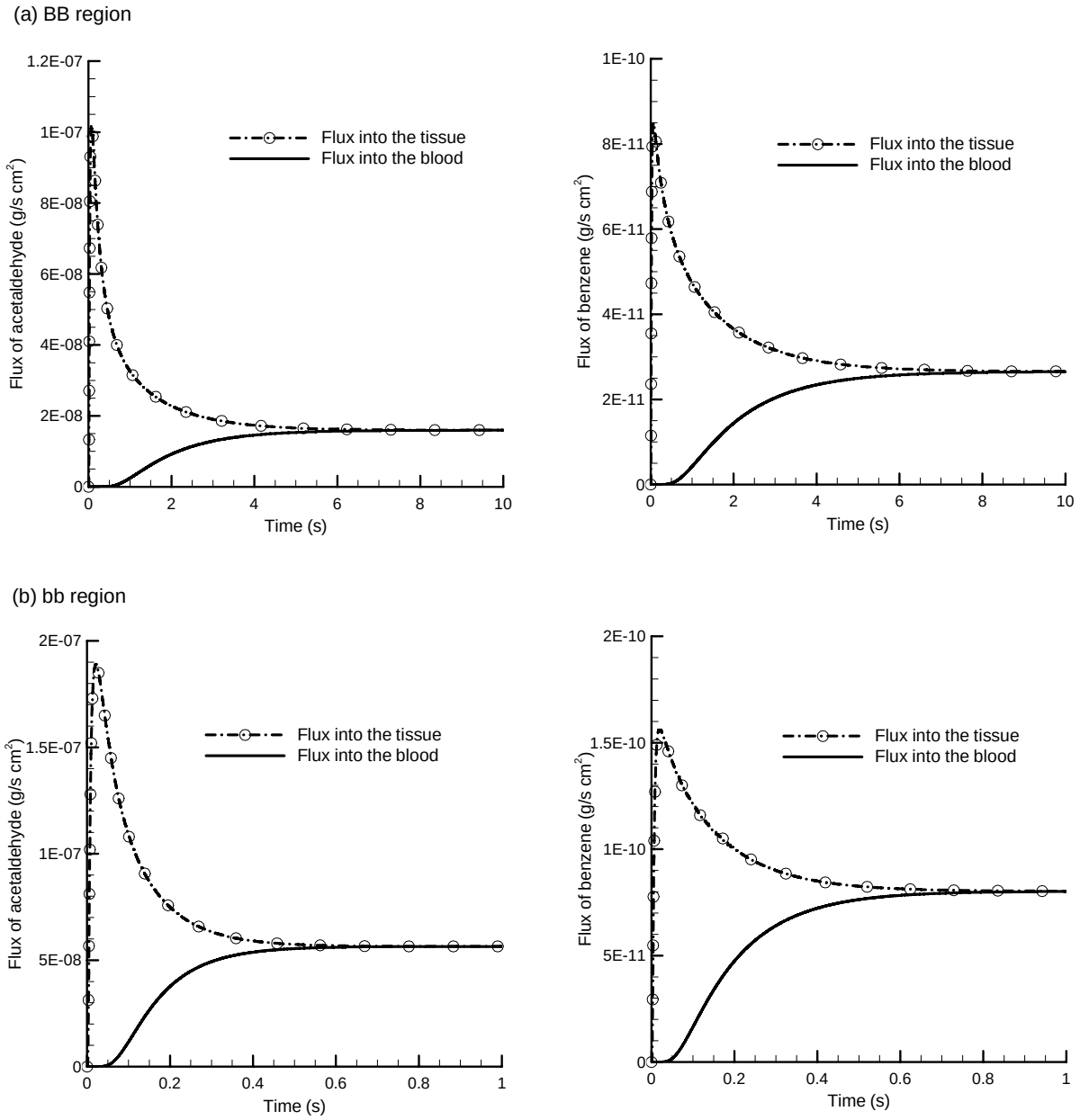

Figure 3.6. Flux of acetaldehyde and benzene into the tissue and blood for the (**a**) BB and (**b**) bb regions.

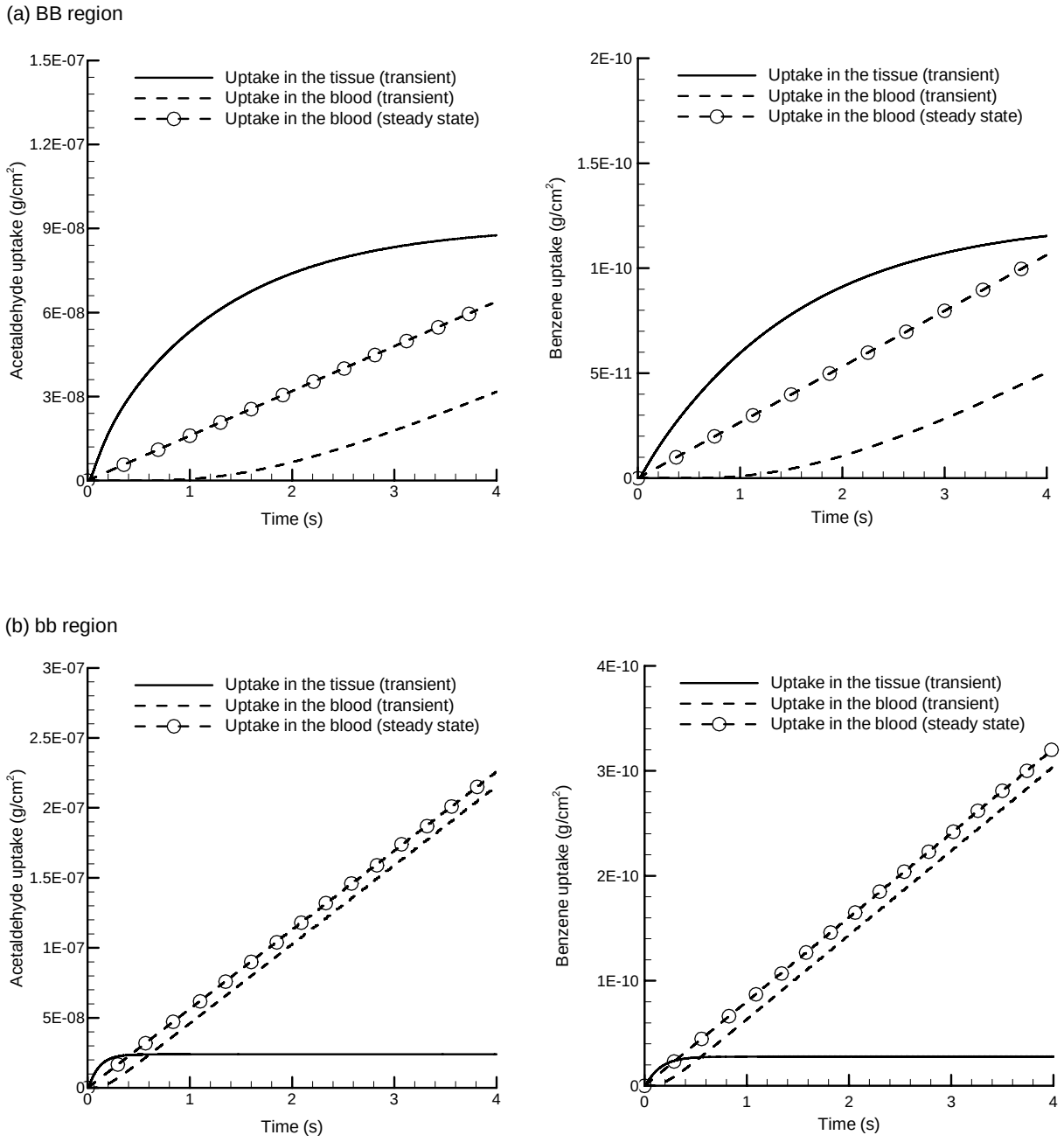

Figure 3.7. Uptake of acetaldehyde and benzene for transient and steady state conditions in the (**a**) BB and (**b**) bb regions.

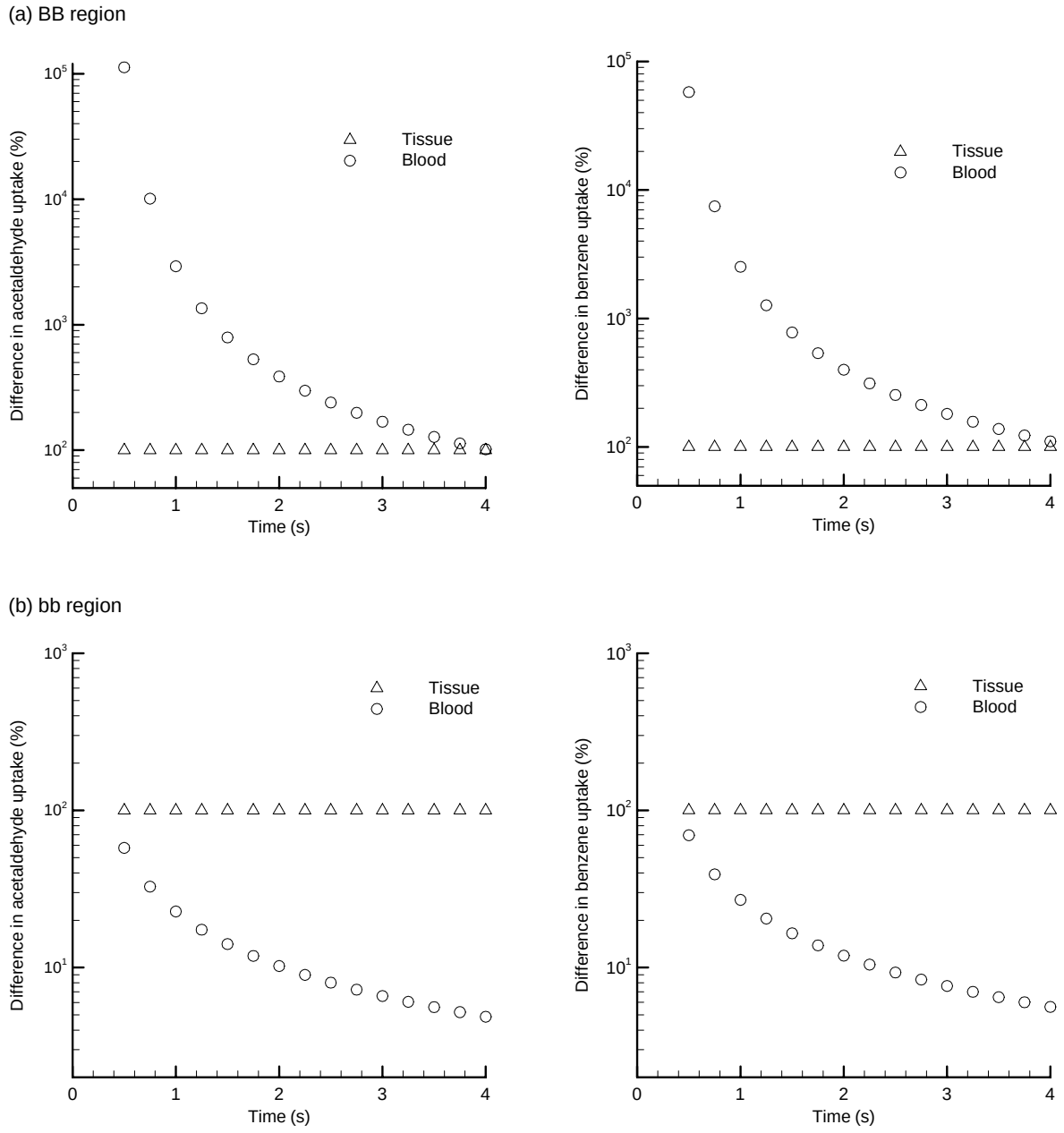

Figure 3.8. Percent differences between steady state vs. transient predictions of uptake for acetaldehyde and benzene in the (**a**) BB and (**b**) bb regions.

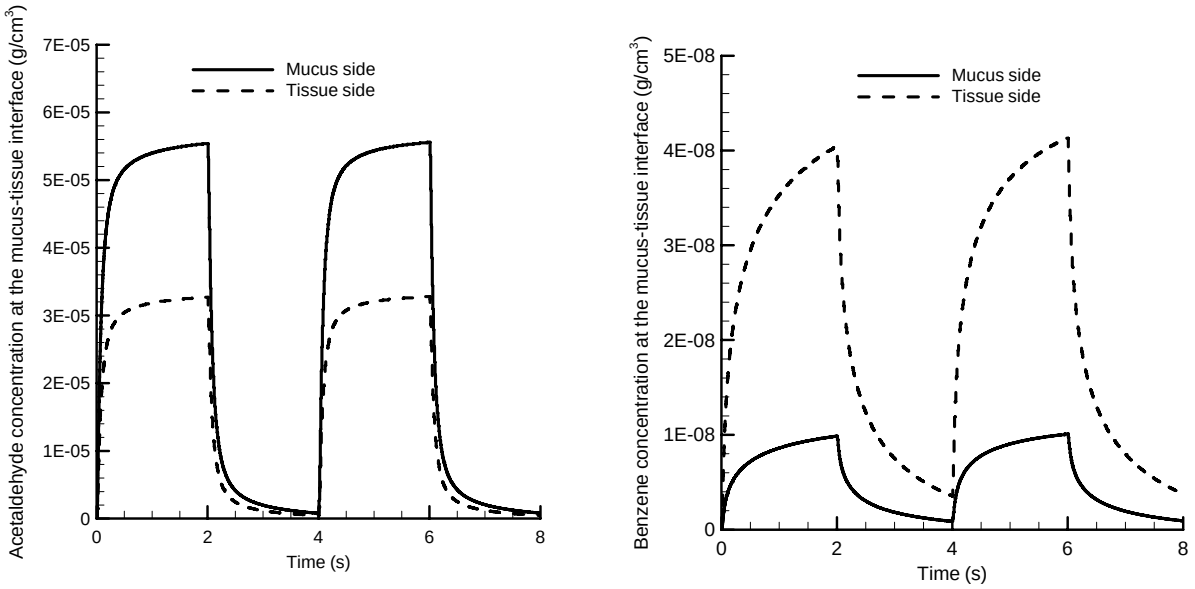

Figure 3.9. Concentrations of acetaldehyde and benzene at the mucus-tissue interface during inhalation (0 – 2 s) and exhalation (2 – 4 s) periods over two breathing cycles.

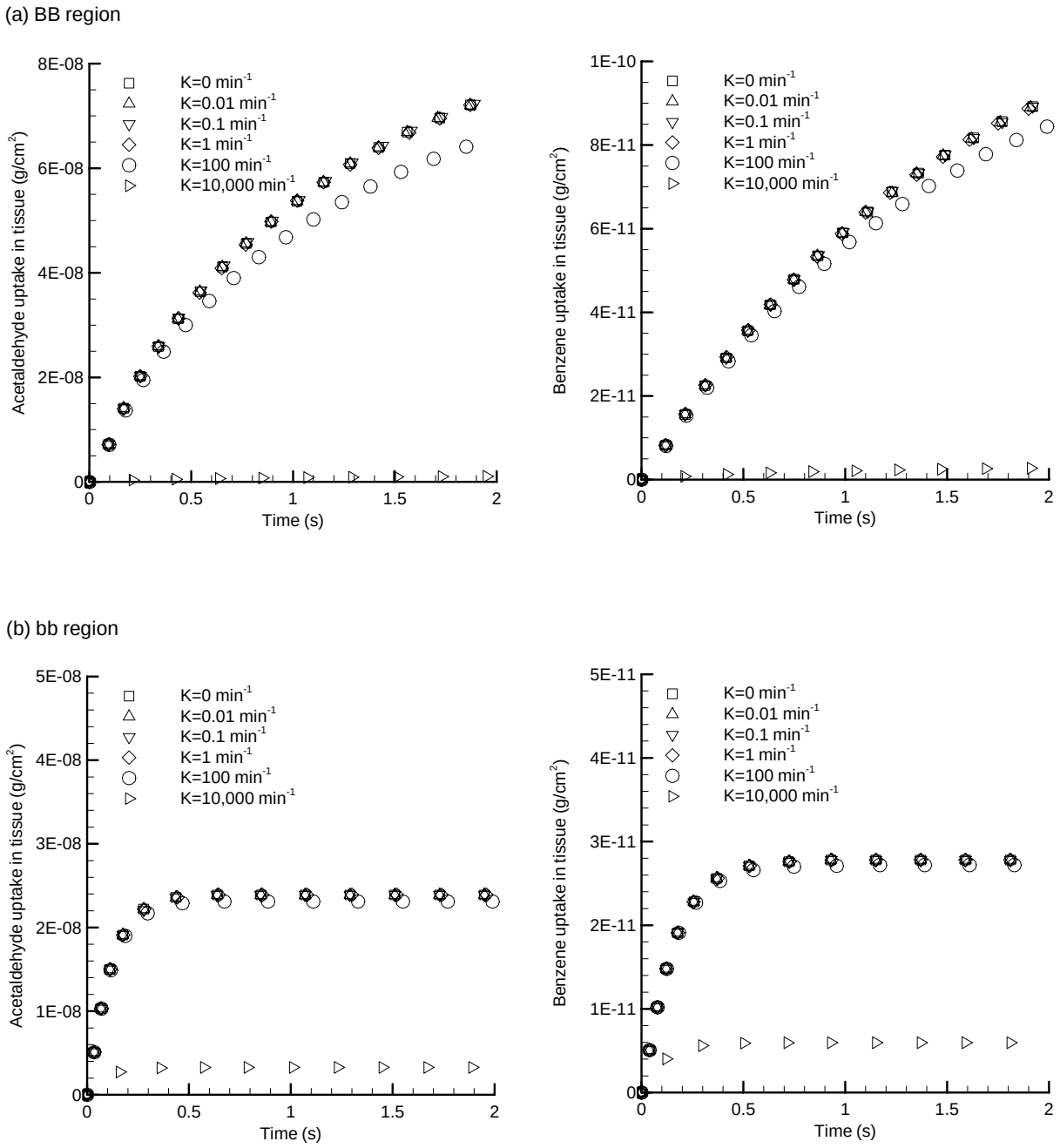

Figure 3.10. Tissue uptake of acetaldehyde and benzene for transient conditions including reactivity in the (**a**) BB and (**b**) bb regions.

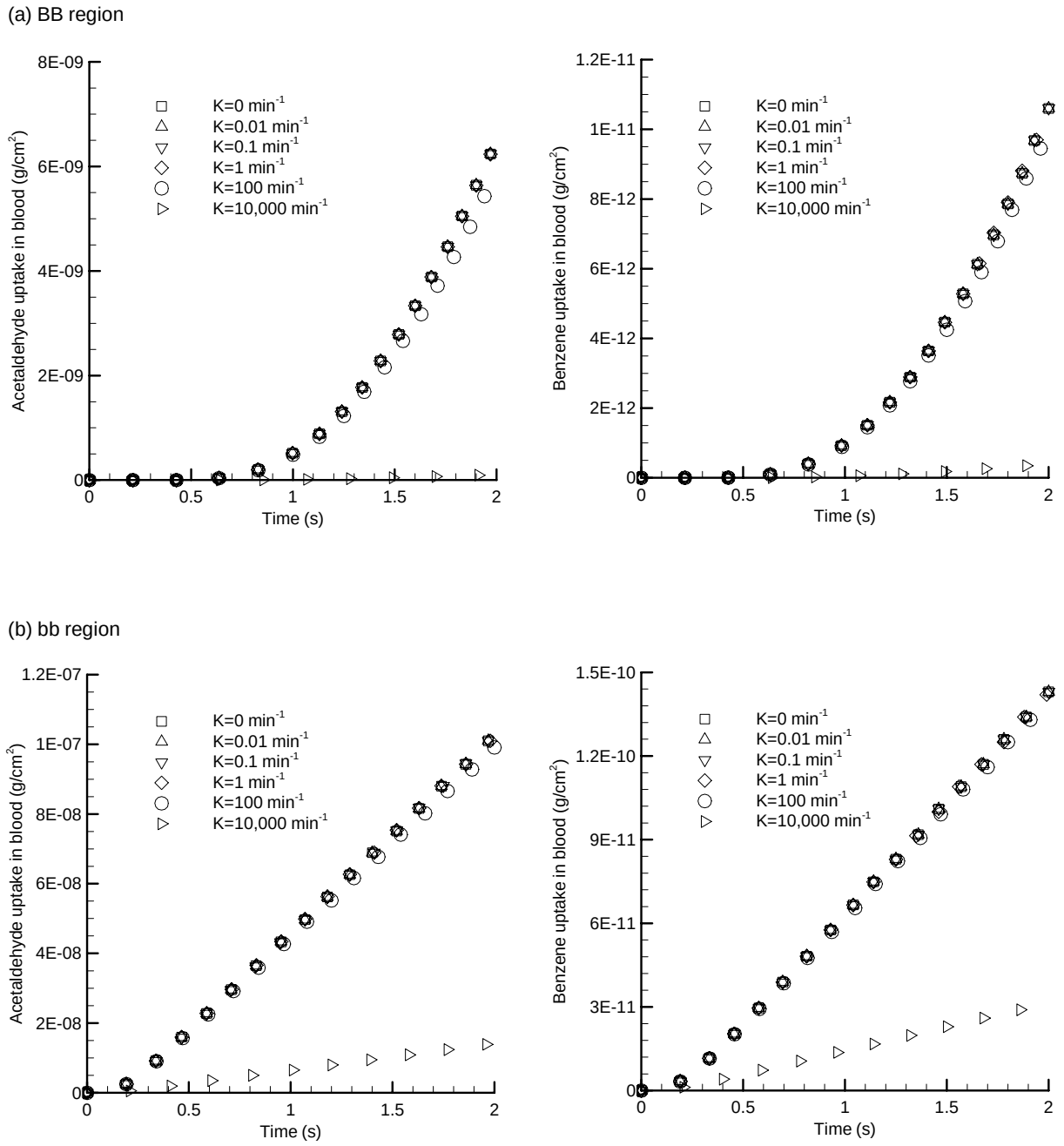

Figure 3.11. Blood uptake of acetaldehyde and benzene for transient conditions including reactivity in the (**a**) BB and (**b**) bb regions.

Chapter 4. Development of a CFD Boundary Condition to Model Transient Vapor Absorption in the Respiratory Airways

4.1 Introduction

We employ both numerical methods and analytical methods to investigate transport and absorption of acetaldehyde and benzene over time in an air-mucus-tissue-blood (AMTB) system. Air phase resistance is considered, and the model allows air phase concentration to change with time. Both analytical and numerical solutions are considered and compared in a simple multilayer AMTB system. The transient analytical solutions of the partial differential equations describing diffusion result a complicated task involving calculation of Fourier series, eigenvalues, and orthogonal eigenfunctions. We also develop a boundary condition at the air-mucus interface that includes the effects of solubility, diffusivity, medium thickness, and duration of exposure. This boundary condition was then used to calculate transient absorption in a realistic nasal-laryngeal model. To our knowledge, no other study has reported the solution of this multiphase system on a transient basis.

4.2 Methods

Models of the Conducting Airway Walls and Nasal-Laryngeal Airway

To approximate transport within the walls of the conducing airway in this study, a multilayer system was considered. As Fig. 4.1a shows, the model is divided into four compartments: i) the air layer, ii) the mucus layer, iii) the tissue layer, and iv) the blood layer. H_a, H_m, and H_t are the thicknesses of the air, mucus,

and tissue in specific regions of the respiratory tract, respectively. In this study, the extrathoracic nasal region was considered, which includes the posterior nasal passages, larynx, pharynx, and mouth. Evaluation of this region is critical considering that it serves as a primary conduit for all vapors entering the lungs. In this region, H_m and H_t are commonly reported to be approximately 1.5×10^{-3} *cm* and 5×10^{-3} *cm*, respectively (ICRP 1994). As shown in Fig. 4.1b, the nasal-laryngeal airway model consists of four parts: the nasal cavity, including the vestibule, valve region (VR), turbinate region (TR), and olfactory region (OR); nasopharynx, pharynx, and larynx. Xi and Longest (2009) constructed the airway model, and generated a computational mesh composed of approximately two million unstructured tetrahedral elements and a very fine near-wall pentahedral grid, which was employed in this study.

Governing Equations in the Mucus and Tissue with Boundary Conditions

We assume that there are no chemical reactions or convection (caused by an imposed mucus flow) occurring in the mucus and tissue layers. The rate at which mass concentration is absorbed into the mucus and tissue is determined by solving a system of transient diffusion equations:

$$\frac{\partial C_m(y,t)}{\partial t} = D_m \frac{\partial^2 C_m(y,t)}{\partial y^2}, \qquad y \in [0, H_m] \tag{4.1a}$$

$$\frac{\partial C_t(y,t)}{\partial t} = D_t \frac{\partial^2 C_t(y,t)}{\partial y^2}, \qquad y \in [H_m, H_m + H_t] \tag{4.1b}$$

where $y \in [0, H_{m+}H_t]$ is the spatial coordinate defining the depth into the mucus and tissue (Fig. 4.2). The variable t is the time dimension, where the period $t > 0$.

$C_m(y,t)$ and $C_t(y,t)$ are the concentrations (bulk densities) of a chemical species in the mucus and tissue with units of g/cm^3. These concentrations are spatially and time dependent in each material. D_m and D_t are the species diffusivities in mucus and tissue, respectively. The diffusivity of each species in each material is constant. Initially, zero concentration is assumed in the mucus and tissue. The boundary conditions are:

$$C_m(y,t)|_{y=0} = \lambda_{ma} C_a(y,t)|_{y=0}, \tag{4.2a}$$

$$C_t(y,t)|_{y=H_m} = \lambda_{tm} C_m(y,t)|_{y=H_m}, \tag{4.2b}$$

$$-D_m \frac{\partial C_m(y,t)}{\partial y}|_{y=H_m} = -D_t \frac{\partial C_t(y,t)}{\partial y}|_{y=H_m}, \tag{4.2c}$$

$$C_t(y,t)|_{y=H_m+H_t} = 0, \tag{4.2d}$$

where $C_a(y,t)|_{y=0}$ is not known and depends on the air layer concentration at the air-mucus interface. Equations (4.2a and 4.2b) imply that equilibrium occurs on each side of the air-mucus and mucus-tissue interfaces, where λ_{ma} and λ_{tm} are the mucus-air and tissue-mucus partition coefficients, respectively. Equation (4.2c) implies that the vapor species mass flux (mass flow rate of a compound per unit area with units of $g/s\text{-}cm^2$) leaving the mucus is equal to the flux entering the tissue. The system is shown in Fig. 4.2.

Analytical Transient Solution

An analytical solution to the coupled transient set of partial differential equations is presented in Appendix A. Briefly, the transient ($\hat{C}_m$) and steady state ($\tilde{C}_m$) components of the solution can be separated. A substitution approach can

then be used to evaluate the transient components of the equations. The resulting combined Fourier series and linear solution is expressed

$$C_m(y,t) = \hat{C}_m(y,t) + f(t)\tilde{C}_m(y)$$
$$= \sum_{n=1}^{\infty} W_n \sin(\mu_n \sqrt{\frac{D_m}{D_t}} \frac{H_t}{H_m}) \sin(\frac{\mu_n y}{H_m}) \int_{\tau=0}^{t} e^{-\mu_n^2 \frac{D_m}{H_m^2}(t-\tau)} \frac{df(\tau)}{d\tau} d\tau + f(t)\left(1 - \frac{1-\tilde{C}_m(y)|_{y=H_m}}{H_m} y\right), \tag{4.3a}$$

and

$$C_t(y,t) = \hat{C}_t(y,t) + f(t)\tilde{C}_t(y)$$
$$= \lambda_{tm} \sum_{n=1}^{\infty} W_n \sin(\mu_n) \sin(\mu_n \sqrt{\frac{D_m}{D_t}} \frac{H_m + H_t - y}{H_m}) \int_{\tau=0}^{t} e^{-\mu_n^2 \frac{D_m}{H_m^2}(t-\tau)} \frac{df(\tau)}{d\tau} d\tau + \tag{4.3b}$$
$$f(t)\left(\frac{\lambda_{tm}\tilde{C}_m(y)|_{y=H_m}}{H_t}(H_m + H_t - y)\right)$$

where $f(t) = C_m(y,t)|_{y=0}$, and $\tilde{C}_m(y)|_{y=H_m} = \frac{H_t D_m}{H_m \lambda_{tm} D_t + H_t D_m}$.

In these equations, the eigenvalues μ_n were determined by solving a transcendental equation using Brent's method (Brent 1973), as described in Appendix A. The Fourier series coefficients W_n were determined by utilizing the orthogonal relation and zero concentration initial conditions.

Flux Boundary Conditions at the Air-Mucus Interface

As Fig. 4.3 shows, there are two boundary conditions at the air-mucus interface; one is Equation (4.2a), and the other boundary condition is:

$$-D_a \frac{\partial C_a(y,t)}{\partial y}|_{y=0} = -D_m \frac{\partial C_m(y,t)}{\partial y}|_{y=0}, \tag{4.4}$$

where $C_a(y,t)$ is the concentration (bulk density) of a chemical species in air with units of g/cm^3. The concentration is spatially and time dependent in each material. D_a is the constant species diffusivity in air.

The analytical solution in the mucus (Eq. 4.3a) and the two boundary conditions (Eqs. 4.2a and 4.4) at the air-mucus interface can combined into a desired transient flux boundary condition at the air-mucus interface. Differentiating $C_m(y,t)$ with respect to y, then substituting $\frac{\partial C_m(y,t)}{\partial y}|_{y=0}$ into Equation (4.4), the transient flux boundary condition at the air-mucus interface becomes

$$\frac{\partial C_a(y,t)}{\partial y}|_{y=0} = \frac{D_m \lambda_{ma}}{D_a}\left(\begin{array}{l} \frac{1}{H_m}\sum_{n=1}^{\infty} \mu_n W_n \sin(\mu_n \sqrt{\frac{D_m}{D_t}}\frac{H_t}{H_m}) \int_{\tau=0}^{t} e^{-\mu_n^2 \frac{D_m}{H_m^2}(t-\tau)} \frac{dC_a(y,\tau)|_{y=0}}{d\tau} d\tau - \\ C_a(y,t)|_{y=0} \frac{1-\tilde{C}_m(y)|_{y=H_m}}{H_m} \end{array} \right), \quad (4.5)$$

Equation (4.5) is the transient flux boundary condition which accounts for the effects of diffusivity, solubility, medium thickness, and duration of exposure. For steady state conditions where $t \to \infty$, this boundary condition (4.5) simplifies to

$$\frac{d\tilde{C}'_a(y)}{dy}|_{y=0} + K\tilde{C}'_a(y)|_{y=0} = 0, \quad (4.6)$$

where $K = \frac{D_m \lambda_{ma}(1-\tilde{C}_m(y)|_{y=H_m})}{D_a H_m}$, (4.7)

In this expression, $\tilde{C}'_a(y)$ is the steady-state concentration in the air layer.

The Air-phase Transport

The concentration in the air layer satisfies the diffusion equation given by

$$\frac{\partial C_a(y,t)}{\partial t} = D_a \frac{\partial^2 C_a(y,t)}{\partial y^2}, y \in [-H_a, 0] \tag{4.8}$$

Initially, zero concentration is assumed in the mucus and tissue. The boundary conditions are:

$$C_a(y,t)|_{y=-H_a} = C_{air}, \tag{4.9}$$

The transient flux boundary condition at the air-mucus interface can be found in Eq. (4.5).

In order to develop a model system to test the importance of transient effects, the height of the air layer is set equal to a constant and small value, which was selected to be H_m. This distance is selected to be small in order to focus the analysis on transport in the mucus, tissue, and blood layers. In part of this study, numerical predictions are used to determine C_a in a simple AMTB model. The concentrations of acetaldehyde and benzene (C_{air}) at the top of the air layer are taken to be 100 ppm (1.83×10^{-7} g/cm^3) and 1 ppm (3.19×10^{-9} g/cm^3), respectively, which are below OSHA short term exposure limits. Values of transport parameters are reported in Table 3.2 for acetaldehyde and benzene.

Solution Techniques in the AMTB Model

In this study, the governing equations for the air-mucus-tissue-blood model were solved using two different solution approaches. First, a numerical solution of the system of Equations (4.1a), (4.1b), and (4.8), and boundary conditions (4.2a-d), (4.4) and (4.9) was found in Transient Absorption of Chemical Species

(TAOCS) 1.0 program using a finite volume method for spatial discretization and an implicit backward Euler method for time stepping. Figure 4.4a shows the system setup for the numerical solutions in the multilayer system. For the second solution technique, a hybrid numerical-analytical method was employed. In the air layer, Equation (4.8) with boundary condition (4.9) and the analytical transient flux boundary condition (4.5) was solved using a finite difference method for spatial discretization and an implicit backward Euler method for time stepping. Analytical solutions in the mucus and tissue, which are dependent on the solution in the air layer, were then solved using Equations (4.3a and 4.3b). Figure 4.4b shows the system setup for the hybrid solution in the multilayer system. The cgs system of units was used for all simulations. Comparison of the two solution techniques is used to verify the hybrid numerical-analytical solution. This approach is then applied as a boundary condition in a CFD simulation of vapor absorption in the nasal-laryngeal geometry, as described below.

Transport Equations in the Nasal-Laryngeal Airway Model

The low-Reynolds-number (LRN) $k-\omega$ model of Wilcox (1998) was selected for simulating the air flow in the nasal-laryngeal model because it has been shown to provide an accurate and numerically efficient solution for transitional and turbulent flows. Furthermore, this model was found to accurately predict laminar flow as the turbulent viscosity approaches zero. The transport equations governing the turbulent kinetic energy (k) and the specific dissipation rate (ω) were provided by Wilcox (1998) and were previously reported in

(Longest and Xi 2007b; Xi and Longest 2007a; Xi and Longest 2008b; Zhang and Kleinstreuer 2004; Zhang and Kleinstreuer 2006).

The turbulent vapor mass transfer equation in turbulent flow can be written on a mass fraction basis as

$$\frac{\partial C_a}{\partial t} + \frac{\partial (u_j C_a)}{\partial x_j} = \frac{\partial}{\partial x_j}\left[\left(D_a + \frac{\nu_T}{\sigma_C}\right)\frac{\partial C_a}{\partial x_j}\right], \tag{4.10}$$

where C_a is the mass fraction of a chemical species in air, D_a is the species diffusivity in air, and ν_T is the turbulent viscosity. Vectors u_j and x_j are the fluid velocity vector and position, respectively, and σ_C is the turbulence Prandtl number, taken to be 0.9.

Deposition Factors

For the transport model, the total or regional deposition fraction at steady state can be expressed as

$$DF_i = \frac{\dot{m}_{w,i}}{\dot{m}_{in}}, \tag{4.11}$$

where $\dot{m}_{w,i}$ is the total mass absorption into the wall surface and $\dot{m}_{in}$ is the inlet mass flow rate. The transient regional deposition fraction can be expressed as

$$DF_i = \frac{\int_0^T \dot{m}_{w,i}\,dt}{\int_0^T \dot{m}_{in}\,dt}, \tag{4.12}$$

where T is the time period of the simulation. In this study, transient absorption is considered for periods of 2 s.

The total mass absorption rate into the wall surface can be expressed as

$$\dot{m}_{w,i} = \sum_{j=1}^{N} -\rho_m A_j (D_a + \frac{\nu_T}{\sigma_C}) \frac{\partial C_a}{\partial n}|_{w,j,} \tag{4.13}$$

where A_j is the local area, and the summation is performed over the total or $i-$region of interest. The mixture density is ρ_m. The vector n is the wall normal coordinate pointing out of the geometry.

The inlet mass flow rate can be determined as

$$\dot{m}_{in} = \rho_m Q C_{in}, \tag{4.14}$$

where Q is the inlet inhalation flow rate. C_{in} is the inlet mass fraction, taken to be 0.05.

A deposition enhancement factor (DEF), similar to that suggested by Xi and Longest (2007b), was defined in order to quantify local deposition in region A_j with respect to the total deposition rate as follows.

$$DEF_j = \frac{DF_j / A_j}{DF_i / A_i}, \tag{4.15}$$

where A_i is the total area.

Flow Rates and Boundary Conditions

Steady inhalation was assumed for all simulations. An inhalation flow rate of *20 L/min* was considered, which is consistent with resting conditions (ICRP 1994). During inhalation, airflow enters the nasal cavity, travels through the nostrils, nasal turbinates, pharynx, and exits the larynx. The transient flux boundary condition (Eq. 4.5) and steady flux boundary condition (Eq. 4.6) were considered for transient and steady absorption into the wall, respectively.

Two cases were considered in the nasal-laryngeal airway model, as outlined in Table 4.1. Case 1 (S:S) and Case 2 (S:T) are intended to quantify the effects of transient absorption compared with steady state absorption. A steady state flow field and mass species profile were considered in both cases. Steady absorption versus transient absorption into the wall are then evaluated over a timescale consistent with one inhalation cycle.

To solve the governing conservation equations, the CFD package Fluent 6.2.16 (Ansys Inc.) was employed. User-supplied C programs were implemented for the calculation of the transient boundary condition, vapor absorption, and deposition enhancement factors.

4.3 Results

Validation of the Transient Analytical Solution in the Air-Mucus-Tissue-Blood System

A comparison between the transient numerical and hybrid solutions of concentration over time are shown in Fig. 4.5 for acetaldehyde and benzene. A point by point comparison of concentration values indicates that the transient numerical and hybrid solutions were on average within 0.1%. Agreement between the approaches considered provides confidence that the analytical flux boundary condition at the air-mucus interface and analytical solutions in the mucus and tissue are correct. The relative values of concentrations in the air, mucus and tissue sides of the interface also illustrate the effects of the air-mucus and mucus-tissue partition coefficients. For example, acetaldehyde is more soluble in mucus than in air at the air-mucus interface ($\lambda_{ma} > 1$) and less soluble in tissue than in

mucus at the mucus-tissue interface ($\lambda_{tm} < 1$). Therefore, concentrations (g/cm^3) of acetaldehyde are higher in the mucus compared with the air and lower in the tissue compared with the mucus. As a result, transient effects are also shown to be highly significant in the mucus and tissue layers over a timescale of approximately 2 seconds.

Concentration Values

Concentration values of acetaldehyde and benzene at the air-mucus and mucus-tissue interfaces are displayed in Fig. 4.6 over time based on the numerical solution. These results indicate the timeframe for establishing steady state transport through the air and mucus. The concentration curves become flat over time as steady state conditions are approached. As observed, it is much faster to reach steady state in the air than in the mucus. Considering the mucus and tissue layers, temporal effects for acetaldehyde and benzene appear relatively small after approximately 2 and 4 s, respectively. In the air layer, where the diffusion process is significantly faster, temporal effects for acetaldehyde and benzene are diminished after approximately 0.1 and 0.05 s, respectively.

Flux and Uptake

The fluxes of acetaldehyde and benzene into the mucus, tissue, and blood layers are reported in Fig. 4.7. Results in Fig. 4.7 indicate that the transient flux values for acetaldehyde and benzene are highly variable over approximately 4 and 6 s, respectively. The fluxes into the mucus, tissue and the blood layers are equal and constant when steady state is reached quantitatively. The fluxes of

acetaldehyde and benzene reach constant steady state conditions (within 99%) in approximately 6 and 8 s, respectively. Since the concentrations at the air-mucus and mucus-tissue interfaces increase rapidly from zero initially, it is seen that the fluxes of each species into the mucus and tissue initially spike. Due to the zero concentration at the blood-tissue interface, the flux of each species into the blood is initially delayed and then approaches a steady state. Uptake within the mucus, tissue, and blood layers was estimated by time integrating the difference between the inlet and outlet flux values. The resulting uptake values for acetaldehyde and benzene are presented in Fig. 4.8. It is observed that transient absorption is significantly different from the steady state conditions. For acetaldehyde, uptake values in the mucus and tissue are higher than in the blood over a transient exposure. Based on these observations, the uptake in the blood is lower for a transient exposure compared with steady state conditions. It is observed that the transient blood uptake for acetaldehyde and benzene varied from steady state values by a factor of approximately 4 after 2 s.

A comparison of steady state and transient blood uptake over time is presented in Fig. 4.9 as percent differences. The percent difference values are calculated as the absolute difference between steady and transient results divided by the transient value. As shown in Fig. 4.9, percent differences for blood uptake range from approximately 100% to 1×10^{5} % through 4 seconds. These percent differences between steady and transient uptake are also presented in Table 4.2.

Effects of Chemical Reactions

To better evaluate the effects of chemical reactions on mucus, tissue, and blood uptake, acetaldehyde and benzene were considered over a range of first order reaction rate constants extending from 0.01 – 1×10^3 min^{-1}. First order reaction rate constants are presented in Table 3.5 for a range of compounds considered to be non-reactive through highly reactive in mucus and tissue.

Evaluation of chemical reactions requires that the governing diffusion equation in mucus, Equation (4.1a), be written as

$$\frac{\partial C_m(y,t)}{\partial t} = D_m \frac{\partial^2 C_m(y,t)}{\partial y^2} - K_m C_m\left(y,t\right), y \in [0, H_m] \qquad (4.16)$$

where K_m is the first-order reaction rate coefficient in mucus. The governing equation for diffusion in tissue contains a similar reaction term for K_t. The boundary conditions expressed as Eqs. (4.2a-d) remain unchanged for the reactive case. The resulting transient uptake values in mucus, tissue, and blood are shown in Fig. 4.10 for acetaldehyde and benzene across a range of K values. In the numerical simulations, K values were assumed equal in mucus and tissue to maximize the effects of reactivity.

It is observed that reactivity appears to only begin influencing uptake for K values greater than 100 min^{-1}. This reaction rate coefficient is three orders of magnitude greater than the reported value of 0.1 min^{-1} for acetaldehyde and four orders of magnitude greater than the value assumed for benzene. Therefore, it can be concluded that reactions do not influence the transient uptake of acetaldehyde and benzene at the concentrations considered in this study.

Deposition Fractions in the Nasal-Laryngeal Model

Deposition fractions (DF) for acetaldehyde and benzene vapors in mucus, tissue, and blood in the nasal-laryngeal airway model for Case 1 (S:S) and Case 2 (S:T) are shown in Fig. 4.11 for a 2 seconds inhalation. The DF values of acetaldehyde and benzene for both cases considered are also tabulated in Table 4.3. It is observed that DF values for transient absorption (Case 2) are significantly different from steady state absorption (Case 1). Furthermore, DF values of acetaldehyde in mucus are approximately 8 times greater for transient absorption compared with steady state absorption. DF values of benzene in mucus are approximately 3 times greater for transient absorption compared with the steady absorption condition. For Case 1, the DF values are equal in mucus, tissue, and blood. For Case 2, the DF values of acetaldehyde in mucus are approximately 6 times higher than in tissue and 40 times higher than in blood. The DF values of benzene in mucus are approximately 2 times higher than in tissue and 16 times higher than in blood. The higher absorption of acetaldehyde vapor may be attributed to its higher solubility in the mucus layer.

Local Deposition

DEF contours of acetaldehyde and benzene vapors are shown in Figures 4.12 and 4.13, respectively, at an inhalation flow rate of 20 *L/min*. High DEF values were observed in the TR and VR regions, and low DEF values were observed in the OR region. Differences of the DEF distribution for Cases 1 and 2 are significant. The DEF values for Case 1 were distributed more uniformly, whereas DEF values for Case 2 were highly heterogeneous and localized.

4.4 Discussion

This study has considered the transient absorption of highly and moderately soluble vapors into a simple multilayer AMTB model of the conducting airway walls. Based on an analytic solution of absorption, a transient boundary condition for CFD simulations of vapor transport was developed for the first time and tested in comparison with the typically applied steady state approach. Considering the AMTB model, results indicated that absorption was highly time dependent over the timescale of one inhalation cycle. At 1 s, transient conditions resulted in approximately 2 – 3 times more uptake in tissue and 20 – 25 times less uptake in blood than at steady state for both acetaldehyde and benzene. These results are consistent with the previous study of Tian and Longest (2010b), which neglected the air phase and only considered a mucus-tissue-blood wall model. Consideration of an AMTB wall representation in the current study allowed for the development of a novel transient flux boundary condition. Application of this boundary condition to CFD simulations of a nasal-laryngeal geometry showed, as expected, that transient absorption significantly affected total deposition fractions in the mucus, tissue, and blood. Moreover, transient absorption was also shown to significantly affect the local deposition pattern of acetaldehyde and benzene based on the DEF parameter. As a result, local tissue doses predicted using the transient absorption model will be significantly higher than when a steady absorption assumption is made. Based on these findings, previous studies that have assumed steady state absorption of vapors into the respiratory walls may have significantly under predicted mucus and tissue absorption, over predicted

blood absorption, and under predicted local vapor absorption in cases where transient uptake is important.

In this study, transient vs. steady state absorption was compared for both the AMTB wall model and the nasal-laryngeal geometry. The resulting difference ratios were calculated as the transient uptake divided by the steady state uptake value. From a dosimetry perspective, uptake in the tissue and blood are most important. Interestingly, difference ratios at 2 s for tissue and blood uptake were nearly identical between the AMTB and nasal-laryngeal models. For both models at 2 s and both species considered, the difference ratios in tissue were approximately 1.5 – 2 and the difference ratios in blood were approximately 0.17 – 0.24. As shown in Tables 4.2 and 4.3, these values are significantly diminished from the differences predicted at 1 s. Similarity in the difference ratio values between the two models indicates that the AMTB model may be used to predict potential errors in CFD calculations using a steady state absorption approximation. Moreover, the application of a steady state absorption model may be considered in future CFD studies in conjunction with corrections predicted by the much simpler AMTB wall model.

Limitations of the current study include the assumption of steady state flow field conditions (air and vapor transport), the consideration of one inhalation cycle, neglecting reactions, selecting an arbitrary height of the air layer, and zero vapor concentration in the blood. The assumption of steady state air flow is not consistent with transient inhalation and exhalation. However, both transient inhalation in the air phase and transient absorption in the wall will affect uptake.

The assumption of a steady state air phase was made in this study to isolate the effect of transient wall absorption. Considering the AMTB model, the timescale of one inhalation cycle was considered. Vapor exposures often consist of exposure over multiple inhalations. For highly and moderately soluble compounds, it is reasonable that full lung absorption occurs. Furthermore, Tian and Longest (2010b) previously showed that concentrations did not accumulate in the mucus, tissue, and blood layers over multiple inhalations, provided that the species was fully absorbed by the lungs. Chemical reactions are generally considered significant for most of the reaction rate values considered, which ranged from 0.01 to 100 min^{-1}. However, by considering transient absorption, reactivity only occurred for K values of approximately 100 min^{-1}, which is significantly greater than the first order reaction constant of acetaldehyde and benzene. As described, a small arbitrary value was used to define the height of the air layer in the AMTB model. By selecting a small value, diffusion through the air had a negligible impact on the transient absorption rates into the mucus, tissue, and blood components. Finally, zero concentration of inhaled vapor was assumed in the blood, which is most accurate for short exposures or compounds that are highly metabolized in the circulation.

In conclusion, transient absorption was found to be significant compared with steady state predictions for highly and moderately soluble compounds in the upper airways. The influence of transient absorption was observed in both a multilayer AMTB wall model and a CFD model of the nasal-laryngeal region. Findings from the CFD model indicated that transient effects influenced both total

absorption as well as local tissue doses. The complex transient flux boundary condition developed and tested in this study may be very useful in future more accurate simulations of vapor uptake in the respiratory airways. Results also indicated that the much simpler AMTB model could be applied to predict the effect of transient absorption compared with steady state conditions in the CFD model of the nasal-laryngeal geometry. Therefore, the AMTB model may be implemented to simplify future simulations of transient vapor uptake. Future studies are needed to evaluate the effects of transient air flow, multiple breathing cycles, blood absorption and concentration levels, and chemical reactions.

Table 4.1. Two cases considered.

	Air phase and mass species	Absorption	Designation
Case 1	Steady	Steady flux	S:S
Case 2	Steady	Transient flux	S:T

Table 4.2. Blood uptake difference (%) between steady state and transient conditions for acetaldehyde and benzene.

Time	Acetaldehyde	Benzene
t=0.5 *s*	7.1×10^{4}	3.5×10^{4}
t=0.75 *s*	7.1×10^{3}	5.2×10^{3}
t=1 *s*	2.2×10^{3}	1.9×10^{3}
t=2 *s*	3.1×10^{2}	3.4×10^{2}
t=3 *s*	1.4×10^{2}	1.6×10^{2}
t=4 *s*	8.5×10^{1}	9.9×10^{1}

Table 4.3. Deposition fraction (%) in mucus, tissue, and blood for Cases 1 and 2 considered during a 2 seconds inhalation.

	Acetaldehyde			Benzene		
	in mucus	in tissue	in blood	in mucus	in tissue	in blood
Case 1	6.22	6.22	6.22	0.58	0.58	0.58
Case 2	53.68	9.71	1.46	1.64	1.07	0.10

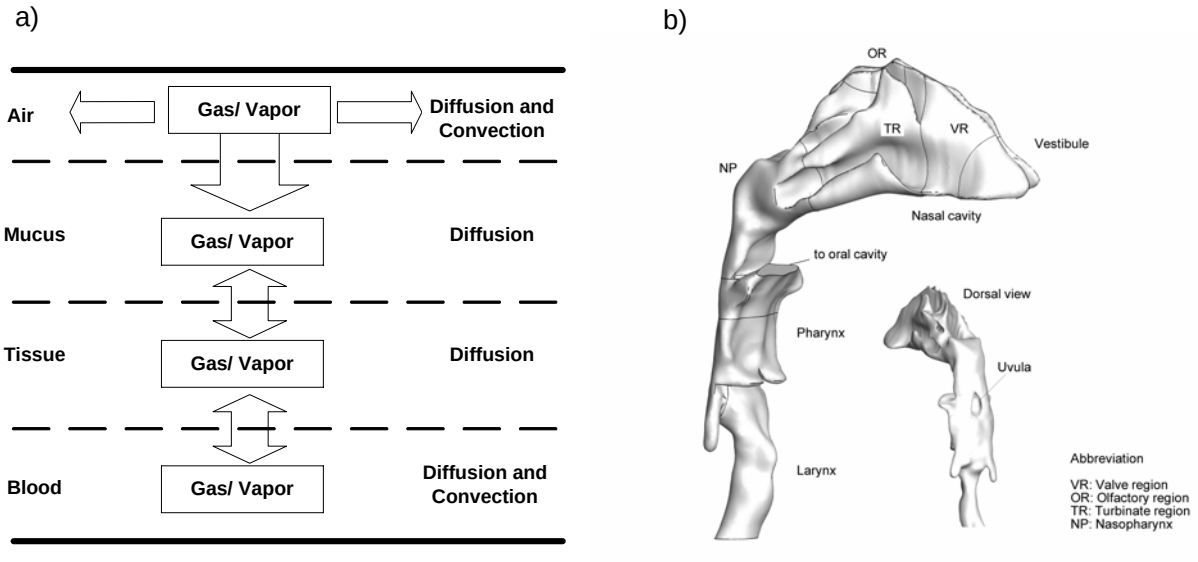

Figure 4.1. (**a**) The AMTB system and (**b**) the nasal-laryngeal airway model.

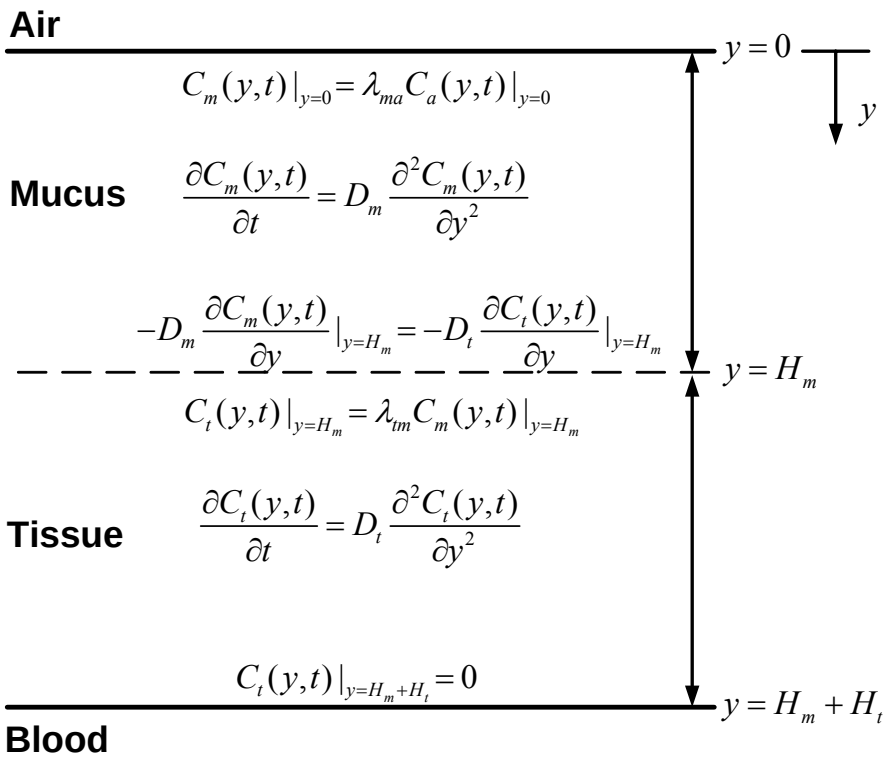

Figure 4.2. System setup for analytic solutions in the mucus and tissue layers.

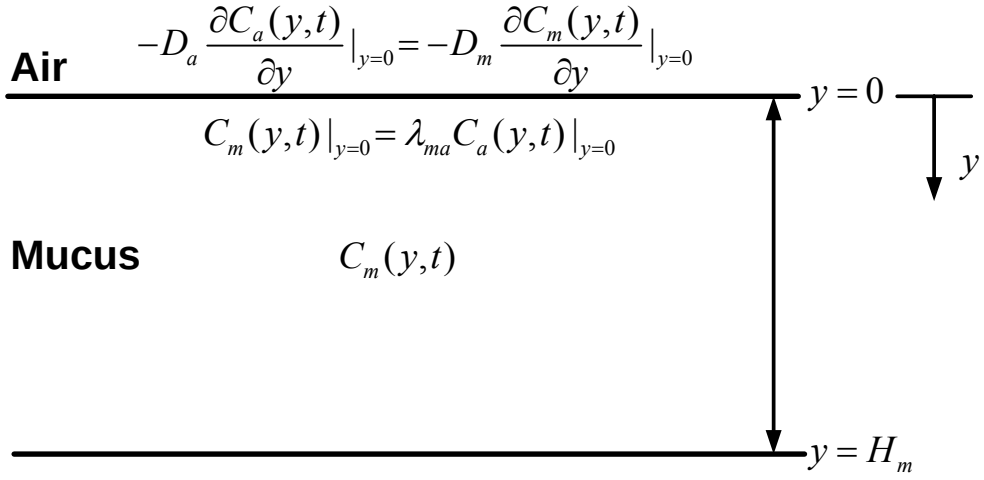

Figure 4.3. Boundary conditions at the air-mucus interface.

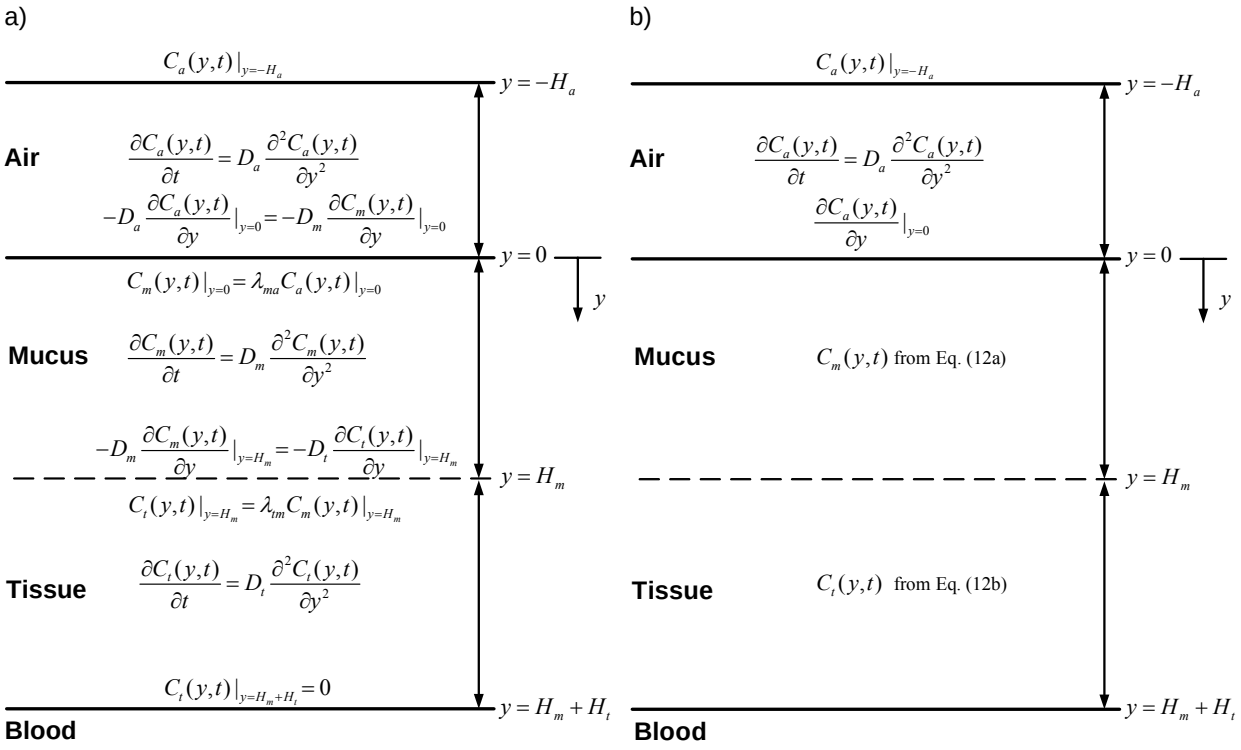

Figure 4.4. System setup for (**a**) the numerical solutions and (**b**) the hybrid solutions in the multilayer system.

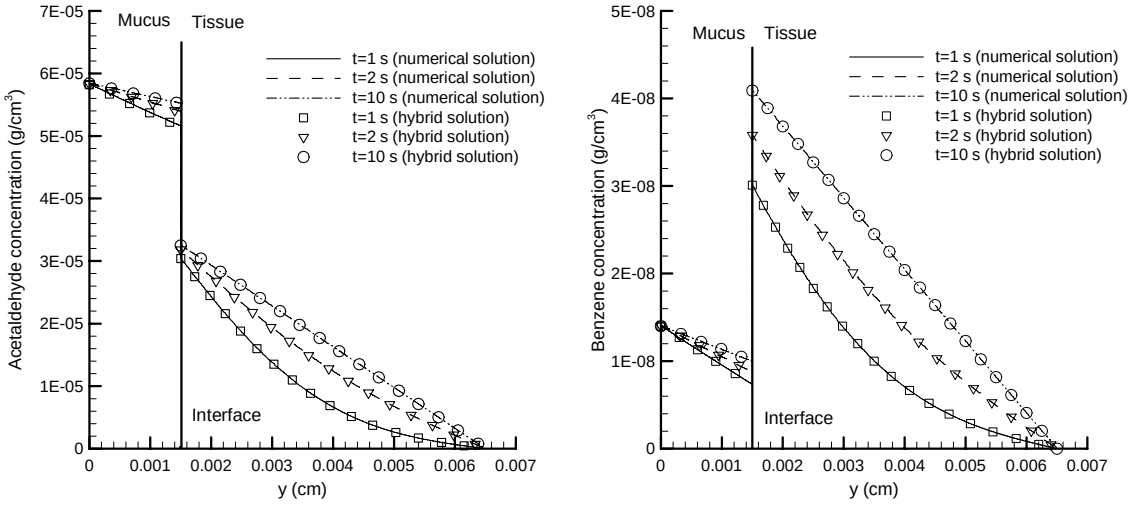

Figure 4.5. Comparison of numerical transient and hybrid solutions for acetaldehyde and benzene concentrations in the mucus and tissue.

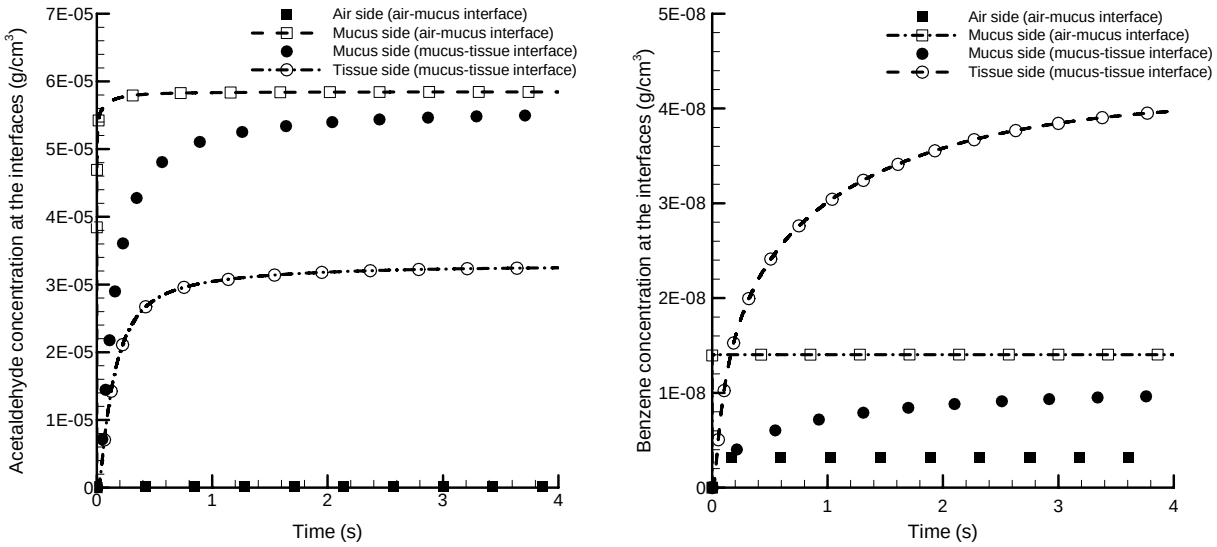

Figure 4.6. Acetaldehyde and benzene concentrations at the air-mucus and mucus-tissue interfaces.

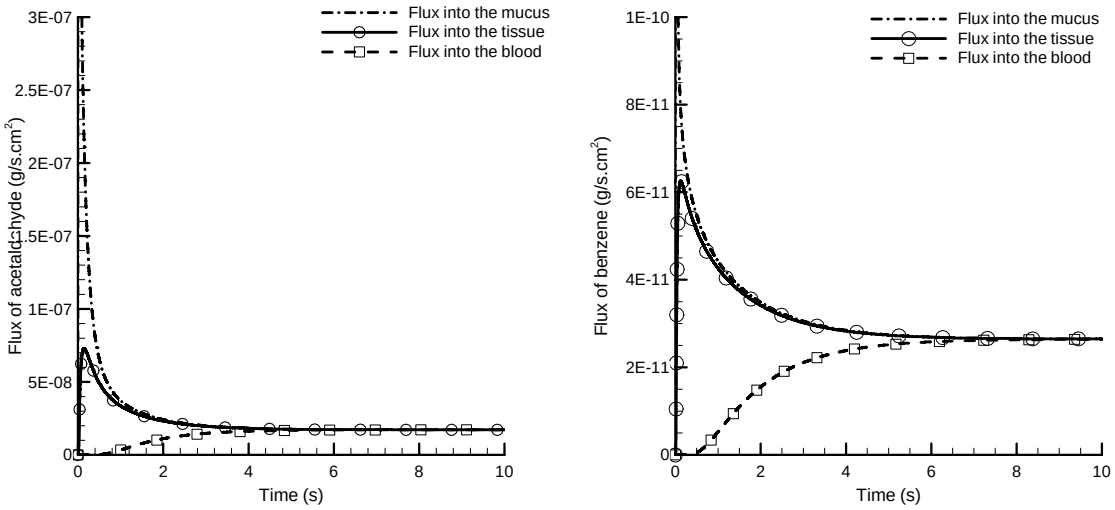

Figure 4.7. Flux of acetaldehyde and benzene into the mucus, tissue and blood layers.

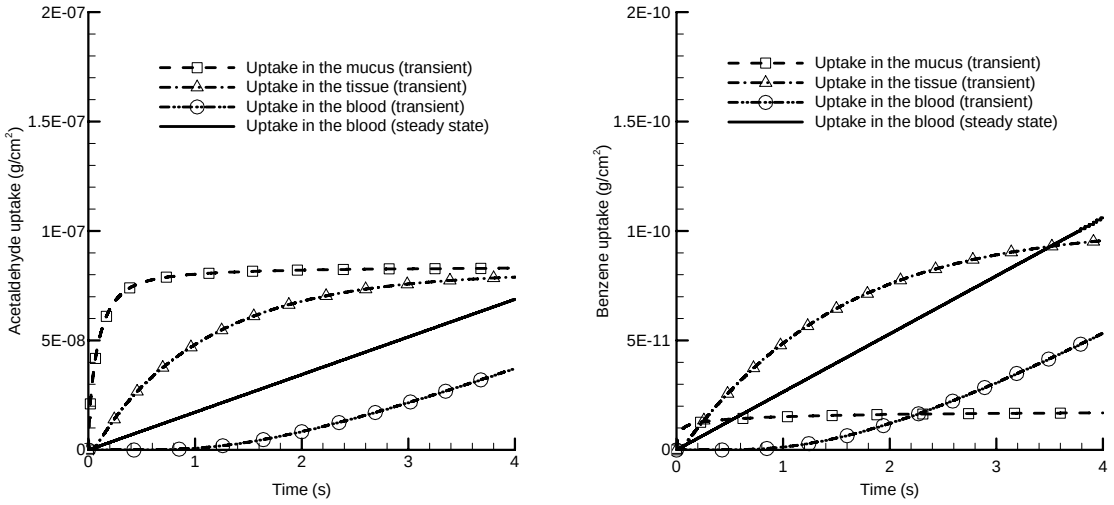

Figure 4.8. Uptake of acetaldehyde and benzene for transient and steady state conditions.

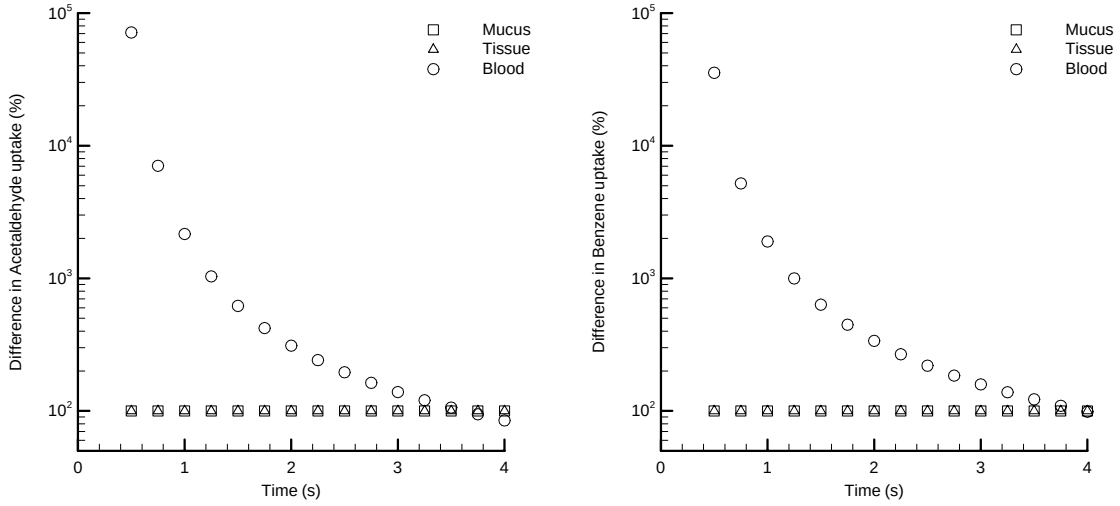

Figure 4.9. Percent differences between steady state vs. transient predictions of uptake for acetaldehyde and benzene.

(a) Mucus

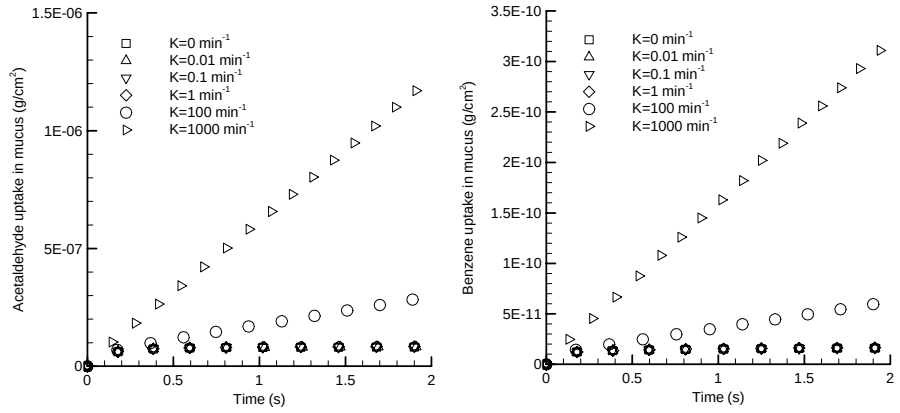

(b) Tissue

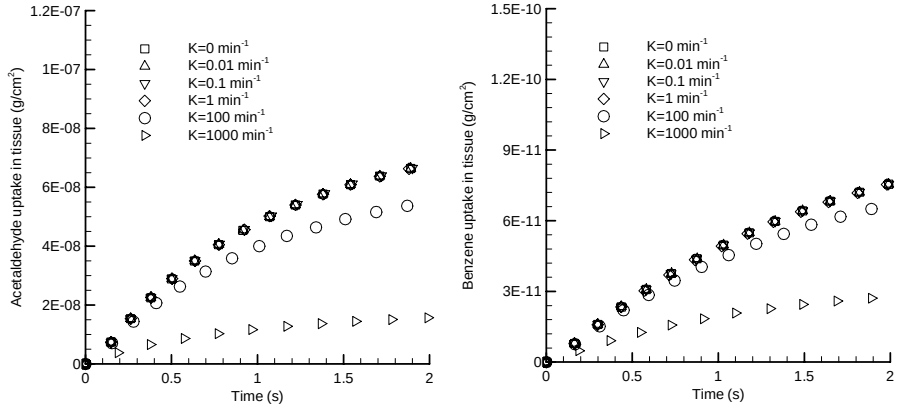

(c) Blood

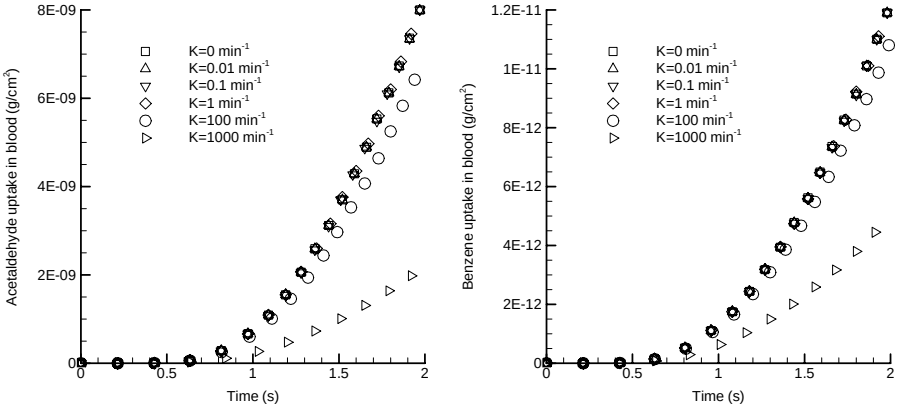

Figure 4.10. Uptake of acetaldehyde and benzene for transient conditions including reactivity.

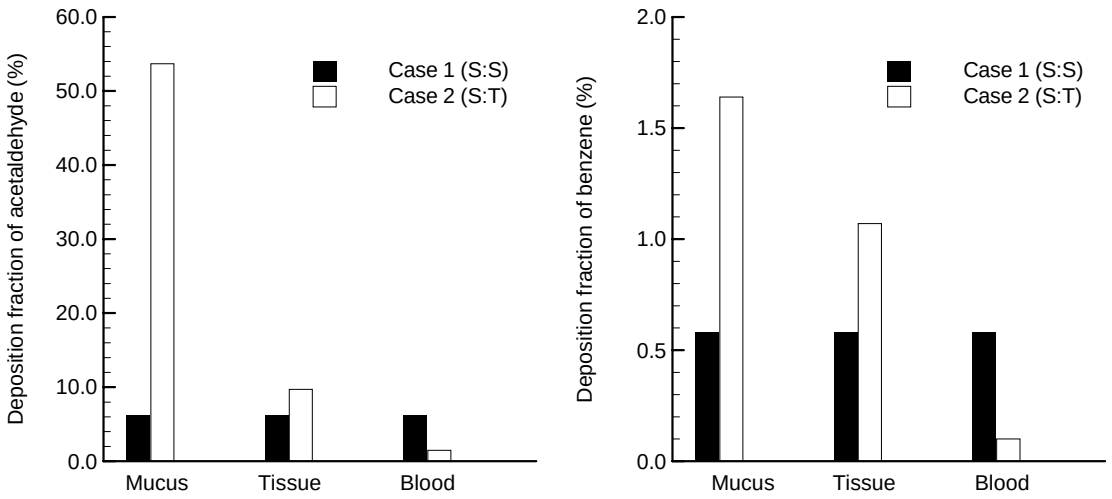

Figure 4.11. Deposition fraction of acetaldehyde and benzene vapors in mucus, tissue, and blood in the nasal-laryngeal airway model for Cases 1 and 2 over a 2 seconds inhalation.

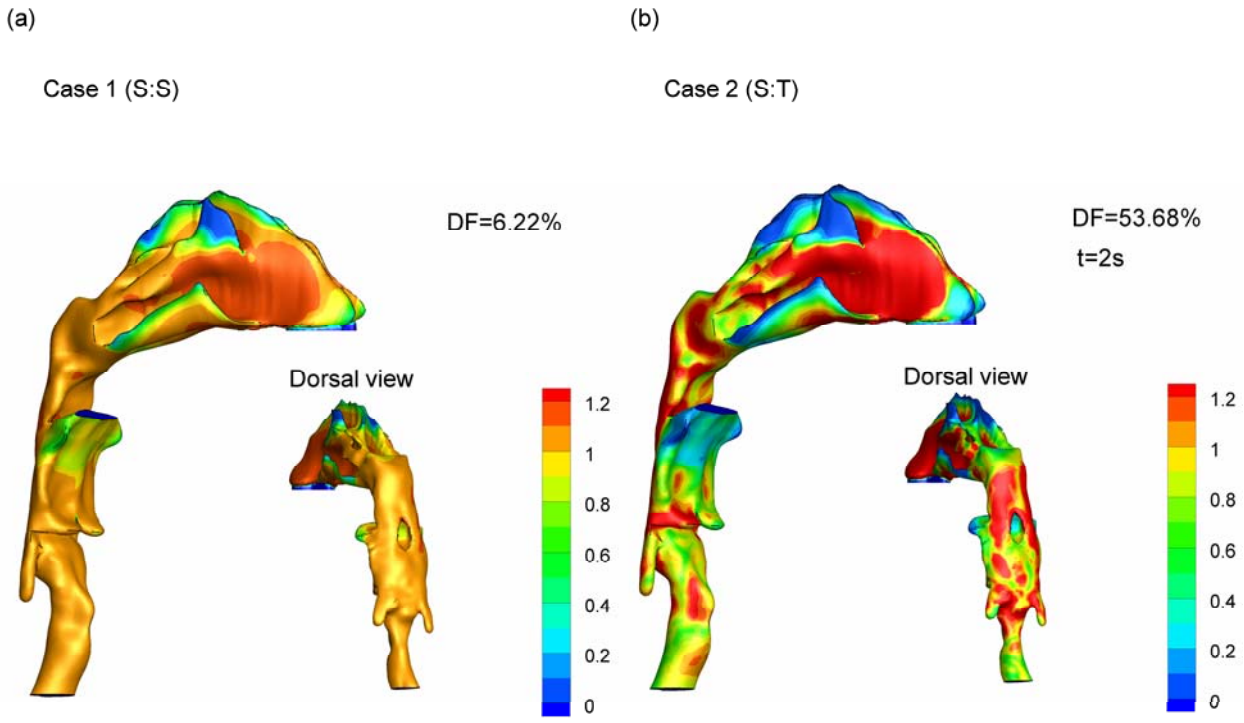

Figure 4.12. DEF contours of acetaldehyde for both cases considered.

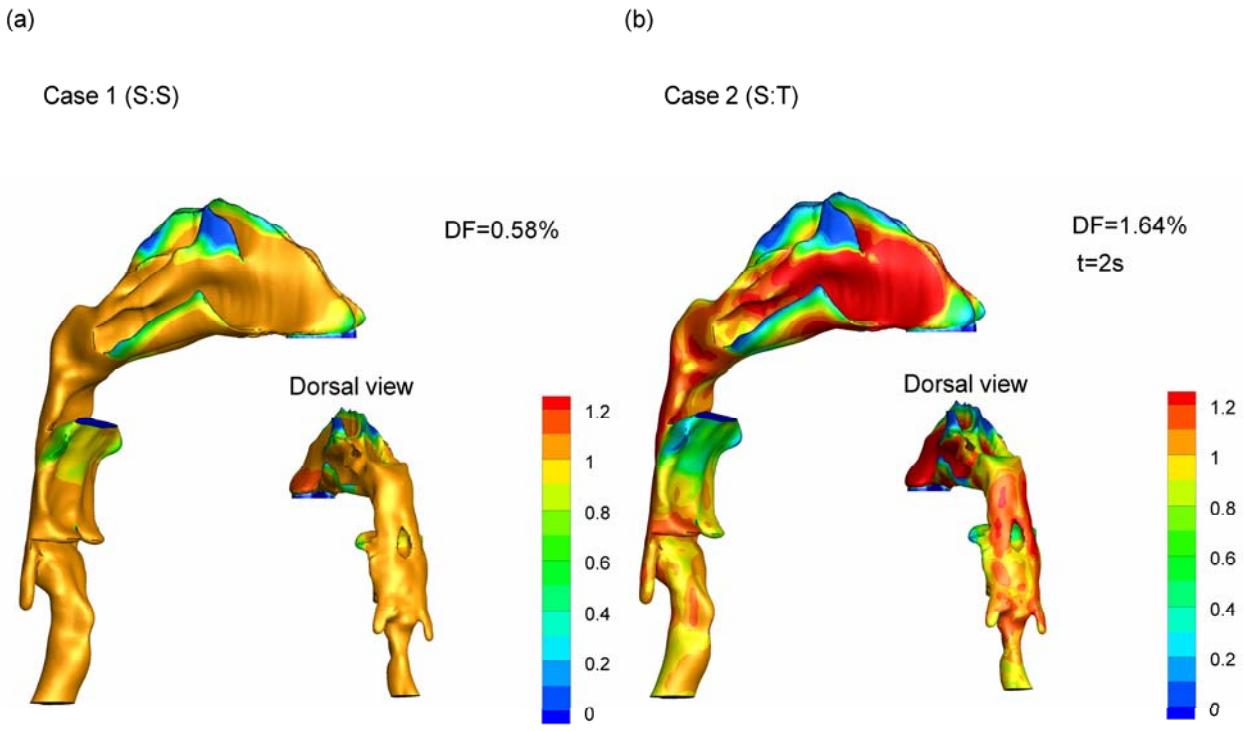

Figure 4.13. DEF contours of benzene for both cases considered.

Chapter 5. Transient Absorption of Inhaled Vapors in the Mouth-Throat Region with an Air-Mucus-Tissue-Blood Wall Boundary Condition

5.1 Introduction

The objective of this study is to predict transient vapor mass absorption of acetaldehyde and benzene in a model of the extrathoracic oral airways with an air-mucus-tissue-blood boundary representation. CFD simulations of air phase transport were coupled with an analytically based boundary condition that accounted for transient absorption into the mucus, tissue, and blood layers of a previously developed mouth-throat (MT) geometry. A well tested low Reynolds number (LRN) $k-\omega$ turbulence model was employed to simulate the flow field. Results of this study indicate that transient absorption can significantly influence the transport and mass absorption of vapors onto the walls of the conducting airways.

5.2 Methods

Upper Airway Geometry

As shown in Fig. 5.1, the upper respiratory tract model considered includes the oral cavity, pharynx, larynx, and upper trachea. This model was originally developed in Xi and Longest (2007b) based on a cast of the oral cavity combined with CT images of the pharyngeal and laryngeal regions. The geometry was then simplified using elliptical cross sections, which maintained the flow area and hydraulic diameter of the original model (Xi and Longest 2007b). The geometry was modified for this study by including an elliptical mouth opening, which is

consistent with relaxed oral inhalation. This model is referred to as the mouth-throat (MT) geometry.

Flow Rates

In this study, transient and steady state airflow fields are considered. Both cases are based on one inhalation cycle with a breathing frequency (f) of 15 *breaths/minute* and a tidal volume (V_T) of 1000 cm^3*/breath*. For steady airflow, the steady state inhalation flow rate Q_S (500 cm^3/s or 30 L/min) is obtained using the equation

$$Q_S = 2f V_T, \tag{5.1}$$

For transient airflow, the transient inhalation flow rate *Q(t)* was approximated as a sinusoidal function with the form

$$Q(t) = Q_m \sin(\omega t), \tag{5.2}$$

where $\omega = 0.5\pi \ \ radians/s$. The mean cyclic flow rate Q_m (785.40 cm^3/s) in Eq. (5.2) can be obtained by solving the equation

$$\int_0^{T/2} Q_m \sin(\omega t)dt = V_T, \tag{5.3}$$

where T = 4 *s/breath.* In this manner, the tidal volume and breathing frequency are consistently applied to find both the steady and transient inhalation flow rates. It is noted that setting Q_s to 500 cm^3/s and satisfying Eq. (5.1) would require artificially modifying the reference inhalation frequency value (f = 15 *breaths/min*) selected. The resulting inlet Reynolds number (based on the inlet hydraulic diameter) for the steady flow rate and mean cyclic flow rate are 2320 and 3645, respectively.

Transport Equations

The low-Reynolds-number (LRN) $k-\omega$ model of Wilcox (1998) was selected for simulating the airflow in the MT model because it has been shown to provide an accurate and numerically efficient solution for transitional and turbulent flows. Furthermore, this model was found to accurately predict laminar flow as the turbulent viscosity approaches zero. The transport equations for the (LRN) $k-\omega$ model, including those governing the turbulent kinetic energy (k) and the specific dissipation rate (ω), were provided by Wilcox (1998) and were previously reported in Xi and Longest (2007b).

The vapor mass transport equation for turbulent flow can be written on a mass fraction basis as

$$\frac{\partial C_a}{\partial t}+\frac{\partial (u_j C_a)}{\partial x_j}=\frac{\partial}{\partial x_j}\left[\left(D_a+\frac{\nu_T}{\sigma_C}\right)\frac{\partial C_a}{\partial x_j}\right], \tag{5.4}$$

where C_a is the mass fraction of a chemical species in air, D_a is the species diffusivity in air, and v_T is the turbulent viscosity. Vectors u_j and x_j are the fluid velocity and position, respectively, and σ_C is the turbulent Prandtl number, taken to be 0.9.

Analytical Solution for Mass Transport in Mucus and Tissue Layers

In this study, vapor absorption and transport are considered in both the airflow field and through the walls of the conducting airways. To approximate transport within the walls of the conducting airways, a model system was considered that consists of air, mucus, tissue, and blood layers. The wall model along with governing equations in each layer are illustrated in Figure 5.2.

Assumptions made in the wall model are that convection is negligible compared with diffusion and that zero concentration of the absorbed chemical species exists in the blood. Zero blood concentration over short term exposures is appropriate due to high convective transport rates in blood relative to diffusion through the wall. However, 1-D models and experiments clearly show that blood concentrations increase over longer timescales (Kumagai and Matsunaga 1995). An analytical solution of this system was previously developed in Chapter 3 and extended to formulate a CFD boundary condition including the air phase in Chapter 4. The analytical solution for the concentration of an absorbed species in the mucus and tissue layers is briefly reviewed below. Flux-based boundary conditions for absorption are then provided for both transient and steady state conditions.

The analytical solution for the transient absorption of a chemical species into a multilayer air-mucus-tissue-blood wall model was previously (Chapter 4) obtained using the Fourier series expansion as

$$C_m = \lambda_{ma}\left(\sum_{n=1}^{\infty} W_n \hat{Y}_m \int_{\tau=0}^{t} e^{-\mu_n^2 \frac{D_m}{H_m^2}(t-\tau)} \frac{dC_a|_{y=0}}{d\tau} d\tau + C_a|_{y=0}\left(1 - \frac{1-\tilde{C}_m|_{y=H_m}}{H_m} y\right)\right), \quad (5.5)$$

$$C_t = \lambda_{ma}\left(\sum_{n=1}^{\infty} W_n \hat{Y}_t \int_{\tau=0}^{t} e^{-\mu_n^2 \frac{D_m}{H_m^2}(t-\tau)} \frac{dC_a|_{y=0}}{d\tau} d\tau + C_a|_{y=0}\left(\frac{\lambda_{tm}\tilde{C}_m|_{y=H_m}}{H_t}(H_m + H_t - y)\right)\right), \quad (5.6)$$

where $\tilde{C}_m|_{y=H_m} = \dfrac{H_t D_m}{H_m \lambda_{tm} D_t + H_t D_m}$, (5.7)

In these expressions, C_m and C_t are the time-dependent mass fractions of a chemical species in mucus and tissue, respectively. D_m and D_t are the species diffusivities in mucus and tissue, respectively, which are assumed to be constant. λ_{ma} and λ_{tm} are the mucus-air and tissue-mucus partition coefficients. H_m and H_t are the thicknesses of the mucus and tissue in a specific region of the respiratory tract, respectively, as shown in Fig. 5.2. Based on ICRP (1994) estimates for the extrathoracic region, values of H_m and H_t in this study were 1.5×10^{-3} cm and 5×10^{-3} cm. The values of transport parameters for two model compounds, acetaldehyde and benzene, are reported in Table 3.1. Based on the reported mucus-air partition coefficients, acetaldehyde can be considered highly soluble in mucus and benzene can be considered moderately soluble. In Equations (5.5) and (5.6), the coefficient W_n can be determined by utilizing the orthogonal relation.

$$W_n = -\frac{\int_0^{H_m} \tilde{C}_m \hat{Y}_m dy + \frac{1}{\lambda_{tm}} \int_{H_m}^{H_m+H_t} \tilde{C}_t \hat{Y}_t dy}{N}, \tag{5.8}$$

where $\tilde{C}_m = 1 - \frac{1-\tilde{C}_m|_{y=H_m}}{H_m} y, \quad y \in [0, H_m]$ (5.9)

$$\tilde{C}_t = \frac{\lambda_{tm} \tilde{C}_m(y)|_{y=H_m}}{H_t}(H_m + H_t - y), \quad y \in [H_m, H_m + H_t] \tag{5.10}$$

$$\hat{Y}_m = \sin(\mu_n \sqrt{\frac{D_m}{D_t}} \frac{H_t}{H_m}) \sin(\frac{\mu_n y}{H_m}), \tag{5.11}$$

$$\hat{Y}_t = \lambda_{tm} \sin(\mu_n) \sin(\mu_n \sqrt{\frac{D_m}{D_t}} \frac{H_m + H_t - y}{H_m}), \tag{5.12}$$

$$N = \int_0^{H_m} \left[\hat{Y}_m\right]^2 dy + \frac{1}{\lambda_{tm}} \int_{H_m}^{H_m+H_t} \left[\hat{Y}_t\right]^2 dy\,, \tag{5.13}$$

The eigenvalues, μ_n, are the sequential positive roots of the transcendental equation

$$\lambda_{tm}\sqrt{\frac{D_t}{D_m}}\tan(\mu_n) + \tan(\mu_n\sqrt{\frac{D_m}{D_t}}\frac{H_t}{H_m}) = 0\,, \tag{5.14}$$

and were determined using Brent's method (Press et al. 1996). The coefficients W_n were determined by utilizing the orthogonal relation and zero concentration initial conditions. The first five values in the eigenvalue and constant series are provided in Table 5.1, which are accurate to four digits.

Transient Flux Boundary Conditions

The analytical solution in the mucus (C_m), the value of the mucus-air partition coefficient, and an assumption of flux ($g/s-cm^2$) conservation can be combined into the transient flux boundary condition at the air-mucus interface. This boundary condition has the following form, which was developed in Chapter 4

$$\frac{\partial C_a}{\partial y}|_{y=0} = \frac{D_m\lambda_{ma}}{D_a}\left(\frac{1}{H_m}\sum_{n=1}^{\infty}\mu_n W_n \sin(\mu_n\sqrt{\frac{D_m}{D_t}}\frac{H_t}{H_m})\int_{\tau=0}^{t} e^{-\mu_n^2\frac{D_m}{H_m^2}(t-\tau)}\frac{dC_a|_{y=0}}{d\tau}d\tau - C_a|_{y=0}\frac{1-\tilde{C}_m|_{y=H_m}}{H_m}\right) \tag{5.15}$$

To determine uptake in the tissue and blood layers, flux boundary conditions into these phases are also needed. The transient flux wall boundary condition at the

mucus-tissue interface can be found by differentiating C_m with respect to y, and has the form

$$\frac{\partial C_m}{\partial y}|_{y=H_m} = \lambda_{ma}\left(\frac{1}{H_m}\sum_{n=1}^{\infty}\mu_n W_n \sin(\mu_n\sqrt{\frac{D_m}{D_t}}\frac{H_t}{H_m})\cos(\mu_n)\int_{\tau=0}^{t} e^{-\mu_n{}^2\frac{D_m}{H_m{}^2}(t-\tau)}\frac{dC_a|_{y=0}}{d\tau}d\tau - C_a|_{y=0}\frac{1-\tilde{C}_m|_{y=H_m}}{H_m}\right) \tag{5.16}$$

The transient flux wall boundary condition at the tissue-blood interface can be found by differentiating C_t with respect to y, and has the form

$$\frac{\partial C_t}{\partial y}|_{y=H_m+H_t} = \lambda_{ma}\lambda_{tm}\left(-\frac{1}{H_m}\sqrt{\frac{D_m}{D_t}}\sum_{n=1}^{\infty}\mu_n W_n \sin(\mu_n)\int_{\tau=0}^{t} e^{-\mu_n{}^2\frac{D_m}{H_m{}^2}(t-\tau)}\frac{dC_a|_{y=0}}{d\tau}d\tau - C_a|_{y=0}\frac{\tilde{C}_m|_{y=H_m}}{H_t}\right) \tag{5.17}$$

Steady State Flux Boundary Conditions

The transient boundary conditions developed above can be simplified to steady state conditions by removing the transient terms. The steady flux boundary condition at the air-mucus interface results in

$$\frac{d\tilde{C}'_a}{dy}|_{y=0} + K_a\tilde{C}'_a|_{y=0} = 0, \tag{5.18}$$

where $K_a = \dfrac{D_m\lambda_{ma}(1-\tilde{C}_m|_{y=H_m})}{D_a H_m}$. (5.19)

In these expressions, $\tilde{C}'_a$ is the steady-state mass fraction of a chemical species in air.

The steady flux boundary condition at the mucus-tissue interface reduces to

$$\frac{d\tilde{C}'_m}{dy}|_{y=H_m} + K_m\tilde{C}'_a|_{y=0} = 0, \tag{5.20}$$

where $K_m = \dfrac{\lambda_{ma}(1-\tilde{C}_m\,|_{y=H_m})}{H_m}$. (5.21)

In these expressions, $\tilde{C}'_m$ is the steady-state mass fraction of a chemical species in mucus.

The steady flux boundary condition at the tissue-blood interface results in

$$\frac{d\tilde{C}'_t}{dy}|_{y=H_m+H_t} + K_t \tilde{C}'_a\,|_{y=0} = 0, \tag{5.22}$$

where $K_t = \dfrac{\lambda_{ma}\lambda_{tm}\tilde{C}_m\,|_{y=H_m}}{H_t} = \dfrac{D_m\lambda_{ma}(1-\tilde{C}_m\,|_{y=H_m})}{D_t H_m}$. (5.23)

In these expressions, $\tilde{C}'_t$ is the steady-state mass fraction of a chemical species in tissue. Furthermore, it can be shown that the steady state fluxes into the mucus, tissue and blood layers are equal and constant, i.e.,

$$-\rho_m D_a \frac{d\tilde{C}'_a}{dy}|_{y=0} = -\rho_m D_m \frac{d\tilde{C}'_m}{dy}|_{y=H_m} = -\rho_m D_t \frac{d\tilde{C}'_t}{dy}|_{y=H_m+H_t}, \tag{5.24}$$

where the mixture density ρ_m is assumed constant. As a result, uptake in the mucus, tissue, and blood layers are equal and constant for steady state conditions.

Deposition Factors

For the transport model, the total deposition fraction at steady state can be expressed as

$$DF_i = \frac{\dot{m}_{w,i}}{\dot{m}_{in}}, \tag{5.25}$$

where $\dot{m}_{w,i}$ is the total mass absorption rate into the wall surface and $\dot{m}_{in}$ is the inlet mass flow rate of the chemical species. The transient total deposition fraction can be expressed as

$$DF_i = \frac{\int_0^{T/2} \dot{m}_{w,i} dt}{\int_0^{T/2} \dot{m}_{in} dt}, \tag{5.26}$$

The breathing period (T) is divided by two in order to account for only one inhalation cycle (T/2 = 2 s) in most cases considered. For turbulent flow, the total mass absorption rate into the wall surface can be expressed as

$$\dot{m}_{w,i} = \sum_{j=1}^{N} -\rho_m A_j (D_a + \frac{\nu_T}{\sigma_C}) \frac{\partial C_a}{\partial n} |_{w,j} \tag{5.27}$$

where A_j is the local area, and the summation is performed over the total or $i-$region of interest. The mixture density is ρ_m. The vector n is the wall normal coordinate pointing out of the geometry. The inlet mass flow rate of the chemical species can be determined as

$$\dot{m}_{in} = \rho_m Q C_{in}, \tag{5.28}$$

where Q is the inlet inhalation flow rate and C_{in} is the inlet mass fraction, taken to be 0.05.

A deposition enhancement factor (DEF), similar to that suggested by Longest and Xi (2007a), was defined in order to quantify local deposition in local area A_j with respect to the total deposition rate, i.e.,

$$DEF_j = \frac{DF_j / A_j}{DF_i / A_i}, \tag{5.29}$$

where A_t is the total area of the model. Deposition enhancement factors represent the ratio of a compound depositing in a local area (taken to be a control volume surface with an area of approximately 0.5 mm x 0.5 mm) to the total deposition within the geometry.

Numerical Method

While effective, implementation of the transient absorption, or even the steady state absorption, boundary conditions can be complex. For the transient case, the flux-based boundary conditions contain a series summation and require the evaluation of an integral term. Eigenvalues μ_n and coefficients W_n are included in the summation term and must be determined from a transcendental equation and integral expression, respectively. Application of this complex boundary condition in a CFD solution of the airflow phase can be difficult. To facilitate implementation of the transient absorption boundary conditions, a new user-friendly program titled Transient Absorption of Chemical Species (TAOCS) 1.0 was developed. The TAOCS 1.0 program is based on the AMTB wall model and equations shown in Fig. 5.2. The TAOCS graphical user interface (GUI) along with several input windows for specifying transport properties and determining the eigenvalues are shown in Fig. 5.3. The user inputs the transport properties of the chemical species (from Table 3.1), wall conditions, and initial surface concentrations. Based on the previous work in Chapters 3 and 4, and the boundary conditions presented in this study, the TAOCS program provides:

1. Ready to implement user-defined functions (UDFs) for use with a commercial CFD program (Fluent 6.3), which specify the transient flux boundary conditions, i.e., Eqs. (15) – (17).
2. The μ_n and W_n coefficients through any order needed to evaluate the flux expressions (cf. Table 5.1).
3. The *analytical* solution of transport into an air-mucus-tissue-blood system based on both steady and transient absorption.
4. The *numerical* solution of transport into an air-mucus-tissue-blood system based on both steady and transient conditions for comparisons with the analytical solution and CFD results.

In this study, the TAOCS program was used to calculate the μ_n and W_n coefficients for use in the transient boundary conditions (Table 5.1) and to generate the UDFs needed for implementation of the boundary conditions in the CFD code.

To solve the governing conservation equations, the CFD package Fluent 6.3 (Ansys Inc.) was employed. User-supplied C programs were implemented for the calculation of the transient boundary condition, vapor absorption, and deposition enhancement factors. All transport equations were discretized to be at least second order accurate in space. For the convective terms, a third order QUICK scheme was used to interpolate values from cell centers to nodes. The diffusion terms were discretized using central differences. A segregated implicit solver was employed to evaluate the resulting linear system of equations. This solver uses the Gauss-Seidel method in conjunction with an algebraic multigrid approach.

The PISO algorithm was employed to evaluate pressure-velocity coupling in the transient solutions. The outer iteration procedure was stopped when the global mass residual had been reduced from its original value by five orders of magnitude and when the residual-reduction-rates for both mass and momentum were sufficiently small. To ensure that a converged solution had been reached, residual and reduction rate factors were decreased by an order of magnitude and the results were compared. The stricter convergence criteria produced a negligible effect on both velocity and vapor absorption predictions. To improve accuracy, cgs units were employed, and all calculations were performed in double precision. Grid converged results based on negligible change in the velocity and concentration fields (< 1%) as well as negligible differences in the total deposition fractions (< 3%) were established for a mesh consisting of 1×10^6 hexahedral control volumes. The size of the first control volume next to the wall surfaces was found to strongly affect mesh convergence. A value of 0.05 mm was needed to produce negligible (< 3%) changes in the absorption predictions.

Cases Considered

Six cases were considered in the MT airway model, as outlined in Table 5.2. Each case is represented by a combination of steady (S) vs. transient (T) airflow conditions and steady vs. transient vs. perfect (P) wall absorption. Perfect wall absorption is defined as a concentration of zero on the wall boundary, which may be appropriate for very high absorption or reactivity rates. These conditions are abbreviated for each case in terms of (flow field condition : wall absorption). For Case 1 (S:S) and Case 3 (S:T), steady state flow fields and mass concentration

fields were assumed. For Case 2 (T:S) and Case 4 (T:T), transient flow fields and mass concentration fields were simulated. Absorption was then modeled based on either the steady state or transient boundary condition over a timescale consistent with one inhalation cycle (2 s). For Case 5 (S:P) and Case 6 (T:P), perfect absorption was assumed, which can be mathematically expressed as $\tilde{C}'_a(y)|_{y=0} = 0$ at the wall. The focus of the results is then to identify differences between the most complex case (Case 4 (T:T)) and the other commonly used approximations.

5.3 Results

Mass Fraction

Effects of airflow and wall absorption conditions on vapor mass fraction distributions of acetaldehyde and benzene in the MT model are shown in Figures 4 and 5, respectively. For the transient conditions shown, a 2 second inhalation period was applied. Beginning with acetaldehyde, the concentration profiles for Case 4 (T:T) are highly complex (Fig. 5.4). Considering airflow effects, steady state conditions appear to significantly change the concentration profiles (Case 3 (S:T) vs. Case 4 (T:T)). Considering absorption, steady state again appears to have a major impact on the concentration profiles (Case 2 (T:S)) vs. Case 4 (T:T)). Of the cases considered, transient airflow and perfect absorption (Case 6) appear to best match the transient conditions of Case 4. However, similar mass fraction concentrations in the flow field do not necessarily imply that absorption into the walls will be similar between Cases 4 and 6.

Considering benzene, the lower solubility coefficient results in nearly constant concentrations for Case 4 (T:T) conditions (Fig. 5.5) at the selected contour levels. Steady airflow is again observed to significantly impact the concentration profile (Case 3 (S:T) vs. Case 4 (T:T)). With respect to absorption, steady state conditions Case 2 (T:S) appear to provide a reasonable approximation to the transient wall conditions of Case 4. As expected, perfect absorption (Case 6 (T:P)) provides very different contours from the transient absorption case.

Deposition Fraction Values of Acetaldehyde and Benzene

Deposition fractions (DF) for acetaldehyde and benzene vapors in mucus, tissue, and blood in the human upper airway model for Cases 1-4 are shown in Fig. 5.6. The DF values of acetaldehyde and benzene for all cases considered are also tabulated in Table 5.3. The DF is defined as the amount of inhaled vapor mass that enters each wall layer normalized by the amount of inhaled mass (cf. Eq. (26)). As such, the DF provides a relative estimate of the amount of the species that reaches each level of the wall over a defined time period. It is observed that DF values for transient absorption (Cases 3 and 4) are significantly different from steady state absorption (Cases 1 and 2). Specifically, DF values of acetaldehyde in the mucus are approximately 10 to 15 times greater for transient absorption compared with steady state absorption. Deposition fraction values of benzene in the mucus are approximately 4 to 6 times greater for transient absorption compared with the steady absorption condition. For Case 1 (S:S), the DF values are equal in mucus, tissue, and blood. For Case 2, the transient flow effects cause little difference in DF values for mucus, tissue, and blood. For Cases 3 and 4, the

DF values of acetaldehyde in mucus are approximately 6 times higher than in tissue and 40 times higher than in blood. The DF values of benzene in mucus are approximately 2 times higher than in tissue and 20 times higher than in blood. The higher deposition of acetaldehyde vapor may be attributed to its higher solubility in the mucus layer compared with benzene. Under the same absorption conditions, the differences of DF values in mucus between Case 1 and Case 2, Case 3 and Case 4, Case 5 and Case 6, are 11.3%, 28.1%, and 27.0% for acetaldehyde and 10.0%, 26.8%, and 27.1% for benzene, respectively. Therefore, it is concluded that the transient flow field also influences the deposition fraction, but to a much lesser extent than the transient absorption condition.

Comparisons of DF values in mucus for the human upper airway model between Case 3 (S:T) and Case 5 (S:P), and between Case 4 (T:T) and Case 6 (T:P) are shown in Fig. 5.7. Case 5 (S:P) and Case 6 (T:P) assume that the airway wall is a perfect sink for vapors, i.e., the boundary condition on the wall is $\tilde{C}_a'(y)|_{y=0} = 0$. However, this assumption is only reasonable for vapors of high solubility, or for estimating the maximum deposition of vapors in the airways. Compared with Case 3, the DF values of Case 5 are approximately 1.5 times greater for acetaldehyde and 40 times greater for benzene. Similarly, compared with Case 4, the DF values of Case 6 are approximately 1.5 times greater for acetaldehyde and 40 times greater for benzene. Therefore, the perfect absorption boundary condition is accurate to within approximately 50% (calculated as a relative percent error) compared with transient absorption for the highly soluble

compound acetaldehyde and should not be applied for compounds with lower solubilities.

Local Deposition

Contours of local deposition enhancement factors (DEFs) for acetaldehyde and benzene vapors are shown in Figures 8 and 9, respectively. As described, the DEF contours represent the locally absorbed mass divided by the area-averaged total absorption to give a normalized representation of local uptake. Similarities in local deposition based on DEF patterns and maximum values were consistent with observations of total deposition fractions. For acetaldehyde, Case 4 (T:T) local deposition values were most similar to Case 3 (S:T) indicating that the absorption condition is most significant. Case 6 (T:P) DEF patterns were also similar with Case 4 (T:T), but with a much higher maximum (8.81 vs. 2.72) as expected for perfect absorption. Considering benzene, Case 4 (T:T) local DEF values were found to be similar with Case 3 (S:T) and Case 2 (T:S). The similarity with Case 3 was expected based on observations made with the total deposition fractions. However, similarity between Cases 4 and 2 was not expected considering the order of magnitude difference in the total deposition fractions.

Mass Absorption into the Wall Layers

Mass absorption into the wall layers for acetaldehyde and benzene under Cases 1 (S:S) and 3 (S:T) conditions are presented in Fig. 5.10. Steady airflow fields are considered to isolate the effects of transient vs. steady state absorption

over time. The mass absorption differences between Case 1 and Case 3 are highly significant. At 2 s, transient mass absorption into the mucus layer for acetaldehyde and benzene is approximately 15 times and 6 times higher than predicted with the steady state solution, respectively. Transient mass absorption into the tissue layer for acetaldehyde and benzene is approximately 3 times higher than predicted with the steady state solution. Similarly, the mass absorption into the blood for acetaldehyde and benzene is lower than with steady state conditions by a factor of approximately 4.

Mass Absorption over Multiple Breaths

The results presented in the previous figures are for one inhalation cycle. However, buildup of species concentrations in the wall layer over multiple breathing cycles may diminish transient absorption effects. To evaluate the buildup of concentrations in the wall layers, three breath cycles (2 s inhalation and 2 s exhalation) were simulated for Case 4 (T:T) and compared with the Case 1 (S:S) results. The species concentrations entering the model at the larynx during exhalation were estimated based on expected lung uptake values. Considering the high and moderate solubilities of acetaldehyde and benzene, the estimated concentrations entering the larynx during expiration were assumed to be 0 and 30% of the inhaled mass concentrations, respectively, which assumes 100 and 70% lung absorption. These values are only intended to explore the potential for buildup in the wall layers during absorption and desorption and may not provide quantitative estimates of acetaldehyde and benzene uptake *in vivo*. It is noted that an accurate prediction of the concentration entering the geometry during

exhalation will require a linked CFD and 1-D model, as performed in other studies (Frederick et al. 1998; Kimbell et al. 2001a; Overton et al. 2001).

Multiple breath simulation results are shown in Fig. 5.11 in terms of absorption rate (g/s). To allow a direct comparison between the steady state Case 1 and transient Case 4 estimates, a time average was taken of the transient mass absorption rate (time-averaged transient rate). During the first inhalation cycle for acetaldehyde and benzene, a rise is observed in the transient absorption rate. However, after the first inhalation cycle the transient absorption rate appears to repeat for subsequent breaths without significant change. Specifically, differences in the maximum transient absorption value between breaths 2 and 3 are less than 0.2% for both compounds. This implies that some buildup of the species occurs in the wall after the first breath due to incomplete desorption. Thereafter, a cyclic pattern emerges that is repeated for subsequent breaths. This first breath buildup has a relatively minimal effect on the absorption rate of acetaldehyde. In contrast, a more visible effect is observed for benzene arising from the non-zero concentration entering the model during exhalation. While concentration buildup in the wall layer is expected to reduce transient effects, the transient fluctuations still clearly influence mass absorption. Specifically, the transient mass absorption rate averaged over breaths 2 and 3 (once a repeating pattern occurs) is 7 times greater than the steady state prediction for acetaldehyde and 3.5 times greater than the steady state prediction for benzene. Absorption results evaluated in the tissue and blood layers were similar to those found in the mucus.

5.4 Discussion

This study has considered transient absorption of inhaled vapors into a multilayer air-mucus-tissue-blood system in a human upper airway model. The transient flux boundary condition at the air-mucus interface was employed for CFD simulations of gas phase transport and mass transfer. Six cases were intended to quantify the effects of transient absorption compared with steady state conditions. A new dosimetry program TAOCS 1.0 was used in conjunction with a CFD model to apply and evaluate both steady state and transient wall absorption conditions.

Conclusions of the model results can be summarized as described below. These conclusions are based on the single inhalation cycle simulations performed in this study, which neglect reactions in the airway wall, and assume zero species concentration in the blood.

- For both highly and moderately soluble compounds:
    - Steady state absorption cannot capture transient absorption conditions. After 2 seconds, differences were at least one order of magnitude.
    - Steady state airflow produces significant changes in the concentration field compared with transient airflow. However, steady state airflow conditions only influence total deposition fractions by approximately 10 – 30%.
    - Steady airflow also produced reasonable approximates of local DEF values compared with transient airflow conditions.

- For highly soluble compounds ($\lambda_{ma} \geq 320$)
    - Perfect absorption provides a reasonable estimate (within ~50%) of total deposition compared with the transient boundary condition.
    - Considering local deposition, perfect absorption significantly over predicts maximum DEF values.
- For moderately soluble compounds ($\lambda_{ma} \sim 4$)
    - Total deposition fractions cannot be approximated with either steady state or perfect absorption boundary conditions. Therefore, consideration of transient wall absorption is required.
    - Based on total absorption findings, local absorption should not be approximated with steady or perfect absorption conditions.

To summarize these observations, steady state airflow provides a reasonable approximately to transient airflow conditions (within 10 – 30%) in terms of total and local deposition. However, the simulation of transient wall absorption is critical unless the compound is highly soluble ($\lambda_{ma} \geq 320$) and a perfect absorption boundary condition can be applied. Still, the perfect absorption boundary condition does not adequately model local DEF values.

A primary limitation of this study is the omission of chemical reactivity in the mucus, tissue, and blood. Other studies have shown that reactivity can significantly influence uptake under steady state absorption conditions (Cohen Hubal et al. 1996b; Cohen Hubal et al. 1997; Keyhani et al. 1997; Kimbell et al. 2001a; Zhang and Kleinstreuer 2006). However, the previous studies of Tian and

Longest (2010a; 2010b) have shown that when transient absorption is considered, the effects of chemical reactions are significantly diminished. This is because of finite reaction rate times over 1 – 2 s with transient absorption vs. infinite reaction rate times associated with a steady absorption model. The results of Tian and Longest (2010a; 2010b) indicated that reactions were not significant compared with transient absorption for both acetaldehyde and benzene at typical inhalation concentrations and short term exposures with zero blood concentrations. However, for highly reactive compounds like ozone, reactions cannot be neglected. Future work is needed to extend the current transient absorption boundary condition developed by our group to account for chemical reactions in a time-dependent manner. Because reactions were neglected in this study, the quantitative values reported for acetaldehyde and benzene should be examined further and interpreted as representative of general highly and moderately soluble compounds.

A second limitation of the current study is the focus on a single breath or a small number of breaths. Buildup of concentrations in the tissue and blood are known to have an effect on absorption (Kumagai and Matsunaga 1995) and are expected to reduce the overall importance of time dependence. To evaluate concentration buildup in the wall under the assumption of zero blood concentration, a multiple breath simulation was conducted (Fig. 5.11). While exact values of concentrations entering the larynx are not known, results of these multiple breath simulations were informative. In summary, it was found that buildup in the wall influences transient flux values between the first and second breaths. Thereafter, a cyclic repeating transient absorption pattern was observed.

Despite an expected reduction in transient absorption effects, the time-averaged transient absorption rate remained 3.5 to 7 times greater than the corresponding steady state estimate. Therefore, it can be concluded that buildup in the wall layers does not significantly diminish transient absorption effects, even if 30% (or potentially more) of the inspired concentration is exhaled.

Similar to buildup in the wall layers, absorption and buildup of chemicals in the blood may diminish transient differences from steady state values. Previous 1-D models have shown that blood concentrations of species can increase over long exposure timescales on the order of hours (Kumagai and Matsunaga 1995). It is expected that until saturated blood levels are reached, transient absorption and desorption from the wall layer into the air will produce absorption rate values different from steady state estimates. However, this analysis is beyond the scope of the current study.

It is stressed that the results of this study are for zero concentration of the absorbed species in the blood, which may be referred to as the initial wash-in phase of vapor exposure. During this period, it is expected that absorption rates will be elevated, potentially heightening the effects of cyclic inhalation and transient wall absorption. In comparison, it is noted that previous experimental and numerical results have indicted that steady and transient exposures produce similar absorption rates. For example, Morris and Blanchard (1992) showed that the fractional upper respiratory tract absorption in a rodent model was similar between steady state and cyclic experimental conditions at equivalent flow rates for an exposure period of 40 minutes. Both steady state and cyclic total

absorption results were reasonably well predicted by the model of Aharonson et al. (1974). Using a CFD-PBPK model that updated blood concentration and exhaled fraction with time, Frederick et al. (1998) showed that transient and steady state predictions of acrylic acid concentration in tissue varied by a factor of 2 over an exposure period of three minutes. As indicated earlier, this study included transient flow field and inlet concentration effects, but the CFD model most likely applied steady state flux equations to describe transport through the walls of the nasal cavity model. Furthermore, previous experimental studies have highlighted the importance of chemical reactions in the airways (Morris and Blanchard 1992; Morris and Cavanagh 1987). One potential reason that the results of the current study differ from previous experimental and numerical results is the time scale considered. It is suggested that during the initial wash-in phase, when zero blood concentrations can be assumed, transient effects are highly significant as suggested in the current study. As blood concentrations increase, absorption is reduced, and the effects of cyclic breathing and transient absorption are diminished. Therefore, long-term exposures to environmental type pollutants may be appropriately modeled using a steady state approach. In contrast, shorter exposures described by the wash-in phase of airway kinetics (and zero or near zero blood concentrations) may need to consider the transient effects described in this study. Examples of short term exposures where transient effects will likely be most important include smoking, the delivery of vaporized pharmaceuticals, and the inhalation of high concentrations of noxious chemicals that may be released during an environmental accident, fire, or chemical weapons attack.

The model presented in this study is a first step toward better estimating transient absorption using CFD predictions, which can provide highly localized uptake values. The simulations clearly show that the implementation of a transient flux boundary condition appears critical to predict total and local deposition characteristics for even highly soluble compounds. However, future work is needed to make toxicologically relevant predictions in many cases. First, the transient absorption boundary condition currently neglects reactions in the airway wall. While Tian and Longest (2010a; 2010b) clearly showed that transient effects diminished the influence of reactivity, future work is needed to confirm this finding over a range of exposure concentrations and times. The transient absorption model is most appropriate for predicting uptake over short term exposures before significant buildup in blood concentrations occurs. Examples of these types of exposures include smoking and inhalation of noxious compounds. Simulations of multiple breaths showed that a cyclic pattern of mucus absorption and desorption is quickly reached. However, buildup of species in the blood and the effect on subsequent absorption needs to be considered in future studies. To address longer term exposures, a combination of the proposed CFD model with a lumped parameter or 1-D whole-body model is suggested which can accurately predict both local transient absorption and blood concentrations over time. Still, the results as presented provide a valuable next step toward time-resolved CFD predictions of vapor absorption in the respiratory airways.

In conclusion, the effects of transient airflow and absorption vs. steady state conditions were considered for highly and moderately soluble compounds in an upper airway model. The use of the TAOCS program in conjunction with CFD simulations resulted in a new dosimetry approach to effectively simulate steady state and transient absorption on a regional and highly localized basis. Findings highlighted the need for considering transient wall absorption. However, differences associated with steady state flow fields may be acceptable. Future studies are needed to consider chemical reactions, the buildup of concentrations in the blood, absorption throughout the respiratory tract and over longer time periods, and to validate the model with experimental results.

Table 5.1. The first five eigenvalues μ_n and coefficients W_n.

Acetaldehyde		Benzene	
μ_1= 0.5092	W_1=-1.4549	μ_1=0.4050	W_1=-1.3355
μ_2=0.9992	W_2=0.5802	μ_2=0.8708	W_2=0.2435
μ_3=1.4243	W_3=-0.4656	μ_3=1.3677	W_3=-0.1033
μ_4=1.7934	W_4=0.3618	μ_4=1.8712	W_4=0.0787
μ_5=2.2359	W_5=-0.2578	μ_5=2.3646	W_5=-0.1027

Table 5.2. Definition of steady and transient cases considered.

	Airflow (Air and mass species)	Absorption	Designation
Case 1	Steady	Steady flux	S:S
Case 2	Transient	Steady flux	T:S
Case 3	Steady	Transient flux	S:T
Case 4	Transient	Transient flux	T:T
Case 5	Steady	$\tilde{C}'_a \mid_{y=0} = 0$	S:P
Case 6	Transient	$\tilde{C}'_a \mid_{y=0} = 0$	T:P

Table 5.3. Total deposition fractions (DF) as percentages in mucus, tissue, and blood.

	Acetaldehyde			Benzene		
	in mucus	in tissue	in blood	in mucus	in tissue	in blood
Case 1	2.13	2.13	2.13	0.20	0.20	0.20
Case 2	1.89	1.87	1.87	0.18	0.17	0.17
Case 3	29.87	4.75	0.71	1.12	0.51	0.05
Case 4	21.49	3.66	0.55	0.82	0.45	0.04
Case 5	44.13	0	0	46.14	0	0
Case 6	32.21	0	0	33.66	0	0

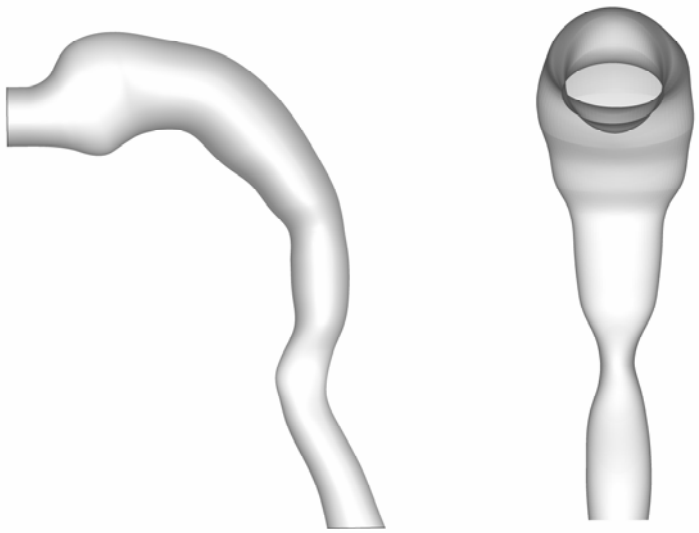

Figure 5.1. Surface model of the mouth-throat region including the oral cavity, pharynx, larynx, and a portion of the upper trachea.

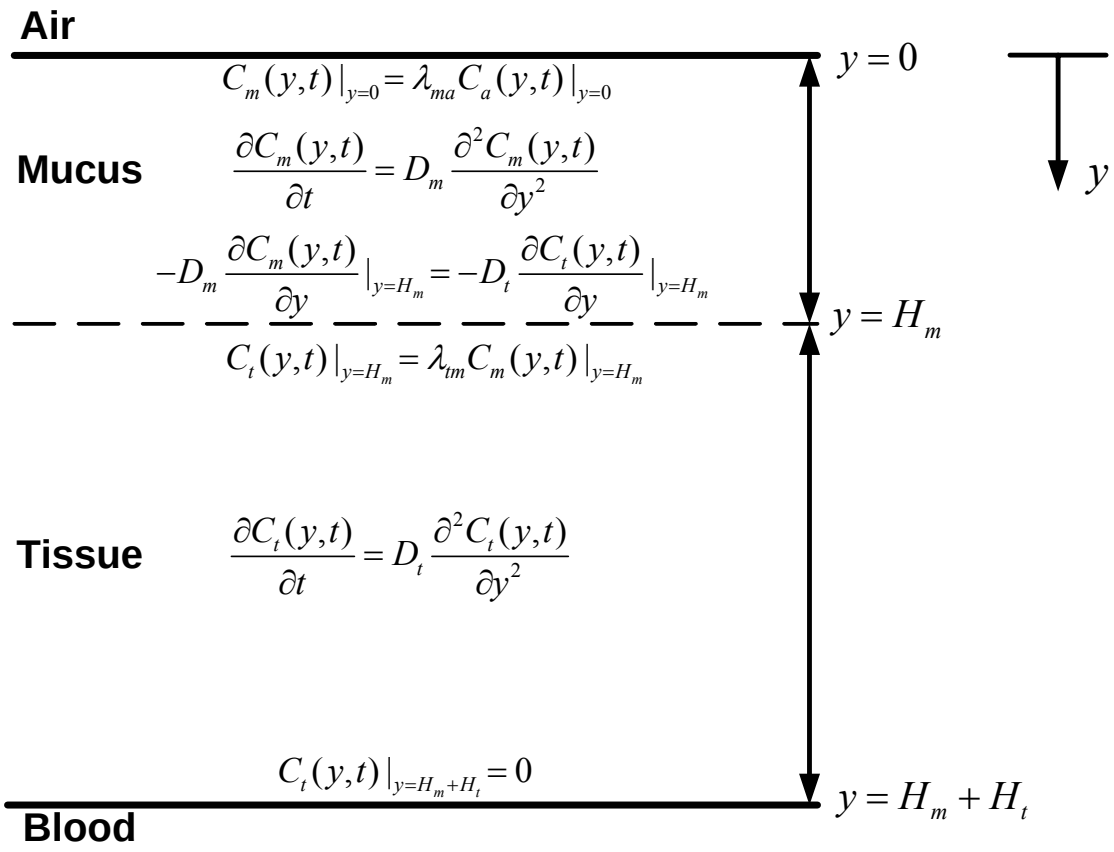

Figure 5.2. Submodel of the airway wall including air, mucus, tissue, and blood (AMTB) layers. Equations governing transport in this multilayer system are also shown.

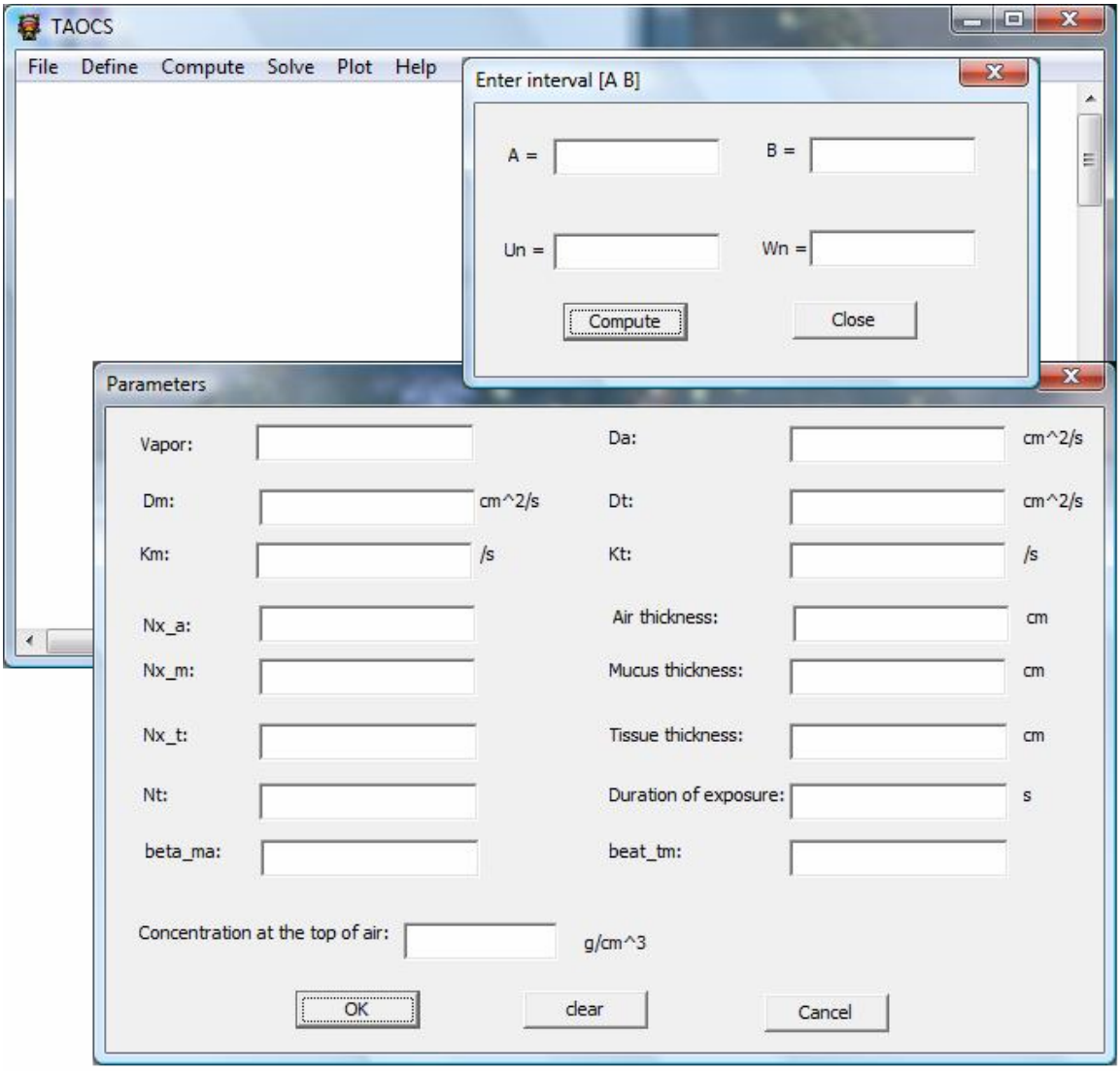

Figure 5.3. Graphical user interface (GUI) of the Transient Absorption of Chemical Species (TAOCS) 1.0 model. Windows shown include the main GUI and input panels for transport properties and finding the eigenvalues.

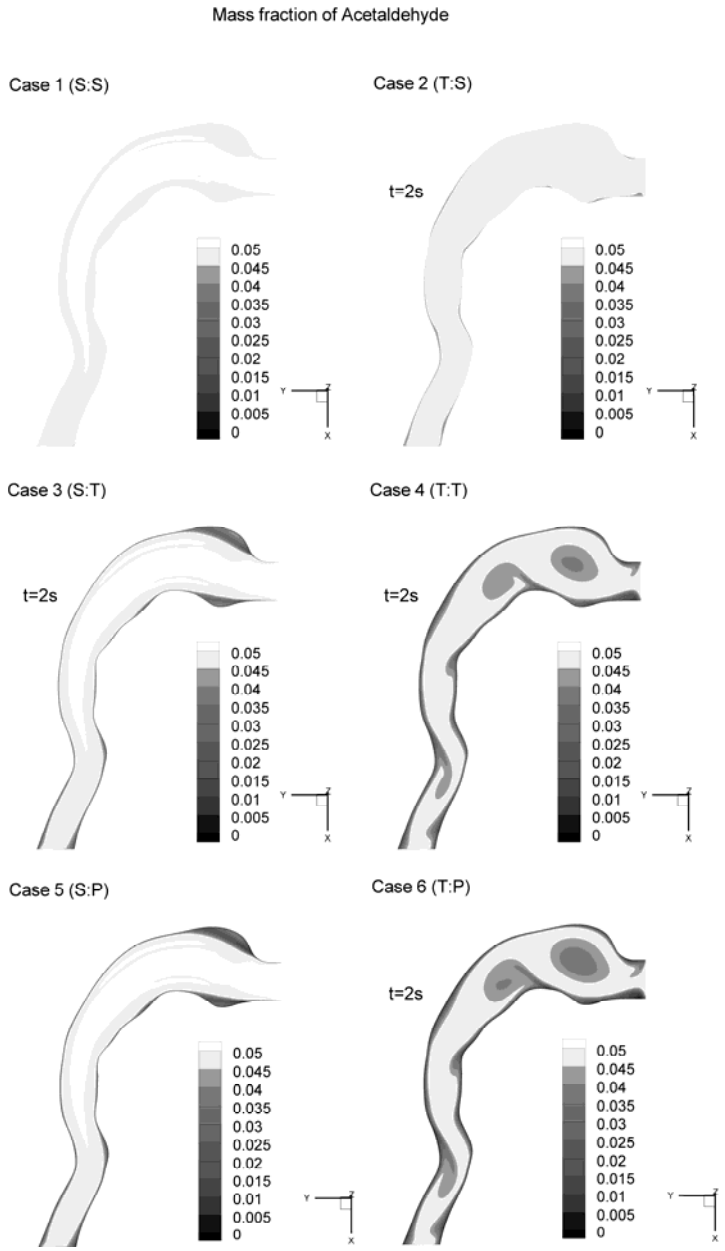

Figure 5.4. Contours of acetaldehyde mass fractions in the air phase (C_a) for all cases considered. For cases with either transient airflow or wall absorption, conditions at 2 seconds are shown. The inlet mass fraction of each chemical species considered was 5% for all cases.

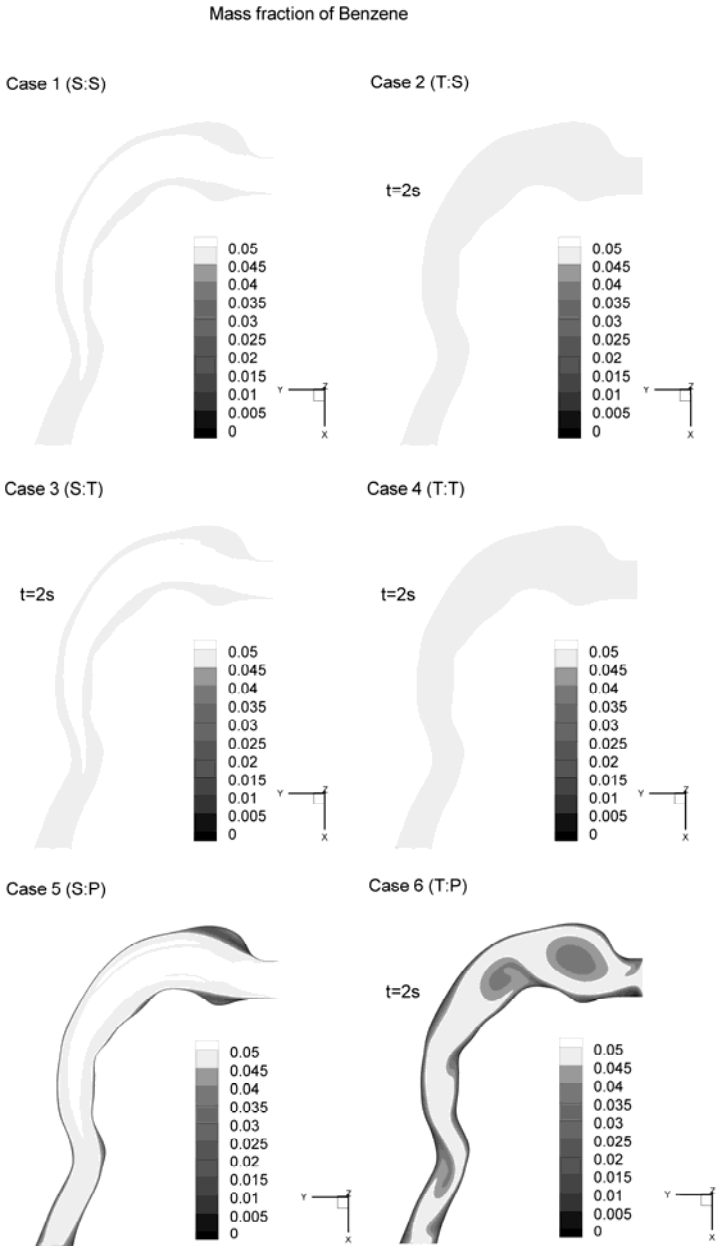

Figure 5.5. Contours of benzene mass fractions in the air phase (C_a) for all cases considered. For cases with either transient airflow or wall absorption, conditions at 2 seconds are shown.

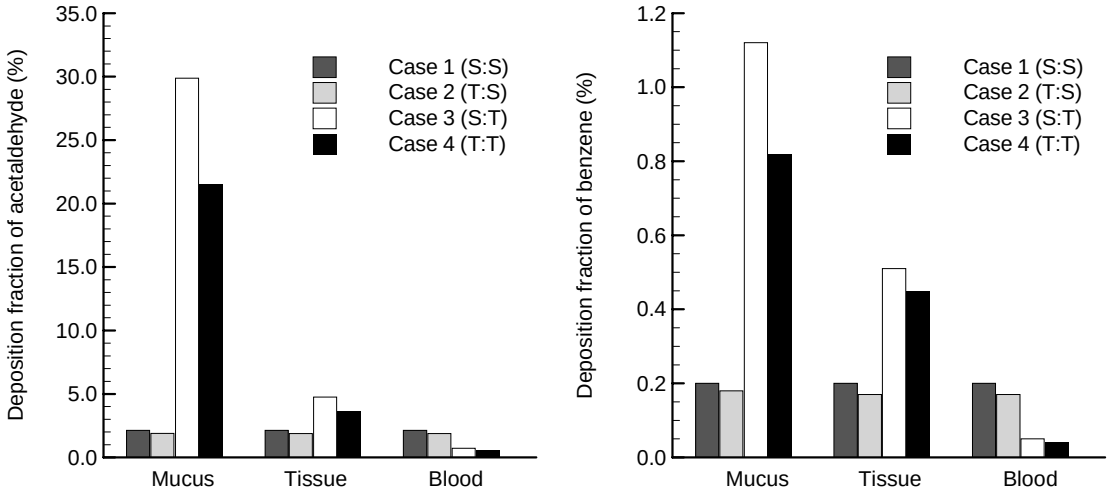

Figure 5.6. Total deposition fractions of acetaldehyde and benzene vapors in mucus, tissue, and blood in the MT model for Cases 1 – 4 after 2 seconds.

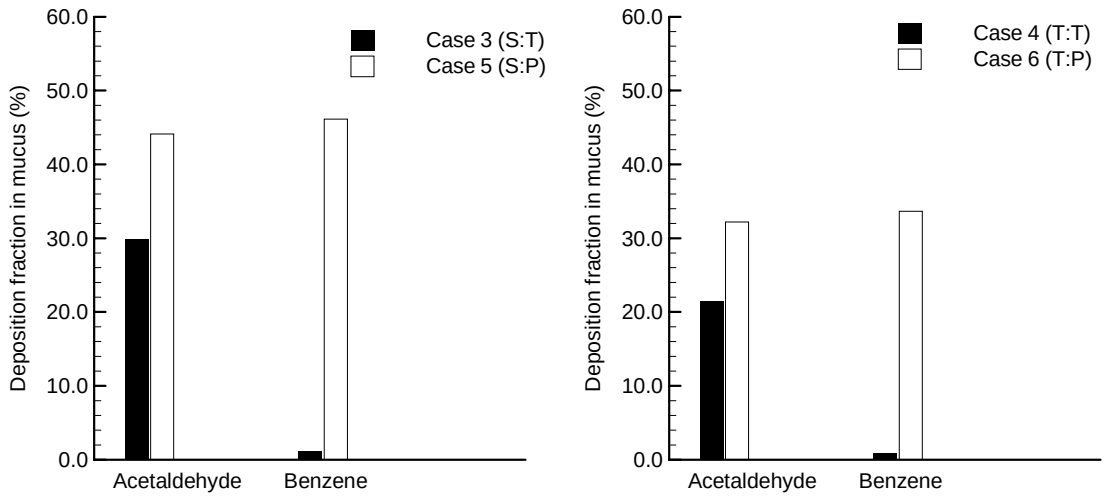

Figure 5.7. Total mucus deposition fraction of acetaldehyde and benzene for the evaluation of the perfect absorption condition.

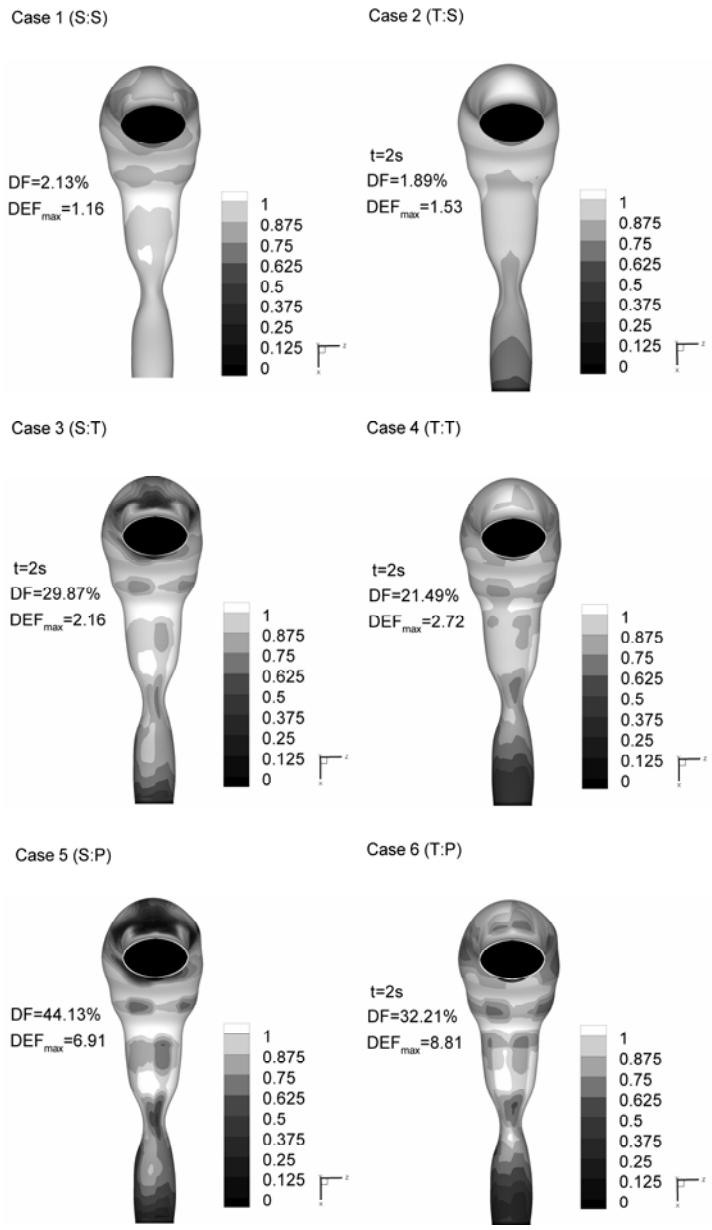

Figure 5.8. Deposition enhancement factors (DEFs) and total deposition fractions (DFs) for acetaldehyde and all cases considered after 2 s.

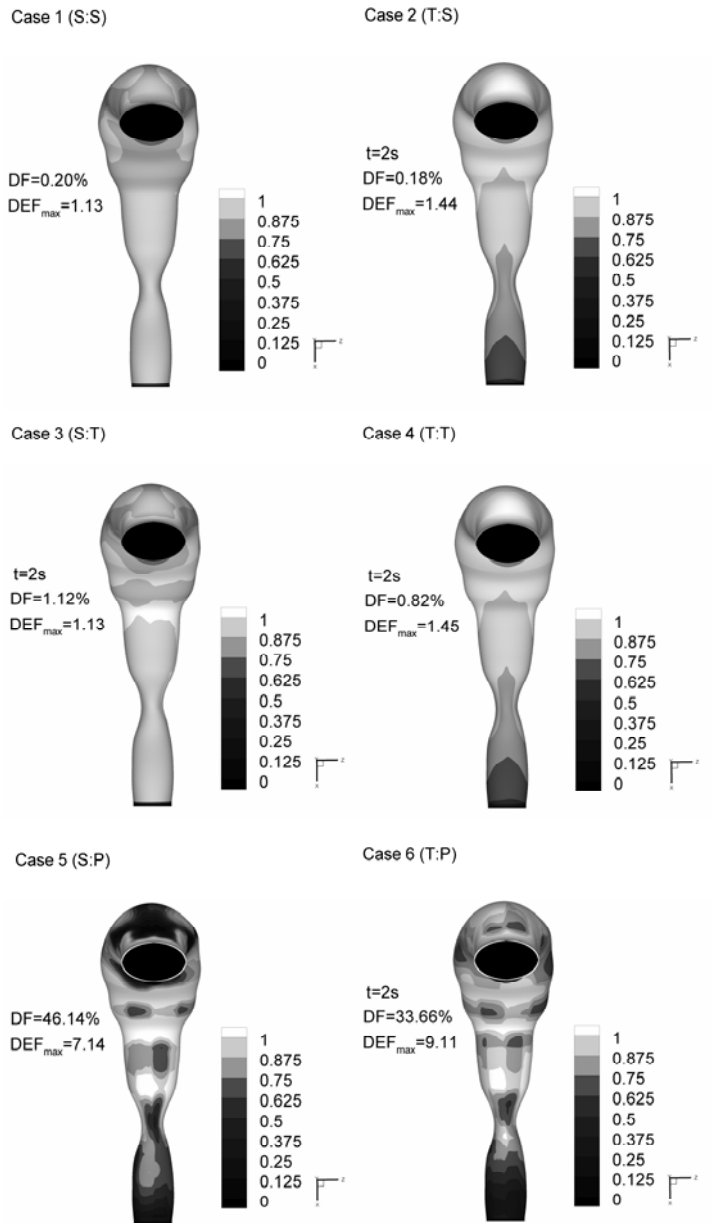

Figure 5.9. Deposition enhancement factors (DEFs) and total deposition fractions (DFs) for benzene and all cases considered after 2 s.

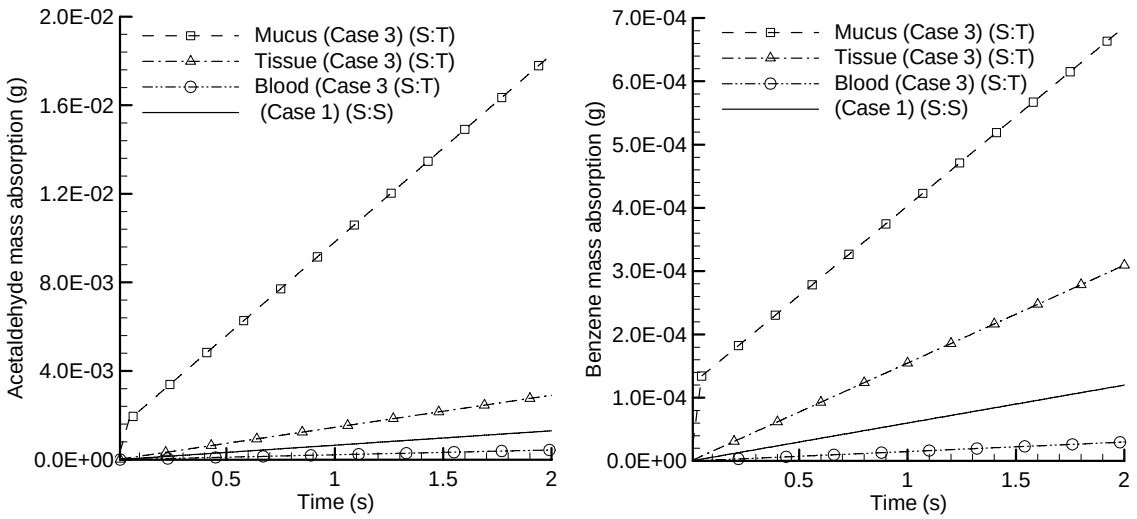

Figure 5.10. Mass absorption of acetaldehyde and benzene in individual wall layers under steady airflow conditions over time.

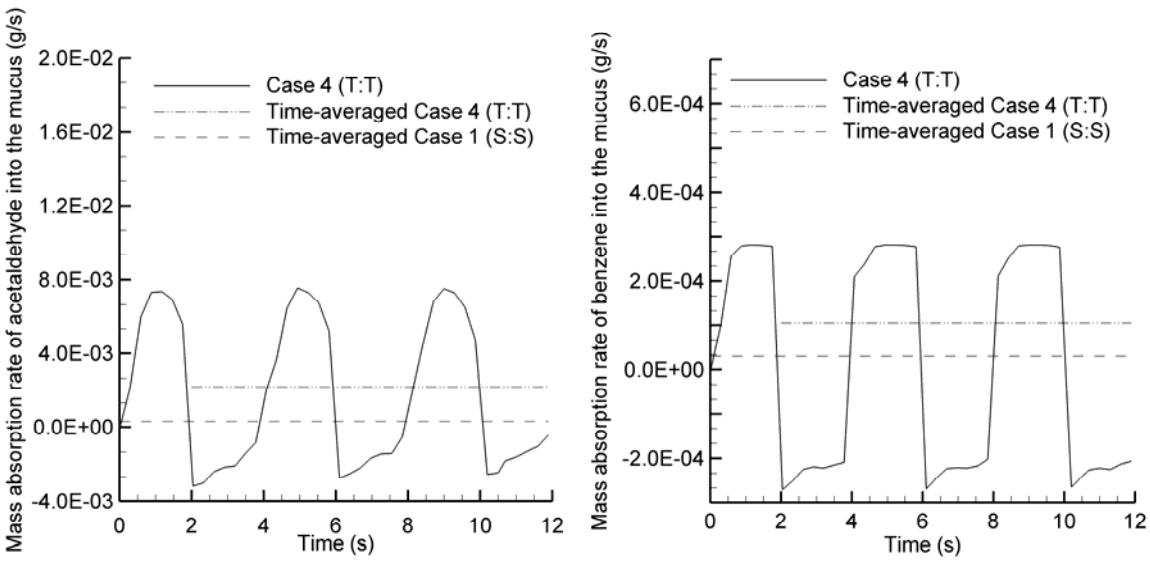

Figure 5.11. Mass absorption rate (g/s) of acetaldehyde and benzene into the mucus based on Case 1 (S:S) and Case 4 (T:T) conditions considered over multiple breaths.

Chapter 6. Evaluation of Enhanced Condensational Growth (ECG) for Respiratory Drug Delivery in a Realistic Mouth-Throat and Tracheobronchial Single Path Model

6.1 Introduction

The feasibility of improving respiratory drug delivery using enhanced condensational growth (ECG) has previously been demonstrated using both *in vitro* and CFD models of the upper respiratory airways. Previous studies have indicated that ECG is an effective approach for significantly reducing MT aerosol deposition and increasing aerosol size from the submicrometer range to approximately 2-4 μm, which is expected to produce nearly 100% lung retention. However, condensational growth and deposition in the tracheobronchial (TB) region beyond approximately generation G4 was not considered. It is currently not clear how far into the lungs condensational growth will continue. It is also conceivable that some evaporation may occur in the deep lung once subsaturated conditions are reached for non-hygroscopic aerosols. To verify full lung retention of the aerosol under ECG conditions, the aerosol size change and deposition needs to be characterized throughout the TB airways. To address these issues, a model of ECG delivery within the medium and small TB airways is needed.

The objective of this study is to evaluate the ECG delivery of respiratory submicrometer pharmaceutical aerosols in a single path model extending from the mouth-throat (MT) to the end of the TB region. This single path model is constructed by continuing only one branch of each bifurcation through generation G16. Separate streams of nebulized submicrometer aerosol and saturated

humidified air are combined as they are introduced into a realistic MT-TB single path geometry. Initially monodisperse aerosol sizes of 560 and 900 nm are delivered in conjunction with control subsaturated air and ECG conditions with saturated air at temperatures of 39 and 42 °C, consistent with previous experimental studies of ECG (Longest et al. 2010). A previously validated CFD model of aerosol transport and deposition during ECG delivery in the respiratory airways is applied.

6.2 Methods

MT-TB Geometry

A physical model of the MT-TB geometry was considered as shown in Fig. 6.1. The geometry consists of the MT region, the upper TB airways extending from the trachea to the third respiratory bifurcation (B3), and an individual path model of the medium and small TB airways extending to the terminal bronchioles (B15). The trachea and the initial part of the main bronchi constitute bifurcation B1. The MT geometry includes the oral cavity, pharynx, and larynx. The MT model was originally developed in Xi and Longest (2007b) based on a cast of the oral cavity (Cheng et al. 1997) combined with CT images of the pharyngeal and laryngeal regions. The geometry was then simplified using elliptical cross sections which maintained the flow area and hydraulic diameter of the original model.

The upper TB airways are considered extending from the trachea to the third bifurcation (B3). This asymmetrical model was generated using the anatomical cast dimensions reported by Yeh and Schum (1980) and scaled to a functional

residual capacity (FRC) of 3.5 L, which is consistent with an adult male (ICRP 1994). The individual bifurcation units were based on the physiological realistic bifurcation (PRB) parameters reported by Heistracher and Hofmann (1995). Surface properties of the bifurcations such as carinal ridge and curvature radius of branches were based on the measurement reported by Horsfield *et al*. (1971) and Hammersley and Olson (1992). These bifurcation parameters such as branch diameter, length, bifurcation angle, and gravity angle were taken from Yeh and Schum (1980). In the TB model, B2 of the right lung braches into the right upper lobe directly, whereas the lower third bifurcation branches into the right middle and right lower lobes. In the left lung, B2 branches into the left upper and left lower lobes.

The upper TB model is asymmetrical and includes out-of-plane rotations of individual bifurcations. The asymmetrical model is considered to be sufficiently accurate to characterize aerosol growth and deposition in the upper airways, which will be verified with comparisons to the upper TB deposition data of Zhou and Cheng (2005).

Beyond the third bifurcation, an individual path model was considered by continuing from the trachea to the end of the TB region (B15) of the right lower lung lobe. Bifurcations within the model were based on PRB units with the airway dimensions reported by Yeh and Schum (1980). Use of the individual path model based on PRB units allows for the application of a hexahedral mesh, which improves solution accuracy, and an adequate number of computational cells to fully resolve the flow domain (Longest and Vinchurkar 2007a; Vinchurkar and

Longest 2008). Based on available data, the bifurcations in the individual path model section (B4-B15) were symmetric and included a symmetric outflow assumption at each bifurcation level. At each bifurcation, continuation of the left or right branch was selected at random. Consecutive branches were rotated at 90° to approximate physiological conditions (Phalen et al. 1978). This individual path model is not intended to exactly mimic a specific connection of bronchi as with a patient specific model. Instead, it is intended to provide and effective 3-D representation of transport and deposition in the medium and small TB airways. Branch 15 was assumed to end with the terminal bronchioles, based on the existing anatomical data (Yeh and Schum 1980).

Boundary and Delivery Conditions

Separated streams of aerosol and humidified air are delivered to the mouth inlet for both control and ECG growth conditions. As illustrated in Fig. 6.1, the humidified air is delivered through an outer circle whereas the aerosol stream is delivered through an inner ring at the mouth inlet. To allow separate streams of aerosol and humidified air to be introduced into the MT, Hindle and Longest (2010) developed and presented a dual flow mouthpiece. As reported by Hindle and Longest (2010), the inlet areas of the aerosol and humidity streams are balanced to maintain a constant velocity. The total inlet flow rate considered in this study is approximately 30 L/min under steady state conditions.

The airway walls were assumed to be at body temperature. As a result, the RH of the airway wall was set at 99.5%. Previous studies have reported variable wall temperatures from the mouth to core body temperature downstream.

However, correlations describing this change are based on the inhalation of ambient environmental conditions. During ECG delivery, which is via a nebulizer and requires multiple inhalations (Hindle and Longest 2010), it is expected that the inhalation of warm air will significantly decrease any airway wall temperature gradients. The walls of the airway model are assumed fixed and rigid.

Outflow conditions from the upper TB model into each lung lobe were based on the estimates of Horsfield *et al*. (1971). Beyond the lobar bronchi, symmetric outflow conditions were assumed at each bifurcation level (B4-B15). This assumption is not expected to largely influence the growth and regional deposition characteristics of interest in this study.

Aerosol and humidified air inlet conditions are shown in Table 6.1 for the delivery of 560 and 900 nm droplets. Both control and ECG delivery cases were considered. For the control scenarios, the aerosol was delivered with ambient air (25 $^{\circ}$C) and assumed to be a non-evaporating particle (Case 1) or a droplet experiencing either evaporation or condensation (Case 2). The humidified air inlet condition for Case 1 is identical to Case 2. Considering the one-way coupled results, continuous field variables such as temperature and RH conditions for Case 1 are the same as for Case 2. ECG conditions were evaluated as the remaining two cases. Under these conditions, the aerosol and humidified air were delivered at either 39 $^{\circ}$C (Case 3) or 42 $^{\circ}$C (Case 4). Increasing the aerosol and humidity stream temperatures allows for more water vapor mass to be delivered to the airways, which is expected to increase the final aerosol size and alter the deposition profile. Albuterol sulfate (AS) was considered as a model drug in the

aerosol. The mass fractions of drug in the initial 560 and 900 nm droplets were assumed to be 31% and 49%, respectively, based on a previous experimental study in which these aerosols were formed using a small particle aerosol generator (Longest et al. 2010). At these mass fractions, the hygroscopic effects of AS are expected to enhance size increase initially for RH values below 100%. However, hygroscopic effects are expected to significantly diminish once the aerosol increases in size above approximately 1 μm (Longest et al. 2010).

Deposition Factors

Deposition within regions of the respiratory tract can be reported as either a fraction or efficiency. The deposition fraction (DF) for the *i*th region is calculated as

$$\mathrm{DF}_i = \frac{\text{number of particles depositing in region } i}{\text{number of particles entering the mouth}} \tag{6.1}$$

In contrast, the corresponding deposition efficiency (DE) for region *i* is calculated as

$$\mathrm{DE}_i = \frac{\text{number of particles depositing in region } i}{\text{number of particles entering region } i} \tag{6.2}$$

To determine a total deposition fraction, $\mathrm{DF_i}$ values in individual regions can be directly summed. Deposition efficiency values are an effective method to report the characteristics of an individual section of the respiratory tract without the influence of upstream aerosol losses. In this study, DE values are calculated for each bifurcation. Sectional DE values are then computed by combining the

individual bifurcation values (ICRP 1994). For example, the DE in region B4 to B7 is calculated as

$$\mathrm{DE}_{B4-7} = 1-(1-\mathrm{DE}_{B4})(1-\mathrm{DE}_{B5})(1-\mathrm{DE}_{B6})(1-\mathrm{DE}_{B7}) \tag{6.3}$$

The total DF for the entire MT-TB network is then calculated as

$$\mathrm{DF}_{MT-TB} = 1-\prod_{i=1}^{I}(1-\mathrm{DE}_i) \tag{6.4}$$

which includes all regions (i=1 to *I*) from the MT to B15. It is noted that the total DE of the model is equal to the total DF.

CFD Simulations

The low-Reynolds-number (LRN) $k-\omega$ model of Wilcox (Longest and Hindle 2009a; Longest et al. 2009) was selected for simulating mixing of the delivery streams and flow in the MT-TB model because it has been shown to provide an accurate and numerically efficient solution for laminar, transitional and turbulent flows. Furthermore, this model was found to accurately predict aerosol transport and deposition in upper airway models (Longest and Xi 2008). The coupled governing equations of heat and mass transport were considered to evaluate the variable temperature and RH fields in the MT-TB model. These transport equations were previously reported in Longest and Xi (2007) and Longest *et al.* (2007). The Lagrangian transport equations interconnected with user defined functions were employed to calculate droplet trajectories, condensation, evaporation, deposition, near-wall anisotropic turbulence correction (Longest and Xi 2007b), near-wall particle interpolation (Longest and Xi 2007b), and Brownian motion (Longest and Vinchurkar 2007a; Vinchurkar and Longest

2008) in the complex three-dimensional temperature and humidity fields. The discrete phase transport model includes the Kelvin effect, drug hygroscopicity, and the effect of droplet temperature on surface vapor pressure. In simulating aerosol evaporation and growth, the effect of the droplets on the continuous phase was typically neglected, resulting in a one-way coupled approach. One-way coupled simulations are expected to be accurate in this study due to the presence of wetted walls. However, to assess the validity of this assumption, the effect of the discrete aerosol phase on the continuous heat and water vapor fields was also included in some simulations, which is referred to as two-way coupling. An experimentally measured concentration of 2.8×10^5 particles/cm^3 for the 900 nm aerosol (after mixing with the humidity stream) was employed to assess the two-way coupling effects.

To solve the governing equations, the CFD package Fluent 6.3, (ANSYS Inc.) coupled with user defined functions was employed. All transport equations were discretized to be at least second order accurate in space. For the convective terms, a third order QUICK scheme was used to interpolate values from cell centers to nodes. The diffusion terms were discretized using central differences. A segregated implicit solver was employed to evaluate the resulting linear system of equations. This solver uses the Gauss-Seidel method in conjunction with an algebraic multigrid approach. The SIMPLEC algorithm was employed to evaluate pressure-velocity coupling. The outer iteration procedure was stopped when the global mass residual had been reduced from its original value by five orders of magnitude and when the residual-reduction-rates for both mass and momentum

were sufficiently small. To ensure that a converged solution had been reached, residual and reduction rate factors were decreased by an order of magnitude and the results were compared. The stricter convergence criteria produced a negligible effect on both velocity and particle deposition fields. To improve accuracy, all calculations were performed in double precision. As shown in Fig. 6.2, the computational mesh was composed of approximately 2×10^6 hexahedral elements and a very fine near-wall grid. Hexahedral meshing has been shown to provide a better quality solution in aerosol deposition studies compared with tetrahedral and hybrid grids (Vinchurkar and Longest 2008). Grid converged results based on negligible change in the velocity and concentration fields (< 1%) as well as negligible differences in the total deposition fractions (< 3%) were established for a mesh consisting of 2.4 million control volumes. In order to produce convergent aerosol deposition results, 1.2×10^5 monodisperse droplets were injected at the aerosol inlet stream for each aerosol size and inlet case considered. MMAD values after growth were calculated based on the midpoint diameters of a standard Andersen cascade impactor (Vinchurkar et al. 2009). Doubling the number of droplets considered had a negligible impact on both total and sectional deposition results.

Model Validation

The CFD model employed in this study has previously been extensively tested in comparison with experimental deposition results. For both constant-sized particles and evaporating droplets, the CFD model was shown to accurately predict local and sectional deposition profiles in comparison with in vitro

experiments (Longest and Hindle 2009a; Longest et al. 2009b; Longest and Vinchurkar 2007b). Longest and Hindle (2010) recently presented a CFD model of ECG aerosol delivery in detail. In this study, excellent agreement was found between experimental measurements of final particle size after condensational growth and CFD predictions. Hindle and Longest (2010) compared in vitro results and numerical predictions of aerosol drug deposition in a MT–TB geometry extending to the fifth respiratory generation. Good agreement was found between the experimental and numerical predictions of deposition for both control and ECG conditions on a sectional basis and for the entire MT–TB geometry.

Comparison of Upper TB Deposition to Previous Studies

As discussed, some differences are observed between the upper TB model considered in this study and previously reported models. An advantage of the current model is the use of a standard well described bifurcation unit (the PRB) that can be reproduced by other researchers. Furthermore, the characteristic TB model considered can accommodate a hexahedral mesh. However, differences in deposition from potentially more realistic models may be a concern. To address this issue, deposition in the current upper TB model was compared to the experimental results of Zhou and Cheng (2005) on a regional basis. Particles in the range of 0.93- 30 μm were considered at an inhalation flow rate of 30 L/min. Particle deposition efficiency in the upper tracheobronchial airway as a function of Stokes number are compared with the correlation by Zhou and Cheng (2005). The Stokes number is defined as $St=\rho_p d_p^2 U/18\mu D_p$, where ρ_p is the particle density, d_p is the particle diameter, U is the mean velocity, μ is the air viscosity,

and D is the parent diameter of each bifurcation. As shown in Fig. 6.3, deposition efficiencies in the trachea, first bifurcation, second bifurcation, and third bifurcation provide an excellent match to the experimental data. As a result, it is concluded that the current model is sufficiently detailed to capture regional deposition characteristics in the upper TB airways. Furthermore, this comparison provides an additional validation study indicating that our CFD model is accurate.

6.3 Results

Temperature Fields

Contours of temperature are shown for the MT, upper TB airways, and selected medium and small TB airways in Fig. 6.4 for Cases 1-4. Temperature contours are presented as mid-plane slices within each of the airway regions shown. For Cases 1 and 2, the initially cool 25 °C airstream is rapidly warmed by effective mixing in the MT and reaches approximately 30-34 °C in the trachea. Temperatures are generally above 34 °C in B4-B7 and near 37 °C in B12-B15. However, some areas below 36.5 °C are observed in the distal airway branches. For the inlet conditions of Cases 3 and 4, rapid cooling is observed in the MT with temperatures in the range of 37-39 °C in the trachea for Case 3, and in the range of 39-41 °C for Case 4. Temperatures of approximately 37 °C are observed in B4-B7 for Case 3, and approximately 38 °C for Case 4. Temperature is nearly uniform at 37°C in the B12-B15 region for Case 3 and 37.5 °C for Case 4.

Relative Humidity

Contours of RH for Cases 1-4, presented as midplane slices, are illustrated in Fig. 6.5. As expected, the cool subsaturated inlet conditions of Cases 1 and 2 result in low RH values through a majority of the upper TB airways. Due to mass transfer from the wet walls, RH values of 95% and greater are observed in bifurcations B4-B7. In the distal bifurcations B12-B15, RH values are predominately equal to the wall value of 99.5%. However, contour levels below walls conditions are also observed even in the most distal airways considered. For inlet conditions of Cases 3 and 4, rapid cooling of the saturated airstream results in a rapid progression to supersaturation, with values as high as 101% observed in the pharynx for Case 3, and as high as 103% for Case 4. RH values remain in the range of 100-101% for Case 3 and 101-103% for Case 4 through a majority of the upper TB geometry and bifurcations B4-B7. In B12-B15, RH values are near wall conditions of approximately 99.5% for Case 3 and in the range of 99.5-101% for Case 4.

Droplet Trajectories

Trajectories of initially monodisperse 900 nm droplets in the full MT–TB geometry are illustrated in Fig. 6.6 for Cases 2–4. Considering Case 2, rapid droplet evaporation occurs in the oral cavity until only a solid drug particle remains. As RH increases due to the warm and wet walls, some hygroscopic growth of the aerosol is observed with B15 trajectories in the range of 0.9–1.0 μm. For ECG delivery (Cases 3 and 4), rapid aerosol growth is observed throughout the MT and first bifurcation. In the medium and small TB branches, growth slows

due to reduced RH values and a decreased hygroscopic effect associated with higher droplet mass fractions of water. However, slower droplet velocities in the more distal airways allow more time for growth to occur. The net result is observed to be continued growth without visible evaporation throughout the airways. For Cases 3 and 4, individual trajectories passing through bifurcation B15 are found to have increased in size from 900 nm to ranges of 2 to >2.5 μm and 2.5 to >3 μm, respectively.

Exit Size Distribution

Droplet size distributions sampled at specific cross-sectional locations in the model are presented in Fig. 6.7 in terms of mass fraction per micrometer of sampling bin size. MMAD values are also presented for each aerosol size distribution. Considering Case 2, MMAD values change little from the initial sizes of 560 and 900 nm. However, mixed evaporation and hygroscopic growth result in a spreading of the size distribution from the initial monodisperse condition. In contrast with Case 2, ECG conditions result in a definite shift in the distribution profile to larger sizes. Considering Case 3 and initial sizes of 560 and 900 nm, both the MMAD and size distribution indicate significant and successive growth at the tracheal inlet and B5 outlet. However, some decrease in MMAD size is observed between the B5 outlet and B15 outlet for the 560 (~0.4 μm reduction) and 900 nm (~0.2 μm reduction) aerosols. This decrease in MMAD may arise from (i) deposition of the larger particles and (ii) minor evaporation as RH approaches 99.5%. Considering that only a small size decrease is observed for the 900 nm aerosol under Case 3 conditions, the decrease of the 560 nm aerosol is

likely due to minor evaporation arising from a lower drug concentration in the droplet and a reduced hygroscopic effect. Under Case 4 delivery conditions, size decreases between the B5 and B15 outlets of approximately 0.2 μm are observed for both aerosol sizes. Size distribution profiles indicate that 20–40% of the aerosol mass is associated with droplets of 4 μm and above. Furthermore, RH values shown in Fig. 6.5 were generally above 100% for Case 4 delivery conditions. As a result, this minor decrease in aerosol size may be primarily due to the deposition of larger droplets in the bifurcating airways.

MMADs of the polydisperse aerosol entering each bifurcation (B1–B15) are presented in Fig. 6.8 for the various delivery conditions. For Case 2, results indicate sudden evaporation followed by very slow growth, as expected. Considering the ECG conditions, rapid growth is observed from the mouth to the tracheal (B1) inlet. It is noted that the reported MMADs are calculated over all droplets entering each bifurcation, i.e., as they cross the inlet plane. However, details of growth for the aerosol ensemble are not resolved within each model segment due to the number of droplets considered. In the figure, significant growth is observed to occur through approximately B3. Thereafter, minor growth is observed through approximately B8, and some size decrease occurs between B8 and B15. As described above, this size decrease is generally in the range of 0.2–0.4 μm and likely arises from both deposition and minor evaporation; however, deposition appears to be the primary cause.

To evaluate the validity of the one-way coupled assumption, two-way coupled simulations were also considered. In two-way coupling, heat and mass

transfer from the droplets are accounted for as source terms in the continuous phase equations and influence subsequent droplet size change. The 900 nm aerosol was considered under Case 3 and 4 conditions, where the effects of two-way coupling are expected to be the strongest (Longest et al. 2010). An aerosol concentration of 2.8×10^5 particles/cm^3 was considered, based on the experimental study of Longest et al. (2010), in which the 900 nm aerosol was formed. In general, two-way coupling is expected to slow both size decrease and increase as changes in air phase RH damp evaporation and condensation. However, the simulation results indicate that two-way coupling has a minimum effect on aerosol size change, likely because of the wet-wall boundary conditions. Specifically, relative percent differences were calculated as $|MMAD_{one\text{-}way} - MMAD_{two\text{-}way}|/MMAD_{two\text{-}way} \times 100$. The comparisons of one-way and two-way coupling on MMADs of the polydisperse aerosol entering each bifurcation (B1–B15) are presented in Fig. 6.9 for Cases 3 and 4. Percent differences in MMADs for aerosols entering each bifurcation were less than approximately 10%.

Aerosol Deposition

Particle deposition locations of individual droplets are illustrated for the 900 nm aerosol with Cases 1-4 delivery conditions in Fig. 6.10. The droplets are colored based on their size at the time of deposition. Deposition efficiencies were calculated for each bifurcation and then combined (e.g., Eq. (6.3)) to represent the total deposition efficiencies for the sections reported along the individual path. Considering Cases 1 and 2, very little deposition is observed with a maximum of only 7.1% in the airways B8–B15. For ECG delivery conditions of Cases 3 and 4,

the MT deposition efficiency remains very small (~1%) as observed by Hindle and Longest (2010). In contrast with this low MT value, deposition efficiencies in B4–B7 and B8–B15 are increased by an order of magnitude compared with the evaporating control case (Case 2). Furthermore, deposited particles beyond B4 are 2 μm and above, which provides evidence that the observed minor reduction in MMAD is due to the loss of the larger aerosols in the polydisperse size distribution.

The results of two-way coupling on particle deposition locations and regional deposition efficiencies (DE) of drug mass for an initially 900 nm aerosol in Cases 3 and 4 are presented in Fig. 6.11. Two-way coupling is observed to slightly increase the DE with relative percent differences less than approximately 10%.

To support the accuracy of transport and deposition within the bifurcations of each lung lobe, two additional individual paths were randomly generated. Particle deposition locations and regional deposition efficiencies of drug mass for an initially 900 nm aerosol of the individual paths 2 and 3 for Case 4 are shown in Fig. 6.12. It is observed that MT and upper TB deposition values are slightly different than previous results. Considering similarities in these results, it appears that use of the stochastic individual path approach provides a reasonable estimate of deposition within an individual lung lobe.

A complete description of deposition efficiencies for each inhalation case considered is presented in Fig. 6.13 and Table 6.2. Deposition efficiencies are again calculated as the combination of the values determined for each bifurcation.

For all cases, MT and upper TB deposition remained extremely low (approximately <2%). Deposition in the more distal airways is then observed to increase by an order of magnitude for the ECG conditions (Cases 3 and 4) vs. the controls (Cases 1 and 2). For both initial sizes, Case 4 conditions approximately double deposition in B4–B7 and increase deposition in B8–B15 by a relative difference of approximately 25% compared with Case 3. Considering the ECG growth cases, minor differences in regional deposition efficiencies are observed for the initial 560 nm aerosol vs. the 900 nm aerosol. As a result, it appears that overall deposition is more influenced by inlet conditions than initial aerosol size. Deposition efficiencies of Case 4 with an initially 900 nm aerosol are reported for multiple paths in Table 6.3. The averages of these deposition efficiencies are also reported and the small standard deviation values provide evidence that the individual path approach is accurate.

Predicted total DEs of the TB airways are compared with the in vivo-based correlations of Stahlhofen et al. (1989) and Chan and Lippmann (1980) in Table 6.4. To calculate the total DE of the TB region from the CFD predictions, the deposition efficiencies of each bifurcation were combined using an expression similar to Eq. (6.3) from B1 to B15. The major assumption here is that the DEs of each bifurcation in the right lower lobe single path are representative of conditions in the other four lung lobes. For comparison, the TB correlations based on in vivo deposition data from Stahlhofen et al. (1989) (Eq. 15) and Chan and Lippmann (1980) (Eq. 3) were employed. The single characteristic aerosol size required in these correlations was assumed to be the calculated MMAD exiting

B5, as shown in Table 6.4. The tracheal inlet flow rate of 30 L/min used in the CFD simulation was approximated in the correlations as an inhalation flow rate of 500 cm^3/s with an inhalation volume of 1500 cm^3 to represent deep inspiration, which is characteristic of pharmaceutical aerosol delivery. As shown in Table 6.4, the predicted DEs from this study are in general agreement with the in vivo data, but the CFD predictions are somewhat higher. Considering the in vivo variability reported by Stahlhofen et al. (1989), it is observed that the CFD predictions are well within the range of the experimental data. The CFD predictions are likely higher than the mean experimental data because of the use of a single lobe and single path model to represent the remainder of the TB airways, a larger CFD lung volume than in the experiments (3.5 vs. ~3.0 L), and the use of a single droplet diameter to account for the deposition of a polydisperse aerosol that is increasing in size.

To approximate whole lung retention of the aerosol, the MT–TB deposition fractions predicted with Eq. (6.4) are reported in Table 6.5. These values are combined with the alveolar deposition efficiency correlation of Stahlhofen et al. (1989) to provide estimates of total lung deposition (DF_{total}). Again, an inhalation rate of 500 cm^3/s was employed along with a volume of 1500 cm^3. As observed from Table 6.5, total lung deposition fractions for the ECG conditions are 90% and above, except for Case 3 and the 560 nm aerosol, where the DF_{total} is 83%. These whole lung deposition values could be increased further with the inclusion of a breath pause. In contrast, for both controls (Cases 1 and 2), the total lung deposition fraction was between approximately 23–38%.

6.4 Discussion

In this study, the concept of ECG applied to respiratory drug delivery was tested in a representative airway model extending from the oral cavity to the end of the TB airways. Droplet transport, size change, and deposition were simulated using a previously well-tested and experimentally validated CFD model. Simulations were conducted in a previously developed MT-TB model whereas deposition throughout the TB region was approximated using an individual path approach. Results indicate that both control and ECG delivery conditions produce very little deposition and aerosol loss in the MT and upper TB airways. With ECG delivery, significant size increases of the initially submicrometer aerosols were observed to occur, resulting in MMADs of 2–3 μm in the medium and small TB airways. This increase in aerosol size was shown to produce an order of magnitude increase in drug deposition in the TB airways, with TB deposition efficiencies of approximately 32–46% for ECG conditions. Estimates of downstream pulmonary deposition indicted near full lung retention of the aerosols during ECG delivery.

As previously demonstrated by Hindle and Longest (2010) delivering pharmaceutical aerosols using the ECG approach resulted in very low MT deposition (~1%). In contrast, MT depositional losses are currently reported as ~60% for a typical MDI with a HFA propellant (Cheng et al. 2001), ~70% for a typical DPI (Zhang et al. 2007) , and 30–40% for state-of-the-art breath-actuated nebulizers (Newman 2009; Nikander et al. 2010). For the same MT and similar upper TB geometry as considered in this study, Hindle and Longest (2010)

reported experimental values of drug deposition using a Proventil HFA MDI. The mean (and standard deviation) AS deposition in the MT–TB model was found to be 49.7 (7.2)% of the dose. The majority of the dose from the MDI was deposited in the MT region (46.0%), with only 3.6% deposited in the B1–B5 airways. Minor differences between this study and that of Hindle and Longest (2010) include the use of an initially monodisperse aerosol and an upper TB model that is complete through B3 in the current study. Equivalent aerosol and humidity inlet temperatures are also employed for ECG conditions in the current study, which were only considered for one case in Hindle and Longest (2010). As a result, MT and upper TB deposition values are slightly different than previously reported. However, the primary motivation behind the current study was to investigate conditions throughout an individual path model of the entire TB region.

Prior to this study, airway conditions and aerosol behavior in the medium and small TB bifurcations was unknown for ECG delivery. Previous results of aerosol size change during the inhalation of cool saturated air in the upper airways indicated that aerosol size increase may be temporary and some evaporation may occur (Ferron et al. 1984; Zhang et al. 2006b). However, results of this study indicate that with the inhalation of warm saturated air, several degrees above body temperature, supersaturated conditions extend well into the respiratory tract. This increased region of supersaturation likely occurs due to the larger mass of water vapor that enters the airways with the inhalation of warm vs. cool saturated air. As a result of extensive supersaturation in the flow field, aerosol growth was observed to occur throughout a majority of the TB airways without visible

evaporation of individual trajectories under ECG conditions. Minor decreases in the aerosol MMAD were observed beginning with B8 (Fig. 6.8). However, this decrease in MMAD can be largely explained as resulting from the higher deposition fraction of the larger droplets in the medium and small TB bifurcations (Fig. 6.9). With ECG, deposition within the TB airways beginning with B4 was increased by an order of magnitude compared to the evaporating control case resulting in single path deposition efficiencies of 32–46%. Aerosols exiting B15 had MMADs ranging from 2.00 to 2.95 μm. As a result of these observations, it is concluded that the advantages of ECG delivery are maintained throughout the TB region and that negligible evaporation of individual droplets occurs. Furthermore, estimates indicate that alveolar deposition will result in near full lung retention of the aerosol (Table 6.4). Based on the aerosol behavior observed in the medium and small TB airways, only negligible evaporation is expected in the alveolar region.

For the prescribed inhalation flow conditions ($Q = 500$ cm^3/s and $V_T = 1500$ cm^3), application of the Stahlhofen et al. (1989) equation for alveolar deposition in combination with the TB deposition values predicted in this study indicated near full lung retention of the aerosol with ECG delivery. The alveolar estimates are based on the aerosol size exiting B5, which is approximately 3 μm for ECG conditions. It is noted that full lung retention of an aerosol is significantly influenced by both particle size and inhalation parameters. In vivo studies of the full lung deposition of monodisperse stable 3 μm particles indicate that retention may be less than 100% for different breathing parameters. For

example, the review article of Kim (2009) shows that the in vivo total lung deposition fraction of a 3 μm aerosol with Q = 500 cm^3/s and V_T = 1000 cm^3 is approximately 60% based on a bolus delivery technique. One factor that may contribute to the predicted high lung deposition values compared with previous in vivo studies is that the approximate aerosol size of 3 μm is based on droplets which have not deposited and exit B15. It is difficult to determine a representative droplet size for predicting full lung deposition with ECG due to the combination of both active growth and deposition in the airways. Figure 6.9 clearly shows that the majority of deposited particles are greater than 3 μm and further analysis of the data indicates a number of deposited 4 μm particles. Table 6.3 also shows that the CFD predicted values for TB deposition are representative of, but greater than, the corresponding correlation-based values using an average static inlet diameter. Therefore, 3 μm may be a small approximate static size for comparing the predictions of the current study with previously reported whole lung deposition data. Further investigation is needed to better predict deposition in the alveolar region and to approximate the total lung doses delivered with ECG. However, the CFD predictions of TB deposition presented in this study are expected to be accurate based on the extensive validations that have previously been performed in terms of both aerosol size increase and deposition (Hindle and Longest 2010; Longest and Hindle 2010).

In addition to significantly reducing MT deposition and enabling full lung retention, results also illustrate the ability of ECG to target deposition within regions of the TB airways. Specifically, increasing the ECG delivery temperature

from 37 to 39 °C approximately doubled the amount of drug mass deposited in region B4–B7 (e.g., 4.7–9.2%). This increase was observed for both aerosol sizes. Increasing both the delivery temperature and initial size increased deposition in B8– B15 by a factor of 1.25 (e.g., 28.6–37.0%). In general, the initial size of the aerosol (560 vs. 900 nm) had a minor influence on the final size and deposition fraction. As observed by Longest et al. (2010), surrounding temperature and RH conditions and not initial size generally control the final aerosol size achieved with ECG delivery. However, the initial size may become a more significant factor if hygroscopic effects are larger, for high number concentration aerosols, and if shorter times are available for growth as may occur with targeted upper airway delivery. The observed variations in TB deposition associated with ECG initial conditions may be reduced in vivo due to variations in patient anatomy and inhalation profiles. Furthermore, ECG does not provide a means to produce highly localized targeted deposition, as may potentially be achieved with magnetic aerosols (Xie et al. 2010).

In this study, an individual path model was used for the first time to characterize flow field conditions and aerosol transport from the fourth bifurcation to the end of the TB region. As indicated above, this approach is not intended to fully resolve all pathways throughout the conducting airways. Instead, it serves as a representative model for assessing transport and deposition. In future analyses, it is proposed to use individual paths to stochastically characterize transport and deposition within the bifurcations of each lung lobe. Randomly generated individual path models can be simulated to create an ensemble of

deposition efficiencies. Averages of these ensemble results can then be used to quantify transport conditions and deposition fractions (branch-averaged and highly localized) on a stochastic basis. However, a full characterization of the entire TB tree was not necessary to achieve the objective of this study. In this study, deposition efficiencies calculated from each branch of the individual path model were used to estimate total deposition in the TB region. The fact that these estimates were in general agreement with existing correlations for TB deposition in vivo provided evidence that the individual path model approach is reasonable and also supports the accuracy of the CFD predictions.

The predicted MT deposition of approximately 1–2% may initially appear low considering that the typical aerosol size entering the trachea is 2 μm with ECG conditions. Furthermore, the elliptical MT model is known to be a representation of a more realistic geometry (Xi and Longest 2007b). The previous study of Longest et al. (2008b) showed that 2 μm particles at a steady flow rate of 30 L/min resulted in a MT deposition of approximately 5%. Xi and Longest (2007b) reported that the deposition of a 2 μm aerosol in the MT model at 30 L/min was approximately 10%. Several factors contributed to the observed reduction in MT deposition in this study. First, droplet growth occurs continuously, so the actual deposition is expected to be smaller than would occur for the final aerosol size at the MT outlet. Second, the dual flow mouthpiece centralized the aerosol and surrounded it with a layer of clean air. The previous study of Longest and Oldham (2006) showed that reducing the aerosol inlet cross-sectional area could significantly reduce aerosol deposition. The deposition results

of Xi and Longest (2007b) are likely high for particles in the 1–2 μm size range, because of the use of the k–ω turbulence model without an anisotropic correction, as employed in the current study. However, the results of Xi and Longest (2007b) did show very little difference in the MT total deposition values between a more realistic geometry and the current elliptical model at 30 L/min, which provides a justification for the use of the elliptical model. The low MT deposition values of the current study are in good agreement with the experimental upper airway results of Hindle and Longest (2010), which further supports the validity of the current simulations. However, some differences between the in vitro data and current results likely arise due to the factors described above, such as the implementation of an initially monodisperse aerosol distribution with the CFD model of this study.

Limitations of the current study are associated with the geometry employed, simulation conditions, and numerical model. As previously discussed, the MT and upper TB models implemented some simplifications to facilitate a mathematically described geometry and allow for the use of more accurate hexahedral meshes (Vinchurkar et al. 2009). Furthermore, wall motion of the airways, particularly in the range of B15, may influence aerosol deposition. The assumed rotation angle of 90° for successive bifurcations may also be an overestimation of physiological conditions. The current model assumed steady state flow, which may impact the transport and deposition of some near-wall particles in the distal branches. The lobar ventilation rates were based on the volume estimates of Horsfield et al (1971). More accurate representations may be

available from numerical models (Asgharian and Price 2006; Asgharian et al. 2006), or for supine individual patients (Yin et al. 2010). Higher accuracy representations of the turbulent laryngeal jet can be computed with more time intensive models, such as direct numerical simulation and large eddy simulation (Lin et al. 2007; Matida et al. 2006). However, our previous results indicate good agreement between the LRN k–ω approximation with near-wall corrections and experimental predictions of growth and deposition. In conclusion, ECG delivery resulted in supersaturated RH fields throughout large portions of the TB airways. Initial submicrometer aerosols were observed to increase in size to a target range of 2–4 μm and evaporation of individual droplets was not evident. As a result, ECG provides an effective method to virtually eliminate MT depositional losses, and the associated intersubject variability, while providing for high TB deposition and near full lung retention of the aerosol. Targeting drug deposition within specific lung regions was also demonstrated. Future studies are needed to consider the effects of unsteady flow, drug concentrations in the droplets, additional individual path models for full TB characterization, and deposition in the alveolar region with moving boundaries.

Table 6.1. All cases considered.

	Aerosol inlet	Humidified air inlet
Case 1: control	*Q*: 9 L/min	*Q*: 20 L/min
non-evaporating	(150 cm^3/s)	(333.3 cm^3/s)
560 and 900 nm	*T*: 25 ^{O}C	*T*: 25 ^{O}C
	RH: 97.5%	*RH*: 50%
Case 2: control	*Q*: 9 L/min	*Q*: 20 L/min
evaporating	(150 cm^3/s)	(333.3 cm^3/s)
560 and 900 nm	*T*: 25 ^{O}C	*T*: 25 ^{O}C
	RH: 97.5%	*RH*: 50%
Case 3: ECG 1	*Q*: 9 L/min (150 cm^3/s)	*Q*: 20 L/min (333.3 cm^3/s)
560 and 900 nm	*T*: 39 ^{O}C	*T*: 39 ^{O}C
	RH: 97.5%	*RH*: 100%
Case 4: ECG 2	*Q*: 9 L/min (150 cm^3/s)	*Q*: 20 L/min (333.3 cm^3/s)
560 and 900 nm	*T*: 42 ^{O}C	*T*: 42 ^{O}C
	RH: 97.5%	*RH*: 100%

Table 6.2. Deposition efficiency (%) for each case.

	MT	Trachea-B3	B4-B7	B8-B15
Case 1: 560 nm	1.65	0.44	1.46	2.49
900 nm	2.26	0.57	1.73	6.98
Case 2: 560 nm	1.35	0.46	1.45	2.47
900 nm	2.18	0.73	1.85	7.09
Case 3: 560 nm	0.92	0.69	4.70	28.57
900 nm	1.31	0.80	7.08	33.00
Case 4: 560 nm	0.90	0.81	9.19	35.36
900 nm	0.92	0.83	13.35	36.97

Table 6.3. Stochastic analysis of deposition efficiency (%) for Case 4.

Case 4: 900 nm	MT	Trachea-B3	B4-B7	B8-B15
Path 1	0.92	0.83	13.35	36.97
Path 2	0.93	0.79	12.06	34.29
Path 3	0.91	0.80	14.46	34.72
Average	0.92	0.81	13.29	35.54
SD	0.0001	0.0002	0.0098	0.0119

Table 6.4. Comparison with existing TB correlations (DE).

	MMAD at the B5 outlet (μm)	Predicted DE_{TB}	DE_{TB} (Stahlhofen et al. 1989; Eq. 15)	DE_{TB} (Chan and Lippmann 1980; Eq. 3)
Case 1: 560 nm	0.56	0.04	0.01	0.01
900 nm	0.9	0.09	0.03	0.03
Case 2: 560 nm	0.47	0.04	0.01	0.01
900 nm	0.74	0.09	0.02	0.02
Case 3: 560 nm	2.39	0.32	0.17	0.19
900 nm	2.58	0.38	0.20	0.22
Case 4: 560 nm	3.13	0.42	0.27	0.30
900 nm	3.28	0.46	0.30	0.32

Table 6.5. Predicted pulmonary and total deposition fractions.

	MMAD at the B15 outlet (μm)	Predicted $DF_{MT\text{-}TB}$	$DF_{alveolar}$ (Stahlhofen et al.,1989; Eq. 19)	DF_{total}
Case 1: 560 nm	0.56	0.06	0.17	0.23
900 nm	0.9	0.11	0.27	0.38
Case 2: 560 nm	0.57	0.06	0.17	0.23
900 nm	0.84	0.11	0.26	0.37
Case 3: 560 nm	2.00	0.33	0.50	0.83
900 nm	2.23	0.39	0.52	0.91
Case 4: 560 nm	2.89	0.42	0.54	0.96
900 nm	2.95	0.46	0.54	1

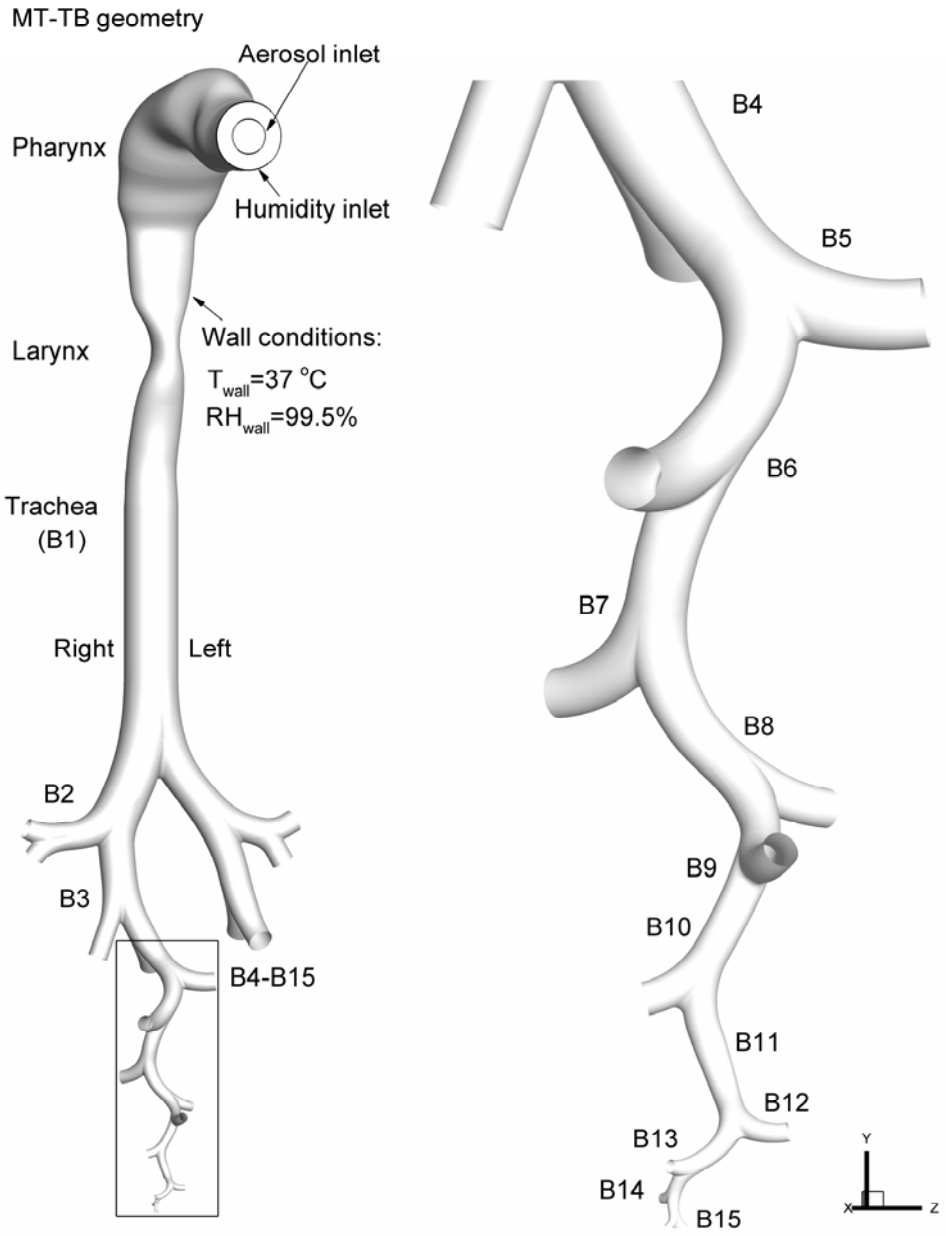

Figure 6.1. Geometry used to evaluate the enhanced condensational growth (ECG) delivery of submicrometer aerosol in the mouth-throat (MT) and tracheaobronchial (TB) regions extending down a single path to bifurcation 15 (B15) of the right lower lung lobe.

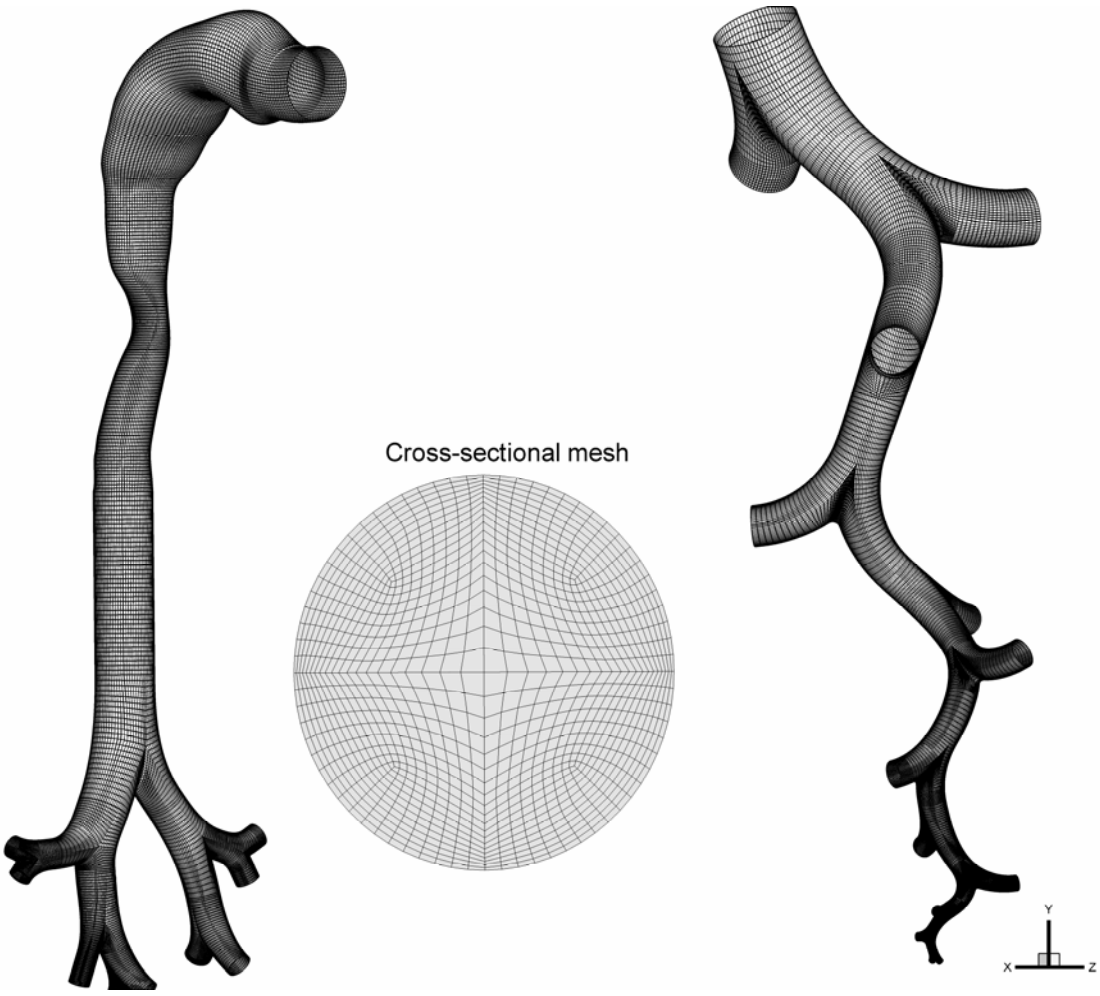

Figure 6.2. Computational mesh of the MT-TB airway model.

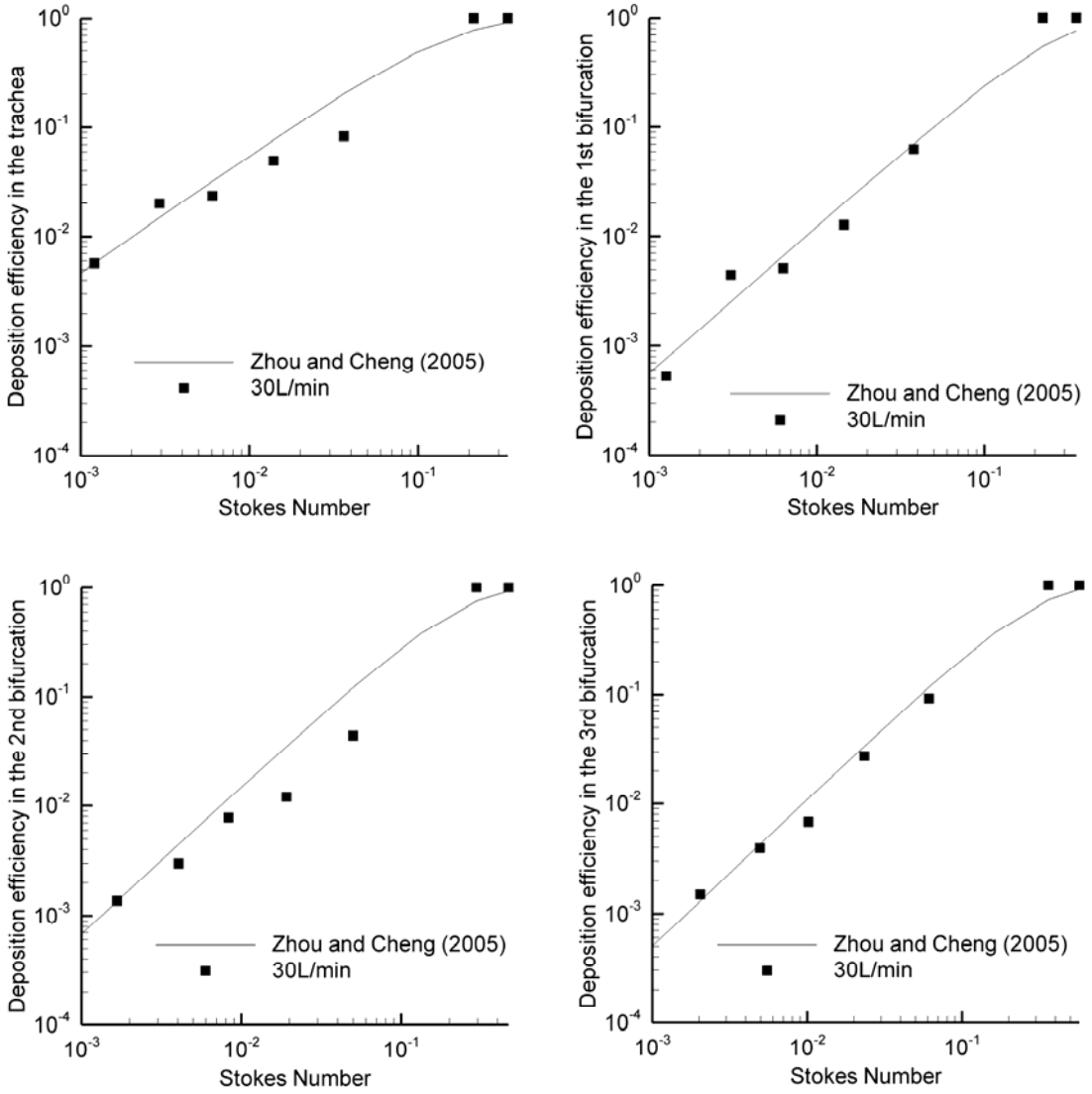

Figure 6.3. Comparison of aerosol deposition efficiency in the upper TB airways between CFD predictions with the MT-TB geometry considered in this study and the experimental results Zhou and Cheng (2005) for a cast-based replica model.

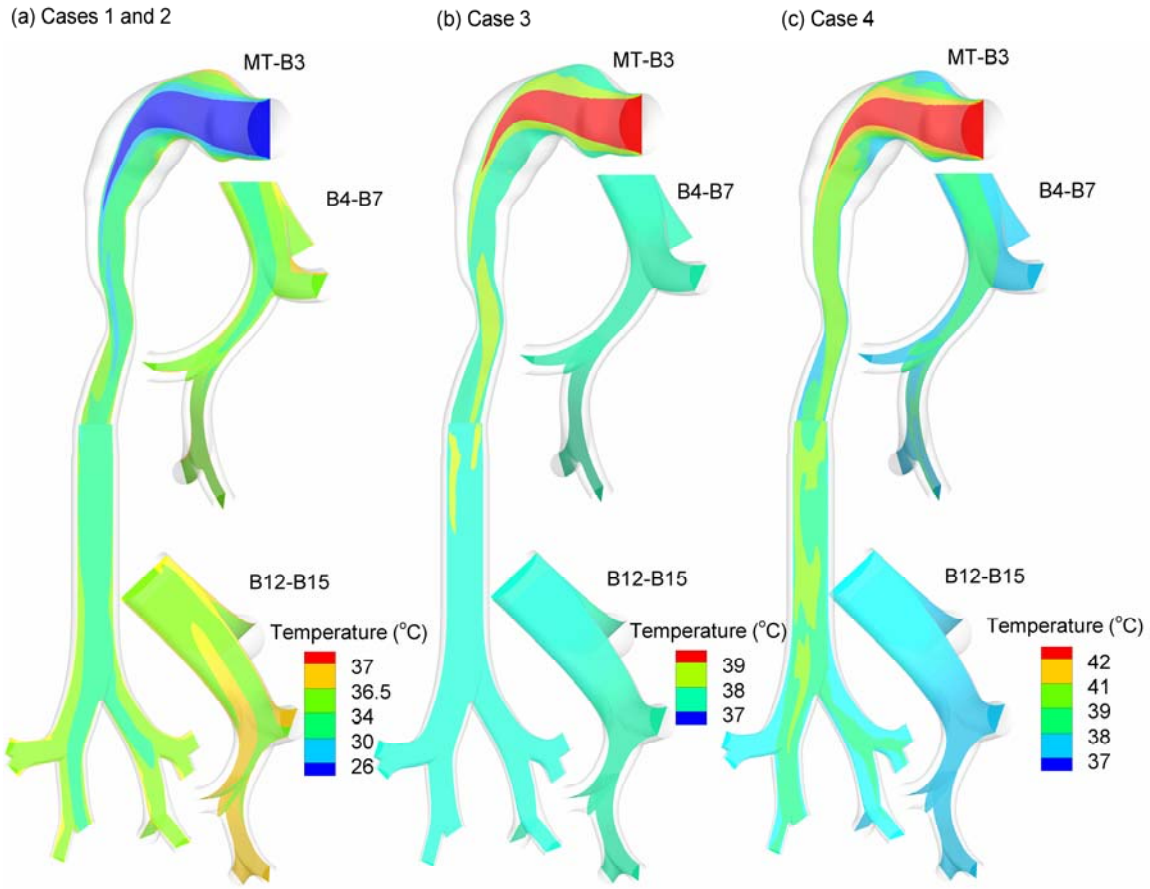

Figure 6.4. Predicted temperature conditions for (**a**) Cases 1 and 2, (**b**) Case 3, and (**c**) Case 4 conditions.

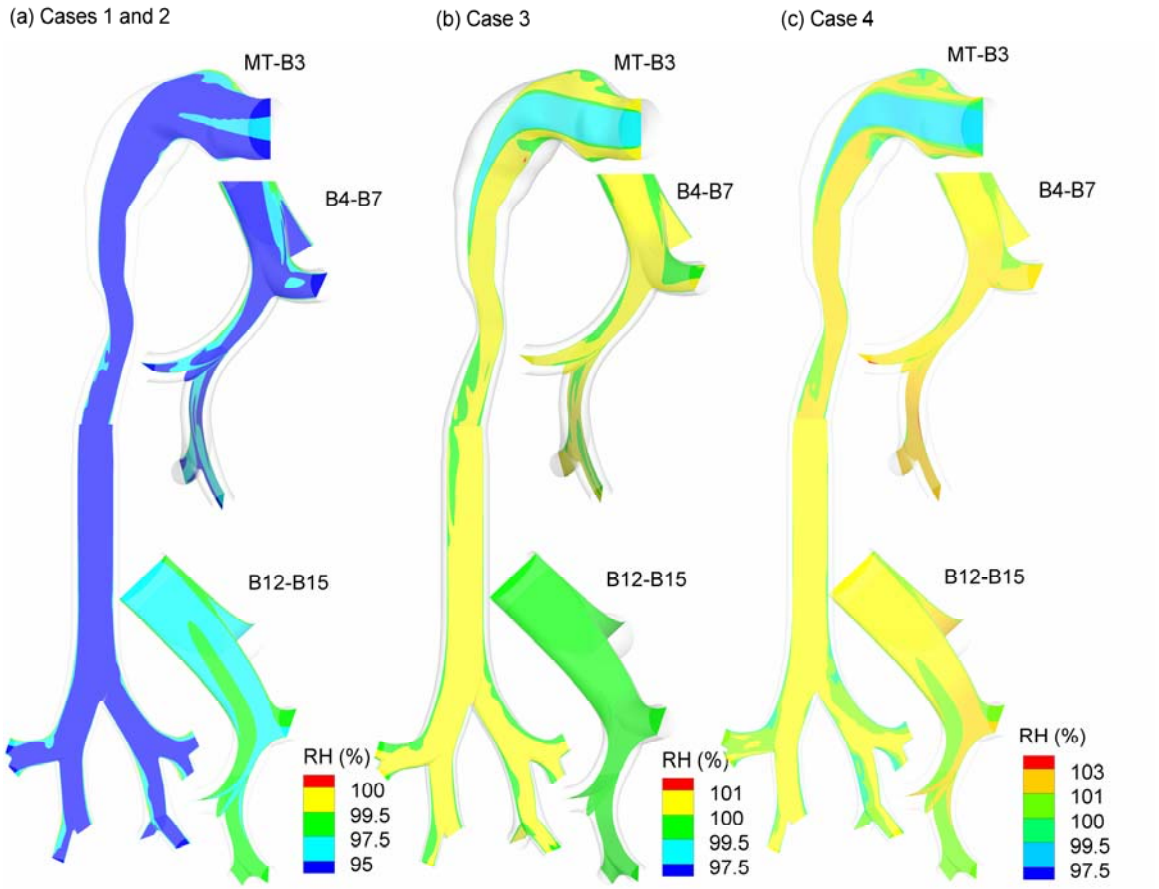

Figure 6.5. Predicted relative humidity (RH) conditions for (**a**) Cases 1 and 2, (**b**) Case 3, and (**c**) Case 4 conditions.

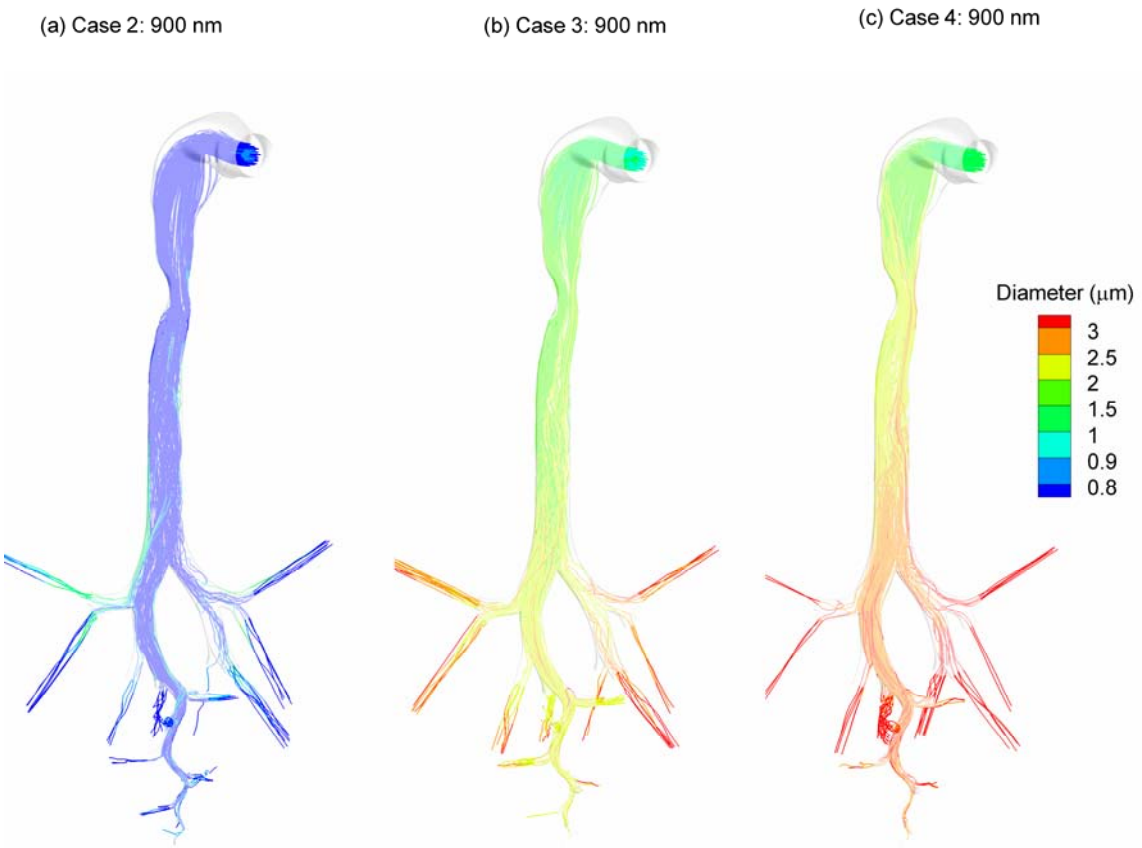

Figure 6.6. Predicted droplet trajectories for initially 900 nm monodisperse aerosols and (**a**) Case 2, (**b**) Case 3, and (**c**) Case 4 conditions.

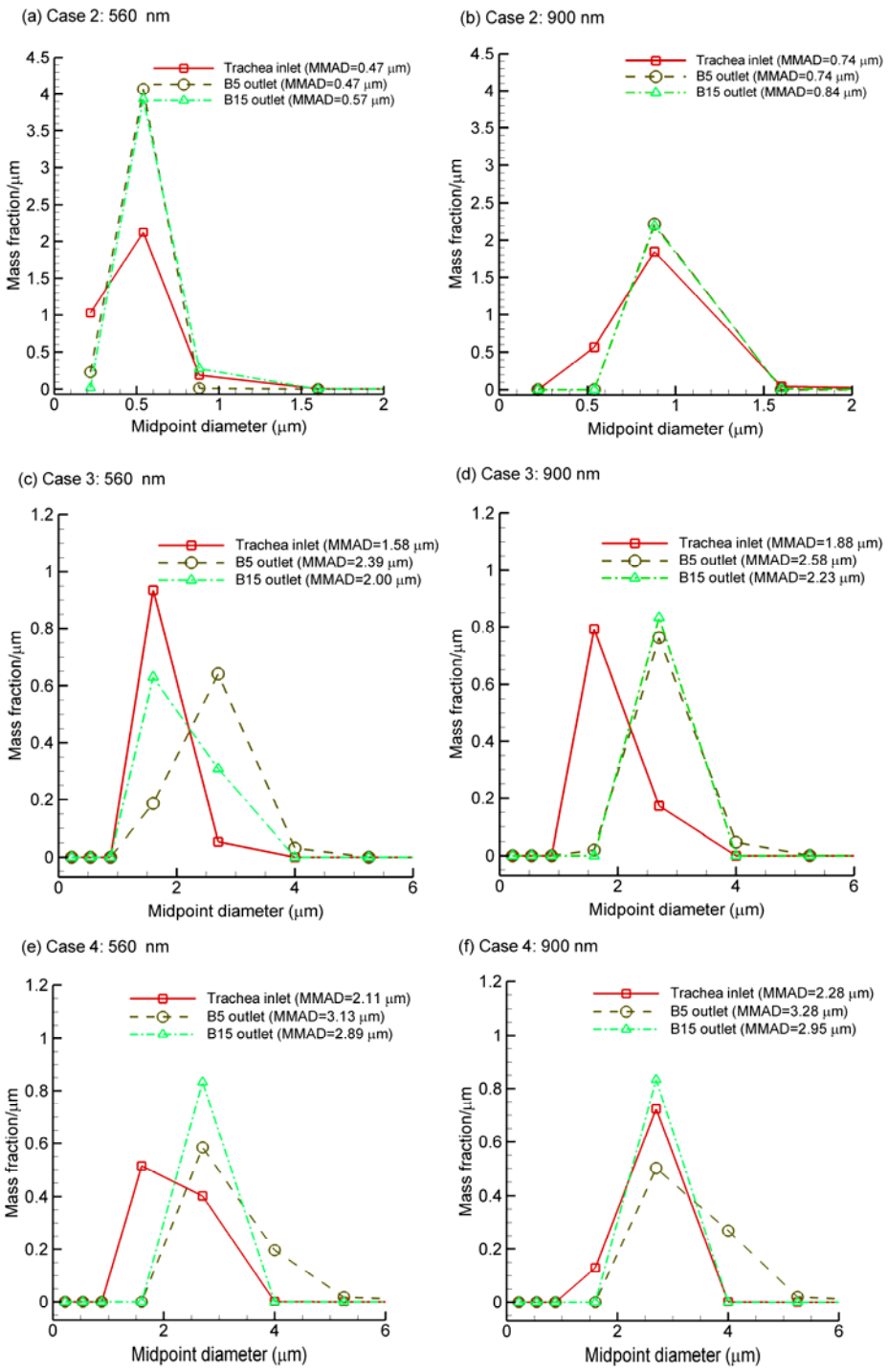

Figure 6.7. CFD predictions of exiting polydisperse size distributions for initially 560 nm and 900 nm monodisperse aerosols under Case 2-4 conditions.

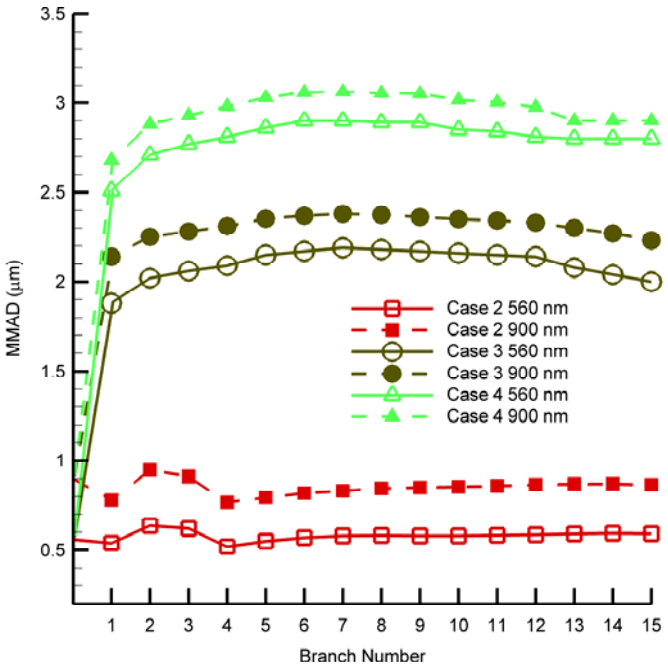

Figure 6.8. Comparisons of the mass median aerodynamic diameters (MMAD) with the aerosol entering one branch of each bifurcation through bifurcation 15 (B15) for Cases 2-4.

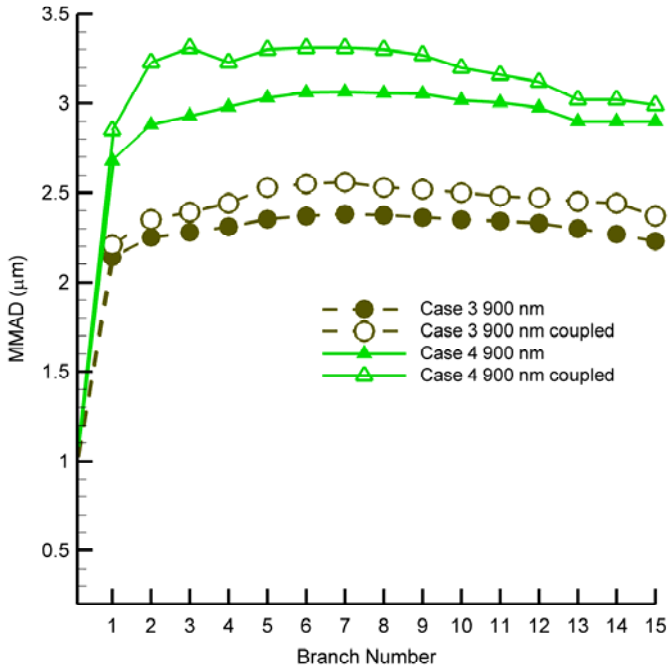

Figure 6.9. Comparisons of the mass median aerodynamic diameters (MMAD) with the aerosol entering one branch of each bifurcation through bifurcation 15 (B15) for Cases 3 and 4 with one-way and two-way coupling.

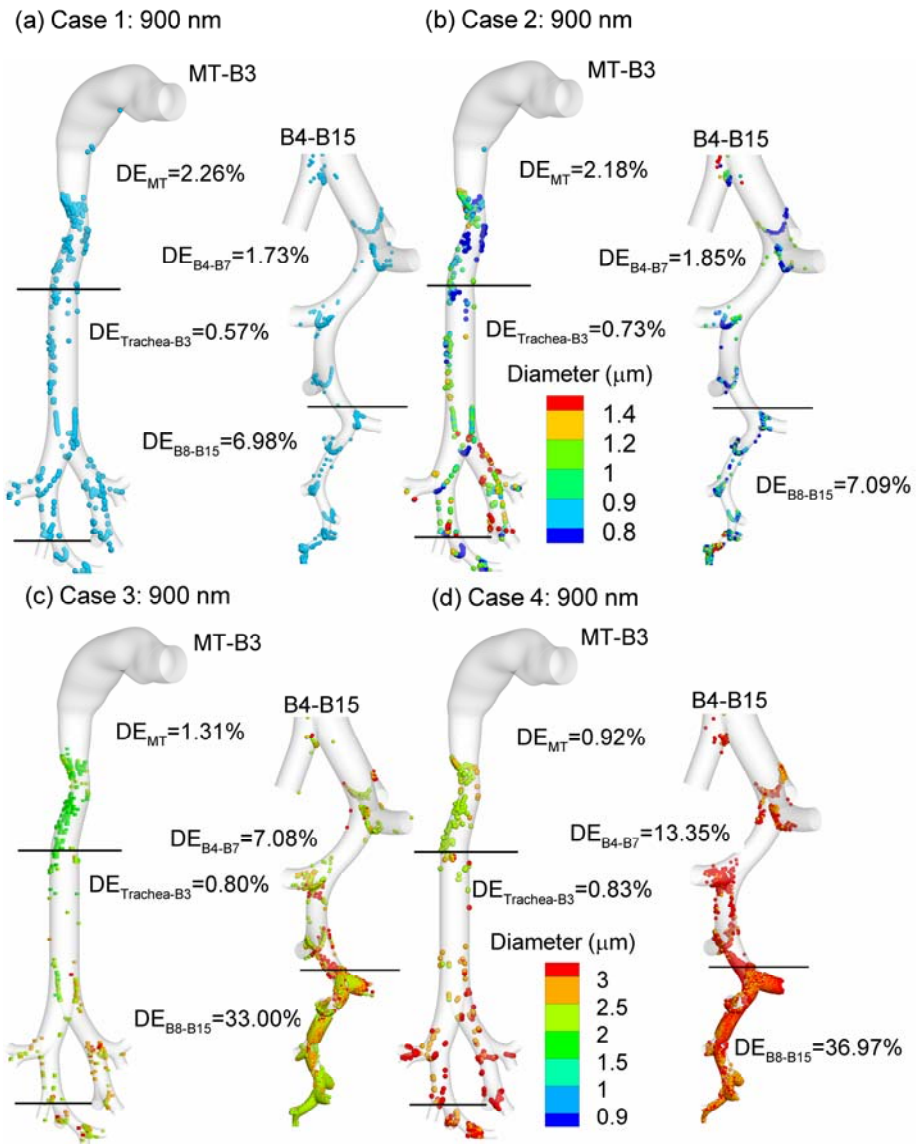

Figure 6.10. Particle deposition locations and regional deposition efficiencies (DE) of drug mass for an initially 900 nm aerosol and (**a**) Case 1, (**b**) Case 2, (**c**) Case 3, and (**d**) Case 4 conditions.

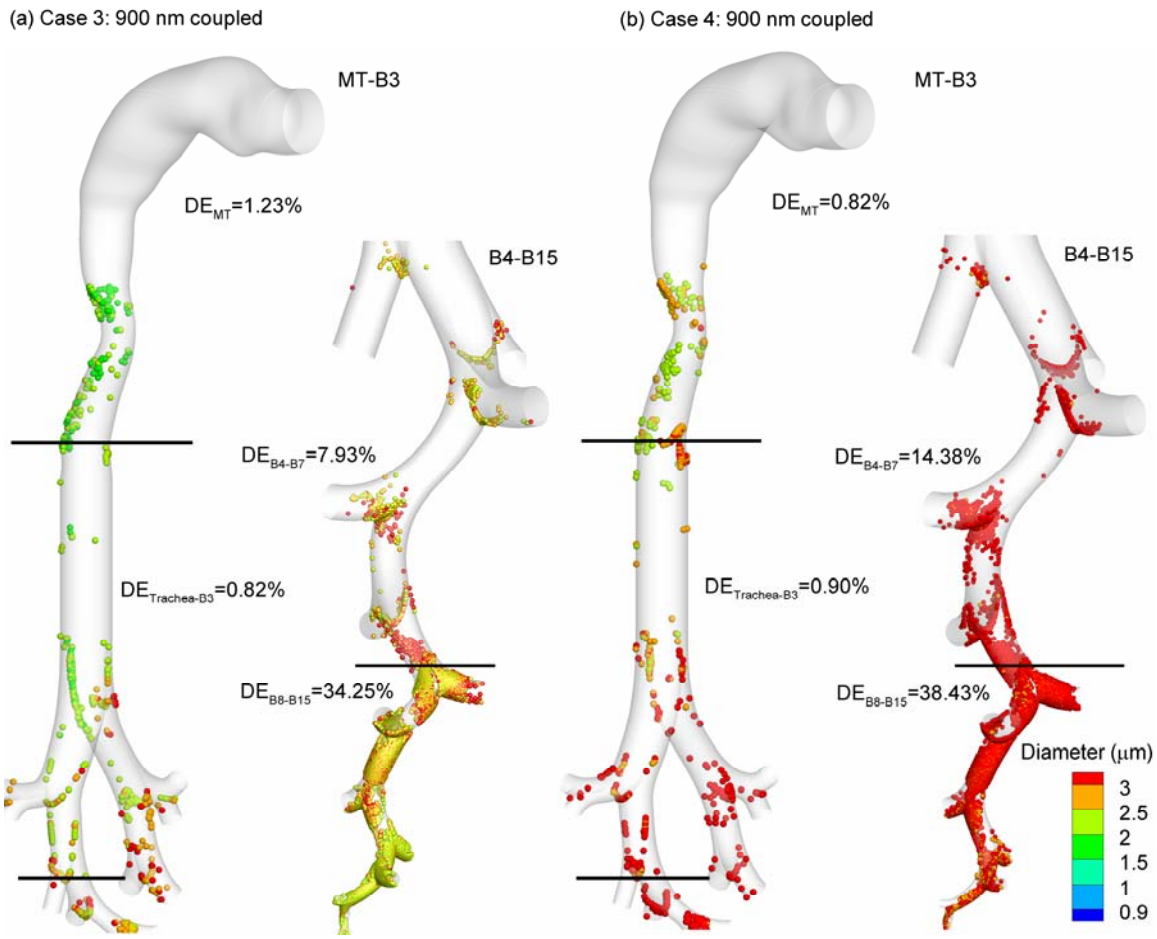

Figure 6.11. Particle deposition locations and regional deposition efficiencies (DE) of drug mass for an initially 900 nm aerosol with (**a**) Case 3 and two-way coupling and (**b**) Case 4 and two- way coupling.

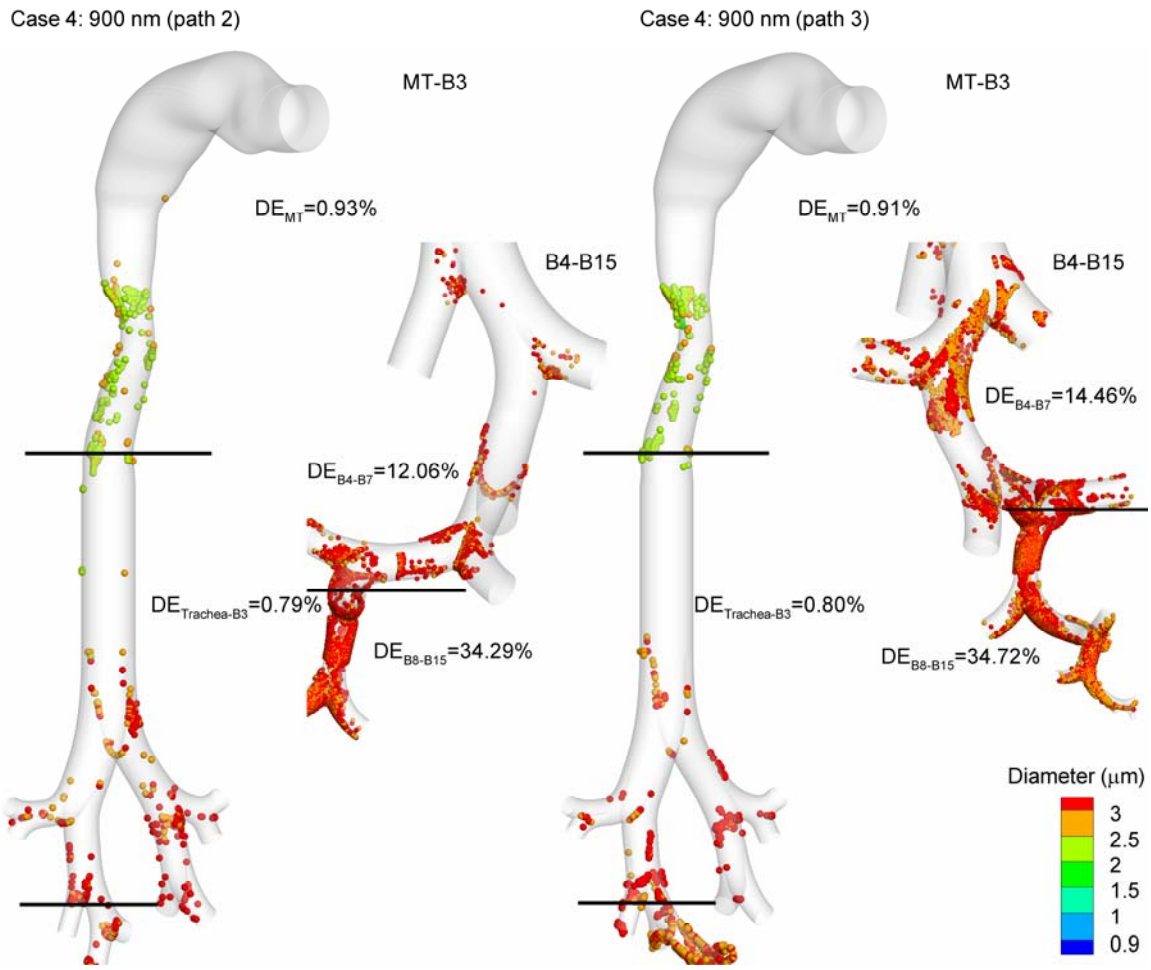

Figure 6.12. Particle deposition locations and regional deposition efficiencies (DE) of drug mass for an initially 900 nm aerosol and (**a**) Case 4 down path 2 vs. (**b**) Case 4 down path 3.

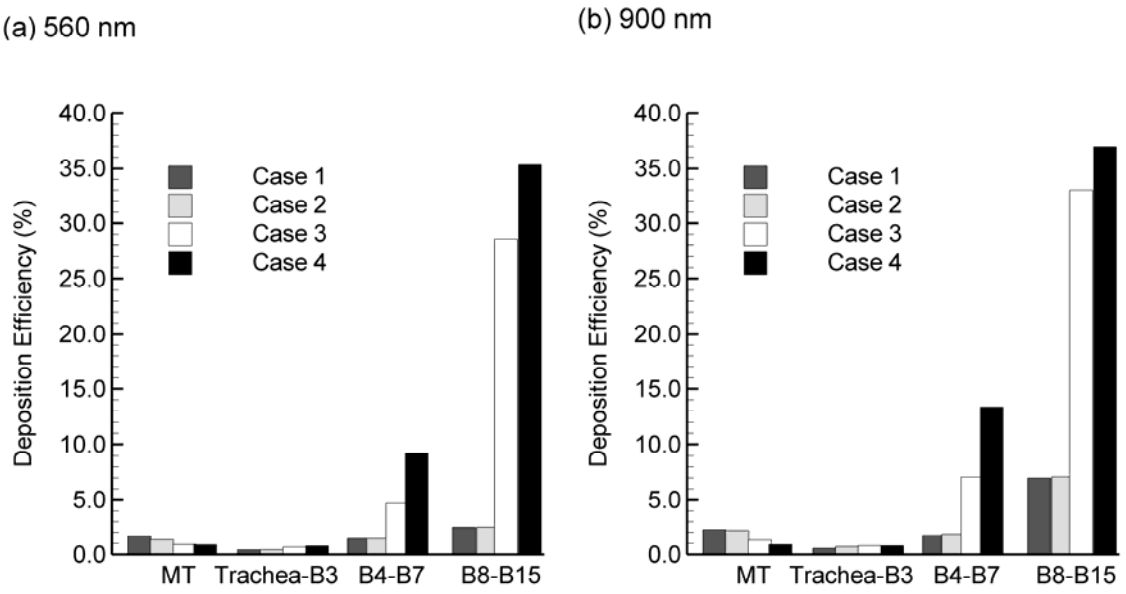

Figure 6.13. Comparison of deposition efficiencies (DE) for initially (**a**) 560 and (**b**) 900 nm droplets.

Chapter 7. Effects of Transient Inhalation on Enhanced Condensational Growth (ECG) in a Realistic Mouth-Throat and Tracheobronchial Single Path Model

7.1 Introduction

Previous results indicate the enhanced condensational growth (ECG) can improve the delivery of pharmaceutical aerosols to the lungs based on steady inhalation conditions in a realistic mouth-throat (MT) and tracheobronchial (TB) single path model. However, transient inhalation will influence the transport, growth, and deposition of droplet aerosols by modifying the (i) inertia of the particles, (ii) the time available for growth, and (iii) the relative humidity (RH) field. A more complete picture of aerosol growth and deposition in the MT-TB single path model is needed.

The objective of this study is to evaluate the effect of a transient inhalation waveform on the ECG delivery of respiratory aerosols, using the realistic MT-TB single path model previously described in Chapter 6. CFD methods will be employed to evaluate aerosol deposition and outlet particle sizes under transient inhalation conditions. The CFD results will then be compared with steady inhalation conditions to determine if steady state approximations are adequate, or if more detailed transient simulations are needed.

7.2 Methods

Transient Inhalation Waveform

The steady state inhalation flow rate considered in Chapter 6 is approximately 30 L/min. In this chapter, one inhalation cycle (2 s inhalation and 2 s exhalation) with a breathing frequency (*f*) of 15 *breaths/minute* and a tidal volume (V_T) of 1 *L/breath* is considered. Using the format from the Chapter 3, the transient inhalation waveform *Q(t) (L/min)* was approximated as the sinusoidal function shown in Fig. 7.1 and represented as

$$Q(t)=47\sin(0.5\pi t) \tag{7.1}$$

This waveform is equivalent to a steady state inhalation flow rate of 30 L/min based on the Eqs. (5.1) and (5.3).

Boundary and Delivery Conditions

As in Chapter 6, a wall temperature of approximately 37 ^{o}C with a surface RH of 99.5% was considered. The airflow and droplet inlet boundary conditions employed in the CFD simulations are presented in Table 7.1. As shown in the table, Case 3 from the Chapter 6 was considered under transient inhalation conditions. In this case, an inlet temperature condition of 39 ^{o}C was selected for both the aerosol and humidity streams. Monodisperse nebulized aerosol droplets with initial diameters of 900 nm were simulated with a surrounding air phase RH condition of 97.5% at a total flow rate of 9 L/min. The humidified air inlet stream was generated with RH conditions of 100% at 20 L/min. The outlet flow

distribution in the MT-TB model was consistent with the values reported by Horsfield *et al.* (1971) at the exit of the third bifurcations.

Transport Equations in MT-TB Single Path Model

The low-Reynolds-number (LRN) $k-\omega$ model of Wilcox (1998) was selected for simulating mixing of the delivery streams in the MT-TB single path model because it has been shown to provide an accurate and numerically efficient solution for laminar, transitional and turbulent flows. Furthermore, this model was found to accurately predict aerosol transport and deposition in upper airway models (Longest and Hindle 2009a; Longest et al. 2009). The coupled governing equations of heat and mass transport were considered to evaluate the variable temperature and RH fields in the MT-TB model. These transport equations were previously reported in Longest and Xi (2008) and Longest *et al.* (2007). The Lagrangian transport equations interconnected with user defined functions were employed to calculate droplet trajectories, condensation, evaporation, deposition, near-wall anisotropic turbulence correction (Longest et al. 2007), near-wall particle interpolation (Longest and Xi 2007b), and Brownian motion (Longest and Xi 2007b) in the complex three-dimensional temperature and humidity fields. The discrete phase transport model includes the Kelvin effect, drug hygroscopicity, and the effect of droplet temperature on surface vapor pressure.

Numerical Methods

To solve the transport governing equations, the CFD package Fluent 6.3, (ANSYS Inc.) coupled with user defined functions was employed. All transport

equations were discretized to be at least second order accurate in space. For the convective terms, a third order QUICK scheme was used to interpolate values from cell centers to nodes. The diffusion terms were discretized using central differences. A segregated implicit solver was employed to evaluate the resulting linear system of equations. This solver uses the Gauss-Seidel method in conjunction with an algebraic multigrid approach. The PISO algorithm was employed to evaluate pressure-velocity coupling in the transient solutions. The outer iteration procedure was stopped when the global mass residual had been reduced from its original value by five orders of magnitude and when the residual-reduction-rates for both mass and momentum were sufficiently small. To ensure that a converged solution had been reached, residual and reduction rate factors were decreased by an order of magnitude and the results were compared. The stricter convergence criteria produced a negligible effect on both velocity and particle deposition fields. To improve accuracy, all calculations were performed in double precision. The computational mesh developed from the Chapter 6 composed of approximately 2.4×10^6 unstructured hexahedral elements and a very fine near-wall grid and was constructed in Gambit 2.3.16 (ANSYS, Inc.). Hexahedral meshing has been shown to provide a better quality solution in aerosol deposition studies compared with tetrahedral and hybrid grids (Longest and Vinchurkar 2007a; Vinchurkar and Longest 2008). Grid converged results based on negligible change in the velocity and concentration fields (< 1%) as well as negligible differences in the total deposition fractions (< 3%) were established for a mesh consisting of 2.4×10^6 control volumes. In order to produce convergent

aerosol deposition results, 1.2×10^5 initially 900 nm monodisperse droplets were released at the aerosol inlet stream from 0-1 s during inhalation.

7.3 Results

Temperature Fields

Contours of temperature are shown for the MT, upper TB airways, and selected medium and small TB airways in Fig. 7.2 for steady and transient inhalation conditions. Temperature contours are presented as mid-plane slices within each of the airway regions shown. For steady state conditions, rapid cooling is observed in the MT with temperatures in the range of 37-39 $^{\circ}$C in the trachea. Temperatures of approximately 37 $^{\circ}$C are observed in the B4-B7 and B12-B15 regions. Temperature values at t=0.5 s were found to be similar with steady state conditions. This similarity is likely because the inhalation flow rate at t=0.5 s is near 30 L/min. Temperature values at t=2 s in the MT are less than the values at t=0.5 s and steady state due to an decreased inhalation rate.

Relative Humidity

Predicted contours of RH for steady and transient conditions (t=0.5 and 2 s) are displayed for midplane and cross-sectional slices in Fig. 7.3. For steady state conditions, rapid cooling of the saturated airstream results in a rapid progression to supersaturation, with values as high as 101% observed in the pharynx. RH values remain in the range of 100-101% through a majority of the upper TB geometry and bifurcations B4-B7. In B12-B15, RH values are near wall conditions of approximately 99.5%. Again, RH values at t=0.5 s were similar to

those values found under steady state conditions. The increased RH values in the MT from t=0.5 s to t= 2 s are likely because of the decreased temperature values already discussed and can be expected to enhance aerosol growth.

Aerosol Transport and Growth

Comparisons of droplet size distributions at specific cross-sectional locations for initially 900 nm monodisperse aerosols in the model between steady and transient inhalation conditions are presented in Fig. 7.4 in terms of mass fraction per micrometer of sampling bin size. Mass median aerodynamic diameters (MMAD) values are also presented for each aerosol size distribution. For steady state conditions, the MMADs of an initially 900 nm aerosol increased to 1.88 μm at the trachea inlet and continued condensational growth was observed with the aerosol exiting B5 with a predicted size of 2.58 μm. The MMAD of the aerosol exiting B15 had decreased to 2.23 μm. This decrease in MMAD likely arises from deposition of the larger particles as discussed in Chapter 6. For the transient case, size increase was based on all particles crossing the planes of interest from particle release at t = 0 s through t=2 s. For the transient simulation, condensational growth was observed as droplets enter the trachea with a predicted MMAD of 1.76 μm and continued with a predicted size of 2.42 μm at the exit of B5. The MMAD of the aerosol exiting B15 had decreased to 2.23 μm. Size distribution profiles indicate that 75-85% of the aerosol mass is associated with droplets of approximately 3 μm exiting B5 and B15 under steady inhalation conditions, but this has decreased to 55-60% in the same locations after 2s in the transient case. This may be because the higher peak flows occurring in the

transient case result in increased deposition of the larger particle sizes. Interestingly, percent differences in MMADs for aerosols at specific locations are less than approximately 2% between steady state and transient cases.

MMADs of the polydisperse aerosol entering each bifurcation (B1–B15) are presented in Fig. 7.5 for steady and transient inhalation conditions. For both conditions, significant growth is observed to occur through approximately B3. Thereafter, minor growth is observed through approximately B8, and some size decrease occurs between B8 and B15. This decrease may arise due to deposition of the larger particles. Percent differences in MMADs for aerosols entering each bifurcation were less than approximately 10% between steady and transient inhalation conditions (t=2 s).

Aerosol Deposition

Particle deposition locations of individual droplets are illustrated for the 900 nm aerosol for steady and transient inhalation conditions in Fig. 7.6. The droplets are colored based on their size at the time of deposition. Deposition efficiencies were calculated for each bifurcation and then combined to represent the total deposition efficiencies for the sections reported along the individual path. For both inhalation conditions, the MT deposition efficiencies remain very small (~1%) as observed by Hindle and Longest (2010). In contrast, deposition efficiencies in Trachea-B3 are increased approximately 2 times compared with the steady state conditions. Percent differences in DE between steady and transient inhalation conditions in B4–B7 and B8–B15 are approximately 9% and 13%, respectively. Predicted total DE of the TB airways under transient conditions is

approximately 12% higher (relative difference) than the total DE under steady state conditions.

To approximate whole lung retention of the aerosol, the predicted MT-TB deposition fractions are combined with the alveolar deposition efficiency in vivo-based correlations of Stahlhofen et al. (1989) and Chan and Lippmann (1980). An inhalation rate of 500 cm^3/s was employed along with a volume of 1500 cm^3. As observed from Table 7.2, total lung deposition fractions under steady and transient inhalation conditions are 91% and 95%, respectively.

7.4 Discussion

In this study, a CFD model was used to evaluate the effect of a transient inhalation waveform on the ECG delivery of respiratory aerosols, using the realistic MT-TB single path model. The CFD model results were then compared with steady inhalation conditions. Results of this study indicate that both steady and transient conditions produce very little deposition and aerosol loss in the MT. The drug deposition in the TB airways increased approximately 10% for transient inhalation conditions. The low MT deposition values of the current study are in good agreement with the experimental upper airway results of Hindle and Longest (2010), which further supports the validity of the current simulations.

Limitations of the current study are associated with simulation conditions. Constant wall temperatures consistent with mean body conditions were previously assumed. The wall temperature of the upper respiratory airways is known to be below average body temperature conditions. This change in wall surface

temperature will alter the RH surrounding the inhaled nanoparticles and modify condensational growth rates.

A number of factors will affect targeted deposition to specific lung region when the ECG approach is employed. These include initial aerosol size, temperature and humidity of the incoming air, hygroscopicity, inhalation flow rate and the release time of the aerosol during the breathing cycle. Modifying the release time of the aerosol, or bolus delivery, is a potentially useful method to target deposition in the lungs. Coupling bolus release with ECG may provide the control required for effectively targeting inhaled aerosols.

In conclusion, an ECG delivery approach under transient inhalation conditions was shown to increase aerosol deposition in the TB airways by only a small amount (relative difference of 12%), as compared with steady state conditions. Future studies are needed to consider transient ECG aerosol delivery under variable wall temperature conditions. The influence of inhalation flow rate, saturated air temperature, and release time of the aerosol also need to be considered.

Table 7.1. Inlet conditions considered.

	Aerosol inlet	Humidified air inlet
900 nm	Q: 9 L/min (150 cm^3/s)	Q: 20 L/min (333.3 cm^3/s)
	T: 39 ^oC	T: 39 ^oC
	RH: 97.5%	RH: 100%

Table 7.2. Pulmonary and total deposition fractions.

	MMAD at the B15 outlet (μm)	Predicted DF_{MT-TB}	$DF_{alveolar}$ (Stahlhofen et al., 1989; Eq. 19)	DF_{total}
Steady state	2.23	0.39	0.52	0.91
t=2 s	2.24	0.43	0.52	0.95

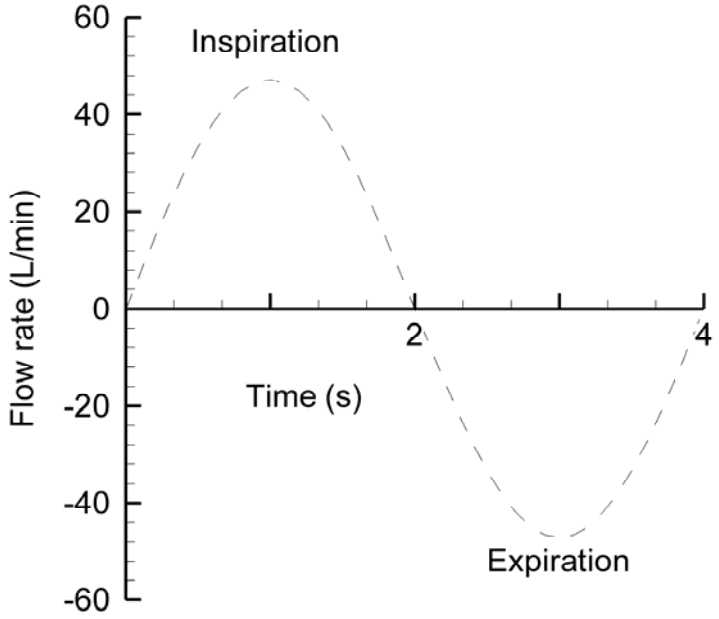

Figure 7.1. Transient inhalation waveform.

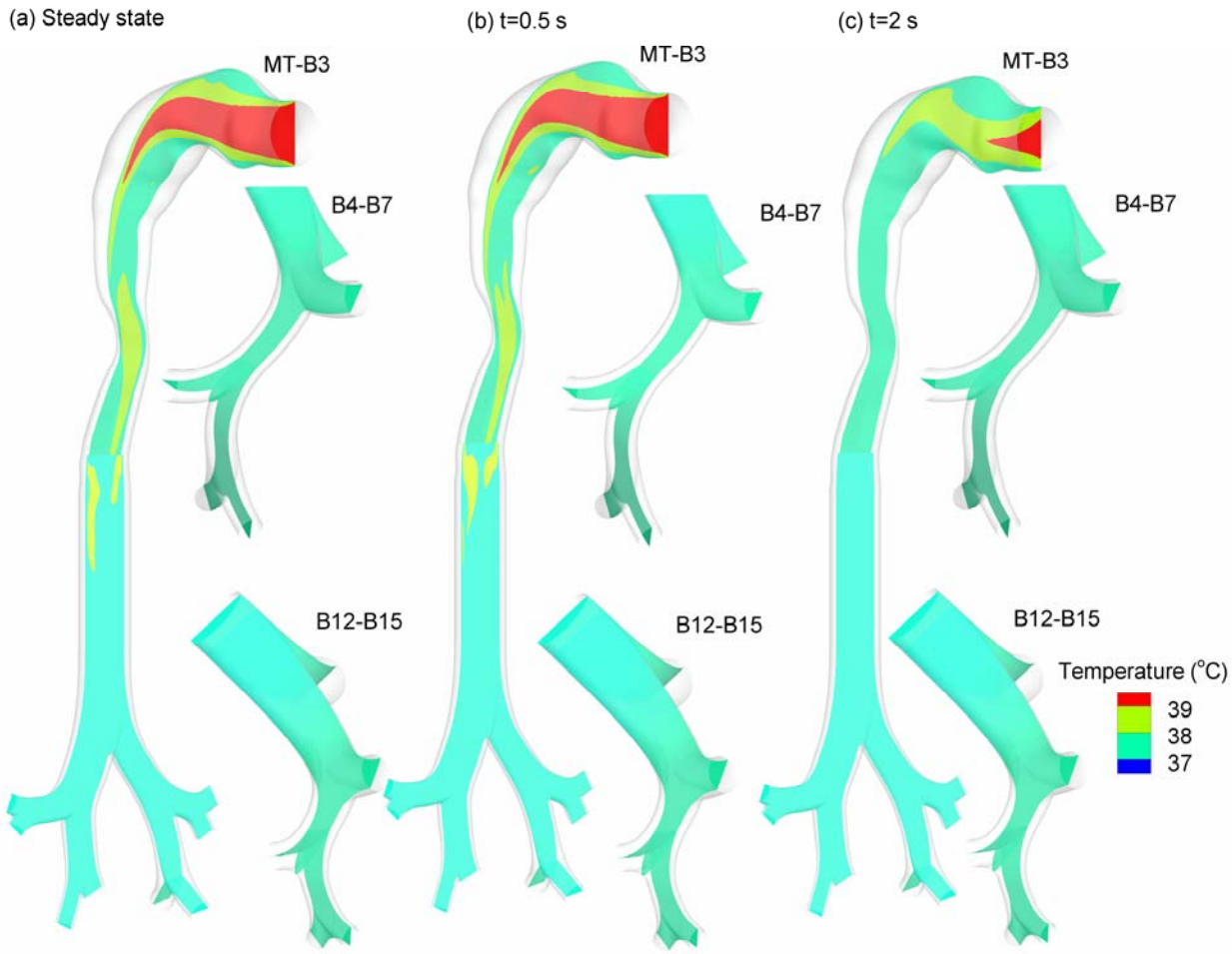

Figure 7.2. Predicted temperature conditions for (**a**) steady state, (**b**) t=0.5 s , and (**c**) t=2 s.

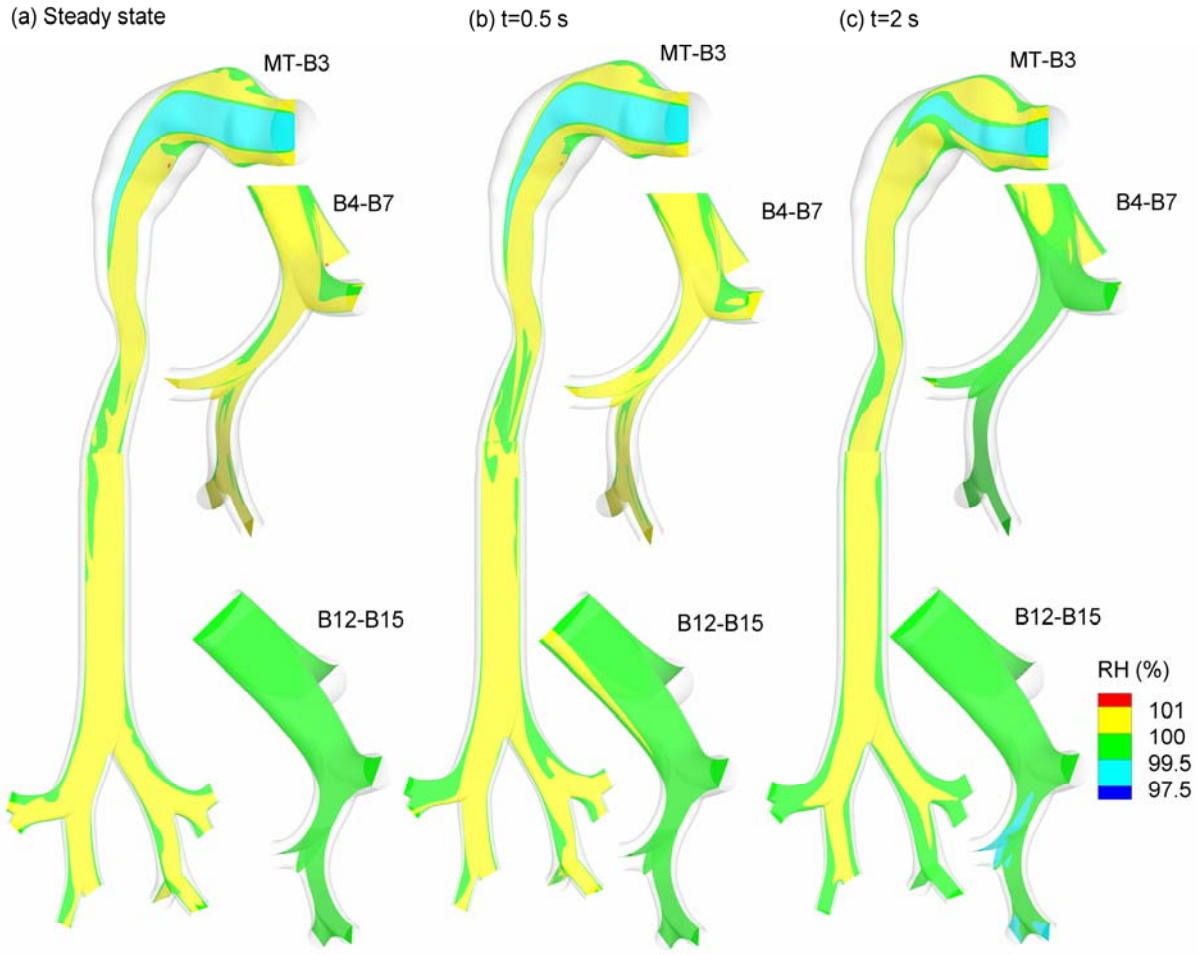

Figure 7.3. Predicted relative humidity (RH) conditions for (**a**) steady state, (**b**) t=0.5 s, and (**c**) t=2 s.

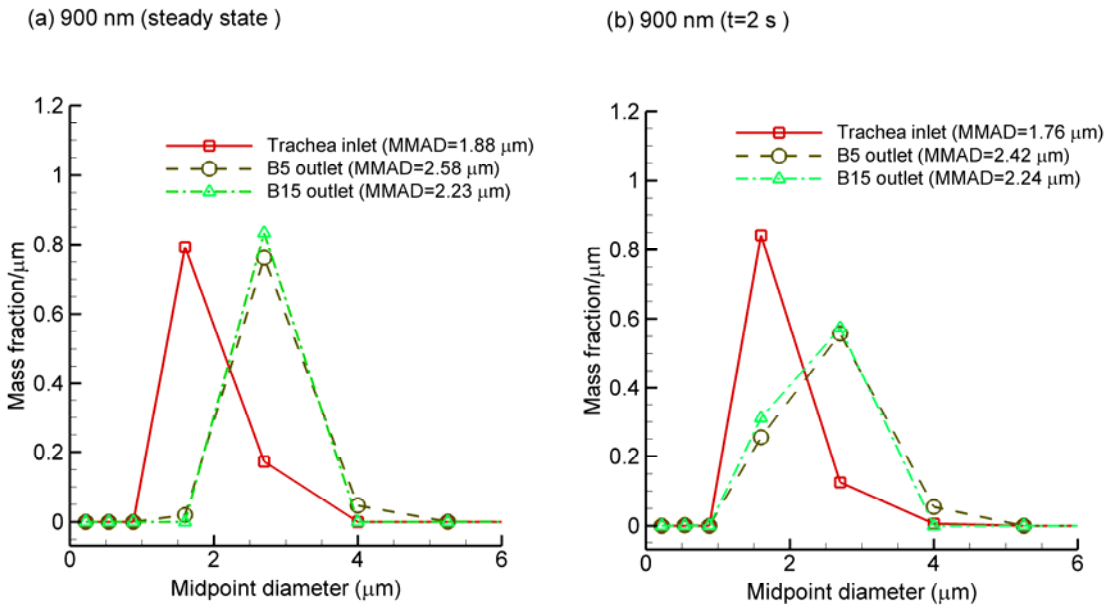

Figure 7.4. CFD predictions of exiting polydisperse size distributions for initially 900 nm monodisperse aerosol during (**a**) steady state and (**b**) transient inhalation (t=2 s).

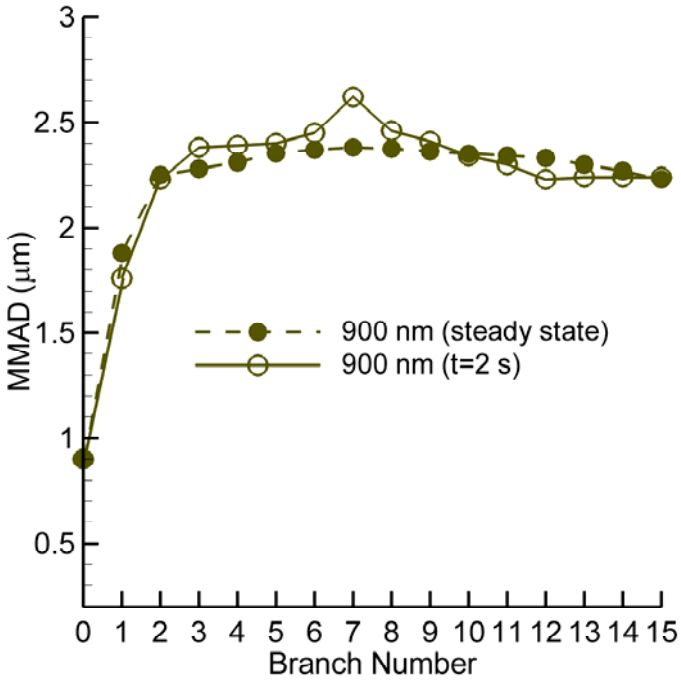

Figure 7.5. Comparisons of the mass median aerodynamic diameters (MMAD) with the aerosol entering one branch of each bifurcation through bifurcation 15 (B15) for steady and transient inhalation conditions (t=2 s).

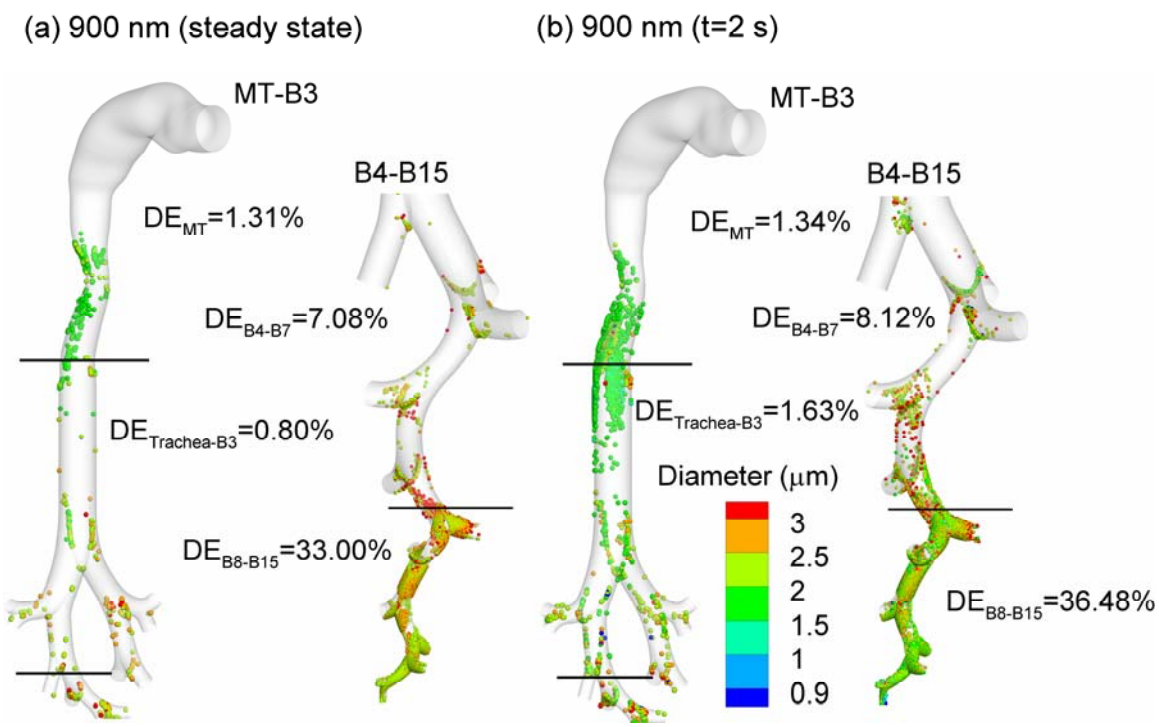

Figure 7.6. Particle deposition locations and regional deposition efficiencies (DE) of drug mass for an initially 900 nm aerosol for (**a**) steady state and (**b**) transient inhalation (t=2s).

Chapter 8. Effects of Inhalation Profiles on the Deposition of MDI and DPI Generated Aerosols in a Representative Model of the Mouth-Throat and Tracheobronchial Airways

8.1 Introduction

A number of recent studies have reported deposition in model geometries of the upper tracheobronchial (TB) airways for environmental and pharmaceutical aerosols (Kleinstreuer and Zhang 2009; Liu et al. 2007; Xi and Longest 2008b; Xi et al. 2008; Zhang et al. 2005; Zhang et al. 2009). Other studies have focused on the deposition of pharmaceutical aerosols from metered dose inhalers (MDIs) and dry powder inhalers (DPIs) in the MT models (Kleinstreuer et al. 2007; Longest and Hindle 2009a; Longest and Hindle 2009b; Longest et al. 2009; Longest et al. 2007; Longest et al. 2008a; Longest et al. 2008b). For current MDIs, approximately 25-60% of drug is lost in the mouth-throat (MT), and for current DPIs, MT deposition is approximately 70% (Cheng et al. 2001; Longest et al. 2008a; Zhang et al. 2007). CFD studies of inhaler performance have highlighted the underlying causes of large MT deposition as high spray momentum for MDIs (Longest et al. 2008a; Longest et al. 2008b) and large jet effects for DPIs (DeHaan and Finlay 2004). Current studies have also highlighted the significant size change of MDI droplets (Longest et al. 2008a). Considering the substantial loss of drug, system complexity, and the associated variability in lung dose, a better understanding of MDI and DPI delivery in the MT and upper tracheobronchial (TB) airways is needed. The objective of this study is to develop a CFD model of orally inhaled drug products that can account for inhaler

attributes (spray or jet momentum), physicochemical properties (polydisperse aerodynamic size distribution), and physiological parameters (breathing pattern, airway geometry) in determining local and regional deposition in a realistic MT and TB model of the upper airways.

8.2 Methods

Upper MT-TB Geometries

In this study, MT and TB deposition will be evaluated for two representative inhalers. The MT geometry is the elliptical model developed by Xi and Longest (2007b) and the upper TB airways are considered extending from the trachea to the third bifurcation (B3). This asymmetrical model was generated using the anatomical cast dimensions reported by Yeh and Schum (1980) and scaled to a functional residual capacity (FRC) of 3.5 L, which is consistent with an adult male (ICRP 1994). Further details of the upper TB model are provided in the Chapter 6. For the current study, cartilaginous rings were added to the trachea of the TB geometry and a crescent-shaped or D-shaped tracheal cross section was adapted. Both of these features are expected to influence deposition and are intended to improve the realism of the model. Crescent-shaped tracheal cross-sections arise due to pressure from the esophagus. This distortion may change depending on the position of the subject (supine, prone, standing) and may also be different during inhalation vs. exhalation. As a general approximation, one-quarter of the tracheal cross-section was assumed to be compressed into a flat profile, which is consistent with in-house medical scans. The cadaver measurements of Russo et al. (2008) were used to include the effects of the

cartilaginous rings on the tracheal geometry. Thirteen rings, spaced 2.98 mm apart, were included protruding into the trachea by a distance of 0.254 mm. A sinusoidal wave was used to approximate the effect of the ring impressions on the soft tissue. The thickness of the rings was 3.21 mm, except near the top of the trachea, where the thickness was 3.07 mm for two of the rings. This was done to allow the rings to fit without altering the geometry of the existing MT.

The elliptical MT model of Xi and Longest (2007b) was modified to fit both the MDI and DPI devices selected for this study. For the MDI, the entire actuator was modeled to better assess the mixing of inhaled air with the spray exiting the nozzle. Based on measurements, the nozzle through which the spray enters the actuator was included with a 0.5 mm diameter (Fig. 8.1a). For the DPI, inner surfaces of the inhalers from the point of aerosol formation to the inlet of the MT were included. These internal surfaces include the 3 mm jet through which the aerosol enters the mouthpiece, two 0.5 mm jets, and the inner surface of the mouthpiece (Fig. 8.1b). The MT geometry of Xi and Longest (2007b) is based on a mouth opening of 22 mm. The MDI mouthpiece has a top to bottom outer diameter of 16 mm, which was judged sufficiently close to the mouth opening of the current model. As a result, modification of the current MT oral cavity was not made and the inhaler was directly connected to the model. For the DPI, the mouthpiece has a leading edge height of 12 mm. To account for this more closed mouth position, the top and bottom profiles of the oral cavity were moved inward 5 mm. The inhaler was then connected to this reduced volume oral cavity. The pharynx and larynx regions of the MT model were not altered. The resulting MT

volumes for the MDI and DPI MT geometries were 57.7 and 55.0 cm^3, respectively.

Hollow Models of Upper MT-TB Geometries

For the *in-vitro* deposition experiments, hollow models of the upper MT-TB geometries with rings included were fabricated using solid modeling software (Gambit 2.6 and SolidWorks) and a rapid prototyping process. To improve comparisons between the *in-vitro* results and CFD predictions, and to better validate the CFD model, a sectioned upper MT-TB geometry was created. The four sections of the geometry are MT, trachea, and upper left and right lung bronchi.

Inhalers

In this study, aerosol deposition will be evaluated for two representative inhalers, both delivering the same corticosteroid, in a MT and upper TB model. For the MDI, the model inhaler considered is the Flovent HFA produced by GSK delivering fluticasone proprionate as a suspension in a HFA 134a formulation. The DPI model is the Flovent Diskus (GSK) delivering fluticasone proprionate as a powder aerosol. The computational models developed in this study can be applied to any MDI, DPI or Nebulizer. However, specific inhalers are required to effectively evaluate MT deposition and validate the model. An investigation of the initial aerosol size distribution was conducted in Dr. Hindle's lab. The size distribution of the drug aerosol emitted from the Flovent HFA MDI was determined using the next generation impactor (NGI) operated at a constant flow

rate of 37 L/min. The Flovent Diskus DPI was sampled directly into a NGI with a square wave inhalation profile and a flow rate of 75 L/min.

Inhalation Waveforms

The inhalation waveforms used by patients with different inhalers and even the same inhaler are highly variable (Byron et al. 2010; Delvadia et al. 2010; Marielle et al. 2003; Meijer et al. 1996; Persson et al. 1997). In this study, two representative waveforms were approximated for healthy subjects based on the existing data. Waveforms representative of "inhale slowly and deeply" (SD) and "inhale quickly and deeply" (QD) were developed from existing data (Byron et al. 2010; Delvadia et al. 2010; Marielle et al. 2003; Meijer et al. 1996; Persson et al. 1997). These SD and QD profiles are intended to represent correct usage of the Flovent MDI and Flovent Diskus DPI, respectively. Considering these two waveforms in both of the inhalers provides a measure of patient waveform variability and its effect on transport and deposition.

Common characteristics among studies reporting waveform characteristics with inhalers are a nearly linear acceleration to peak flow followed by a sinusoidal pattern during deceleration (Byron et al. 2010; Delvadia et al. 2010; Marielle et al. 2003; Meijer et al. 1996; Persson et al. 1997). Furthermore, the peak inhalation flow rate (PIFR) typically occurs during the first 1/6 to 1/4 of the inhalation period. Equations describing this waveform pattern and developed for this study are

$$Q(t) = \frac{PIFR}{T_{PIFR}} t \quad 0 \le t \le T_{PIFR} \tag{8.1}$$

$$Q(t) = PIFR\cos\left(\frac{2\pi(t - T_{PIFR})}{4\left(1 - TF_{PIFR}\right)T}\right) \tag{8.2}$$

$$\bar{Q} = \frac{1}{T}\int_0^T Q(t)dt \tag{8.3}$$

where all parameters are defined in Table 8.1. To describe the SD and QD waveforms, inhalation volume and mean inhalation flow rate need to be set. The remaining parameters are then derived from the waveform shape. In this study, deep inhalation is represented by a 3L inhaled volume. This value is consistent with the study of Broeders et al. (2003), who report an approximate 3L inhalation volume with the use of both an MDI and DPI (Diskus) for stable asthmatic and mild to moderate COPD patients. The mean inhalation flow rate was also a defined parameter to allow for comparisons between steady state and transient deposition results. A mean inhalation flow rate of 37 L/min was selected for the SD profile, as a typical value for MDI steady state testing. A mean inhalation flow rate of 75 L/min (which is approximately twice the SD value) was selected to represent QD inspiration. Based on observations from reported waveforms as described above, the time fractions to peak inhalation flow rate (TF_{PIFR}) for the SD and QD waveforms was 1/4 and 1/6, respectively. Equations to find the remaining inhalation parameters are shown below.

$$\frac{PIFR\left[L/\min\right]\times T_{PIFR}}{2\times 60} + \int_{T_{PIFR}}^{T} \frac{PIFR}{60}\cos\left(\frac{2\pi(t - T_{PIFR})}{4\left(1 - TF_{PIFR}\right)T}\right)dt = V\left[L\right] \tag{8.4}$$

$$T\left[s\right] = \frac{60V\left[L\right]}{\bar{Q}\left[L/\min\right]} \tag{8.5}$$

Results from solving these equations for the SD and QD parameters are reported in Table 8.2. The resulting PIFRs for the SD and QD profiles are 61.4 L/min and 122.2 L/min, respectively. The SD and QD waveforms are shown in Fig. 8.2. Considering the MDI, the typical recommended PIFR for correct usage is between 25 and 90 L/min (Broeders et al. 2003). Furthermore, Ross and Schultz (1996) showed that inhalation flow rate had little effect on MDI drug delivery. The PIFR of the MDI (i.e., 61.4 L/min) is approximately in the middle of the recommended range and therefore a representative approximation of correct usage. For the Diskus DPI, Broeders et al. (2003) observed a characteristic PIFR of approximately 120 L/min after training among 42 patients with stable asthma and mild to moderate COPD. Van der Palen (2003) observed an average PIFR of 118 L/min for Diskus among 50 patients that received medication for asthma and COPD. Byron et al. (2010) reported a PIFR of approximately 120 L/min for a single healthy subject with a Novolizer DPI, which has a similar resistance compared with the Diskus. As a result, the PIFR of the Diskus appears consistent with literature data for both healthy and asthmatic/COPD patients.

CFD Simulations

Based on Reynolds number conditions, laminar through fully turbulent flow is expected in the upper airway model. To resolve these multiple flow regimes, the low Reynolds number (LRN) k-ω model will be implemented based on its ability to accurately predict pressure drop, velocity profiles, and shear stress for transitional and turbulent flows on a transient basis (Ghalichi et al. 1998;

Wilcox 1998) as well as particle deposition profiles (Longest and Vinchurkar 2007b). The Reynolds-averaged equations governing the conservation of mass and momentum were previously reported by Longest et al. (2006). Simulations of thermal energy and water vapor transport, along with the laminar and turbulent governing equations, were previously described (Longest and Hindle 2010; Longest and Xi 2008). For the MDI simulations, the firing process induces significant spray momentum that affects the aerosol and surrounding flow field. The resulting transport conditions are locally supersonic near the nozzle and compressible. As a result, the individual species of air and water vapor were assumed to behave as ideal gases. For the DPI simulations, an incompressible flow field was assumed.

The Lagrangian transport equations governing particle motion in the upper airways were solved using Fluent 12. Our previous validation case studies have indicated that this CFD algorithm produces an effective solution for aerosol transport and deposition results provided that a number of user-defined enhancements and corrections are supplied. These user-defined supplements include (i) a correction for near-wall anisotropic turbulence (Longest et al. 2007), (ii) a correction for the Brownian motion routine (Longest and Xi 2007b), and (iii) a modification for near-wall interpolation of particle locations (Longest and Xi 2007b). In order to produce convergent deposition results for all particle sizes considered with the MDI inhaler, a total of 72000 particles were released over 0.2 seconds. For the DPI inhaler, a total of 36000 particles were released over 0.5 seconds. The experimentally determined initial droplet distributions were used in

the CFD simulations. Doubling the number of droplets considered had a negligible impact on both total and sectional deposition results.

Model Validation

CFD simulations of aerosol deposition for the MDI and DPI inhalers are compared to the in vitro experimental results in Fig. 8.3. The simulations were conducted to be as similar to the *in vitro* experiments as possible. For the MDI simulation, an airflow of 37 L/min was established through the actuator before the inhaler was fired with an aerosol generation time of 0.2 s. For the DPI simulation, a square inhalation waveform was implemented with a mean of 75 L/min. The aerosol was released over the course of the first 0.5 s, consistent with the experiments.

Results indicate that the CFD model predictions match the in vitro experiments to a high degree. Differences in the MT deposition between the model and experiments remain below 7%, which is very good considering the complexity of the system. Due to the presence of significant turbulence, deposition of multiple particle sizes is observed throughout the geometry.

The MDI inhaler demonstrates less MT deposition than the DPI. However, when the MDI actuator fraction is added with the MT loss, the amount of wasted dose is similar between the inhalers. The DPI delivers approximately 4 times more dose to the TB section under square waveform inhalation conditions. This increase in deposition is clearly beneficial for bronchodilators, but is undesirable for medicines targeted to the alveolar airways.

8.3 Results

Velocity Fields in the Upper MT-TB Model

Velocity fields in the MDI and DPI from the CFD simulations for SD and QD waveforms at selected times are displayed in Figs. 8.4-6. Midplane and cross-sectional slices of velocity magnitude and velocity vectors are shown. Times considered for each waveform are mean accelerating flow ($T_{a\text{-}mean}$), peak inspiratory flow (T_{PIFR}), and mean decelerating flow ($T_{d\text{-}mean}$), as shown in Fig. 8.2. Flow conditions from the MDI simulations for SD and QD at $T_{a\text{-}mean}$ are shown in Figs. 8.4a and c, respectively. The activation of the inhaler and resulting spray exiting the nozzle creates a significant source of momentum in the flow field. As a result, high velocity and turbulent flow is induced. Under QD conditions for the MDI, the momentum continues to increase and propagates quickly through the flow field, creating further flow disruption at $t=T_{PIFR}$ (Fig. 8.5c), while the momentum change has dispersed at $T_{d\text{-}mean}$ (Fig. 8.6c) due to the completion of the activation. Similarly for the SD conditions, momentum near the MT inlet has dispersed at $t=T_{PIFR}$ and $T_{d\text{-}mean}$ (Fig. 8.5a and 8.6a). For the DPI, significant flow disruption and a high velocity jet flow were observed in the region near the MT inlet (Fig. 8.4b and d). At $t= T_{PIFR}$, the jet velocity increases due to acceleration (Fig. 8.5b and d). At $t= T_{d\text{-}mean}$, the jet velocity decreases due to deceleration (Fig. 8.6b and d).

Transient MDI Drug Deposition in the Upper MT-TB Model

Figure 8.7 illustrates transient MDI simulation results for the SD and QD waveforms. The SD waveform is considered to be the correct usage for the MDI and has a mean flow rate of 37 L/min. In contrast, the QD waveform is considered incorrect use of the MDI with a mean flow rate of 75 L/min. Inhaler deposition is markedly reduced and TB deposition is increased for both transient waveforms compared with steady state conditions (Fig. 8.7 vs. Fig. 8.3). The correct usage of the MDI (SD waveform) results in approximately 10% lower MT deposition and 2% more TB deposition than with the QD inhalation. These differences are likely small compared with expected intersubject variability. Therefore, it is concluded that the MDI device is not largely sensitive to the transient inhalation waveform employed.

Transient DPI Drug Deposition in the Upper MT-TB Model

Transient SD and QD waveforms results for the DPI are illustrated in Fig. 8.8. For the DPI, QD inhalation is preferred and SD inhalation can be considered incorrect. As expected, the QD results are the most similar to the square inhalation waveform because both had a mean flow rate of 75 L/min. However, reducing the mean flow rate to 37 L/min with the SD waveform only reduced MT deposition by 2% and upper TB deposition by 1%. Compared with the MDI SD and QD cases, the DPI inhaler delivered less aerosol to the upper TB region. This is surprising because with the square inhalation waveform validation case (Fig. 8.3), the DPI delivered more drug dose to the TB airways. As a result, it appears

very important to consider the transient inhalation waveform when assessing aerosol deposition in the MT and upper TB airways, especially for MDI devices.

8.4 Discussion

In this study, a CFD model was developed to evaluate aerosol deposition for the MDI and DPI inhalers in a realistic MT and upper TB model. Variations in breathing profiles were considered using SD and QD conditions, based in part on common characteristics among the reported waveforms. The CFD results were then compared with *in vitro* results. Results of this study indicate that the CFD model predictions match the in vitro experiments to a high degree. The DPI delivers approximately 4 times more dose to the TB section under square waveform inhalation conditions compared with MDI delivery under steady state inhalation conditions. The CFD results also indicate that it is critical to consider transient inhalation effects when assessing aerosol deposition, especially for MDI devices.

This current study only considered transport and deposition in the upper airways. However, transport and deposition in the medium and small TB airways should be also evaluated to better understand differences in MDI and DPI delivery to the lung under correct and incorrect inhalation profiles.

In conclusion, this study has demonstrated that transient inhalation can significantly influence the transport and deposition of aerosol in the upper airways, especially for MDI devices. Future studies are needed to consider aerosol deposition in the lower airways under both steady and transient conditions.

Table 8.1. Parameters describing transient inhalation waveforms.

Parameter	Units	Description
PIFR	L/min	Peak inspiratory flow rate
Q(t)	L/min	Transient inspiratory flow rate
$\bar{Q}$	L/min	Mean inhalation flow rate
T	s	Period of inhalation
$T_{a\text{-}mean}$	s	Time to mean inhalation flow rate during acceleration
T_{PIFR}	s	Time to peak inhalation flow rate
$T_{d\text{-}mean}$	s	Time to mean inhalation flow rate during deceleration
TF_{PIFR}	--	Time fraction of peak inspiratory flow rate to total inhalation period (T)
V	L	Total volume inhaled

Table 8.2. Waveform parameters for the QD and SD profiles.

Parameters	QD Profile	SD Profile
PIFR [L/min]	122.2	61.4
$\bar{Q}$ [L/min]	75	37
T [s]	2.40	4.86
$T_{a\text{-}mean}$ [s]	0.25	0.73
T_{PIFR} [s]	0.4	1.22
$T_{d\text{-}mean}$ [s]	1.56	3.38
TF_{PIFR}	1/6	1/4
V [L]	3	3

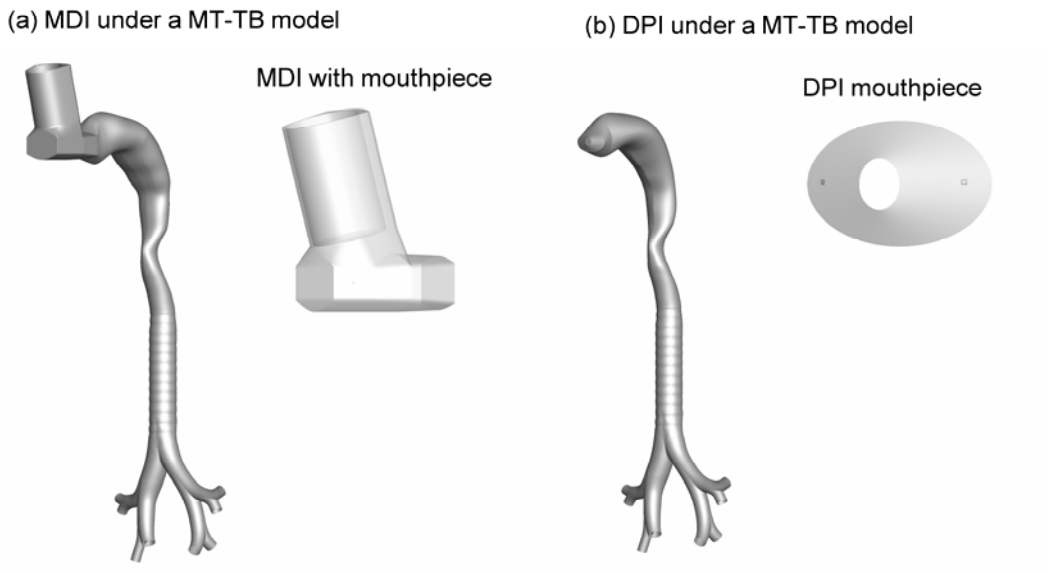

Figure 8.1. Upper MT-TB geometries for testing drug aerosol deposition connected to the (**a**) Flovent MDI and (**b**) Flovent Diskus DPI. The MDI model includes a narrow air passage between the actuator body and canister and a 0.5 mm nozzle for the introduction of the propellant and particles/droplets. The DPI model includes a 5 mm jet for the introduction of the drug powder and airflow, two 0.5 mm jets, which are consistent with the Flovent Diskus Inhaler, as well as the inner surface of the mouthpiece.

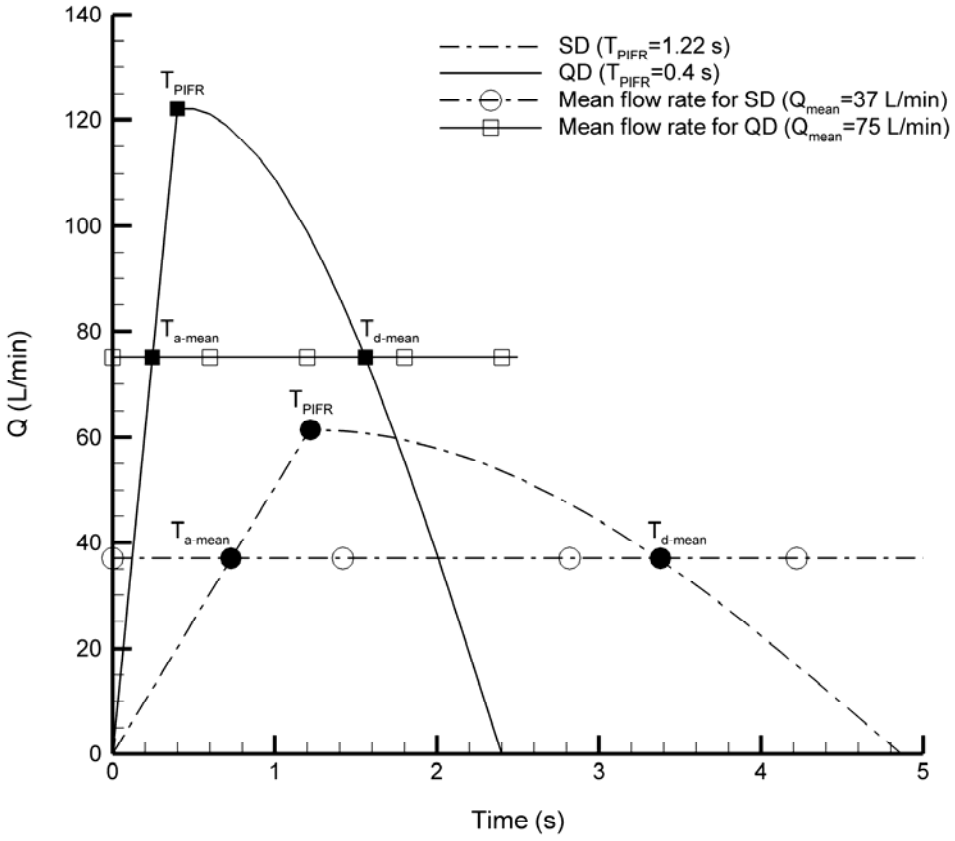

Figure 8.2. Inhalation waveforms for SD and QD waveforms.

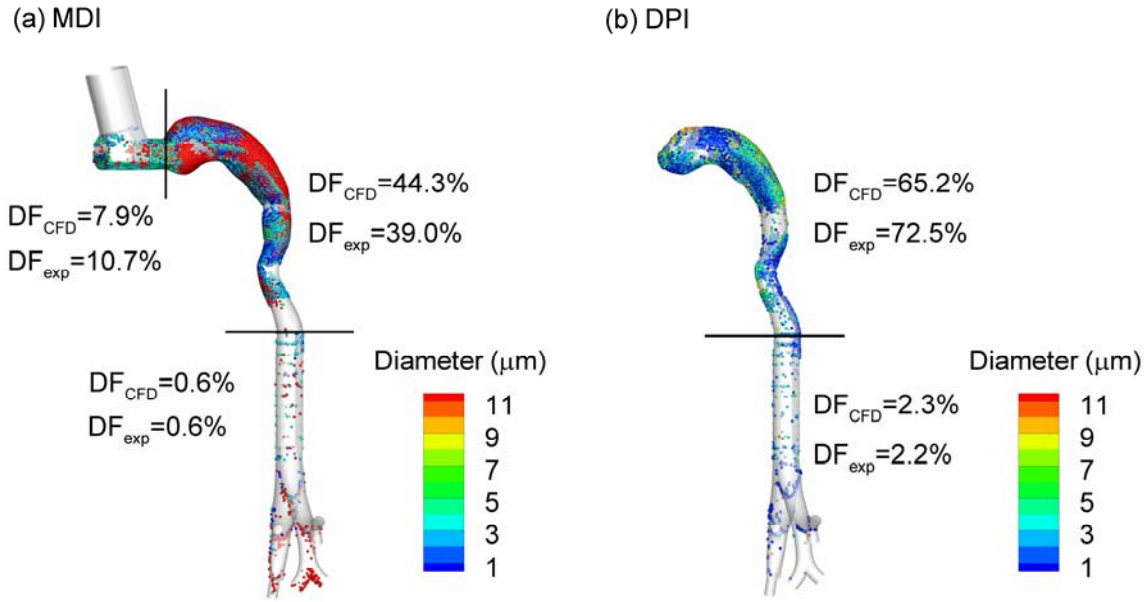

Figure 8.3. Comparison of experimental (exp) and simulated deposition results with steady state and square waveform inhalation flow conditions for the (**a**) MDI at 37 L/min and (**b**) DPI at 75 L/min. The CFD predictions are shown to match the *in vitro* results to a high degree.

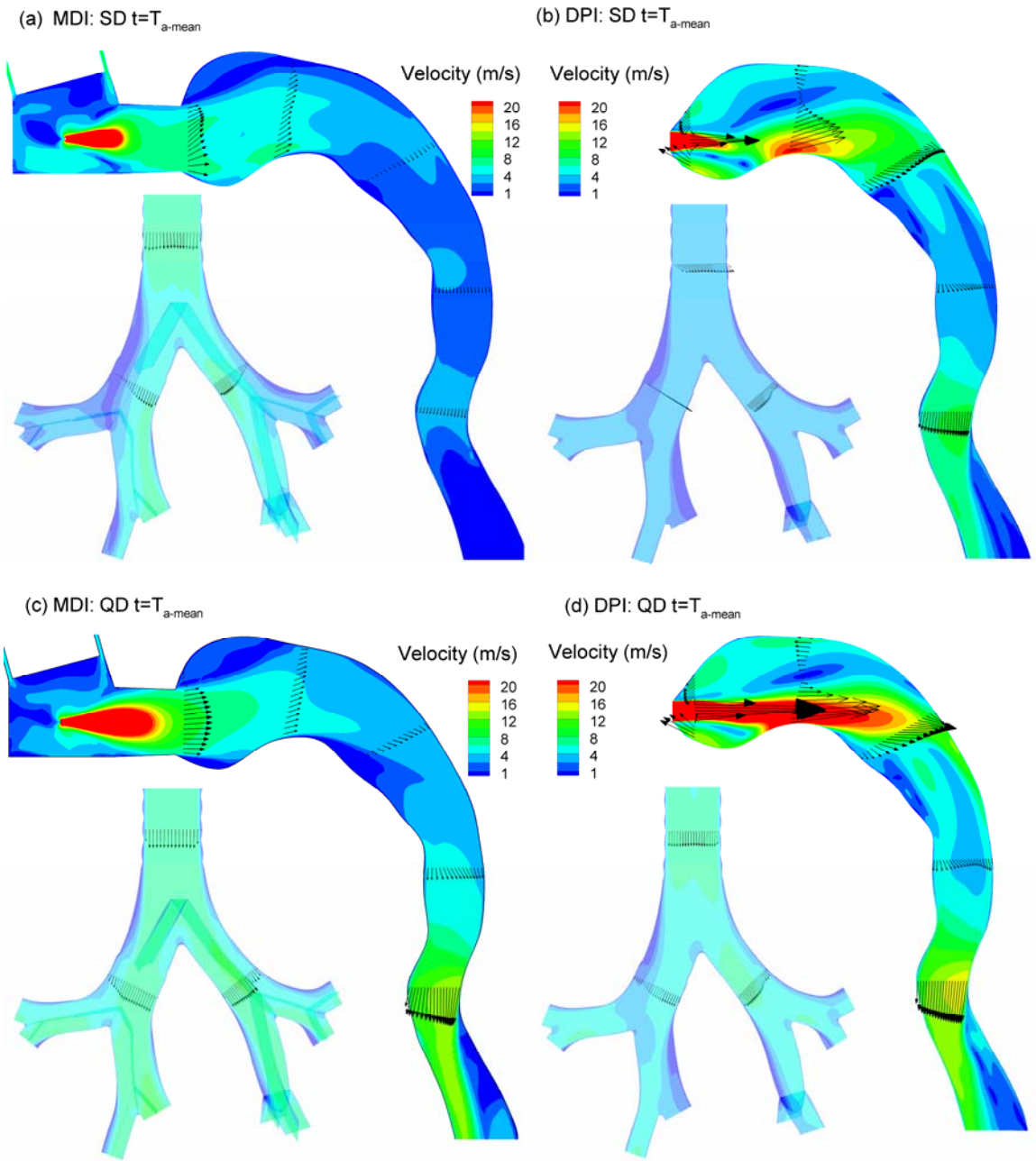

Figure 8.4. Velocity vectors and contours for SD and QD waveforms at t= $T_{a\text{-}mean}$.

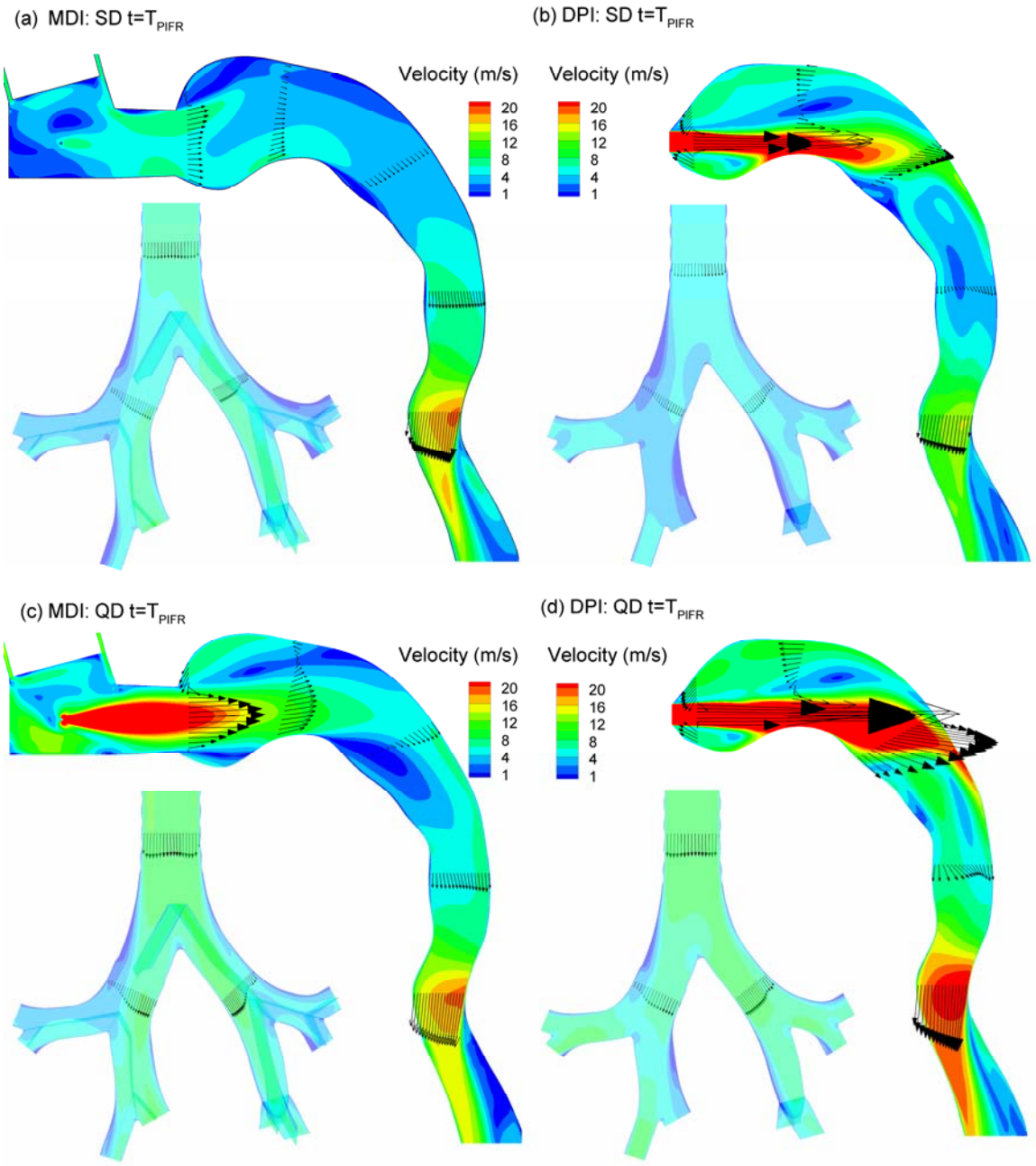

Figure 8.5. Velocity vectors and contours for SD and QD waveforms at $t=T_{PIFR}$.

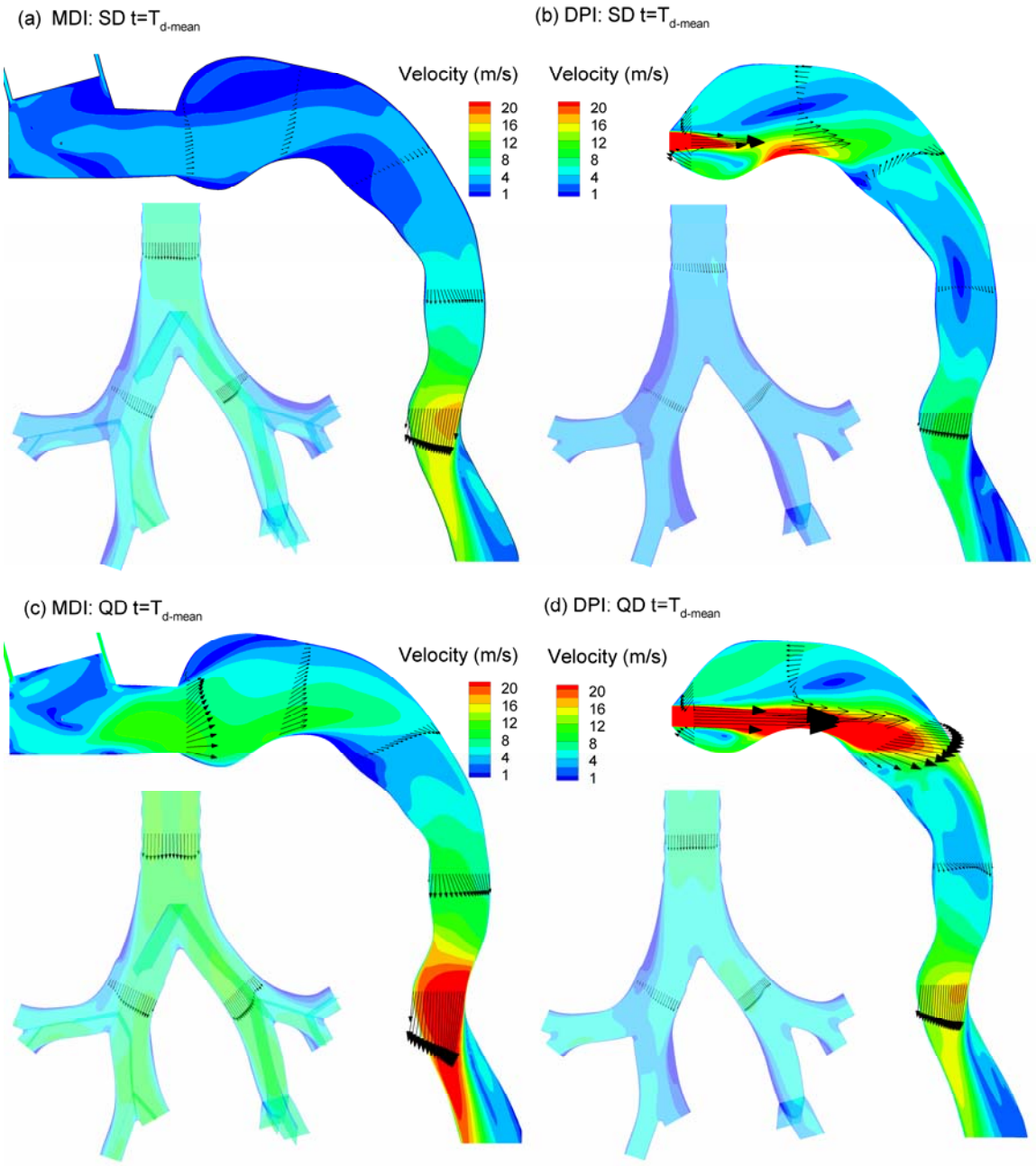

Figure 8.6. Velocity vectors and contours for SD and QD waveforms at t= $T_{d\text{-}mean}$.

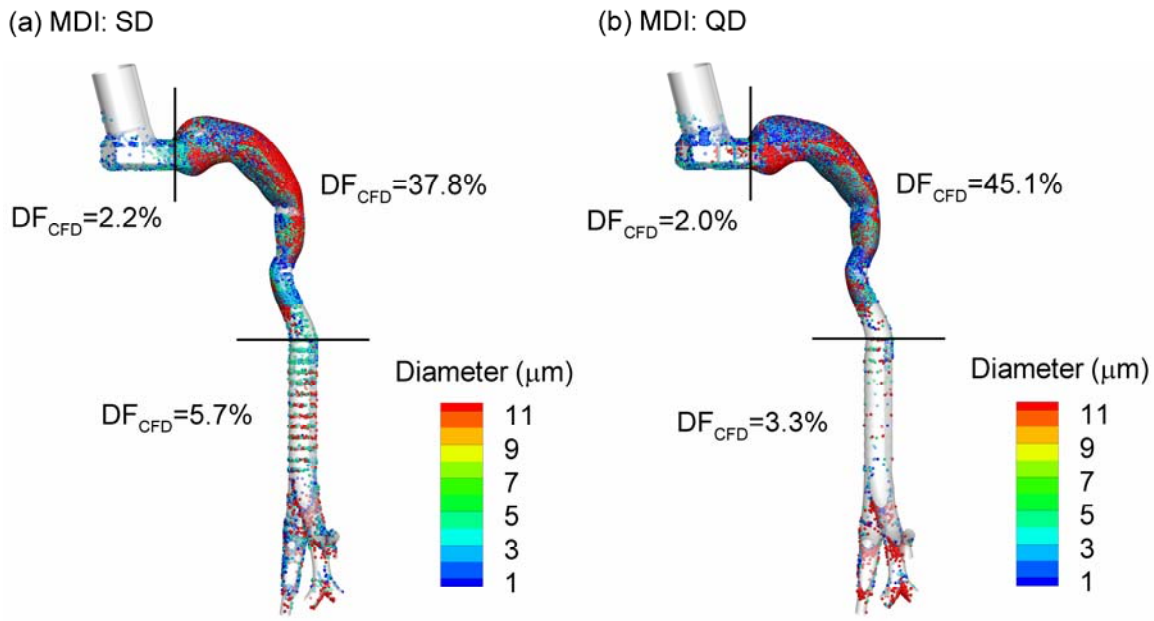

Figure 8.7. CFD predicted results of MDI deposition in the MT-TB model for (**a**) SD and (**b**) QD inhalation waveforms. Deposition results are similar between the two inhalations. However, significant differences are observed between the transient inhalation, shown here, and steady state conditions shown in Figure 8.3.

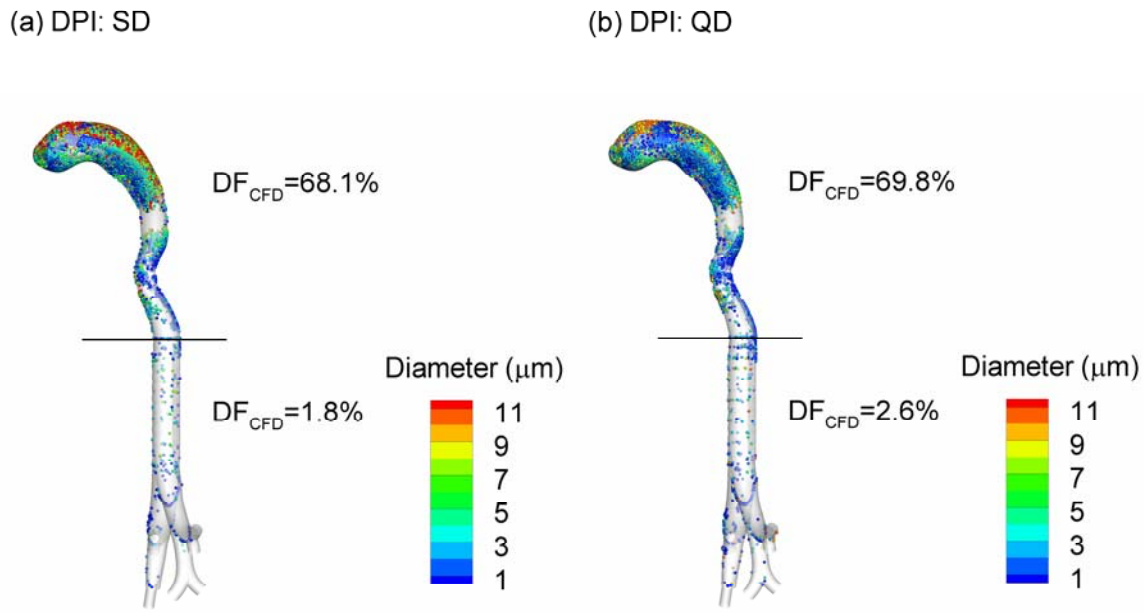

Figure 8.8. CFD predicted results of DPI deposition in the MT-TB model for (**a**) SD and (**b**) QD inhalation waveforms. Deposition results are similar between the two inhalations. Furthermore, deposition appears similar between the transient inhalation, shown here, and square wave conditions shown in Figure 8.3.

Chapter 9. Development of a Stochastic Individual Path Model for Assessing Pharmaceutical Aerosol Deposition: Effects of Transient Inhalation Waveform and Sampling the Tracheobronchial Airways

9.1 Introduction

In Chapter 8 the deposition of pharmaceutical aerosols from metered dose inhalers (MDIs) and dry powder inhalers (DPIs) was reported in a realistic mouth-throat (MT) and upper tracheobronchial (TB) model extending to the third respiratory bifurcation (B3). However, conditions beyond B3, where deposition is expected to be the highest, were not considered. Lin et al. (2009) reported a coupled 3-D and 1-D lung transport model that mimicked the entire TB region on a patient specific basis. However,1-D models do not provide information about aerosol distributions at the level of individual bifurcations. Koblinger and Hofmann (1990) introduced the idea of a Monte Carlo lung simulation approach in which paths down the airway tree were generated at random and used 1-D algebraic predictions of lung deposition. Depositions within these "individual paths" were used to build a representation of deposition within the lung. This approach is applied in this study for 3-D CFD modeling and termed stochastic individual path (SIP) modeling.

The objective of this study is to evaluate the effects of steady state vs. a transient waveform on transport and deposition of pharmaceutical aerosols from a DPI within the right lower lung lobe using the SIP modeling approach. Deposition variability among different SIP paths in the right lower lung lobe will also be assessed. The transient QD waveform, consistent with patient instructions

to "inhale quickly and deeply" (previously developed in Chapter 8) is implimented. The transient QD results will then be compared with steady state (SS) conditions to determine if steady state approximations are adequate, or if more detailed transient simulations are needed. Deposition within multiple SIP paths is also assessed.

9.2 Methods

DPI MT-TB SIP Geometry

In this study, deposition in the lower TB airways will be evaluated for the DPI. For this inhaler, inner surfaces of the device from the point of aerosol formation to the inlet of the MT were included. These internal surfaces include the 3 mm jet through which the aerosol enters the mouthpiece, two 0.5 mm jets, and the inner surface of the mouthpiece (Fig. 9.1). The upper MT-TB geometry previously developed in the Chapter 8 was used. Beyond the third bifurcation, three individual paths of the right lower lung lobe are considered in which one branch of each bifurcation is continued and one is not (Fig. 9.1). This approach allows for upstream effects of the flow field and drug aerosol profile to be fully integrated in a highly efficient manner. Furthermore, use of the individual path model based on PRB units allows for the application of a hexahedral mesh, which improves solution accuracy, and an adequate number of computational cells to fully resolve the flow domain (Longest and Vinchurkar 2007a; Vinchurkar and Longest 2008). Bifurcations within the model are constructed as PRB units with the dimensions of Yeh and Schum (1980), scaled to an adult FRC of 3.5 L. Based on available data, the bifurcations in the individual path model are symmetric and

include a symmetric outflow assumption. At each bifurcation, continuation of the left or right branch is selected at random. However, if the selection leads out of the general region of the particular lung lobe, the other branch is selected. Consecutive branches are rotated at 90^{o} to approximate physiological conditions. This individual path model is not intended to exactly mimic a specific connection of bronchi in a patient specific model. Instead, it is intended to provide an effective 3-D representation of transport and deposition in the medium and small TB airways. Branch 15 is assumed to end with the terminal bronchioles, based on existing anatomical data (Weibel 1963; Yeh and Schum 1980).

Stochastic Individual Path (SIP) Modeling

Koblinger and Hofmann (1990) proposed a Monte Carlo approach to simulating deposition throughout the airways using a 1-D algebraic model. In this method, an individual path is selected at random down the TB tree. Deposition is then calculated in this simulated path using algebraic correlations. Additional paths and deposition fractions are then calculated and an average deposition fraction is estimated on a regional and local basis. Once a sufficient number of paths have been simulated, the deposition fraction converges. In this study, paths are selected to remain in the general region of the right lower lung-lobe, based on the lobar position taken from CT scans. Three paths are shown in Fig. 9.1 and considered to provide convergent local and regional deposition fractions.

CFD Simulations

The low-Reynolds-number (LRN) $k-\omega$ model of Wilcox (1998) was selected for simulating flow regimes in the MT-TB SIP model because it has been shown to provide an accurate and numerically efficient solution for laminar, transitional and turbulent flows. Furthermore, this model was found to accurately predict aerosol transport and deposition in the airway models (Longest and Hindle 2009a; Longest et al. 2009). The Lagrangian transport equations interconnected with user defined functions were employed to calculate deposition, near-wall anisotropic turbulence correction (Longest et al. 2007), near-wall particle interpolation (Longest and Xi 2007b), and Brownian motion (Longest and Xi 2007b). In order to produce convergent deposition results for all particle sizes considered and the DPI inhaler, total of 36000 particles were released over 0.5 seconds. Experimentally determined initial droplet distributions were used in the CFD simulations. Doubling the number of droplets considered had a negligible impact on both total and sectional deposition results.

Model Validation

CFD simulations of aerosol deposition for the DPI inhaler in the upper airways are compared to the *in vitro* experimental results in Fig. 9.2. These results were presented in Chapter 8, but are repeated here for completeness and discussed in more detail. The simulations were conducted to be as similar to the *in vitro* experiments as possible. For the DPI simulation, a square inhalation waveform was implemented with a mean flow rate of 75 L/min. The aerosol was

released over the course of the first 0.5 s, consistent with experimental observations. Results indicate that the CFD model predictions match the *in vitro* experiments to a high degree. Differences in deposition fraction (DF) values in the MT between the model and experiments remain below 7%, which is very good considering the complexity of the system. Due to the presence of significant turbulence, deposition of multiple particle sizes is observed throughout the geometry. It was necessary to simulate the square waveform used in the experiments to match the in vitro deposition data. Use of steady state conditions over-predicted the experimental deposition values by an unacceptable amount.

Outlet Distributions and Flow Profiles for use as Inputs in SIP models

The geometry consists of the MT region, upper TB airways (Trachea-B3) and the middle/lower TB airways (B4-B15). Stochastic individual path (SIP) modeling will be employed to simulate DPI deposition in the middle and lower TB airways (B4-B15). A sufficient number of paths will be considered in each lobe to provide convergent local and regional deposition fractions. Therefore, an interpolation routine is needed to reduce computing time. Specifically, flow and particle outlet conditions from the B3 outlet were used as inlet conditions for the SIP model. The necessary interpolation modules have been developed and are proven effective in Fig. 9.3. Specifically, the algorithm for the flow field interpolation is the following:

1. Read data from each face in the outlet boundary zone.

2. Store and write flow variables at each face to a data file at the end of each time step.

3. According to the coordinates, allocate these values to the faces in the inlet boundary zone.

Note that

1. Face (grid) size in the inlet boundary zone must be same as the previous outlet boundary zone.

2. Time step size and number of time steps in the current simulation must be same as the previous simulation.

The algorithm for the particle interpolation is the following:

1. Store and write particle data from the outlet boundary zone.

2. Read and assign these data onto the inlet boundary zone.

9.3 Results

DPI Drug Deposition in the MT and Upper TB Airways

Deposition results for the steady state and transient QD waveforms and the DPI are illustrated in Fig. 9.4. It is observed that deposition fraction (DF) values in the upper airways for the QD conditions are significantly different from steady state conditions. Deposition fraction values are approximately 25% (relative difference) less in the MT region and approximately 100% (relative difference) higher in the upper TB airways for the QD conditions compared with steady state conditions. As a result, it appears very important to consider the transient

inhalation waveform when assessing deposition values in the upper airways, as observed in Chapter 8.

DPI Drug Deposition in the Individual Paths of the Right Lower Lung Lobe

Deposition locations of polydisperse aerosols in the lower TB airways are illustrated for three SIPs with SS and QD conditions in Fig. 9.5. The aerosols are colored based on their size at time of deposition. Deposition efficiencies were calculated for each bifurcation and then combined (e.g., Eq. (6.3)) to represent the total deposition efficiencies (DE) for the sections reported along the three individual paths. It is observed that DE values in both the B4-B7 and B8-B15 sections are slightly higher under QD conditions than the values under SS conditions. However, the maximum total difference was less than 2% for all cases considered. Furthermore, large size particles (> 9 μm) deposited in B4-B7 under QD conditions were more densely populated than under SS conditions. This is likely due to higher flow rates associated with the QD waveform compared with the SS case.

Fig. 9.6 compares the mean deposition efficiencies of polydisperse aerosols in the trachea-B3, B4-B7, B8-B15, and total TB airways between SS and QD conditions. The mean values were computed across the three SIP models considered and the error bars in the figure represent standard deviations. The predictions under SS conditions match the QD results well. The percentage differences in deposition efficiency between SS and QD conditions in the Trachea-B3, B4-B7, and B8-B15 are 10%, 8%, and 3%, respectively. To calculate

the total DE of the TB region from the CFD predictions, the deposition efficiencies of each bifurcation were combined from B1-B15 (e.g., Eq. (6.3)). The relative difference in the total DE between SS and QD conditions is approximately 8%.

The mean deposition efficiencies of polydisperse aerosols are illustrated in Fig. 9.7 for each bifurcation of 3 SIPs between SS and QD conditions. The SS results produced an excellent agreement with the QD results, especially between B9 and B15. It is observed that deposition efficiency increases through B6, and decreases between B6 and B15. A complete description of deposition efficiencies for SS and QD conditions are reported for each bifurcation in Tables 9.1 and 9.2.

9.4 Discussion

In this study, the effects of transient vs. steady state flow fields on the transport and deposition of pharmaceutical aerosols from a DPI were evaluated within the right lower lung lobe using the SIP modeling approach. The transient results were compared with steady state (SS) conditions and variability in the results across three SIP models was assessed. Results indicate that steady state approximations are adequate (within a total difference of 2%) to predict deposition efficiencies in the TB airways. Therefore, a steady state inhalation approximation can be used to evaluate deposition in the SIP model. Furthermore, deposition estimates changed very little between the three SIP models considered with maximum total differences of approximately 2% for the regions considered. Therefore, it also seems reasonable that deposition within a lobe lung can be

estimated using a single SIP geometry. However, this finding only holds true when considering averaged regions such as B4-B7, B8-B15 and the total TB airways in a single lobe, as assessed in this study.

The current study only considered transport and deposition in the right lower lung lobe. However, transport and deposition values in the right upper, right middle, left upper, and left lower lung lobes are needed to better predict total TB, alveolar regional, and whole lung deposition.

In conclusion, this study has demonstrated that steady state inhalation can be used to predict deposition efficiencies in the TB airways using SIP model and that a single SIP model can be used to assess deposition within a single lobe. Future studies are needed to generate SIP models in each lung lobe.

Table 9.1. Deposition efficiency under QD conditions for 3 SIP models.

QD	SIP 1 (%)	SIP 2 (%)	SIP 3 (%)	Mean (%)	SD (%)
B4	2.78	2.64	1.93	2.45	0.37
B5	3.42	3.06	3.06	3.18	0.17
B6	4.01	3.48	3.06	3.52	0.39
B7	3.63	3.23	2.73	3.20	0.37
B8	2.18	3.1	2.6	2.63	0.38
B9	2.05	2.72	1.59	2.12	0.46
B10	1.48	1.34	1.47	1.43	0.06
B11	1.39	1.25	1.21	1.28	0.08
B12	1.34	1.07	0.95	1.12	0.16
B13	0.94	0.72	0.74	0.80	0.01
B14	0.81	0.72	0.61	0.71	0.08
B15	0.63	0.54	0.44	0.54	0.08

Table 9.2. Deposition efficiency under steady state (SS) conditions for 3 SIP models.

SS	SIP 1 (%)	SIP 2 (%)	SIP 3 (%)	Mean (%)	SD (%)
B4	2.30	1.79	1.73	1.94	0.26
B5	3.16	2.91	2.82	2.96	0.14
B6	3.65	3.40	2.94	3.33	0.29
B7	3.16	3.15	2.58	2.96	0.27
B8	2.05	2.66	2.34	2.35	0.25
B9	1.92	2.66	1.25	1.94	0.58
B10	1.42	1.29	1.12	1.28	0.12
B11	1.29	1.16	1.00	1.15	0.12
B12	1.16	1.03	0.87	1.02	0.12
B13	0.91	0.70	0.63	0.75	0.12
B14	0.78	0.65	0.50	0.64	0.11
B15	0.52	0.52	0.38	0.47	0.07

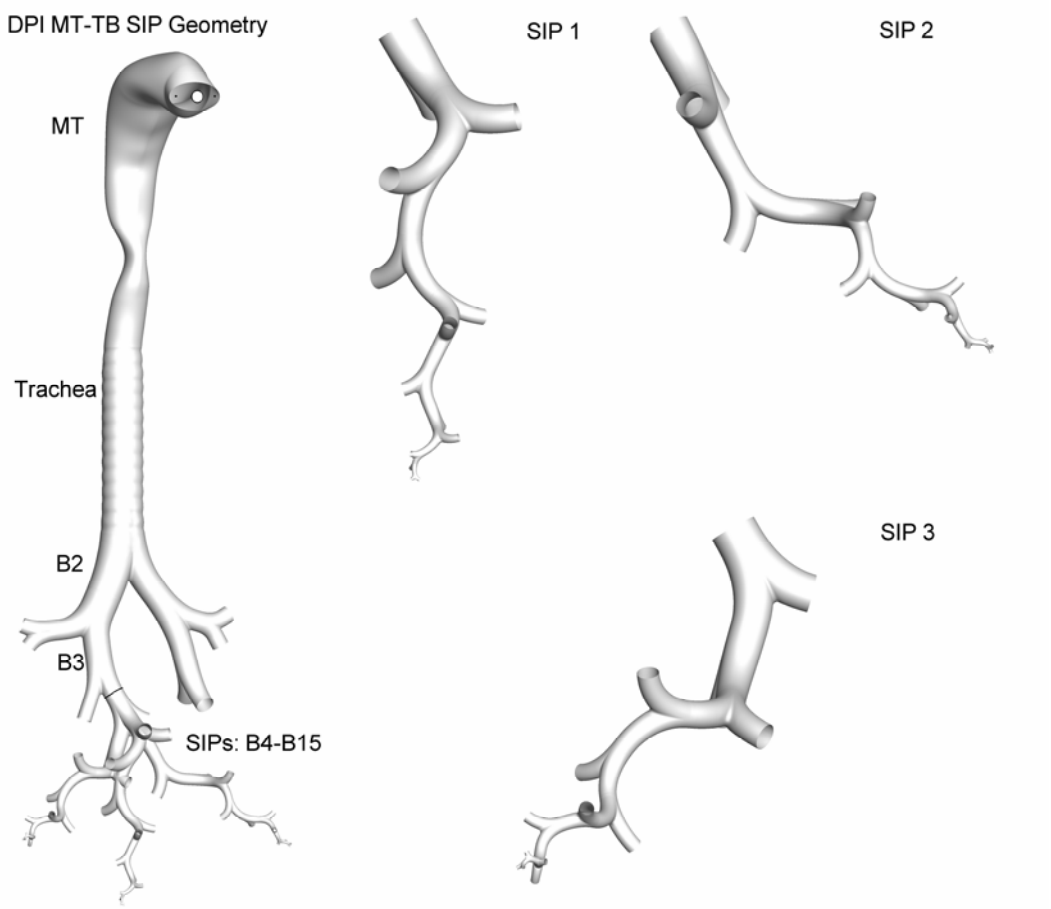

Figure 9.1. MT-TB SIP geometries for testing drug aerosol deposition from a Flovent Diskus DPI.

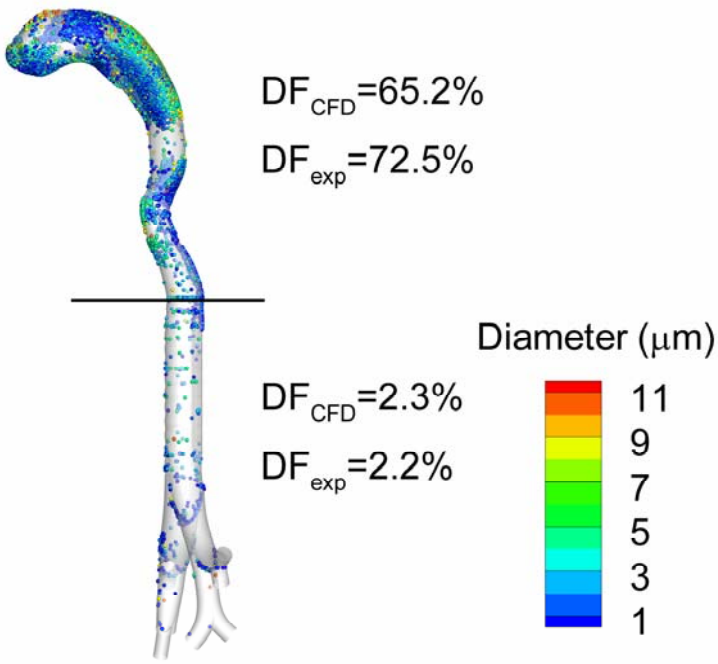

Figure 9.2. Comparison of *in vitro* and simulated deposition results with square waveform inhalation flow conditions for the DPI at 75 L/min. The CFD predictions are shown to match the *in vitro* results to a high degree.

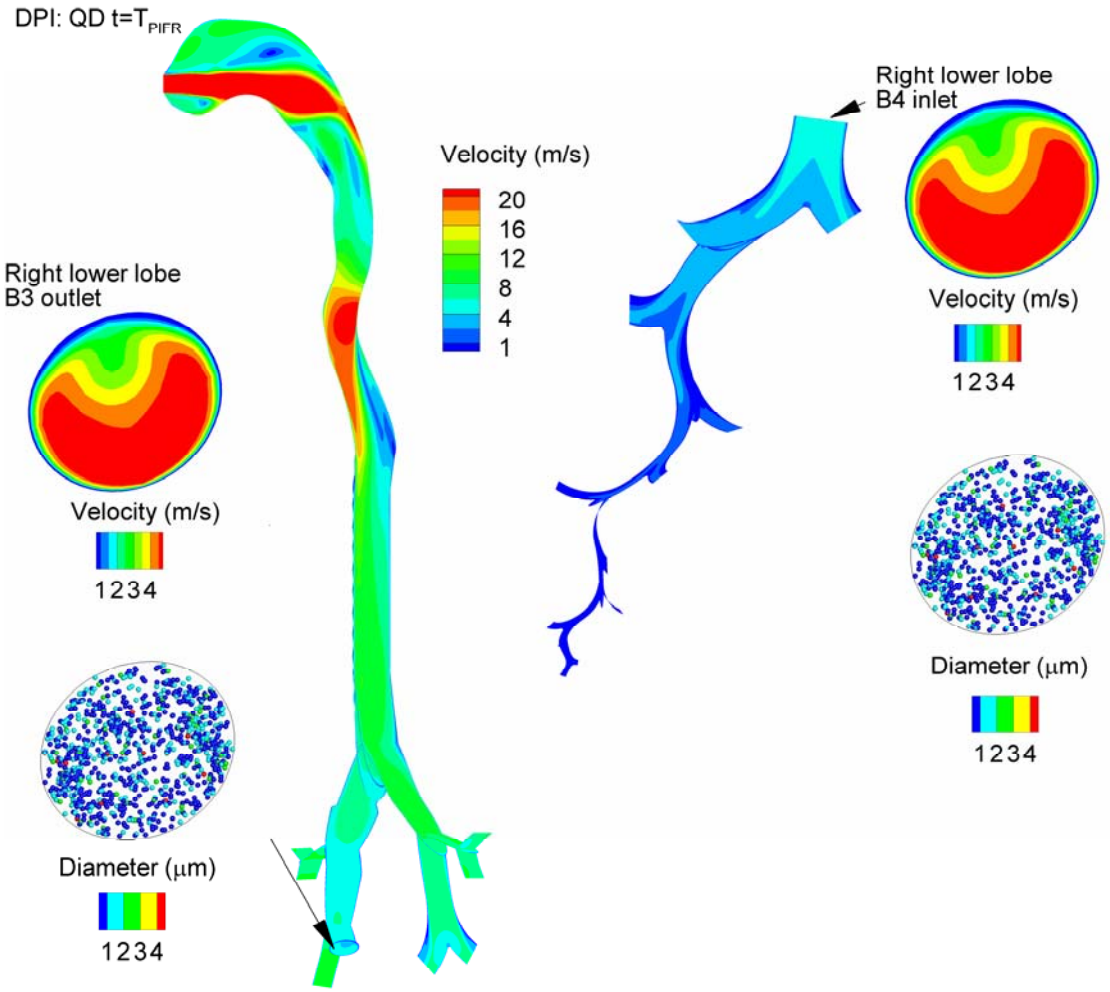

Figure 9.3. Stochastic individual path (SIP) model extending from the end of the MT-TB geometry into the right lower lung. The arrow indicates the site of velocity field and particle profile interpolation between the upper airway model and SIP geometry.

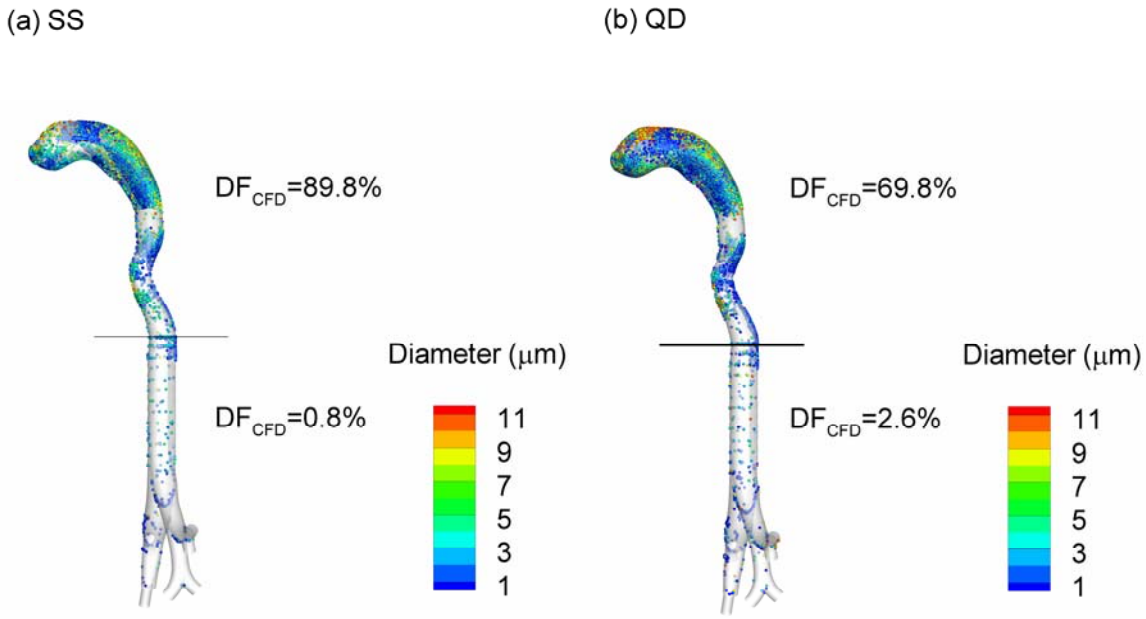

Figure 9.4. CFD predicted results of DPI deposition in the upper MT-TB model for (**a**) SS and (**b**) QD inhalation waveforms.

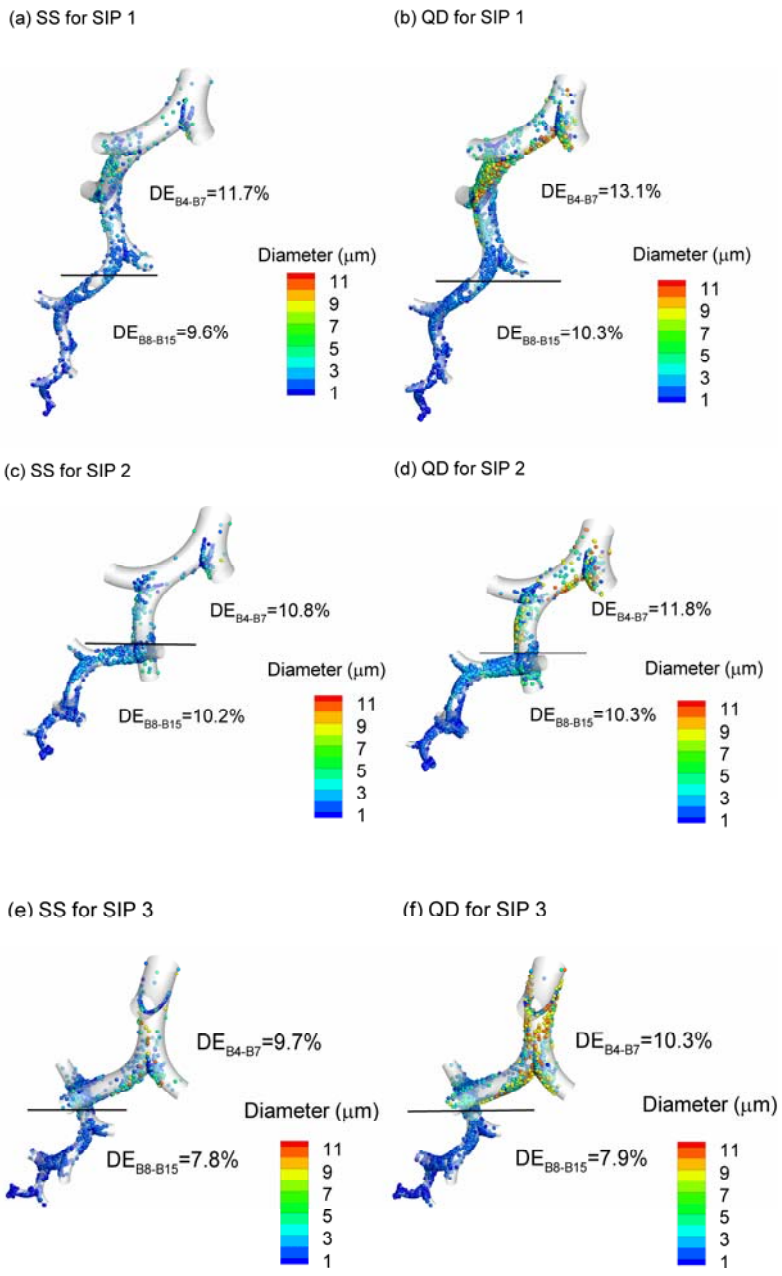

Figure 9.5. Particle deposition locations and regional deposition efficiencies (DE) of drug mass for (**a**) SS for SIP 1, (**b**) QD for SIP 1, (**c**) SS for SIP 2, (**d**) QD for SIP 2, (**e**) SS for SIP 3, and (**f**) QD for SIP 3.

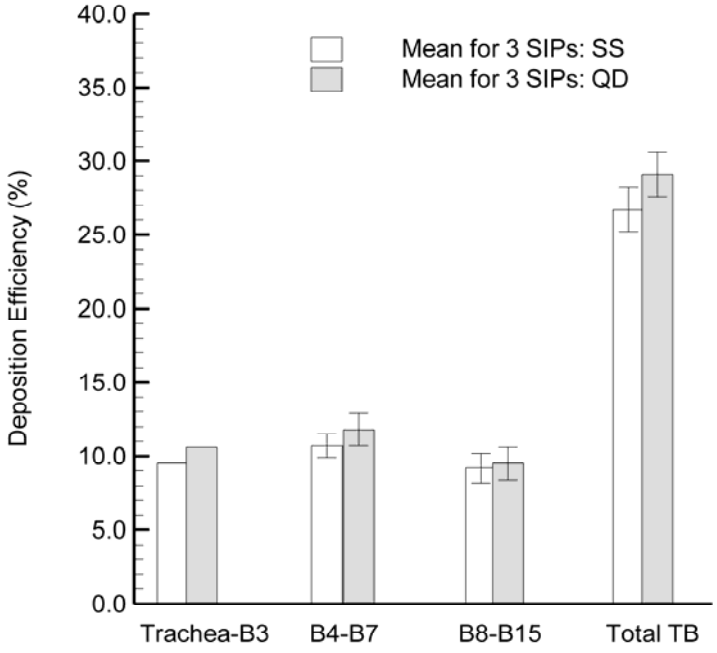

Figure 9.6. Comparison of steady state and transient deposition efficiencies of drug mass within specific regions. The error bars denote +/- one standard deviation.

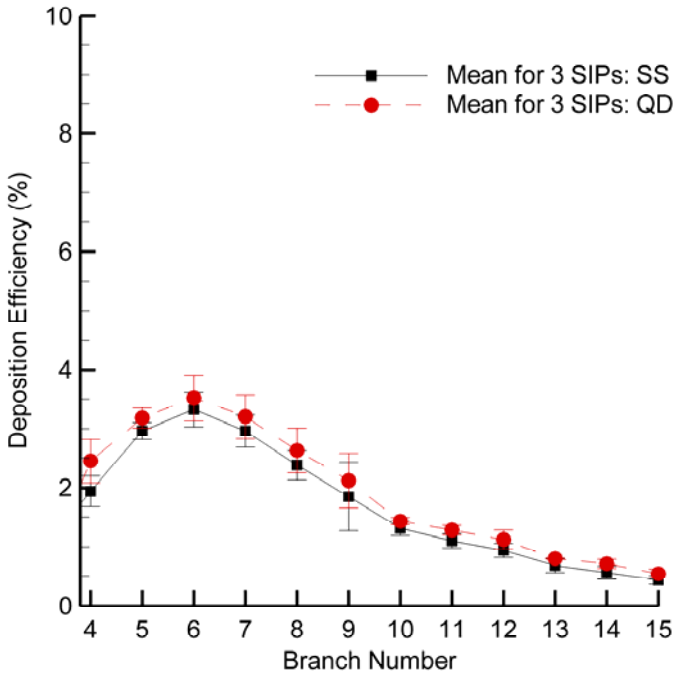

Figure 9.7 Comparison of steady state and QD deposition efficiencies of drug mass in each bifurcation of 3 SIPs. Symbols represent mean values and the error bars denote +/- one standard deviation.

Chapter 10. Conclusions and Future Work

The three objectives stated in Chapter 1 have been achieved in this dissertation. In conclusion: (1.1) a CFD model was developed to predict the transient absorption of inhaled vapors into a multilayer mucus-tissue-blood (MTB) system; (1.2) a transient CFD boundary condition in a multilayer air-mucus-tissue-blood (AMTB) system was developed in a nasal-laryngeal airway model; (1.3) effects of both transient inhalation and transient absorption on regional and local uptake in a representative upper airway model were evaluated; (2.1) enhanced condensational growth (ECG) for respiratory drug delivery was evaluated for models of the mouth throat (MT) and tracheobronchial (TB) region; (2.2) effects of transient inhalation waveforms on the ECG process in the upper TB airways were considered; (3.1) transport and deposition of pharmaceutical polydisperse aerosols from inhalers in upper airways were evaluated; (3.2) transport and deposition of pharmaceutical polydisperse aerosols from inhalers throughout the TB airways were evaluated using a stochastic individual path (SIP) modeling approach. Results of these studies and suggested topics for future analyses are summarized below.

10.1 Transient Absorption of Inhaled Vapors.

Objective 1.1: Considering transient absorption of inhaled vapors into a multilayer mucus-tissue-blood (MTB) system, three models of the wall were evaluated based on dimensions for the ET_2, BB, and bb regions. Results indicated

that transient absorption can significantly influence the transport and uptake of vapors in the walls of the conducting airways. Objective 1.2: In order to investigate transport and absorption of inhaled vapors over time into a multilayer air-mucus-tissue-blood (AMTB) system in a nasal-laryngeal airway model, a transient CFD boundary condition was developed. Results indicated that absorption was highly time dependent over the timescale of one inhalation cycle. Objective 1.3: Evaluating the effects of both transient inhalation and transient absorption on regional and local uptake in a model upper airway geometry, the transient CFD boundary condition was employed for CFD simulations of gas phase transport and mass transfer. A new dosimetry program TAOCS 1.0 was used in conjunction with a CFD model to apply and evaluate both steady state and transient wall absorption conditions. Results indicated that the implementation of a transient flux boundary condition appears critical to predict total and local deposition characteristics for even highly soluble compounds.

10.2 The Concept of Enhanced Condensational Growth.

Objective 2.1: Using both control and ECG delivery cases, the effectiveness for respiratory drug delivery in a realistic mouth-throat (MT) and tracheobronchial (TB) single path model was evaluated. Results indicated that ECG is an effective method to virtually eliminate MT depositional losses, and the associated intersubject variability, while providing for high TB deposition and near full lung retention of the aerosol. Objective 2.2: Considering the effects of transient inhalation waveforms on the ECG process in the upper TB airways, CFD

methods were employed to evaluate aerosol deposition. Results indicated that the ECG delivery approach under transient inhalation conditions increased aerosol deposition in the TB airways by only a small amount, as compared with steady state conditions.

10.3 Local and Regional Deposition of Pharmaceutical Aerosols.

Objective 3.1: The effect of transient waveforms and interactions at the patient-device interface on the transport and deposition of pharmaceutical polydisperse aerosols from inhalers in upper airways was considered. Results indicated that the CFD model predictions matched the in vitro experiments to a high degree. The DPI delivers approximately 4 times more dose to the TB section under square waveform inhalation conditions compared with MDI delivery under steady state inhalation conditions. The CFD results also indicate that it is critical to consider transient inhalation effects when assessing aerosol deposition, especially for MDI devices. Objective 3.2: The stochastic individual path (SIP) modeling approach was implemented to evaluate the transport and deposition of pharmaceutical polydisperse aerosols from inhalers in the lower airways. Results indicated that steady state inhalation can be used to predict deposition efficiencies in the TB airways.

List of References

Aharonson, E. F., Menkes, H., Gurtner, G., Swift, D. L., and Proctor, D. F. (1974) Effects of respiratory airflow rate on removal of soluble vapors by the nose. *Journal of Applied Physiology.* 37, 654-657.

Anderson, J. C., Babb, A. L., and Hlastala, M. P. (2003) Modeling soluble gas exchange in the airways and alveoli. *Annals of Biomedical Engineering.* 31, 1402-1422.

Asgharian, B., Hofmann, W., and Bergmann, R. (2001) Particle deposition in a multiple-path model of the human lung. *Aerosol Science and Technology.* 34, 332-339.

Asgharian, B., and Price, O. T. (2006) Airflow distribution in the human lung and its influence on particle deposition. *Inhalation Toxicology.* 18, 795-801.

Asgharian, B., Prince, O. T., and Hofmann, W. (2006) Prediction of particle deposition in the human lung using realistic models of lung ventilation. *Aerosol Sci.* 37, 1209-1221.

ATSDR, Agency for Toxic Substances and Disease Registry. (2007a) Toxicological Profile for Acetaldehyde (Update). Atlanta, GA: U.S. Department of Public Health and Human Services, Public Health Service.

ATSDR, Agency for Toxic Substances and Disease Registry. (2007b) Toxicological Profile for Benzene (Update). Atlanta, GA: U.S. Department of Public Health and Human Services, Public Health Service.

Balashazy, I., Hofmann, W., and Heistracher, T. (2003) Local particle deposition patterns may play a key role in the development of lung cancer. *Journal of Applied Physiology.* 94, 1719-1725.

Bird, R. B., Steward, W. E., and Lightfoot, E. N. (1960) *Transport Phenomena*, John Wiley & Sons, New York.

Brent, R. (1973) *Algorithms for Minimization and Without Derivatives*, Prentice-Hall.

Broday, D. M., and Georgopoulous, G. (2001) Growth and deposition of hygroscopic particulate matter in the human lung. *Aerosol Science and Technology.* 34, 144-159.

Broeders, M. E. A. C., Molema, J., Hop, W. C. J., and Folgering, H. T. M. (2003) Inhalation profiels in asthmatics and COPD patients: Reproducibility and effect of instruction. *Journal of Aerosol Medicine.* 16(2), 131-141.

Byron, P. R., Delvadia, R. R., Longest, P. W., and Hindle, M. (2010) Stepping into the trachea with realstic physical models: uncertainties in regional drug deposition from powder inhalers. *Respiratory Drug Delivery.* 1, 215-224.

Chan, T. L., and Lippmann, M. (1980) Experimental measurements and emperical modeling of the regional deposition of inhaled particles in humans. *American Industrial Hygiene Association Journal.* 41, 399-409.

Chang, J. C. F., Gross, E. A., Swenberg, J. A., and Barrow, C. S. (1983) Nasal cavity deposition, histopathology, and cell proliferation after single or repeated formaldehyde exposures in B6C3F1 mice and F-344 rats. *Toxicol. Appl. Pharmacol.* 68, 161-176.

Cheng, K. H., Cheng, Y. S., Yeh, H. C., and Swift, D. L. (1997) Measurements of airway dimensions and calculation of mass transfer characteristics of the human oral passage. *Journal of Biomechanical Engineering.* 119, 476-482.

Cheng, Y. S. (2003) Aerosol deposition in the extrathoracic region. *Aerosol Science and Technology.* 37, 659-671.

Cheng, Y. S., Fu, C. S., Yazzie, D., and Zhou, Y. (2001) Respiratory deposition patterns of salbutamol pMDI with CFC and HFA-134a formulations in a human airway replica. *Journal of Aerosol Medicine.* 14(2), 255-266.

Cinkotai, F. F. (1971) The behavior of sodium chloride particles in moist air. *Journal of Aerosol Science.* 2, 325-329.

Cohen, B. S., Sussman, R. G., and Lippmann, M. (1990) Ultrafine particle deposition in a human tracheobronchial cast. *Aerosol Science and Technology.* 12, 1082-1093.

Cohen Hubal, E. A., Fedkiw, P. S., and Kimbell, J. S. (1996a) Mass-transport models to predict toxicity of inhaled gases in the upper respiratory tract. *Journal of Applied Physiology.* 80(4), 1415-1427.

Cohen Hubal, E. A., Kimbell, J. S., and Fedkiw, P. S. (1996b) Incorporation of nasal-lining mass-transfer resistance into a CFD model

for prediction of ozone dosimetry in the upper respiratory tract. *Inhalation Toxicology.* 8, 831-857.

Cohen Hubal, E. A., Schlosser, P. M., Conolly, R. B., and Kimbell, J. S. (1997) Comparison of inhaled formaldehyde dosimetry predictions with DNA-protein cross-link measurements in the rat nasal passages. *Toxicology and Applied Pharmacology.* 143, 47-55.

Comer, J. K., Kleinstreuer, C., Hyun, S., and Kim, C. S. (2000) Aerosol transport and deposition in sequentially bifurcating airways. *Journal of Biomechanical Engineering.* 122(2), 152-158.

Darquenne, C. (2002) Heterogeneity of aerosol deposition in a two-dimensional model of human alveolated ducts. *Journal of Aerosol Science.* 33(9), 1261-1278.

Darquenne, C., and Paiva, M. (1996) Two- and three dimensional simulations of aerosol transport and deposition in alveolar zone of human lung. *Journal of Applied Physiology.* 80(4), 1401-1414.

DeHaan, W. H., and Finlay, W. H. (2004) Predicting extrathoracic deposition from dry powder inhalers. *Journal of Aerosol Science.* 35, 309-331.

Delvadia, R. R., Byron, P. R., Longest, P. W., and Hindle, M. (2010) In Vitro prediction of regional drug deposition from dry powder inhalers. *Respiratory Drug Delivery.* 1, 908-912.

EPA. (1999) National-Scale Air Toxics Assessment. *http://www.epa.gov/ttn/atw/nata1999/.*

Ferron, G. A. (1977) The size of soluable aerosol particles as a function of the humidity of the air: Application to the human respiratory tract. *Journal of Aerosol Science.* 3, 251-267.

Ferron, G. A., Haider, B., and Kreyling, W. G. (1984) Conditions for measuring supersaturation in the human lung using aerosols. *Journal of Aerosol Science.* 15, 211-215.

Ferron, G. A., Kreyling, W. G., and Haider, B. (1988) Inhalation of salt aerosol particles - II. Growth and deposition in the human respiratory tract. *Journal of Aerosol Science.* 19(5), 611-631.

Ferron, G. A., Oberdorster, G., and Hennenberg, R. (1989) Estimation of the deposition of aerosolised drugs in the human respiratory tract due to hygroscopic growth. *Journal of Aerosol Medicine.* 2, 271.

Finlay, W. H., and Stapleton, K. W. (1995) The effect on regional lung deposition of coupled heat and mass-transfer between hygroscopic droplets and their surrounding phase. *Journal of Aerosol Science.* 26(4), 655-670.

Foster, W. M., Langenback, E., and Bergofsky, E. H. (1980) Measurement of tracheal And bronchial mucus velocities in man - Relation to lung clearance. *Journal of Applied Physiology.* 48(6), 965-971.

Franks, S. J. (2005) A mathematical model for the absorpiton and metabolism of formaldehyde vapors in humans. *Toxicology And Applied Pharmacology.* 206, 309-320.

Frederick, C. B., Bush, M. L., Lomax, L. G., Black, K. A., Finch, L., Kimbell, J. S., Morgan, K. T., Subramaniam, R. P., Morris, J. B., and Ultman, J. S. (1998) Application of a hybrid computational fluid dynamics and physiologically based inhalation model for interspecies dosimetry extrapolation of acidic vapors in the upper airways. *Toxicology And Applied Pharmacology.* 152(1), 211-231.

George, S. C., Babb, A. L., Deffebach, M. E., and Hlastala, M. P. (1996) Diffusion of nonelectrolytes in the canine trachea: Effect of thigh junction. *Journal of Applied Physiology.* 80, 1687-1695.

Ghalichi, F., Deng, X., Champlain, A. D., Douville, Y., King, M., and Guidoin, R. (1998) Low Reynolds number turbulence modeling of blood flow in arterial stenoses. *Biorheology.* 35(4&5), 281-294.

Goswami, C., and Banerji, K. K. (1970) The mechanism of the oxidation of acetaldehyde by chromic acid. *Bulletin of the Chemical Society of Japan.* 43, 2643-2645.

Hammersley, J. R., and Olson, D. E. (1992) Physical models of the smaller pulmonary airways. *Journal of Applied Physiology.* 72, 2402-2414.

Heistracher, T., and Hofmann, W. (1995) Physiologically realistic models of bronchial airway bifurcations. *Journal of Aerosol Science.* 26(3), 497-509.

Hindle, M., and Longest, P. W. (2010) Evaluation of enhanced condensational growth (ECG) for controlled respiratory drug delivery in a mouth-throat and upper tracheobronchial model. *Pharm. Res.* 27, 1800-1811.

Hlastala, M. P., and Robertson, H. T. (1998) *Complexity in Structure and Function of the Lung*, Informa Health Care.

Hofmann, W., Golser, R., and Balashazy, I. (2003) Inspiratory deposition efficiency of ultrafine particles in a human airway bifurcation model. *Aerosol Science and Technology.* 37(12), 988-994.

Horsfield, K., Dart, G., Olson, D. E., and Cumming, G. (1971) Models of the human bronchial tree. *Journal of Applied Physiology.* 31, 207-217.

Ibsen, L. M., and Bratton, S. L. (1999) Current therapies for severe asthma exacerbations in children. *New Horizons-The Science and Practice of Acute Medicine.* 7(3), 312-325.

ICRP. (1994) *Human Respiratory Tract Model for Radiological Protection*, Elsevier Science Ltd., New York.

Isaacs, K. K., Rosati, J. A., and Martonen, T. B. (2005) Mechanisms of particle deposition. Aerosols Handbook, L. S. Ruzer and N. H. Harley, eds., CRC Press, New York, 75-99.

Jarabek, A. M. (1995) The application of dosimetry models to identify key processes and parameters for default dose-response assessment approaches. *Toxicology Letters.* 79, 171-184.

Karch, S. B., and Peat, M. (2007) *Drug Abuse Handbook*, CRC Press.

Karl, A., Henry, F. S., and Tsuda, A. (2004) Low Reynolds number viscous flow in an alveolated duct. *Journal Of Biomechanical Engineering-Transactions Of The Asme.* 126(4), 420-429.

Keyhani, K., Scherer, P. W., and Mozell, M. M. (1997) A numerical mdoel of nasal odorant transport for the analysis of human olfocation. *Journal of Theoretical Biology.* 186, 279-301.

Kim, C. S. (2009) Deposition of aerosol particles in human lungs: in vivo measurement and modeling. *Biomakers.* 14(S1), 54-58.

Kimbell, J. S., Gross, E. A., Joyner, D. R., Godo, M. N., and Morgan, K. T. (1993) Application of computational fluid dynamics regional dosimetry of inhaled chemicals in the upper respiratory tract of the rat. *Toxicol. Appl. Pharmacol.* 121, 253-263.

Kimbell, J. S., Overton, J. H., Subramaniam, R. P., Schlosser, P. M., Morgan, K. T., Conolly, R. B., and Miller, F. J. (2001a) Dosimetry

modeling of inhaled formaldehyde: Binning nasal flux predictions for quantitative risk assessment. *Toxicological Sciences.* 64(1), 111-121.

Kimbell, J. S., and Subramaniam, R. P. (2001) Use of computational fluid dynamics models for dosimetry of inhaled gases in the nasal passages. *Inhalation Toxicology.* 13(5), 325-334.

Kimbell, J. S., Subramaniam, R. P., Gross, E. A., Schlosser, P. M., and Morgan, K. T. (2001b) Dosimetry modeling of inhaled formaldehyde: Comparisons of local flux predictions in the rat, monkey, and human nasal passages. *Toxicological Sciences.* 64(1), 100-110.

Kleinstreuer, C., Shi, H., and Zhang, Z. (2007) Computational analyses of a pressurized metered dose inhaler and an new drug-aerosol targeting methodology. *Journal of Aerosol Medicine.* 20(3), 294-309.

Kleinstreuer, C., and Zhang, Z. (2009) An adjustable triple-bifurcation unit model for air-particle flow simulations in human tracheobronchial airways. *Journal of Biomechanical Engineering.* 131(021007).

Koblinger, L., and Hofmann, W. (1990) Monte Carlo modeling of aerosol deposition in human lungs. Part I: Simulation of particle transport in a stochastic lung structure. *Journal of Aerosol Science.* 21(5), 661-674.

Kumagai, S., and Matsunaga, I. (1995) Physiologically based pharmacokinetic model for acetone. *Occup. Environ. Med.* 52, 344-352.

LaBelle, C. W., Long, J. E., and Christofano, E. E. (1955) Synergistic effects of aerosols. *Arch. Ind. Health.* 11, 297-304.

Li, W., and Hopke, P. K. (1993) Initial size distributions and hygroscopicity of indoor combustion aerosol particles. *Aerosol Science and Technology.* 19, 305-316.

Lin, C. L., Tawhai, M. H., Mclennan, G., and Hoffman, E. A. (2007) Characteristics of the turbulent laryngeal jet and its effect of airflow in the human intro-thoracic airways. *Respir. Physiol. Neurobiol.* 157, 295-309.

Lin, C. L., Tawhai, M. H., Mclennan, G., and Hoffman, E. A. (2009) Multiscale simulation of gas flow in subject-specific models of the human lung. *IEEE Eng. Med. Biol.* 28, 25-33.

Liu, Y., Matida, E. A., Gu, J., and Johnson, M. R. (2007) Numerical simulation of aerosol deposition in a 3-D human nasal cavity using RANS, RANS/EIM, and LES. *Aerosol Science.* 38, 683-700.

Liu, Y., So, R. M. C., and Zhang, C. H. (2002) Modeling the bifurcation flow in a human lung airway. *Journal of Biomechanics.* 35, 465-473.

Longest, P. W., and Hindle, M. (2009a) Evaluation of the Respimat Soft Mist inhaler using a concurrent CFD and in vitro approach. *J. Aerosol Med. Pulm. Drug Deliv.* 22(2), 99-112.

Longest, P. W., and Hindle, M. (2009b) Quantitative analysis and design of a spray aerosol inhaler. Part 1: Effects of dilution air inlets and flow paths. *Journal of Aerosol Medicine and Pulmonary Drug Delivery.* 22(3), 271-283.

Longest, P. W., and Hindle, M. (2010) CFD simulations of enhanced condensational growth (ECG) applied to respiratory drug delivery with comparisons to in vitro data. *J. Aerosol Sci.* 41, 805-820.

Longest, P. W., Hindle, M., and Das Choudhuri, S. (2009) Effects of generation time on spray aerosol transport and deposition in models of the mouth-throat geometry. *Journal of Aerosol Medicine and Pulmoary Drug Delivery.* 22(3), 67-84.

Longest, P. W., Hindle, M., Das Choudhuri, S., and Byron, P. R. (2007) Numerical simulations of capillary aerosol generation: CFD model development and comparisons with experimental data. *Aerosol Science and Technology.* 41, 952-973.

Longest, P. W., Hindle, M., Das Choudhuri, S., and Byron, P. R. (2008a) Developing a better understanding of spray system design using a combination of CFD modeling and experiment. Proceedings of Respiratory Drug Delivery 2008, R. N. Dalby, P. R. Byron, J. Peart, J. D. Suman, S. J. Farr, and P. M. Young, eds., Davis Healthcare International Publishing, Illinois, 151-163.

Longest, P. W., Hindle, M., Das Choudhuri, S., and Xi, J. (2008b) Comparison of ambient and spray aerosol deposition in a standard induction port and more realistic mouth-throat geometry. *Journal of Aerosol Science.* 39, 572-591.

Longest, P. W., Mcleskey, J. T., and Hindle, M. (2010) Characterization of nanoaerosol size change during enhanced condensational growth. *Aerosol Sci. Technol.* 44, 473-483.

Longest, P. W., and Oldham, M. J. (2006) Mutual enhancements of CFD modeling and experimental data: A case study of one micrometer particle deposition in a branching airway model. *Inhalation Toxicology.* 18(10), 761-772.

Longest, P. W., and Vinchurkar, S. (2007a) Effects of mesh style and grid convergence on particle deposition in bifurcating airway models with comparisons to experimental data. *Medical Engineering and Physics.* 29(3), 350-366.

Longest, P. W., and Vinchurkar, S. (2007b) Validating CFD predictions of respiratory aerosol deposition: effects of upstream transition and turbulence. *Journal of Biomechanics.* 40, 305-316.

Longest, P. W., Vinchurkar, S., and Martonen, T. B. (2006) Transport and deposition of respiratory aerosols in models of childhood asthma. *Journal of Aerosol Science.* 37, 1234-1257.

Longest, P. W., and Xi, J. (2007a) Computational investigation of particle inertia effects on submicron aerosol deposition in the respiratory tract. *Journal of Aerosol Science.* 38(1), 111-130.

Longest, P. W., and Xi, J. (2007b) Effectiveness of direct Lagrangian tracking models for simulating nanoparticle deposition in the upper airways. *Aerosol Science and Technology.* 41, 380-397.

Longest, P. W., and Xi, J. (2008) Condensational growth may contribute to the enhanced deposition of cigarette smoke particles in the upper respiratory tract. *Aerosol Science and Technology.* 42, 579-602.

Marielle, E. A. C., Broeders, Molema, J., Hop, W. C. J., and Flgering, H. T. M. (2003) Inhalation profiles in asthmatics and COPD patients: reproducibility and effect of instruction. *Journal of Aerosol Medcine.* 16, 131-141.

Martonen, T., Fleming, J., Schroeter, J., Conway, J., and Hwang, D. (2003) In silico modeling of asthma. *Advanced Drug Delivery Reviews.* 55, 829-849.

Martonen, T. B. (1993) Mathematical model for the selective deposition of inhaled pharmaceuticals. *Journal of Pharmaceutical Sciences.* 82(12), 1191-1199.

Martonen, T. B., Bell, K. A., Phalen, R. F., Wilson, A. F., and Ho, A. (1982) Growth rate measurements and deposition modeling of hygroscopic aerosols in human tracheobronchial models. Inhaled Particles V, W. H. Walton, ed., Pergamon Press, Oxford, 93-107.

Martonen, T. B., Burton, R., and Fleming, J. S. (2005a) *3D in silico modeling of aerosol behavior within airways of the human head and throat.* Frontiers in Aerosol Dosimetry Research, Irvine, CA.

Martonen, T. B., Guan, X., and Schreck, R. M. (2001) Fluid dynamics in airway bifurcations: I. Primary flows. *Inhalation Toxicology.* 13(4), 261-279.

Martonen, T. B., Rosati, J. A., and Isaacs, K. K. (2005b) Modeling deposition of inhaled particles. Aerosols Handbook, L. S. Ruzer and N. H. Harley, eds., CRC Press, New York, 113-155.

Matida, E. A., Finlay, W. H., Breuer, M., and Lange, C. F. (2006) Improving prediction of aerosol deposition in an idealized mouth using large-eddy simulation. *Journal of Aerosol Medicine.* 19(3), 290-300.

McClellan, R. O., and Henderson, R. F. (1995) *Concepts in Inhalation Toxicology*, CRC Press.

Meijer, R. J., Mark Th, W. v. d., Aalders, B. J., Postma, D. S., and Koeter, G. H. (1996) Home assessment of peak inspiratory flow through the Turbohaler in asthmatic patients. *Thorax.* 51, 433-434.

Miller, F. J., Overton, J. H., Jaskot, R. H., and Menzel, D. B. (1985) A model of the regional uptake of gaseous pollutants in the lung. *Toxicology and Applied Pharmacology.* 79, 11–27.

Morris, J. B., and Blanchard, K. T. (1992) Upper respiratory tract deposition of inspired acetaldehyde. *Toxicol. Appl. Pharmacol.* 114, 140-146.

Morris, J. B., and Cavanagh, D. G. (1986) Deposition of ethanol and acetone vapors in the upper respiratory tract of the rat. *Fundam. Appl. Toxicol.* 6, 78-88.

Morris, J. B., and Cavanagh, D. G. (1987) Metabolism and deposition of propanol and acetone vapors in the upper respiratory tract of the hamster. *Fundam. Appl. Toxicol.* 9, 34-40.

NCRP. (1997) *Deposition, Retention and Dosimetry of Inhaled Radioactive Substances*, National Council on Radiation Protection and Measurements, Bethesda.

Newman, S. (2009) Respiratory Drug Delivery: Essential Theory and Practice. *Richmond: RDD online.*

Nikander, K., Prince, I., Coughlin, S., Warren, S., and Taylor, G. (2010) Mode of breathing-tidal or slow and deep through the I-ned adaptive delivery (ADD) system affects lung deposition of 99mTc-DTPA. *J. Aerosol Med.* 23(S1), S37-S43.

NIST.(2008) NIST Chemistry WebBook. *http://webbook.nist.gov/chemistry/.*

Oldham, M. J., Phalen, R. F., and Heistracher, T. (2000) Computational fluid dynamic predictions and experimental results for particle deposition in an airway model. *Aerosol Science and Technology.* 32(1), 61-71.

Overton, J. H., Kimbell, J. S., and Miller, F. J. (2001) Dosimetry modeling of inhaled formaldehyde: The human respiratory tract. *Toxicological Sciences.* 64, 122-134.

Peng, C., Chow, A. H. L., and Chan, C. K. (2000) Study of the hygroscopic properties of selected pharmaceutical aerosols using single particle levitation. *Pharmaceutical Research.* 17, 1104-1109.

Persson, G., Olsson, B., and Soliman, S. (1997) The impact of inspiratory effort on inspiratory flow through Turbuhaler in asthmatic patients. *Eur Respir J.* 10, 681-684.

Phalen, R. F., Yeh, H. C., Schum, G. M., and Rabbe, O. G. (1978) Application of an idealized model to morphometry of the mammalian tracheobronchial tree. *Anat, Rec.* 190, 167-176.

Press, W. H., Teukolsky, S. A., Vetterling, W. T., and Flannery, B. P. (1996) *Numerical Recipes in Fortran 77: The Art of Scientific Computing*, Cambridge University Press, Cambridge.

Robinson, R., and Yu, C. P. (1998) Theoretical analysis of hygroscopic growth rate of mainstream and sidestream cigarette smoke particles in the human respiratory tract. *Aerosol Science and Technology.* 28, 21-32.

Ross, D. L., and Schultz, R. K. (1996) Effect of inhalation flow rate on the dosing characteristics of dry powder inhaler (DPI) and metered dose inhaler (MDI) products. *Journal of Aerosol Medicine.* 9(2), 215-226.

Russo, J., Robinson, R., and Oldham, M. J. (2008) Effects of cartilage rings on airflow and particle deposition in the trachea and main bronchi. *Medical Engineering and Physics.* 30, 581-589.

Sakuma, H., Kusama, M., Yamaguchi, K., Matsuki, T., and Sugawara, S. (1984) The distribution of cigarette smoke components between

mainstream and sidestream smoke. I. Acidic Components. *Beitr. zur Tabakforschung.* 12(2), 63-71.

Schroeter, J. D., Musante, C. J., Hwang, D. M., Burton, R., Guilmette, R., and Martonen, T. B. (2001) Hygroscopic growth and deposition of inhaled secondary cigarette smoke in human nasal pathways. *Aerosol Science and Technology.* 34(1), 137-143.

Shi, H., Kleinstreuer, C., and Zhang, Z. (2006) Laminar airflow and nanoparticle or vapor deposition in a human nasal cavity model. *Journal of Biomechanical Engineering.* 128, 697-706.

Stahlhofen, W., Rudolf, G., and James, A. C. (1989) Intercomparison of experimental regional aerosol deposition data. *Journal of Aerosol Medicine.* 2(3), 285-308.

Talhout, R., Opperhuizen, A., and van Amsterdam, J. G. C. (2007) Role of acetaldehyde in tobacco smoke addiction.
European Neuropsychopharmacology. 17, 627-636.

Taylor, A. B., Borhan, A., and Ultman, J. S. (2007) Three-dimensional simulations of reactive gas uptake in single airway bifurcations. *Annals of Biomedical Engineering.* 35(2), 235-249.

Tian, G., and Longest, P. W. (2010a) Development of a CFD boundary condition to model transient vapor absorption in the respiratory airways. *ASME Journal of Biomechanical Engineering.* 132, 051003.

Tian, G., and Longest, P. W. (2010b) Transient absorption of inhaled vapors into a multilayer mucus-tissue-blood system. *Annals of Biomedical Engineering.* 38(2), 517-536.

US_Department_of_Environmental_Quality. (1994). "DEQ Remediation and Redevelopment Operational Memorandum ".

van der Palen, J. (2003) Peak inspiratory flow through Diskus and Turbuhaler, measured by means of a peak inspiratory flow meter (In-Check Dial). *Respiratory Medicine.* 97, 285-298.

Varghese, S. K., and Gangamma, S. (2009) Particle deposition in human respiratory system: Deposition of concentrated hygroscopic aerosols. *Inhalation Toxicology.* 21(7), 619-630.

Vinchurkar, S., and Longest, P. W. (2008) Evaluation of hexahedral, prismatic and hybrid mesh styles for simulating respiratory aerosol dynamics. *Computers and Fluids.* 37, 317-331.

Vinchurkar, S., Longest, P. W., and Peart, J. (2009) CFD simulations of the Andersen cascade impactor: Model development and effects of aerosol charge. *Journal of Aerosol Science* 40, 807-822.

Weibel, E. R. (1963) *Morphometry of the Human Lung*, Springer Verlag, Berlin.

Wilcox, D. C. (1998) *Turbulence Modeling for CFD, 2nd Ed.*, DCW Industries, Inc., California.

Xi, J., and Longest, P. W. (2007a) Effects of improved near-wall modeling on micro-particle deposition in oral airway geometries. *Proceedings of the 2007 ASME Summer Bioengineering Conference, Keystone, CO.* . Paper No. SBC2007-176227.

Xi, J., and Longest, P. W. (2007b) Transport and deposition of micro-aerosols in realistic and simplified models of the oral airway. *Annals of Biomedical Engineering.* 35(4), 560-581.

Xi, J., and Longest, P. W. (2008a) Effects of oral airway geometry characteristics on the diffusional deposition of inhaled nanoparticles. *ASME Journal of Biomechanical Engineering.* 130, 011008.

Xi, J., and Longest, P. W. (2008b) Evaluation of a novel drift flux model for simulating submicrometer aerosol dynamics in human upper tracheobronchial airways. *Annals of Biomedical Engineering.* doi:10.1007.

Xi, J., Longest, P. W., and Martonen, T. B. (2008) Effects of the laryngeal jet on nano- and microparticle transport and deposition in an approximate model of the upper tracheobronchial airways. *Journal of Applied Physiology.* 104, 1761-1777.

Xi, J. X., and Longest, P. W. (2009) Characterization of Submicrometer Aerosol Deposition in Extrathoracic Airways during Nasal Exhalation. *Aerosol Sci. and Technol.* 43, 808-827.

Xie, Y., Zeng, P., Siegel, R., Wiedmann, T. S., Hammer, B. E., and Longest, P. W. (2010) Magnetic deposition of aerosols composed of aggregated superparamagnetic nanoparticles. *Pharm. Res.* 27(5), 855-865.

Yeates, D. B., Besseris, G. J., and Wong, L. B. (1997) Physicochemical properties of mucus and its propulsion. The Lung: Scientific Foundations, R. G. Crystal and J. B. West, eds., Lippincott - Raven Publishers, Philadelphia, 487-503.

Yeh, H. C., and Schum, G. M. (1980) Models of human lung airways and their application to inhaled particle deposition. *Bull. Math. Biology.* 42, 461–480.

Yin, Y., Choi, J., Hoffman, E. A., Tawhai, M. H., and Lin, C. L. (2010) Simulation of pulmonary air flow with a subject specific boundary condition. *J. Biomech.* 43, 2159-2163.

Zhang, Y., Gilbertson, K., and Finlay, W. H. (2007) In vivo-in vitro comparison of deposition in three mouth-throat models with Qvar and Turbuhaler inhalers. *Journal of Aerosol Medicine.* 20(3), 227-235.

Zhang, Z., and Kleinstreuer, C. (2002) Transient airflow structures and particle transport in a sequentially branching lung airway model. *Physics of Fluids.* 14(2), 862-880.

Zhang, Z., and Kleinstreuer, C. (2003) Species heat and mass transfer in a human upper airway model. *International Journal of Heat and Mass Transfer.* 46(25), 4755-4768.

Zhang, Z., and Kleinstreuer, C. (2004) Airflow structures and nano-particle deposition in a human upper airway model. *Journal of Computational Physics.* 198(1), 178-210.

Zhang, Z., and Kleinstreuer, C. (2006) Transport and uptake of MTBE and ethanol vapors in a human upper airway model. *Inhalation Toxicology.* 18, 169-184.

Zhang, Z., Kleinstreuer, C., Donohue, J. F., and Kim, C. S. (2005) Comparison of micro- and nano-size particle depositions in a human upper airway model. *Journal of Aerosol Science.* 36(2), 211-233.

Zhang, Z., Kleinstreuer, C., and Kim, C. S. (2006a) Isotonic and hypertonic saline droplet deposition in a human upper airway model. *Journal of Aerosol Medicine.* 19(2), 184-198.

Zhang, Z., Kleinstreuer, C., and Kim, C. S. (2006b) Water vapor transport and its effects on the deposition of hygroscopic droplets in a human upper airway model. *Aerosol Science and Technology.* 40, 52-67.

Zhang, Z., Kleinstreuer, C., and Kim, C. S. (2009) Comparison of analytical and CFD models with regard to micron particle deposition in a human 16-generation tracheobronchial airway model. *Aerosol Sci.* 36(2), 211-233.

Zhang, Z., Kleinstreuer, C., Kim, C. S., and Cheng, Y. S. (2004) Vaporizing microdroplet inhalation, transport, and deposition in a human upper airway model. *Aerosol Science and Technology.* 38(1), 36-49.

Zhao, K., Scherer, P. W., Hajiloo, S. A., and Dalton, P. (2004) Effects of anatomy on human nasal air flow and odorant transport patterns: Implictions for olfaction. *Chem. Senses.* 29(5), 365-379.

Zhou, Y., and Cheng, Y. S. (2005) Particle deposition in a cast of human tracheobrochial airways. *Aerosol Science and Technology.* 39, 492-500.

APPENDIX A

Transient Analytic Solutions in the Mucus-Tissue-Blood System

In this section, the analytic transient solution for time-dependent variables $C_m(y,t)$ and $C_t(y,t)$ is developed. Knowing the steady state solution for $\tilde{C}_m(y)$ and $\tilde{C}_t(y)$, it is appropriate to represent $\hat{C}_m(y,t)$ and $\hat{C}_t(y,t)$ as the transient concentration distribution (Powers 1972)

$$\hat{C}_m(y,t) = C_m(y,t) - \tilde{C}_m(y) \quad \text{and} \quad \hat{C}_t(y,t) = C_t(y,t) - \tilde{C}_t(y) \tag{A.1}$$

By using these expressions, we have the following relations

$$\frac{\partial \hat{C}_m(y,t)}{\partial t} = \frac{\partial C_m(y,t)}{\partial t} - \frac{d\tilde{C}_m(y)}{dt} = \frac{\partial C_m(y,t)}{\partial t}, \tag{A.2a}$$

$$\frac{\partial \hat{C}_t(y,t)}{\partial t} = \frac{\partial C_t(y,t)}{\partial t} - \frac{d\tilde{C}_t(y)}{dt} = \frac{\partial C_t(y,t)}{\partial t}, \tag{A.2b}$$

$$\frac{\partial^2 \hat{C}_m(y,t)}{\partial y^2} = \frac{\partial^2 C_m(y,t)}{\partial y^2} - \frac{d^2\tilde{C}_m(y)}{dy^2} = \frac{\partial^2 C_m(y,t)}{\partial y^2}, \quad \text{and} \tag{A.2c}$$

$$\frac{\partial^2 \hat{C}_t(y,t)}{\partial y^2} = \frac{\partial^2 C_t(y,t)}{\partial y^2} - \frac{d^2\tilde{C}_t(y)}{dy^2} = \frac{\partial^2 C_t(y,t)}{\partial y^2}. \tag{A.2d}$$

Therefore, we get the following Equations for $\hat{C}_m(y,t)$ and $\hat{C}_t(y,t)$

$$\frac{\partial \hat{C}_m(y,t)}{\partial t} = D_m \frac{\partial^2 \hat{C}_m(y,t)}{\partial y^2}, \; y \in [0, H_m] \tag{A.3a}$$

$$\frac{\partial \hat{C}_t(y,t)}{\partial t} = D_t \frac{\partial^2 \hat{C}_t(y,t)}{\partial y^2}, \; y \in [H_m, H_m + H_t] \tag{A.3b}$$

The initial conditions are

$$\hat{C}_m(y,0) = C_m(y,0) - \tilde{C}_m(y) = \frac{\lambda_{ma} C_{air} - \tilde{C}_m(y)|_{y=H_m}}{H_m} y - \lambda_{ma} C_{air} \text{ and} \quad \text{(A.4a)}$$

$$\hat{C}_t(y,0) = C_t(y,0) - \tilde{C}_t(y) = \frac{\lambda_{tm} \tilde{C}_m(y)|_{y=H_m}}{H_t} y - \frac{\lambda_{tm} \tilde{C}_m(y)|_{y=H_m}}{H_t} (H_m + H_t). \quad \text{(A.4b)}$$

The boundary conditions are

$$\hat{C}_m(y,t)|_{y=0} = C_m(y,t)|_{y=0} - \tilde{C}_m(y)|_{y=0} = 0, \quad \text{(A.5a)}$$

$$\hat{C}_t(y,t)|_{y=H_m} = \lambda_{tm} \hat{C}_m(y,t)|_{y=H_m}, \quad \text{(A.5b)}$$

$$-D_m \frac{\partial \hat{C}_m(y,t)}{\partial y}|_{y=H_m} = -D_t \frac{\partial \hat{C}_t(y,t)}{\partial y}|_{y=H_m}, \text{ and} \quad \text{(A.5c)}$$

$$\hat{C}_t(y,t)|_{y=H_m+H_t} = C_t(y,t)|_{y=H_m+H_t} - \tilde{C}_t(y,t)|_{y=H_m+H_t} = 0. \quad \text{(A.5d)}$$

Introducing a dimensionless variable $\xi = y / H_m$, Equations (A.3a) and (A.3b) become

$$\frac{\partial \hat{C}_m(\xi,t)}{\partial t} = \frac{D_m}{{H_m}^2} \frac{\partial^2 \hat{C}_m(\xi,t)}{\partial \xi^2}, \xi \in [0,1] \quad \text{(A.6a)}$$

$$\frac{\partial \hat{C}_t(\xi,t)}{\partial t} = \frac{D_t}{{H_m}^2} \frac{\partial^2 \hat{C}_t(\xi,t)}{\partial \xi^2}, \xi \in [1, 1 + H_t / H_m] \quad \text{(A.6b)}$$

Substitution of the product $\hat{C}_m(\xi,t) = \hat{Y}_m(\xi) T(t)$ into Equation (A.3a) gives

$$\frac{1}{\hat{Y}_m} \frac{d^2 \hat{Y}_m}{d\xi^2} = \frac{{H_m}^2}{D_m} \frac{1}{T} \frac{dT}{dt} = -\mu^2, \mu \neq 0 \quad \text{(A.7a)}$$

Similarly, substitution of the product $\hat{C}_t(\xi,t) = \hat{Y}_t(\xi) T'(t)$ into Equation (A.3b) after multiplying by D_t / D_m gives

$$\frac{D_t}{D_m} \frac{1}{\hat{Y}_t} \frac{d^2 \hat{Y}_t}{d\xi^2} = \frac{{H_m}^2}{D_m} \frac{1}{T'} \frac{dT'}{dt} = -\mu^2, \mu \neq 0 \quad \text{(A.7b)}$$

where μ^2 is a separation constant. Equations (A.7a) and (A.7b) immediately result in four ordinary differential equations

$$\frac{d^2\hat{Y}_m}{d\xi^2} + \mu^2 \hat{Y}_m = 0\,, \tag{A.8a}$$

$$\frac{dT}{dt} = -\mu^2 \frac{D_m}{H_m{}^2} T\,, \tag{A.8b}$$

$$\frac{d^2\hat{Y}_t}{d\xi^2} + \frac{\mu^2 D_m}{D_t} \hat{Y}_t = 0\,, \quad \text{and} \tag{A.8c}$$

$$\frac{dT'}{dt} = -\mu^2 \frac{D_m}{H_m{}^2} T'\,. \tag{A.8d}$$

The solutions for the spatially-dependent functions $\hat{Y}_m(y)$ and $\hat{Y}_t(y)$ are obtained from Equations (A.8a) and (A.8c), and substituting for ξ gives

$$\hat{Y}_m(y) = A\cos(\frac{\mu y}{H_m}) + B\sin(\frac{\mu y}{H_m}) \quad \text{and} \tag{A.9a}$$

$$\hat{Y}_t(y) = A'\cos(\mu\sqrt{\frac{D_m}{D_t}}\frac{y}{H_m}) + B'\sin(\mu\sqrt{\frac{D_m}{D_t}}\frac{y}{H_m})\,. \tag{A.9b}$$

The solutions for the time-variable functions $T(t)$ and $T'(t)$ are obtained from Equations (A.8b) and (A.8d) as

$$T(t) = T'(t) = e^{-\mu^2 \frac{D_m}{H_m{}^2} t} > 0\,. \tag{A.9c}$$

Considering $\hat{C}_m(0,t) = \hat{Y}_m(0)T(t) = 0$, it follows that $\hat{Y}_m(0) = 0$, which results in $A = 0$. As a result, Equation (A.9a) simplifies to

$$\hat{Y}_m(y) = B\sin(\frac{\mu y}{H_m})\,. \tag{A.10a}$$

Similarly, as $\hat{C}_t(y,t)|_{y=H_m+H_t} = \hat{Y}_t(H_m+H_t)T(t) = 0$, it follows that $\hat{Y}_t(H_m+H_t) = 0$,

and Equation (A.9b) simplifies to (Jeffrey 2002)

$$\hat{Y}_t(y) = P\sin(\mu\sqrt{\frac{D_m}{D_t}}\frac{H_m+H_t-y}{H_m}). \tag{A.10b}$$

Substituting (A.10a) and (A.10b) into the Equations (A.5b) and (A.5c), the boundary conditions become,

$$\lambda_{tm}B\sin(\mu) = P\sin(\mu\sqrt{\frac{D_m}{D_t}}\frac{H_t}{H_m}) \tag{A.11a}$$

and

$$-D_m B\frac{\mu}{H_m}\cos(\mu) = D_t P\frac{\mu}{H_m}\sqrt{\frac{D_m}{D_t}}\cos(\mu\sqrt{\frac{D_m}{D_t}}\frac{H_t}{H_m}). \tag{A.11b}$$

Dividing Equation (A.11a) by (A.11b), the eigenvalues, μ_n, are the sequential positive roots of the transcendental equation

$$\lambda_{tm}\sqrt{\frac{D_t}{D_m}}\tan(\mu) + \tan(\mu\sqrt{\frac{D_m}{D_t}}\frac{H_t}{H_m}) = 0. \tag{A.12}$$

The eigenvalues μ can be calculated numerically using Brent's method which combines bisection, secant, and inverse quadratic interpolation methods. The first five eigenvalues μ in the series, are provided in Tables A.1 – A.3 at the end of this section.

Constants B and P come directly from the Equation (A.11a)

$$B = \sin(\mu\sqrt{\frac{D_m}{D_t}}\frac{H_t}{H_m}) \quad \text{and} \tag{A.13a}$$

$$P = \lambda_{tm}\sin(\mu). \tag{A.13b}$$

Substituting Equations (A.13a) and (A.13b), Equation (A.11b) becomes

$$-\sqrt{\frac{D_m}{D_t}}\frac{1}{\lambda_{tm}}\sin(\mu\sqrt{\frac{D_m}{D_t}}\frac{H_t}{H_m})\cos(\mu)=\sin(\mu)\cos(\mu\sqrt{\frac{D_m}{D_t}}\frac{H_t}{H_m}). \quad \text{(A.14)}$$

Substituting Equations (A.13a) and (A.13b), Equations (A.10a) and (A.10b) become

$$\hat{Y}_m(y)=\sin(\mu\sqrt{\frac{D_m}{D_t}}\frac{H_t}{H_m})\sin(\frac{\mu y}{H_m}) \quad \text{and} \quad \text{(A.15a)}$$

$$\hat{Y}_t(y)=\lambda_{tm}\sin(\mu)\sin(\mu\sqrt{\frac{D_m}{D_t}}\frac{H_m+H_t-y}{H_m}). \quad \text{(A.15b)}$$

The concentration solutions $\hat{C}_m(y,t)$ and $\hat{C}_t(y,t)$ lead to classical Fourier series solutions that take the following form

$$\hat{C}_m(y,t)=\sum_{n=1}^{\infty}W_n\sin(\mu_n\sqrt{\frac{D_m}{D_t}}\frac{H_t}{H_m})\sin(\frac{\mu_n y}{H_m})e^{-\mu_n^2\frac{D_m}{H_m^2}t}, y\in[0,H_m] \quad \text{(A.16a)}$$

$$\hat{C}_t(y,t)=\lambda_{tm}\sum_{n=1}^{\infty}W_n\sin(\mu_n)\sin(\mu_n\sqrt{\frac{D_m}{D_t}}\frac{H_m+H_t-y}{H_m})e^{-\mu_n^2\frac{D_m}{H_m^2}t}, y\in[H_m,H_m+H_t] \quad \text{(A.16b)}$$

The coefficient W_n (g/cm^3) can be determined by utilizing the orthogonal relation and initial condition of zero mucus and tissue concentration.

$$W_n=\frac{\int_0^{H_m}\hat{C}_m(y,0)\hat{Y}_m(y)dy+\eta\int_{H_m}^{H_m+H_t}\hat{C}_t(y,0)\hat{Y}_t(y)dy}{\int_0^{H_m}\left[\hat{Y}_m(y)\right]^2dy+\eta\int_{H_m}^{H_m+H_t}\left[\hat{Y}_t(y)\right]^2dy}, \quad \text{(A.16c)}$$

where η is a weight function that must satisfy

$$\int_0^{H_m}\hat{Y}_{mi}(y)\hat{Y}_{mj}(y)dy+\eta\int_{H_m}^{H_m+H_t}\hat{Y}_{ti}(y)\hat{Y}_{tj}(y)dy=0, i\neq j \quad \text{(A.16d)}$$

By a detailed derivation, the eigen functions are orthogonal with $\eta = 1/\lambda_{tm}$ over the interval $[0, H_m + H_t]$. Thus, substituting $\eta = 1/\lambda_{tm}$ into Equation (A.16c), the coefficients W_n can be determined. These coefficients were calculated numerically and the first five values in the series are tabulated in Tables A.1 – A.3.

The resulting analytic transient solutions for $C_m(y,t)$ and $C_t(y,t)$ have the following form

$$C_m(y,t) = \hat{C}_m(y,t) + \tilde{C}_m(y)$$
$$= \sum_{n=1}^{\infty} W_n \sin(\mu_n \sqrt{\frac{D_m}{D_t}} \frac{H_t}{H_m}) \sin(\frac{\mu_n y}{H_m}) e^{-\mu_n^2 \frac{D_m}{H_m^2} t} + \lambda_{ma} C_{air} - \frac{\lambda_{ma} C_{air} - \tilde{C}_m(y)|_{y=H_m}}{H_m} y, \quad \text{(A.17a)}$$

$$C_t(y,t) = \hat{C}_t(y,t) + \tilde{C}_t(y)$$
$$= \lambda_{tm} \sum_{n=1}^{\infty} W_n \sin(\mu_n) \sin(\mu_n \sqrt{\frac{D_m}{D_t}} \frac{H_m + H_t - y}{H_m}) e^{-\mu_n^2 \frac{D_m}{H_m^2} t} + \frac{\lambda_{tm} \tilde{C}_m(y)|_{y=H_m}}{H_t} (H_m + H_t - y), \quad \text{(A.17b)}$$

The value of $\tilde{C}_m(y)|_{y=H_m}$ is determined from the steady state solution, shown previously.

Transient Analytic Solutions in the Air-Mucus-Tissue-Blood System

In this section, the analytic transient solution for time-dependent variables $C_m(y,t)$ and $C_t(y,t)$ is developed. To achieve the desired solution we now construct the transient analytic solutions $C_m(y,t)$ and $C_t(y,t)$ of the problem by the superposition of the solutions of two simpler sub-problems in the form (Ozisik 1980)

$$C_m(y,t) = \hat{C}_m(y,t) + f(t)\tilde{C}_m(y), \text{ and } C_t(y,t) = \hat{C}_t(y,t) + f(t)\tilde{C}_t(y), \tag{A.18}$$

By using these expressions, we have the following system of equations

$$\frac{\partial C_m(y,t)}{\partial t} = \frac{\partial \hat{C}_m(y,t)}{\partial t} + \tilde{C}_m(y)\frac{df(t)}{dt}, \tag{A.19a}$$

$$\frac{\partial C_t(y,t)}{\partial t} = \frac{\partial \hat{C}_t(y,t)}{\partial t} + \tilde{C}_t(y)\frac{df(t)}{dt}, \tag{A.19b}$$

$$\frac{\partial^2 C_m(y,t)}{\partial y^2} = \frac{\partial^2 \hat{C}_m(y,t)}{\partial y^2} + f(t)\frac{d^2\tilde{C}_m(y)}{dy^2} = \frac{\partial^2 \hat{C}_m(y,t)}{\partial y^2}, \tag{A.19c}$$

$$\frac{\partial^2 C_t(y,t)}{\partial y^2} = \frac{\partial^2 \hat{C}_t(y,t)}{\partial y^2} + f(t)\frac{d^2\tilde{C}_t(y)}{dy^2} = \frac{\partial^2 \hat{C}_t(y,t)}{\partial y^2}, \tag{A.19d}$$

where $f(t)$ is a time-dependent variable that can be defined as $f(t) = C_m(y,t)|_{y=0}$. This variable is used to account for an arbitrary concentration on the mucus layer at the air-mucus interface. $\tilde{C}_m(y,t)$, $\tilde{C}_t(y,t)$, $\hat{C}_m(y)$, and $\hat{C}_t(y)$ are the solutions of the following sub-problems.

1. $\tilde{C}_m(y,t)$ and $\tilde{C}_t(y,t)$ are the steady state solutions with a time constant air phase concentration.

$$\frac{d^2\tilde{C}_m(y)}{dy^2} = 0\,,\ y \in [0, H_m] \tag{A.20a}$$

$$\frac{d^2\tilde{C}_t(y)}{dy^2} = 0\,,\ y \in [H_m, H_m + H_t] \tag{A.20b}$$

The boundary conditions from the steady state case are:

$$\tilde{C}_m(y)\,|_{y=0} = 1\,, \tag{A.21a}$$

$$\tilde{C}_t(y)\,|_{y=H_m} = \lambda_{tm}\tilde{C}_m(y)\,|_{y=H_m}\,, \tag{A.21b}$$

$$-D_m \frac{d\tilde{C}_m(y)}{dy}\,|_{y=H_m} = -D_t \frac{d\tilde{C}_t(y)}{dy}\,|_{y=H_m}\,, \tag{A.21c}$$

$$\tilde{C}_t(y)\,|_{y=H_m+H_t} = 0\,, \tag{A.21d}$$

The analytic solutions of the steady diffusion Equations (A.3a and b) are:

$$\tilde{C}_m(y) = 1 - \frac{1 - \tilde{C}_m(y)\,|_{y=H_m}}{H_m}\,y\,,\ y \in [0, H_m] \tag{A.22a}$$

$$\tilde{C}_t(y) = \frac{\lambda_{tm}\tilde{C}_m(y)\,|_{y=H_m}}{H_t}(H_m + H_t - y)\,,\ y \in [H_m, H_m + H_t] \tag{A.22b}$$

The concentration on the mucus side at the mucus-tissue interface $\tilde{C}_m(y)\,|_{y=H_m}$ can be obtained from Equations (A.21c), (A.22a), and (A.22b); the resulting expression is

$$\tilde{C}_m(y)\,|_{y=H_m} = \frac{H_t D_m}{H_m \lambda_{tm} D_t + H_t D_m}\,, \tag{A.23}$$

At steady state, Equation A.18 has the following form by substituting $f(t \to \infty) = \tilde{C}_m(y)\,|_{y=0} = \lambda_{ma}\tilde{C}'_a(y)\,|_{y=0}$;

$$\tilde{C}'_m(y) = \lambda_{ma}\tilde{C}'_a(y)\,|_{y=0}\ \tilde{C}_m(y)\,,\ \text{and}\ \tilde{C}'_t(y) = \lambda_{ma}\tilde{C}'_a(y)\,|_{y=0}\ \tilde{C}_t(y)\,, \tag{A.24}$$

where $\tilde{C}'_m(y)$ and $\tilde{C}'_t(y)$ are the steady-state solutions of Equation 18. $\tilde{C}'_a(y)|_{y=0}$ is the steady-state concentration on the air side at the air-mucus interface. The value can be obtained by solving a steady-state transport equation in the air layer.

2. $\hat{C}_m(y)$ and $\hat{C}_t(y)$ are the solutions of the following time-dependent problem.

$$\frac{\partial \hat{C}_m(y,t)}{\partial t} = D_m \frac{\partial^2 \hat{C}_m(y,t)}{\partial y^2} - \tilde{C}_m(y)\frac{df(t)}{dt}, y \in [0, H_m] \quad \text{(A.25a)}$$

$$\frac{\partial \hat{C}_t(y,t)}{\partial t} = D_t \frac{\partial^2 \hat{C}_t(y,t)}{\partial y^2} - \tilde{C}_t(y)\frac{df(t)}{dt}, y \in [H_m, H_m + H_t] \quad \text{(A.25b)}$$

The initial conditions are:

$$\hat{C}_m(y,0) = C_m(y,0) - f(0)\tilde{C}_m(y) = 0, \quad \text{(A.26a)}$$

$$\hat{C}_t(y,0) = C_t(y,0) - f(0)\tilde{C}_t(y) = 0, \quad \text{(A.26b)}$$

The boundary conditions are:

$$\hat{C}_m(y,t)|_{y=0} = C_m(y,t)|_{y=0} - f(t)\tilde{C}_m(y)|_{y=0} = 0, \quad \text{(A.27a)}$$

$$\hat{C}_t(y,t)|_{y=H_m} = \lambda_{tm}\hat{C}_m(y,t)|_{y=H_m}, \quad \text{(A.27b)}$$

$$-D_m \frac{\partial \hat{C}_m(y,t)}{\partial y}|_{y=H_m} = -D_t \frac{\partial \hat{C}_t(y,t)}{\partial y}|_{y=H_m}, \quad \text{(A.27c)}$$

$$\hat{C}_t(y,t)|_{y=H_m+H_t} = C_t(y,t)|_{y=H_m+H_t} - f(t)\tilde{C}_t(y,t)|_{y=H_m+H_t} = 0, \quad \text{(A.27d)}$$

The concentration solutions $\hat{C}_m(y,t)$ and $\hat{C}_t(y,t)$ lead to a Fourier series solutions that takes the following form (Ozisik 1980)

$$\hat{C}_m(y,t) = \sum_{n=1}^{\infty} \frac{e^{-\mu_n^2 \frac{D_m}{H_m^2}t}}{N(\mu_n)} \hat{Y}_m(\mu_n, y)\left[F(\mu_n) + \int_{\tau=0}^{t} e^{\mu_n^2 \frac{D_m}{H_m^2}\tau} A(\mu_n, \tau)d\tau\right], y \in [0, H_m] \quad \text{(A.28a)}$$

$$\hat{C}_t(y,t)=\sum_{n=1}^{\infty}\frac{e^{-\mu_n{}^2\frac{D_m}{H_m{}^2}t}}{N(\mu_n)}\hat{Y}_t(\mu_n,y)\left[F(\mu_n)+\int_{\tau=0}^{t}e^{\mu_n{}^2\frac{D_m}{H_m{}^2}\tau}A(\mu_n,\tau)d\tau\right] \quad ,$$

$$y\in[H_m,H_m+H_t] \tag{A.28b}$$

where

$$N(\mu_n)=\int_0^{H_m}\left[\hat{Y}_m(\mu_n,y)\right]^2dy+\eta\int_{H_m}^{H_m+H_t}\left[\hat{Y}_t(\mu_n,y)\right]^2dy\,, \tag{A.29a}$$

$$F(\mu_n)=\int_0^{H_m}\hat{C}_m(y,0)\hat{Y}_m(\mu_n,y)dy+\eta\int_{H_m}^{H_m+H_t}\hat{C}_t(y,0)\hat{Y}_t(\mu_n,y)dy=0\,, \tag{A.29b}$$

$$A(\mu_n,\tau)=-\frac{df(\tau)}{d\tau}\left(\int_0^{H_m}\tilde{C}_m(y)\hat{Y}_m(\mu_n,y)dy+\eta\int_{H_m}^{H_m+H_t}\tilde{C}_t(y)\hat{Y}_t(\mu_n,y)dy\right). \tag{A.29c}$$

By using methods of separating variables and the orthogonal condition, we have

$$\hat{Y}_m(\mu_n,y)=\sin(\mu_n\sqrt{\frac{D_m}{D_t}}\frac{H_t}{H_m})\sin(\frac{\mu_n y}{H_m})\,, \tag{A.30a}$$

$$\hat{Y}_t(\mu_n,y)=\lambda_{tm}\sin(\mu_n)\sin(\mu_n\sqrt{\frac{D_m}{D_t}}\frac{H_m+H_t-y}{H_m})\,, \tag{A.30b}$$

$$\eta=1/\lambda_{tm}\,, \tag{A.30c}$$

The eigenvalues μ_n, were determined by solving the transcendental equation:

$$\lambda_{tm}\sqrt{\frac{D_t}{D_m}}\tan(\mu)+\tan(\mu\sqrt{\frac{D_m}{D_t}}\frac{H_t}{H_m})=0\,, \tag{A.31}$$

The eigenvalues μ can be calculated numerically using Brent's method, which combines bisection, secant, and inverse quadratic interpolation methods. The first five eigenvalues μ , are provided in Tables A.4 and A.5 at the end of this section.

Based on the expressions above, the analytical solutions for $C_m(y,t)$ and $C_t(y,t)$ can be obtained by using the Fourier series expansion, which results in

$$C_m(y,t) = \hat{C}_m(y,t) + f(t)\tilde{C}_m(y)$$
$$= \sum_{n=1}^{\infty} W_n \hat{Y}_m(\mu_n, y) \int_{\tau=0}^{t} e^{-\mu_n^2 \frac{D_m}{H_m^2}(t-\tau)} \frac{dC_m(y,\tau)|_{y=0}}{d\tau} d\tau + C_m(y,t)|_{y=0} \left(1 - \frac{1-\tilde{C}_m(y)|_{y=H_m}}{H_m} y\right), \tag{A.32a}$$

$$C_t(y,t) = \hat{C}_t(y,t) + f(t)\tilde{C}_t(y)$$
$$= \sum_{n=1}^{\infty} W_n \hat{Y}_t(\mu_n, y) \int_{\tau=0}^{t} e^{-\mu_n^2 \frac{D_m}{H_m^2}(t-\tau)} \frac{dC_m(y,\tau)|_{y=0}}{d\tau} d\tau + C_m(y,t)|_{y=0} \left(\frac{\lambda_{tm}\tilde{C}_m(y)|_{y=H_m}}{H_t}(H_m + H_t - y)\right), \tag{A.32b}$$

where

$$W_n = -\frac{\int_0^{H_m} \tilde{C}_m(y)\hat{Y}_m(\mu_n, y)dy + \eta \int_{H_m}^{H_m+H_t} \tilde{C}_t(y)\hat{Y}_t(\mu_n, y)dy}{N(\mu_n)}, \tag{A.33}$$

The coefficients W_n were calculated numerically to 4 decimal places and are tabulated in Tables A.4 and A.5. The value of $\tilde{C}_m(y)|_{y=H_m}$ is determined from the steady state solution, shown in Eq. (A.23).

Table A.1. The first five eigenvalues μ and coefficients W (g/cm^3) for the ET_2 model **MTB** wall.

Acetaldehyde		Benzene	
μ_1= 0.5092	W_1=-8.5258×10^{-5}	μ_1=0.4050	W_1=-1.8697×10^{-8}
μ_2=0.9992	W_2=3.3998×10^{-5}	μ_2=0.8708	W_2=3.4088×10^{-9}
μ_3=1.4243	W_3=-2.7282×10^{-5}	μ_3=1.3677	W_3=-1.4458×10^{-9}
μ_4=1.7934	W_4=2.1203×10^{-5}	μ_4=1.8712	W_4=1.1024×10^{-9}
μ_5=2.2359	W_5=-1.5109×10^{-5}	μ_5=2.3646	W_5=-1.4375×10^{-9}

Table A.2. The first five eigenvalues μ and coefficients W (g/cm^3) for the BB model **MTB** wall.

Acetaldehyde		Benzene	
μ_1=0.3469	W_1=-1.1550×10^{-4}	μ_1=0.2903	W_1=-2.7590×10^{-8}
μ_2=0.6905	W_2=3.6056×10^{-5}	μ_2=0.6044	W_2=5.3716×10^{-9}
μ_3=1.0244	W_3=-2.3299×10^{-5}	μ_3=0.9366	W_3=-2.0081×10^{-9}
μ_4=1.3343	W_4=2.0736×10^{-5}	μ_4=1.2772	W_4=1.1003×10^{-9}
μ_5=1.8954	W_5=1.3921×10^{-5}	μ_5=1.9639	W_5=7.6020×10^{-10}

Table A.3. The first five eigenvalues μ and coefficients W (g/cm^3) for the bb model **MTB** wall.

Acetaldehyde		Benzene	
μ_1=0.6625	W_1=-7.2539×10^{-5}	μ_1=0.5099	W_1=-1.4215×10^{-8}
μ_2=1.2579	W_2=3.6264×10^{-5}	μ_2=1.1278	W_2=2.6088×10^{-9}
μ_3=1.7129	W_3=-2.7475×10^{-5}	μ_3=1.7827	W_3=-1.4502×10^{-9}
μ_4=2.2560	W_4=1.9307×10^{-5}	μ_4=2.4215	W_4=1.9762×10^{-9}
μ_5=2.9062	W_5=-3.7751×10^{-5}	μ_5=2.9732	W_5=-8.2184×10^{-9}

Table A.4: The first five eigenvalues μ and the coefficients W for the ET_2 model **AMTB** wall.

Acetaldehyde		Benzene	
μ_1= 0.5092	W_1=-1.4549	μ_1=0.4050	W_1=-1.3355
μ_2=0.9992	W_2=0.5802	μ_2=0.8708	W_2=0.2435
μ_3=1.4243	W_3=-0.4656	μ_3=1.3677	W_3=-0.1033
μ_4=1.7934	W_4=0.3618	μ_4=1.8712	W_4=0.0787
μ_5=2.2359	W_5=-0.2578	μ_5=2.3646	W_5=-0.1027

Table A.5. The first five eigenvalues μ and coefficients W for the BB model **AMTB** wall.

Acetaldehyde		Benzene	
μ_1=0.3469	W_1=-1.9710	μ_1=0.2903	W_1=-1.9708
μ_2=0.6905	W_2=0.6153	μ_2=0.6044	W_2=0.3837
μ_3=1.0244	W_3=-0.3976	μ_3=0.9366	W_3=-0.1434
μ_4=1.3343	W_4=0.3538	μ_4=1.2772	W_4=0.0786
μ_5=1.8954	W_5=0.2376	μ_5=1.9639	W_5=0.0543

VITA

GENG TIAN

401 West Main Street, Room E3235, Richmond, VA 23284-3015, P.O. Box 843015
tiang@vcu.edu, 804 564-3544

EDUCATION

- **Ph.D. Candidate in Mechanical Engineering** (May, 2011)
  Virginia Commonwealth University (VCU), VA USA

- **Ph.D. Candidate in Computer Science** (2005-2007)
  University of Saskatchewan (U of S), SK Canada

- **Master of Science in Math and Computer Science** (2005)
  Saint Mary's University (SMU), NS Canada

- **Bachelor of Science in Computer Science** (2002)
  Xi'an University of Science and Technology (XUST), Xi'an China

PUBLICATIONS

Journal Articles:

- Tian, G and Longest, P. W. (2010) Transient Absorption of Inhaled Vapors into a Multilayer Mucus-Tissue-Blood System. *Annals of Biomedical Engineering,* 38(2), 517-536. (IF=2.409)

- Tian, G and Longest, P. W. (2010) Development of a CFD Boundary Condition to Model Transient Vapor Absorption in the Respiratory Airways. *Journal of Biomechanical Engineering.132*(5), 051003. (IF=1.6)

- Tian, G. and Longest, P. W. (2010) Application of a New Dosimetry Program TAOCS to Assess Transient Vapor Uptake in the Upper Airways. *Inhalation Toxicology, 22*(13), 1047-1063. (IF=3.202)

- Tian, G., Longest, P. W., Su, G., and Hindle, M. (2011) Characterization of Respiratory Drug Delivery with Enhanced Condensational Growth (ECG) using an Individual Path Model of the Entire Tracheobronchial Airways. *Annals of Biomedical Engineering*, 39(3), 1136-1153. (IF=2.409)

- Longest, P. W., Tian, G., and Hindle, M. (2011) Improving the Lung Delivery of Nasally Administered Aerosols during Noninvasive Ventilation- An Application of Enhanced Condensational Growth (ECG), *Journal of Aerosol Medicine and Pulmonary Drug Delivery*, 24(2), 103-118. (IF=1.824)

Conference Abstracts:

- Tian, G., Hindle, M, Longest, P.W., Su, G.G. (2010) An initial analysis of enhanced condensational growth (ECG) for respiratory drug delivery. BMES Annual Meeting (October 6-9), Austin, TX. (Presentation and peer-reviewed abstract)

- Hindle, M., Tian, G., Longest, P.W. (2009) Enhanced condensational growth of submicrometer aerosol droplets investigated using in vitro and numerical lung models. AAPS Annual Meeting (November 8-12), Los Angeles, CA. (Poster, presentation, and peer-reviewed abstract)

- Longest, P. W., Hindle, M., and Tian, G. (2009) Improved inhalation drug delivery of submicrometer aerosols through enhanced condensational growth: Numerical and experimental proof of concept studies. AAAR Annual Conference (October 26 – 30), Minneapolis, MN. (Invited presentation and peer-reviewed abstract)

- Tian, G. (2006) Numerical Simulation of Multiphase Flows, MITACS-CAIMS Annual Conference, Toronto, June 15-20.

AWARDS

- Virginia Commonwealth University Graduate Students Scholarship, Sept. 2007 – Dec. 2010

- University of Saskatchewan Graduate Students Scholarship, Sept. 2005 – Feb. 2007

- Saint Mary's University Graduate Students Scholarship, Sept. 2003 – Aug. 2005

- Excellent graduate of Xian University of Science and Technology, July 2002

- First-Class Student Scholarship, Excellent Student Scholarship Award of Xi'an University of Science and Technology, Sept. 1999 – July 2002